Chemical Tuning of Topological Materials

Mahmoud Elgaml

A thesis submitted in part fulfilment of the requirements for the degree of Doctor of Philosophy at the University of Oxford

St Edmund Hall

University of Oxford

June 2023



Abstract

Chemical Tuning of Topological Materials

DPhil Thesis Mahmoud Elgaml June 2023

This DPhil project is titled the 'Chemical Tuning of Topological Materials' in accordance with the Leverhulme grant project, which funded this work. However, this DPhil has moved to cover a broader topic covering materials that are not strictly topological. In this thesis, three distinct systems are investigated, with the common theme being that they are layered chalcogenide materials.

Intercalation of alkali and alkaline earth metals into $ZrSe_3$ is shown here to have a significant effect on the selenide dimer linkages. PXRD studies on K, Rb and Cs intercalations will be compared to a high-temperature synthesis variant previously reported, where it will be shown that different polymorphs are obtainable at low temperatures. For example, for K_xZrSe_3, previous authors reported a structure with an *Immm* space group when synthesised at high temperatures. However, using low-temperature soft chemistry allows access to the $Cmc2_1$ structure, and the opposite is true for Cs_xZrSe_3. The structures are related to each other by the relative shifting of the $ZrSe_3$ layers. The intercalation of Ca using liquid ammonia is shown here to facilitate the co-intercalation of the solvent. This resulted in severe stacking faults, which are modelled in this thesis.

The $Nb_2Pd_xCh_5$ (*Ch* = S, Se) is a family of superconductors. $Nb_2Pd_{0.74}S_5$ (T_c of 6.5 K) is intercalated with Li/NH_3 or electrochemically to produce a phase with expanded lattice parameters. The structure maintains the *C*2/*m* symmetry and rigidity due to the PdS_4 units linking the layers. Experimental and computational analysis showed that Li occupies triangular prismatic sites between the layers with an occupancy of 0.33(4). This level of intercalation suppresses the superconductivity. Deintercalation using I_2 is shown to partially restore the superconductivity. Electrochemical intercalation reproduces the chemical intercalation product at low Li content (< 0.4), but at higher Li contents (≥ 0.4) accessed by this route, phase separation occurs with the indication that Li occupies another site. Similar results are found for the $Nb_2Pd_{0.82}Se_5$ superconductor (T_c of 4.5 K). However, for the selenide, PND was not sufficient to locate Li and the combination of Li NMR and DFT suggest Li may occupy the octahedral site with ICP-MS suggesting an occupancy of 0.87.

The final system investigated is $A_2Ga_2S_5$ (*A* = Mn, Fe), consisting of a buckled-honeycomb lattice which, in theory, could allow long-range magnetic ordering. However, the spin-glass behaviour of these systems using SQUID magnetometry will be shown, along with the absence of any sharp magnetic peaks using PND. A broad Warren-like peak is observed and can be modelled, indicating 2D magnetic behaviour with a very short correlation length. The diffuse peak will also be modelled using Monte Carlo simulations. The solid-solution $Mn_{2-x}Fe_xGa_2S_5$ is synthesised here for the first time, and the transition from the 1*T* (*P*-3*m*1) polytype to the 3*R* (*R*-3*m*) polytype is seen. The glassy behaviour remains, and an increase in the spin-freezing temperature with *x* is shown.

Acknowledgements

First and foremost, I am grateful to God for blessing me with this opportunity to spend some of the best years of my life here.

I want to thank my supervisor Prof. Simon Clarke for being an endless source of guidance, knowledge, enthusiasm, and support and for helping me shape this thesis. I have learnt so much being here, and I am extremely grateful to be a part of this group.

This DPhil experience would have been a fraction of what it is without the wonderful people I have been surrounded with. I feel fortunate to say that I have been going to work with some of my best friends. Brad and Penny, I thank them both for being a constant source of laughter and entertainment since Part II. I will look back at our time together with great fondness. I thank Rob, the final member of the "core four", for the unforgettable warzone memories and for being my table tennis rival. I want to thank Dr Simon Cassidy for showing me the ways of the TOPAS and for support on the SQUID and X-ray machines. To Drs Viktoria Falkowski, Machteld Kamminga, Shunsuke Sasaki, Nicola Kelly, Xabier Martinez de Irujo-Labalde and Bertold Rasche, I thank them for showing me that you can still have fun whilst being a post-doc. I thank Vicky for the help with SEM and the games nights. I thank Machteld for importing the finest Dutch cuisine. I thank Shunsuke for his boundless energy, which seems to increase as the evening goes on. I thank Nicola for being one of the kindest people I've met. I thank Xabi for the corridor chats and the very occasional chemistry knowledge.

I want to thank other DPhils of the group: Souvik for his enthusiasm for chemistry, football, and ringtones; Mila for getting me involved with badminton which I thoroughly enjoyed; Lexy for the baked goods; Xiaoyu for the panda biscuits and Katie for finding the mylar.

To the Part IIs who have come and gone during my time: James, Max, Ben, Billy, Emily, Fergus, Lemuel, Jamie, Henry, Adam and Saumitra, I thank them all for adding to the wholesome atmosphere of the group.

I am grateful to all the collaborators whom, without, this thesis would be much smaller and less interesting: Dr Sunita Dey (Cambridge) for carrying out electrochemical intercalations and NMR, Jiayi Cen (UCL) for all the computational help, Prof. Max Avdeev (ANSTO), Dr Ron Smith (ISIS) and Dr Pascal Manuel (ISIS) for neutron measurements on my samples. I also thank Dr Pascal Manuel for teaching me Monte-Carlo simulations, Eric Yang for help with Raman spectroscopy and Dr Dharmalingam Prabhakaran (Oxford Physics) for help with heat capacity measurements.

Finally, I owe an enormous amount of gratitude to my family for always having my back and putting up with my absence, and to Nadine, for always brightening up my day.

Table of Contents

1 Introduction 1

1.1 Solid-State Chemistry 1

1.2 Layered Materials 4

1.2.1 Binary Chalcogenides 5

1.2.1.1 Transition Metal Dichalcogenides (TMDC) 6

1.2.1.2 Transition Metal Trichalcogenides (TMTC) 6

1.2.2 Ternary Chalcogenides 9

1.2.2.1 $M_xX_yCh_z$ (M = Nb, Ta; X = Ni, Pd; Ch = S, Se, Te) 10

1.2.2.2 MGa$_2$S$_4$ and A_2Ga$_2$S$_5$ (M = Fe, Ni; A= Mn, Fe) 11

1.2.3 Topochemical Intercalation Chemistry 12

1.3 Band Theory 16

1.4 Magnetic Properties of Solids 19

1.4.1 Diamagnetism 19

1.4.2 Paramagnetism 19

1.4.2.1 Pauli Paramagnetism 19

1.4.2.2 Curie Paramagnetism 20

1.4.3 Ferromagnetism 21

1.4.4 Antiferromagnetism 22

1.4.5 Curie-Weiss Law 23

1.4.6 Frustration and Spin Glass Behaviour 24

1.4.6.1 AGa$_2$S$_4$ (A = Fe, Ni) 25

1.5 Magnetic Exchange Mechanism 26

1.5.1 Direct Exchange 26

1.5.2 Superexchange 26

1.6 Superconductivity 28

1.6.1 Conventional Superconductivity 28

1.6.2 Bardeen-Cooper-Schrieffer (BCS) Theory 29

1.6.3 Cuprate Superconductors 32

1.6.4 Chalcogenide and Pnictide Superconductors 32

1.7 Aims of the Thesis 33

2 Experimental Methods 36

2.1 Synthetic Techniques 36

2.1.1 Ceramic Synthesis 36

2.1.2 Air-sensitive Synthesis 36

2.1.3 Topotactic Synthetic Methods 37

2.1.3.1 *n*-butyllithium Intercalation 38
2.1.3.2 Metal/naphthalene Intercalation 39
2.1.3.3 Metal/ammonia Intercalation 39
2.1.3.4 Deintercalation using Iodine 39
2.1.3.5 Electrochemical Intercalation 40
2.2 Characterisation Techniques 41
2.2.1 Diffraction 41
2.2.2 X-ray Diffraction 41
2.2.2.1 Powder X-ray Diffraction 45
2.2.2.2 Laboratory Powder X-ray Diffraction 47
2.2.2.3 Bruker D8 Advance Eco Diffractometer 48
2.2.2.4 PANalytical Empyrean & PANalytical X'pert Diffractometers 49
2.2.3 Synchrotron X-ray Diffraction 49
2.2.3.1 I11 Beamline, Diamond Light Source 52
2.2.4 Neutron Powder Diffraction 53
2.2.4.1 POLARIS (ISIS, TS1) 57
2.2.4.2 WISH (ISIS, TS2) 58
2.2.4.3 Echidna (ANSTO) 58
2.2.5 Structural Refinement 59
2.2.5.1 Rietveld Refinement 59
2.2.5.2 Pawley Refinement 61
2.2.6 SQUID Magnetometry 61
2.2.6.1 DC Magnetometry 62
2.2.6.2 Superconductivity 66
2.2.6.3 AC Magnetometry 67
2.2.7 X-ray Absorption Spectroscopy (XAS) 68
2.2.8 SEM-EDX 71
2.2.9 Nuclear Magnetic Resonance (NMR) Spectroscopy 72
2.2.9.1 Solid-state ^{7}Li NMR 73
2.2.10 Computational Methods 74
2.2.10.1 Density Functional Theory (DFT) 74
2.2.10.2 Monte Carlo Simulations 75
2.2.11 Raman Spectroscopy 76
2.2.12 Elemental Analysis 77
2.2.12.1 ICP-MS 77
2.2.12.2 Dumas Combustion Method 78
2.2.13 Specific Heat Capacity 78
3 Intercalation reactions of $ZrSe_3$ 80

3.1 Introduction 80
3.2 $ZrSe_3$ 82
3.3 K Intercalation 83
3.4 Rb Intercalation 87
3.5 Cs Intercalation 90
3.6 Discussion and Comparison 93
3.7 Ca Intercalation 95
3.7.1 Stacking Fault Refinement 98
3.7.2 Low-temperature Structure 109
3.7.3 Variable Temperature XRD 112
3.8 Magnetometry 113
3.9 Raman Spectroscopy 115
3.10 Conclusion 117
4 Li Intercalation of $Nb_2Pd_xCh_5$ (*Ch* = S, Se) 120
4.1 Introduction 120
4.2 $Nb_2Pd_xS_5$ 122
4.2.1 Synthesis and characterisation of $Nb_2Pd_xS_5$ 122
4.2.2 Chemical Intercalation 126
4.2.3 Lithium Intercalate 127
4.2.3.1 Powder X-ray Diffraction 127
4.2.3.2 Powder Neutron Diffraction 129
4.2.3.3 ^{7}Li NMR Spectroscopy and DFT Calculations 132
4.2.3.4 Lithium Site 135
4.2.3.5 Deintercalation 138
4.2.4 Magnetometry 139
4.2.5 Electrochemical Intercalation 143
4.3 $Nb_2Pd_xSe_5$ 151
4.3.1 Synthesis and characterisation of $Nb_2Pd_xSe_5$ 151
4.3.2 Chemical Intercalation 157
4.3.3 Powder X-ray and Neutron Diffraction 162
4.3.4 Electrochemical Intercalation 166
4.3.5 DFT Calculations and ^{7}Li NMR Spectroscopy 170
4.3.6 Deintercalation 176
4.3.7 Magnetometry 177
4.3.8 XANES 181
4.4 Conclusions 182
5 Magnetic Behaviour of $A_2Ga_2S_5$ (*A* = Mn, Fe) 187
5.1 Introduction 187

5.2 Synthesis and Characterisation 190
5.2.1 $Mn_2Ga_2S_5$ 190
5.2.2 $Fe_2Ga_2S_5$ 195
5.3 Magnetism 199
5.3.1 SQUID Magnetometry 199
5.3.2 Powder Neutron Diffraction 206
5.3.3 Monte Carlo Simulation 210
5.3.4 Heat Capacity 220
5.4 Discussion 221
5.5 $Mn_{2-x}Fe_xGa_2S_5$ 226
5.5.1 Characterisation 226
5.5.2 Magnetometry 232
5.6 Conclusion 237
6 Summary and Conclusions 240
References 247
Appendix I i
Appendix II iii
Appendix III iv

Chapter 1

1 Introduction

1.1 Solid-State Chemistry

Solid-state Chemistry is a broad and well-established area of study focusing on the synthesis, structure, properties, and subsequent application of materials in the solid state. To correlate a given material's structure with its properties is fundamental in designing materials for application. This was made possible by the pioneering work of Max von Laue and W.H. and W.L. Bragg in the early 20th century. Their investigation into how X-rays interact with a crystal led to the discovery of the technique to probe the atomic structure of a material, which is now the foundation of solid-state chemistry. More recently, this field has been strongly driven by technology, and much of our everyday lives involves solid-state chemistry without one necessarily realising it. The most notable are rechargeable Li-ion batteries found in our mobile phones and other portable devices based on the $LiCoO_2$ cathode.[1] Other examples include silicon-doped transistors and hard disks found in computers which use ferromagnetic materials such as γ-Fe_2O_3 and CoPtCr.[2,3] Traditional filament bulbs are being replaced by more efficient light-emitting diodes (LEDs) based on GaN.[4] Touch-screen panels in many electronic devices use indium tin oxide (ITO) due to its high optical transparency and electrical conductivity.[5] Both these properties also make ITO applicable in aircraft windshields.[5] A voltage can be applied across the ITO film, generating heat, which defrosts the windshield. Some applications are more subtle, such as white TiO_2 with a large refractive index due to a band gap that lies just outside the visible region, giving TiO_2-based white paint its high opacity.[6] Advancement in solid-state chemistry has also led to progression in other fields, such as the medical field. Superconducting magnets have been developed using

materials, for example, Nb-Ti alloy, for application in medical instruments such as MRI machines, as they enable a large magnetic field to be generated.[7]

The main challenge in designing new materials is the synthesis. Targeting a specific material or composition can be difficult as there is relatively little control when carrying out a typical reaction in the solid state at high temperatures. In a solid-state reaction, the reorganisation of atoms has a large kinetic barrier which usually cannot be overcome at ambient temperatures. Instead, high temperatures (500-1500 °C) are needed to overcome the barrier. Even with elevated temperatures, the reaction may take many hours, days, or weeks due to the slow diffusion of atoms in the solid state. This process is often referred to as 'ceramic synthesis'. The result of this is that the most thermodynamically stable products are formed. This is a limitation if the target composition with the desired properties is not the most thermodynamically stable. However, this does not mean only one product can be accessed in ceramic synthesis. Differing temperatures can favour the formation of one phase over another. Some phases are only metastable in that they will not form when slowly cooled and instead can be obtained by quenching from high temperature immediately to low temperature.

Since ceramic synthesis allows access to thermodynamically stable products, 'soft chemistry' is used to achieve metastable kinetic products that are otherwise inaccessible via ceramic synthesis. Soft chemistry refers to the use of low-temperature methods to favour kinetics over thermodynamics. Examples include intercalation reactions (section 1.2.3) which involve inserting ions/molecules into a host structure. The classic example is the famed $LiCoO_2$ battery.[1] The layered structure of $LiCoO_2$, due to Co^{3+} strongly polarising the O^{2-} anion, gives a low barrier to small cation mobility within the interlayer space. Layered chalcogenides, such as TiS_2, also have low barriers to small cation mobility, and the

coulombic interaction between the small cation intercalant and the chalcogen can overcome the weak van der Waals interaction between the layers. Chapters 3 and 4 of this thesis will investigate these reactions.

Another example is low-temperature reductions using metal hydrides. Metal hydrides such as NaH and CaH_2 are powerful reducing reagents and are very effective in producing highly reduced oxides such as $LaNiO_2$ from a $LaNiO_3$ precursor and Sr_2FeO_3 from a Sr_2FeO_4 precursor.[8,9] These highly reduced oxides are inaccessible using traditional ceramic methods. New and novel methods are constantly being developed to achieve new compositions and structures. For instance, the formation of $SrCoO_2$ from $SrCoO_{2.5}$ by first electrochemically protonating to form $HSrCoO_{2.5}$, then dehydrating to $SrCoO_2$.[10] The electrochemical protonation destabilises the precursor and significantly changes the reaction energy landscape allowing $SrCoO_2$ to form. The structure goes from a brownmillerite structure type to one with square spin tubes.

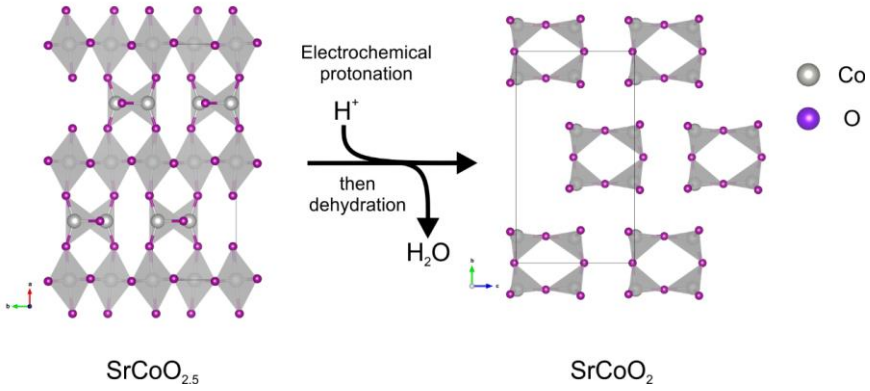


Figure 1.1: The reaction of $SrCoO_{2.5}$ forming $SrCoO_2$ with a unique square spin tube structure.[10] Only the Co coordination is shown here to showcase how the Co environment changes.

Out of all the solid-state compounds, oxides are the most explored and studied class of compounds due to their inherent stability and ease of availability. Synthesis of oxides tends to be the simplest as precursors are reacted at high temperatures in standard atmospheric conditions. Compounds that are non-oxides and mixed-anions are less investigated in part to

their general lower abundance in nature but mainly due to the lower stability compared to oxides which result in oxidation or hydrolysis of these compounds when they are formed or stored in air. Synthesis of non-oxide and mixed-anion materials is usually more complex as it involves using air-sensitive techniques.

1.2 Layered Materials

The differences between oxides and non-oxide compounds are further highlighted in the type of crystal structures adopted. These structures reflect the general bonding interactions these anions prefer. In oxides, ionic bonding (*i.e.* 'hard' interactions) is the most dominant as it maximises the Coulombic potential. In contrast, chalcogenides and pnictides have a greater preference for 'soft' interactions due to the higher polarisability of the anion. These include covalency with the metal centre or another anion to form dimers and van der Waals interaction between two polarisable anions.[11] The higher polarisability allows many non-oxide and mixed-anion compounds to adopt two-dimensional layered structures where van der Waals interactions bridge the layers. A good example to showcase this difference is the comparison of TiO_2 and TiS_2. TiO_2 adopts a three-dimensional arrangement of the TiO_6 octahedra. Whereas for TiS_2, the larger S^{2-} anion is more easily polarised by Ti^{4+}. As a result, TiS_2 adopts a layered arrangement of TiS_6 octahedra, with the layers separated with a van der Waals gap.

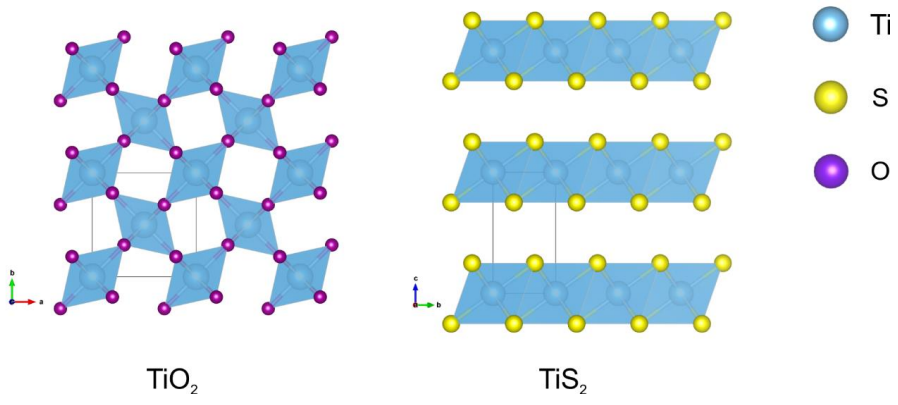


Figure 1.2: Structures of TiO_2 (left) and TiS_2 (right), showing how the anion influences the structure.

In the case of mixed-anion compounds, the different anions are separated into different layers. A good example is $CeAg_{0.8}OS$ which adopts the ZrCuSiAs structure type adopted by over 150 different compounds.[12,13] Here, the structure can be seen as alternating Ce-O and Ag-S layers described as PbO and anti-PbO type, respectively. Ionic bonding dominates the Ce-O layer between the hard Ce^{3+} and O^{2-} ions, whereas the Ag-S layer has greater covalent character due to the highly polarisable Ag^{+} and S^{2-} ions. Ag can be removed chemically from its tetrahedral site, causing a collapse in the structure with oxidation of Ce^{3+}.[14] CeSO adopts the PbFCl structure type, again a common structure type for mixed-anions with over 200 examples.[15] The removal of Ag results in a van der Waals gap between the S, which can be exploited (see section 1.2.3)

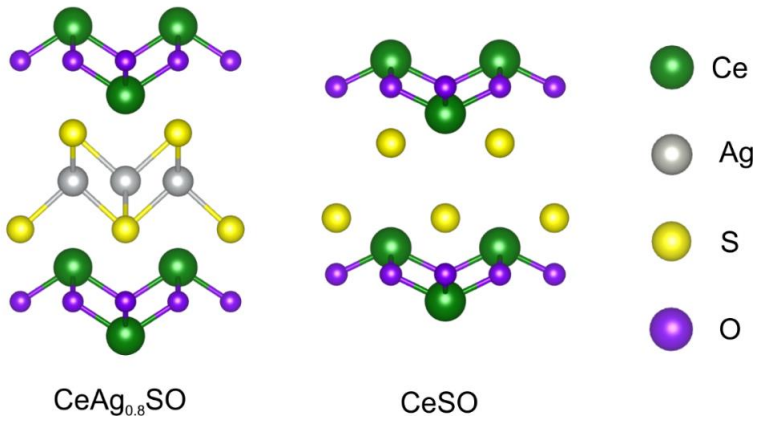


Figure 1.3: Left: $CeAg_{0.8}SO$ adopting the ZrCuSiAs type.[12,13] Right: CeSO adopting the PbFCl structure type.[15]

1.2.1 Binary Chalcogenides

With the number of combinations of electropositive metal with chalcogen possible, numerous binary metal chalcogenides are known. With many chalcogenide compounds having a large preference for adopting two-dimensional structures,[11] over two-thirds of binary chalcogenides are layered. This area is very diverse, with various structures and properties exhibited.

1.2.1.1 Transition Metal Dichalcogenides (TMDC)

Early series TMDCs such as TiS_2 contain sulfide ions, S^{2-}, and there is no chalcogenide-chalcogenide bonding.[16] The layered structure and the reducible transition metal enable the Li_xTiS_2 ($0 < x < 1$) system to be used as a prototypical positive electrode material in a Li-ion secondary battery.[17] Other layered TMDCs display a range of desirable properties. For example, MoS_2 is an excellent lubricating material due to the weak van der Waals interactions resulting in a low coefficient of friction.[18] The presence of catalytically active sites in the structure makes MoS_2 a candidate for catalysis in hydrogen evolution reactions.[19,20] WTe_2 has been shown to exhibit large magnetoresistance, and $NbSe_2$ exhibits superconductivity.[21,22] Moving across the periodic table, the high oxidation states of the metals become difficult to stabilise, and one finds chalcogenide-chalcogenide bonds in MnS_2 and FeS_2 with divalent metal cations and disulfide $[S_2]^{2-}$ ions and the structures are no longer layered.[23]

1.2.1.2 Transition Metal Trichalcogenides (TMTC)

Transition metal trichalcogenides (TMTCs) are another member of the extensive layered chalcogenide family. Although TMTCs are less studied than dichalcogenide variants, it has been proposed that they may have technological potential in optoelectronic, nanoelectronic and photovoltaic applications.[24–26] This results from some of their structures being viewed as pseudo-one-dimensional,[27] offering strong anisotropy in their optical and electrical properties. For example, TiS_3 is a promising candidate for field-effect transistors and photodetectors.[28,29] TiS_3 has also been explored as a potential electrode material in Li- and Na-ion batteries.[30] $ZrTe_3$ has been reported to exhibit superconductivity at ~ 2 K as well as a charge density wave (CDW) distortion at 63 K.[31–33]

TMTCs consist of the formula MCh_3 (*Ch* = S, Se, Te), where *M* belongs to the group IV (Ti, Zr, Hf) or V (Nb, Ta) transition metals. Group VI (Mo, W) trichalcogenides have been synthesised but have been reported to be amorphous compounds.[34] The structures are based on covalently bonded layers held together by van der Waals forces. The layer consists of slightly distorted MCh_6 triangular prisms stacked infinitely along the *b* axis where it can be viewed as pseudo one-dimensional.

The group IV trichalcogenides (*M* = Ti, Zr, Hf) all adopt the same $ZrSe_3$ type monoclinic structure with the $P2_1/m$ space group. This layered structure, shown in Figure 1.4, consists of MCh_6 triangular prisms stacked via shared faces to form infinite chains extending along the *b*-axis. These prisms are bi-capped (i.e. capped on two of their rectangular faces), with *M* coordinating to 2 *Ch* in the neighbouring chains. This gives each *M* a coordination number of 8 and forms layers of chains in the *ab* plane. MCh_3 is conveniently represented as $M^{4+}[Ch^{2-}][Ch_2]^{2-}$. The $[Ch_2]^{2-}$ dimers form the base of the prism and are parallel to the *a*-axis.[35–37]

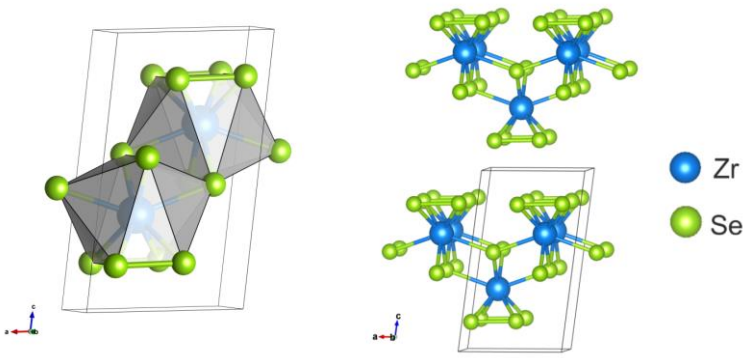


Figure 1.4: The $ZrSe_3$ structure type.

When the structures of MCh_3 were first determined by Furuseth *et al.* in the 1970s, two different structural variants (type A and B) in $P2_1/m$ were reported for MCh_3.[38] The two variants were viewed as almost mirror images, where for the *x* coordinate of the *M* and *Ch*

atoms, $x_A = 1\text{-}x_B$. Given the $P2_1/m$ symmetry reported, this resulted in type B having an unusually large spread of *M-Ch* distances. In 1991, Furuseth *et al.* re-examined the crystal structure of $ZrTe_3$ and found that all group IV MCh_3 adopt type A and that the existence of type B was doubtful.[39] The structural determination of these layered structures is challenging even with single crystal diffraction studies because the layers can shift freely relative to each other, causing disorder in the stacking.

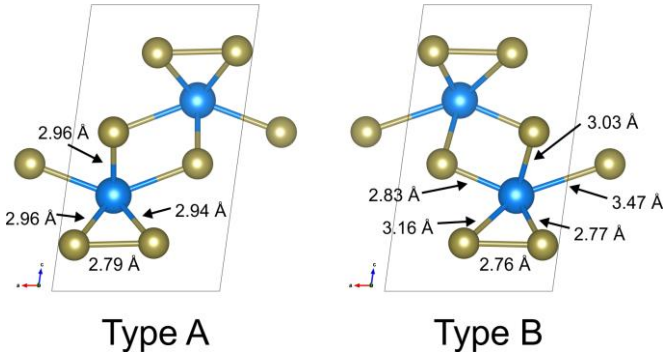


Figure 1.5: The two structural variants of $ZrTe_3$ that were initially reported.[38] Re-examination of the crystal structure led to type B being doubtful. [39]

On the other hand, group V TMTCs show differing structures. $TaSe_3$ and $NbSe_3$ are also both monoclinic crystallising with the $P2_1/m$ space group. However, unlike the one type of MCh_3 chain present in the $ZrSe_3$-type structure with a $[Se_2]^{2-}$ bond length of 2.34 Å in $ZrSe_3$,[38] they have two and three types of MCh_3 chains, respectively.

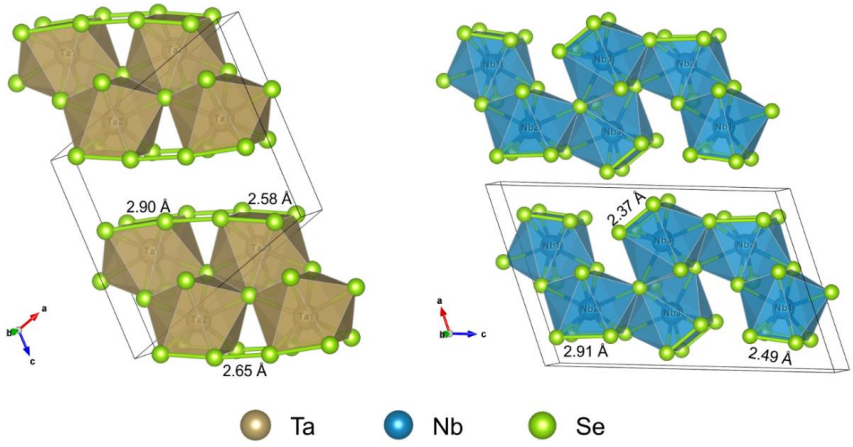


Figure 1.6: Structures of $TaSe_3$ (left) and $NbSe_3$ (right).

In $TaSe_3$, there are two types of prisms with Se-Se bond lengths of 2.58 Å and 2.90 Å, with the distance between them 2.65 Å.[40] These different bond lengths indicate the formal oxidation of the two Ta sites, with the short dimer suggesting Ta(2) is close to a 4+ oxidation state, whereas, with the long dimer, Ta(1) may be close to 5+ (stronger Ta-Se bonding and consequently weaker Se-Se bonding). In $NbSe_3$, the structure consists of short, medium and long Se dimers with bond lengths of 2.37 Å, 2.49 Å and 2.91 Å, respectively.[41] As seen in $TaSe_3$, this suggests that in the short dimer, Nb(3) is likely to be 4+ (similar bond length in $ZrSe_3$). The medium dimer suggests an intermediate oxidation state for Nb(1) between 4+ and 5+, and the long dimer indicates the Nb(2) site is nearly 5+.[42] The sulfides NbS_3 and TaS_3 differ somewhat from the selenides and crystallise in a triclinic and orthorhombic structure, respectively.[43,44]

1.2.2 Ternary Chalcogenides

The majority of transition metal chalcogenides reported are binary compounds. However, with the improvement in air-sensitive synthesis and characterisation methods, the 1970s and 1980s saw a wave of new ternary chalcogenides. The extra element makes this branch of chalcogenides extremely varied with more unique structures. The additional degree of freedom can lead to ternary chalcogenides competing with their binary counterpart in desirable properties and applications. For example, Ta_2NiS_5 has been reported to be a candidate for fluorescence sensors used in DNA detection due to its high fluorescence quenching ability.[45] The excellent selectivity and high sensitivity were found to exceed previously reported MoS_2-based sensors.[46] A large portion of ternary chalcogenides can be classified into transition metal/transition metal chalcogenide and transition metal/main group chalcogenide, two subsets this thesis will investigate.

1.2.2.1 $M_xX_yCh_z$ (M = Nb, Ta; X = Ni, Pd; Ch = S, Se, Te)

These families of compounds display diverse structural chemistry. From the highly two-dimensional, such as Ta_2NiSe_5 and Nb_2PdS_6,[47,48] to the structures with interlayer connectivity, for instance, in Nb_2PdSe_5.[49] Even more exotic structures are seen, such as a zig-zag arrangement of layers found in $Nb_2Pd_3Se_8$.[50]

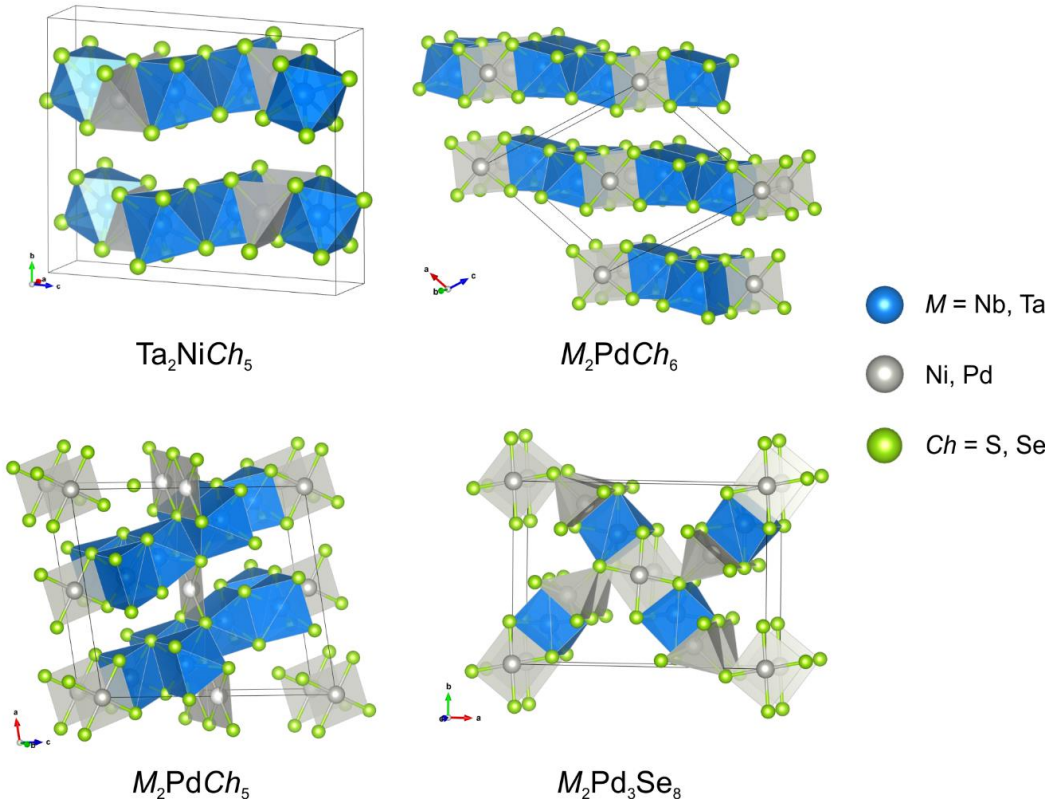


Figure 1.7: Structures of the ternary chalcogenides Ta_2NiCh_5, M_2PdCh_5, M_2PdCh_6 and $M_2Pd_3Se_8$.

Substitutional chemistry can tune structural and electronic properties, and new compounds have emerged by replacing Nb with Ta or Ni with Pd and Pt. Take Ta_2NiS_5, for instance; the structure is highly layered, consisting of TaS_6 octahedra and NiS_4 tetrahedra in chains along the *c*-axis. Substituting Ni for Pd results in a much-changed structure with layers consisting of TaS_6 and TaS_7 prisms and PdS_4 square planar with the layers connected by an additional square planar PdS_4, highlighting the difference in variation with respect to the ligand field of Ni compared to Pd. The material Ta_2PdS_5 now exhibits superconductivity at ~ 6 K.[51]

Substituting the chalcogen S in Ta_2NiS_5 for Se keeps the same arrangement of layers. However, the compound exhibits an excitonic insulating transition at 328 K.[52] In an excitonic insulator, below a critical temperature, electrons and holes in a semiconductor combine forming 'excitons', resulting in an insulating state (a schematic is shown in Figure 1.8).[53] Replacing S for Se raises the energy of the valence bands, reducing the band gap from 0.25 eV to 0.16 eV.[54] The band gap in Ta_2NiSe_5 is now smaller than the exciton binding energy, and the transition occurs. Compounds related to this family of compounds will be discussed in Chapter 4.

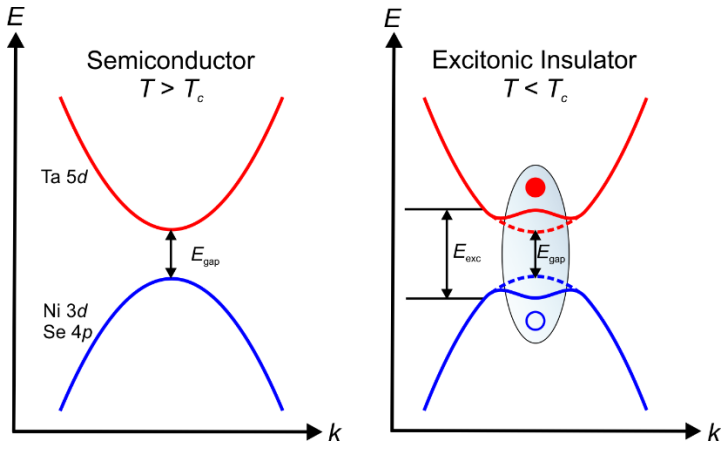


Figure 1.8: Schematic showing the excitonic transition to an insulating state for a narrow band gap semiconductor.

1.2.2.2 MGa$_2$S$_4$ and A_2Ga$_2$S$_5$ (M = Fe, Ni; A= Mn, Fe)

Another set of layered ternary chalcogenide compounds involves the transition metal gallium sulfides MGa$_2$S$_4$ and A_2Ga$_2$S$_5$ (M = Fe, Ni; A= Mn, Fe). The structure of MGa$_2$S$_4$ consists of slabs of two GaS layers consisting of GaS$_4$ tetrahedral sandwiching one MS$_2$ layer composed of octahedrally coordinated M.[55] In A_2Ga$_2$S$_5$, the MS$_2$ layer is replaced by A_2S$_3$. In essence, the compound is viewed as the bilayer variant of MGa$_2$S$_4$.[56] The main interest in these sets of compounds, especially for MGa$_2$S$_4$, is the arrangement of the metal sulfide layer. Here the

metal cations are arranged in a triangular lattice which introduces spin frustration (see section 1.4.6). Compounds related to this will be discussed in Chapter 5.

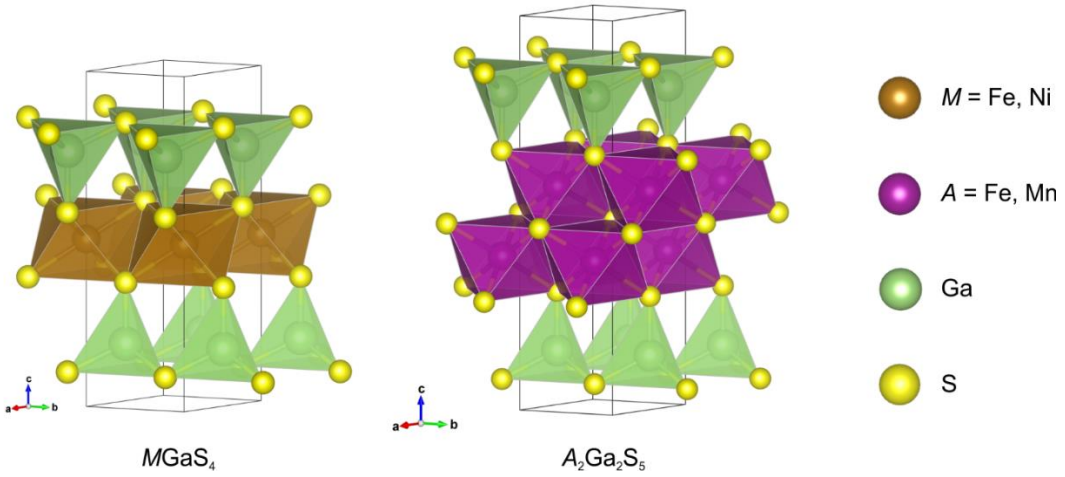


Figure 1.9: Structures of $(Fe/Ni)Ga_2S_4$ and its bilayer variant $(Fe/Mn)_2Ga_2S_5$.

1.2.3 Topochemical Intercalation Chemistry

With layered materials comes the ability to carry out topotactic reactions. Topotactic reactions insert (intercalate) or remove (deintercalate) ions, leaving the parent structure largely unchanged. In layered structures, this commonly occurs in the form of a guest ion inserted in the van der Waals gap between layers.

Intercalation chemistry has opened a door for applications, the most notable and profound being in battery technology. Many topotactic reactions using Li were carried out on TMDCs and TMTCs with the aim of finding practical materials for Li-ion batteries. Three Li ions were found to intercalate into TiS_3, but the reaction was not readily reversible. Hence TMTCs were found to be not ideal candidates for electrodes.[57] Intercalation into the layered TiS_2 was found to be a reversible process which led to TiS_2 being proposed as a potential candidate for cathodes.[17] However, its lower output voltage meant that its capability in batteries was soon found to be surpassed by $LiCoO_2$.[1]

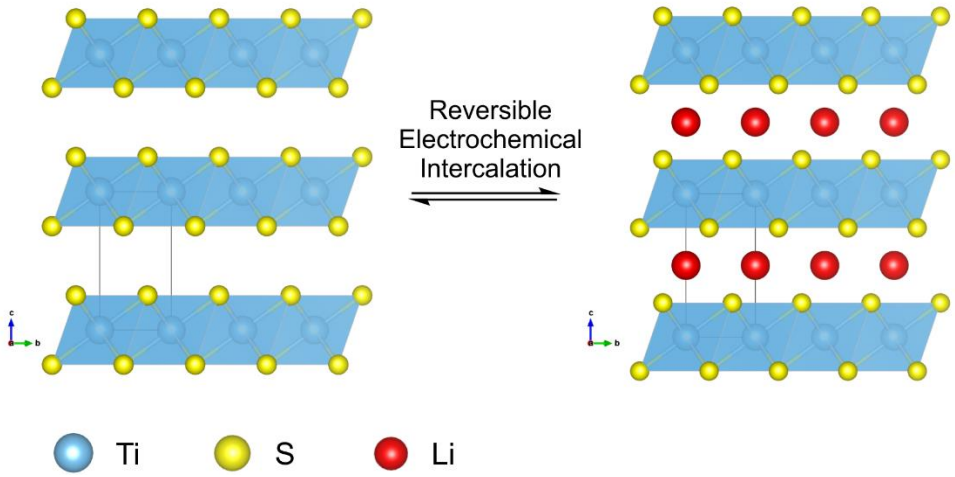


Figure 1.10: Electrochemical intercalation of Li into TiS_2.

Whilst most intercalation reactions involve the insertion of alkali metals between the layers, there are cases in which molecular species are also intercalated. The drive to find potential battery materials led to a surge in studies into other different ions and molecules that could be intercalated into transition metal chalcogenides. There are several different intercalation methods, such as sealed tube reactions with the host and intercalant in the vapour phase,[58] intercalations in solution,[59] and electrochemical intercalations using the corresponding salt as the electrolyte in aqueous solutions.[60] Topotactic methods used in this thesis will be discussed in section 2.1.3.

In recent times, FeSe has undergone novel and exotic intercalation chemistry. The tetragonal polymorph of FeSe is a superconductor with a transition temperature (T_c) of ~ 8 K.[61] First successful intercalation with alkali metal in a solution of ammonia was reported by Ying *et al.* to increase the interlayer spacing from 5.52 Å to 8-10.25 Å and the superconductivity to 30-46 K depending on the metal used.[62] It was first proposed that the structure of the intercalates was the common $ThCr_2Si_2$ structure type with simply the alkali metal inserted between the layers. This model was found to be unrealistic as there was no correlation between interlayer separation and the size of the cation. With the use of neutron diffraction, it was later shown by Burrard-Lucas *et al*. that in a Li intercalated FeSe sample,

ammonia/amide species were being co-intercalated into the structure with a formula of $Li_{0.6(1)}(ND_2)_{0.2(1)}(ND_3)_{0.8(1)}Fe_2Se_2$.[63] To take it further, Sedlmaier *et al.* showed using *in-situ* X-ray diffraction that an ammonia-rich intermediate phase exists before the sample was subject to vessel evacuation, which reduces the amount of ammonia in the system.[64] A similar case was later seen for Li/NH_3 intercalation of Bi_2Se_3.[65]

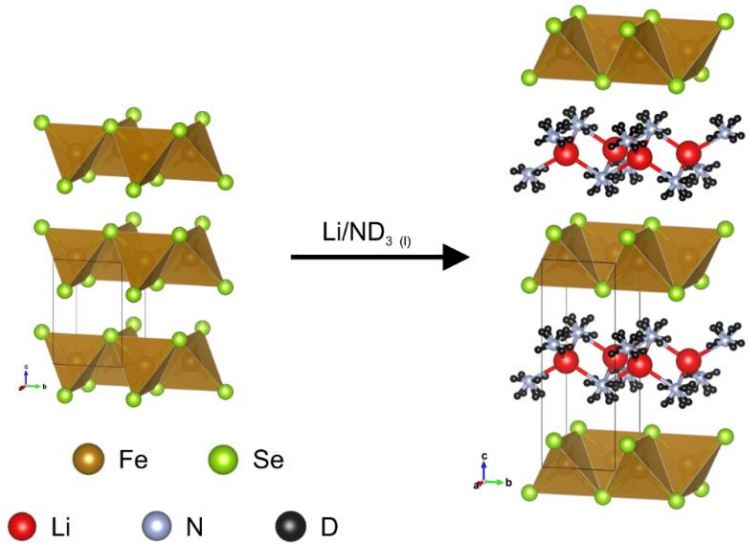


Figure 1.11: Li/NH_3 intercalation into FeSe.

FeSe was also found to intercalate Li via hydrothermal methods. Here, hydroxides are incorporated, giving a formula of $Li_{1-x}Fe_x(OH)Fe_{1-y}Se$ ($x \sim 0.2$; $0.02 < y < 0.15$).[66] In this structure, between the $Fe_{1-y}Se$ layers, one finds $Li_{1-x}Fe_x(OH)$ layers. This can be further manipulated by subsequently undergoing reductive lithiation.[67] It was shown that lithiation displaces the Fe in the $Li_{1-x}Fe_x(OH)$ layer (which acts as an iron reservoir) into the $Fe_{1-y}Se$ layer resulting in $Li_{1-x+y}Fe_{x-y}(OH)FeSe$. Once the FeSe layer is fully occupied, further lithiation expels the Fe out of the system as elemental Fe, approaching the compositional limit Li(OH)FeSe.

Along with reductive intercalation, as seen in the previous examples above, conversely oxidative deintercalation is also a route to manipulate phases in a topochemical manner.

$CeAg_xSO$ can be subjected to a solution of iodine which pulls out the highly mobile Ag from the system forming AgI and oxidises the Ce to Ce^{4+}, forming the metastable CeSO, which cannot be formed via ceramic synthesis.[14] The structure is defective and shows signs of faulting originating from the difficulty stabilising the high 4+ oxidation state in Ce in the presence of sulphide. This can then be subjected to electrochemical lithiation forming LiCeSO, which can also be formed directly from the $CeAg_xSO$ starting material via lithiation using *n*-BuLi. Deintercalation chemically using iodine or electrochemically can convert LiCeSO back to CeSO.

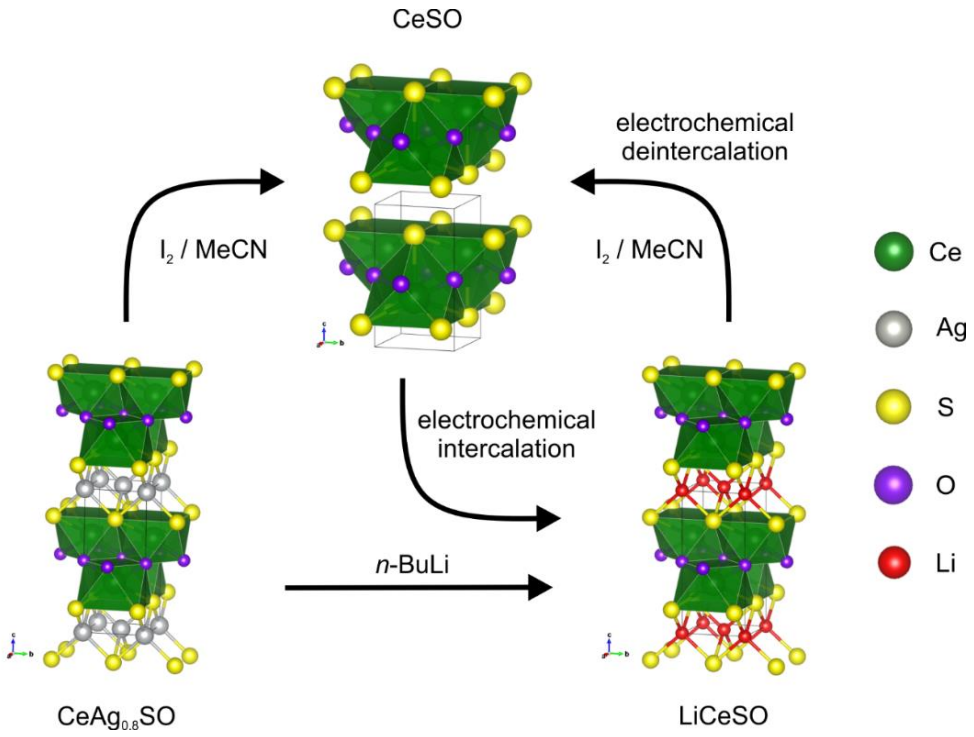


Figure 1.12: $CeAg_{0.8}SO$ reactions forming LiCeSO and CeSO.

The examples mentioned show the intercalation/deintercalation process involving the reduction or oxidation of the host structure. However, this can be limited by the ability of the host to maintain charge balance and structural stability. Koski *et al.* demonstrated a technique of zerovalent intercalation incorporating zerovalent metals such as Cu, Sn, Co, Fe and Ni into two-dimensional materials, including Bi_2Se_3, Sb_2Te_3 and GaSe.[68,69] This was

achieved using a solution disproportionation redox reaction or carbonyl decomposition. The typical ionic nature of the intercalant limits most intercalant concentrations. However, with a zerovalent intercalant, since no change in the oxidation state of the host structure is required, intercalations can proceed with a high concentration. Up to 60 atomic per cent of Cu^0 was reported to intercalate into Bi_2Se_3.[70] This was further extended to dual element intercalation.[71]

Since over two-thirds of the binary metal chalcogenides are layered, intercalation chemistry on these compounds has been extensively investigated. However, for ternary chalcogenides, intercalation chemistry is much less diverse. However, those that are layered have the potential for intercalation. Early reports on the Li intercalation into Ta_2NiSe_5 and Ta_2PdSe_6 showed that Li intercalation proceeds but with a substantial change in structure and loss of crystallinity.[72] Intercalations can bring forth more exotic properties, as seen in the ethylenediamine intercalation of Ta_2PdSe_6 reported to induce superconductivity with T_c = 4.5 K.[73]

1.3 Band Theory

In a free atom, electrons occupy atomic orbitals, each with a discrete energy level. In a crystal lattice, many atoms *n* come together, and the atoms' atomic orbitals overlap with orbitals nearby.[74] Each discrete energy level then splits into *n* levels with differing energies. On a macroscopic level, *n* is very large (~ 10^{22}), and thus the number of orbitals is very large, and the energies are very closely spaced. Since energies of adjacent levels are close together, they can be viewed as a continuous energy band. The width of the bands depends on the degree of overlap of the orbitals. If there is good overlap, the bands will be broad, and the density of states (defined as the number of crystal orbitals per unit volume in a given energy interval) will be small. The opposite is seen with poor overlapping orbitals. These energy

bands are particularly relevant to valence electrons as they are involved in chemical bonding and electrical conductivity. Core electrons have bands that are very narrow due to poor overlap and are very low in energy so are disregarded as they remain always filled. Since bands have a finite width, band gaps occur and whether the Fermi level, E_F (the mean of the highest filled and lowest empty orbital), lies in a band gap or not dictates the compound's electrical properties.

If the Fermi level lies within a band gap, the bands below and above are known as valence and conduction bands. A large band gap results in the material being insulating. If the band gap is small, the compound is classed as a semiconductor. When the Fermi level is within a band, the material is metallic. Controlling the size of the band gap is crucial in areas such as solar cell technology. GaAs has a larger band gap than Si and is closer to the peak solar cell efficiency.[75] This is due to the difference in electronegativity, which gives the valence band more As-character and the conducting band more Ga-character making a GaAs a better candidate.

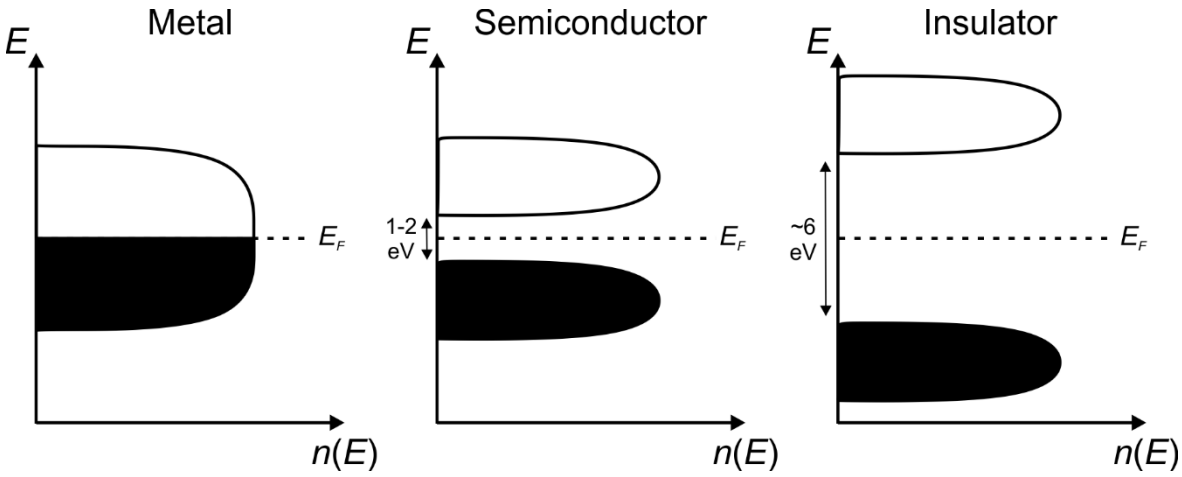


Figure 1.13: Band structures of a metal, semiconductor, and insulator.

Intercalation chemistry, as mentioned before, is an important tool in modifying a compound's properties. For TiS_2, the host compound is insulating as the metal bands are

empty due to Ti^{4+}. When intercalating with Li, not only does the alkali metal intercalate between the layers, as shown in Figure 1.10, but the electron from the alkali metal is injected into the conduction band of the solid resulting in a partially filled metal *d* band, and the product material is metallic.

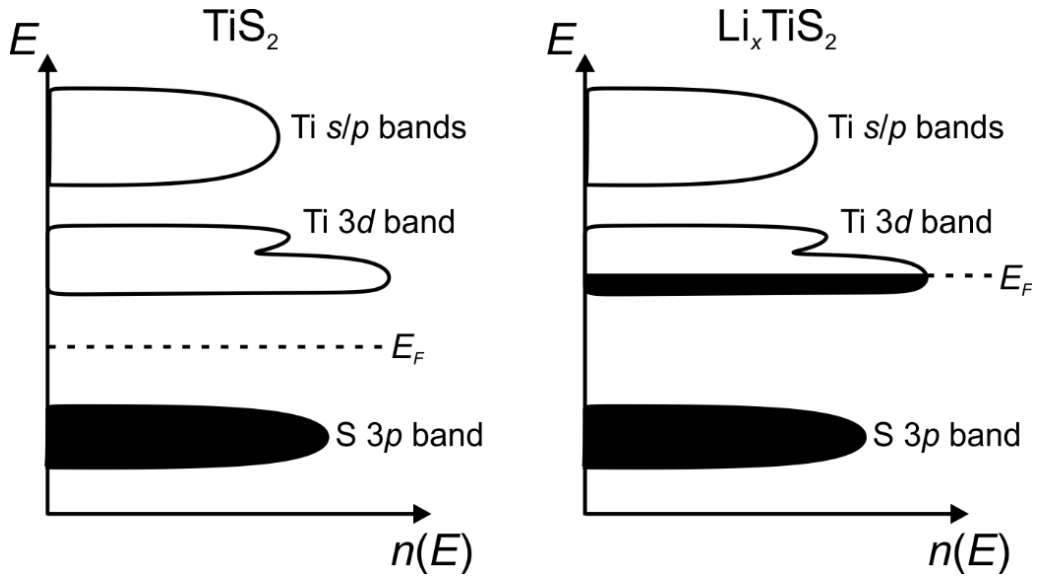


Figure 1.14 Band structure of TiS_2 (left) and Li_xTiS_2 (right). The electron fills the Ti 3*d* band upon intercalation, making the material metallic.

Electron count can have a drastic effect on the structure. A good example is seen when comparing layered chalcogenides NbS_2 and MoS_2. Both metal cations have a coordination of 6 with the anion, with both adopting a triangular prismatic environment. For the NbS_2, the compound is metallic, as predicted, with the partially filled *d* band in Nb^{4+}. However, for MoS_2, the edge-linking trigonal prisms enable a closer approach of the Mo^{4+} centres. Since *d*-orbitals of early second-row transition metals are well extended, it facilitates Mo-Mo bonding which minimises the energy of the system as the lowest lying *d* are filled, resulting in MoS_2 being an insulator. When MoS_2 is intercalated with Li, the extra electron must occupy the higher-lying band, which is Mo-Mo antibonding. The triangular prism is no longer favourable, and Mo prefers octahedral coordination.

1.4 Magnetic Properties of Solids

1.4.1 Diamagnetism

Diamagnetism is inherent to all atoms and ions due to paired electrons which weakly repel an applied magnetic field. A small current is induced when an electron is in precession in an applied magnetic field, generating an opposing magnetic field as described by Lenz's law.

The magnetisation generated by the inherent diamagnetism is typically weaker and several orders of magnitude less (~ 10^{-5} emu mol^{-1}) than most other types of magnetic phenomena seen (discussed below) and is usually overlooked when looking at materials with unpaired electrons. Diamagnetism is usually observed in non-metallic compounds with only paired electrons and is seen as a negative susceptibility that is largely temperature independent.

1.4.2 Paramagnetism

When compounds contain atoms or ions with unpaired electrons, their spins prefer to align with an applied external magnetic field. This is seen as a positive magnetic susceptibility. Paramagnets can be further divided into two subclasses depending on whether the unpaired electrons are itinerant (*i.e.* in a metallic band or localised).

1.4.2.1 Pauli Paramagnetism

When electrons are itinerant instead of localised, Pauli paramagnetism is seen. An unpolarised metal conduction band contains an equal amount of spin-up and spin-down electrons. However, when a magnetic field is applied, the band loses its degeneracy as the spin state aligned parallel with the field becomes energetically favourable, and the spin state aligned anti-parallel becomes disfavoured. The spin state that is lower in energy becomes preferentially occupied, resulting in a net positive magnetisation in the field direction. The magnetisation is usually weak (of a similar magnitude to diamagnetism) and several orders

of magnitude less than paramagnetism arising from localised spins (Curie paramagnetism). The size of the Pauli paramagnetism is proportional to the density of states at the Fermi level and hence is larger when the bands are narrower.

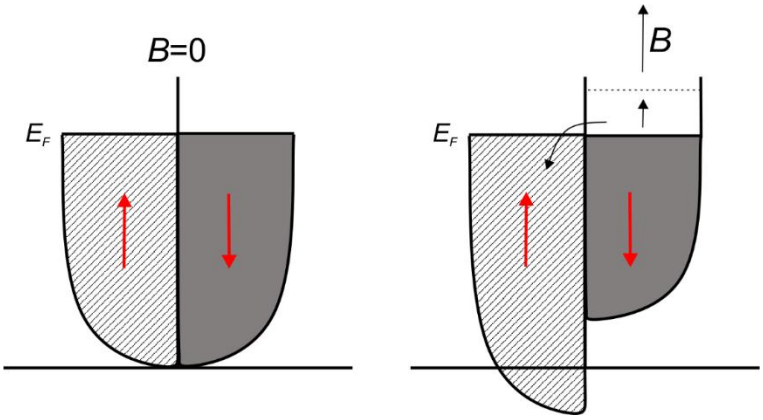


Figure 1.15 Pauli paramagnetism effect on a metal conduction band.

1.4.2.2 Curie Paramagnetism

Where electron spins are localised and not interacting, the spins will align to be parallel to the applied external field. However, the thermal energy of the system randomises the spins away from this alignment. The Curie law describes the inverse relationship between paramagnetic susceptibility and temperature.

$$\chi = \frac{C}{T} \qquad \text{Equation 1.1}$$

Where C is the Curie constant, defined below in Equation 1.2, where N_A is Avogadro's constant, μ_{eff} is the effective magnetic moment, and k_B is the Boltzmann constant. This can be simplified to Equation 1.3.

$$C = \frac{N_A \mu_{eff}^2 \mu_B^2}{3k_B} \qquad \text{Equation 1.2}$$

$$\mu_{eff} = 2.84\sqrt{C} \qquad \text{Equation 1.3}$$

Using this, the effective magnetic moment, μ_{eff}, can be calculated for a given paramagnetic material by plotting the $1/\chi$ against T, which gives a gradient C. The law applies if the effective moment itself is not temperature dependent.

1.4.3 Ferromagnetism

Like a paramagnet, a ferromagnet consists of unpaired electrons with the spins aligning parallel to the direction of the applied magnetic field. However, the spin alignment occurs even without the external magnetic field due to the strong coupling interaction between the spins. The strength of the interaction dictates the extent of alignment. The alignment is countered by thermal energy k_BT, which randomises the spins. Therefore, above a critical temperature described as the Curie temperature (T_C), the strong coupling is disrupted, and paramagnetic behaviour is observed. Examples of ferromagnet compounds include $CsMnF_4$,[76] Rb_2CrCl_4,[77] and Fe_3GeTe_2.[78]

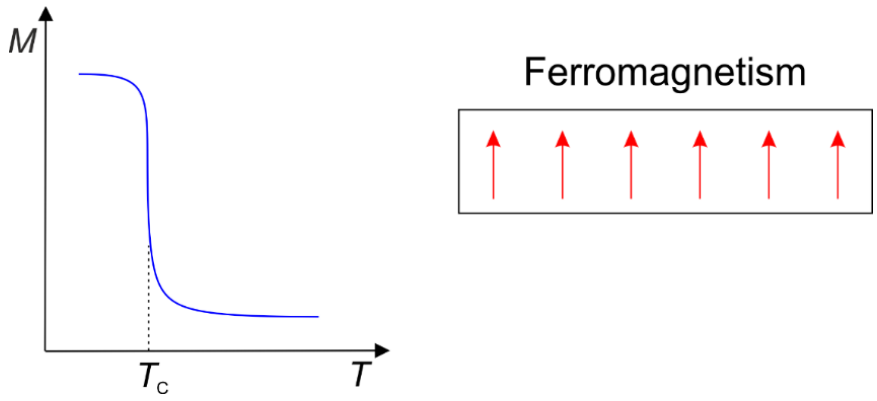


Figure 1.16: Left: Typical magnetisation vs temperature plot for a ferromagnetic showing the transition at the Curie temperature, T_C. Right: Alignment of spins in a ferromagnetic.

In a ferromagnet, spins tend to align in microscopic domains. However, the domains themselves do not necessarily align with each other and will be orientated differently with respect to their neighbours. This leads to the total moment of the sample material being zero. In the presence of an applied field, these magnetic domains will align along the direction of

the applied field resulting in a net positive magnetisation that holds even when the applied field is removed. The lower the temperature, or the stronger the field, the more the domains will align until all domains align, known as saturation. The magnetisation is several orders of magnitude larger than that of a paramagnet due to the strength of the coupling between spins being stronger than the external coupling to the magnetic field.

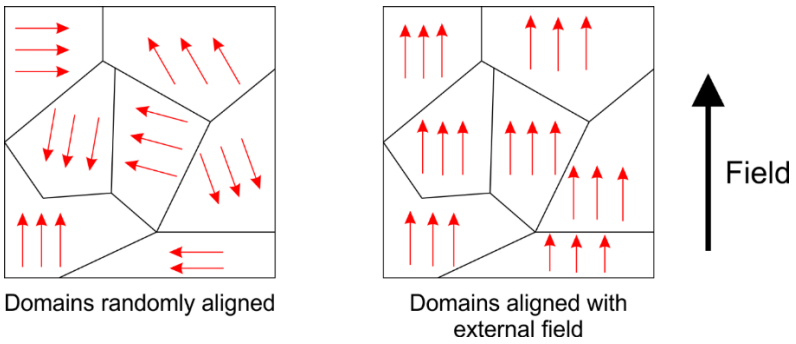


Figure 1.17: Domains in a ferromagnetic that are randomly aligned (left) then align with an external field (right).

1.4.4 Antiferromagnetism

Like a ferromagnet, an antiferromagnet contains unpaired electrons interacting strongly with their neighbouring spins. Rather than being parallel like in a ferromagnet, the spins in an antiferromagnet couple antiparallel. Therefore, the net magnetic moment will be zero. This occurs at a temperature known as the Néel temperature (T_N). Below T_N, susceptibility decreases with decreasing temperature as the energy of the coupling interaction becomes increasingly larger than the thermal energy. Above T_N, thermal energy overcomes these magnetic interactions, and paramagnetic behaviour is observed. Antiferromagnetic materials are common as it is the default state for a system with localised moments when there is no mixed valency. Examples of antiferromagnetic materials include MnS,[79] and $Sr_2CaFe_2O_5Cu_2S_2$,[80] and $Ba_2CoO_2Ag_2Se_2$.[81]

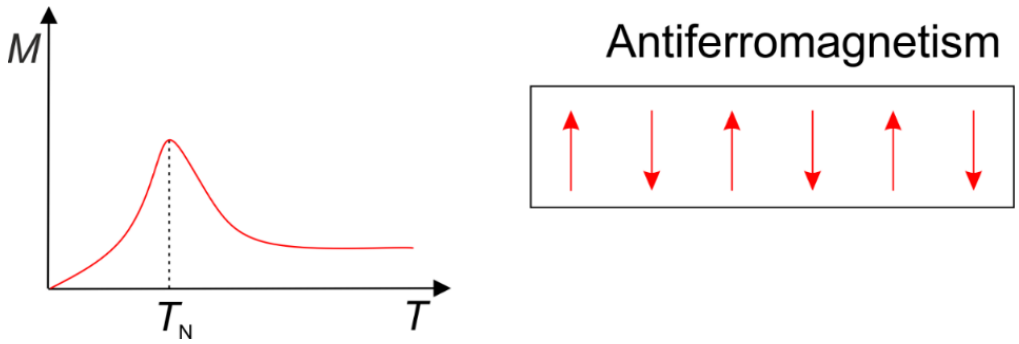


Figure 1.18: Left: Typical magnetism vs temperature plot for an antiferromagnetic showing the transition at the Neel temperature, T_N. Right: Alignment of spins in an antiferromagnetic.

1.4.5 Curie-Weiss Law

It is uncommon to find simple Curie paramagnetism in solid materials. Usually, magnetic atoms or ions do experience a degree of interaction with one another. In most cases, this would be in the form of ferromagnetism or antiferromagnetism. Here, the magnetic susceptibility deviates from the Curie law and is best described by the Curie-Weiss law:

$$\chi = \frac{C}{(T-\theta)} \qquad \text{Equation 1.4}$$

Where θ is the Weiss constant and is found by taking the intercept of the temperature axis, as shown in Figure 1.19. The type of interaction present can be determined from the sign of θ. A positive Weiss constant indicates the interactions are ferromagnetic (parallel), whilst a negative Weiss constant indicates an antiferromagnetic (antiparallel) interaction. The magnitude of the Weiss constant describes the strength of the interaction between localised spins. For a ferromagnet, this is described as the Curie temperature (T_C), and for an antiferromagnet, it is denoted as the Neel temperature (T_N). If there is frustration, T_N may be much lower than the Weiss temperature.

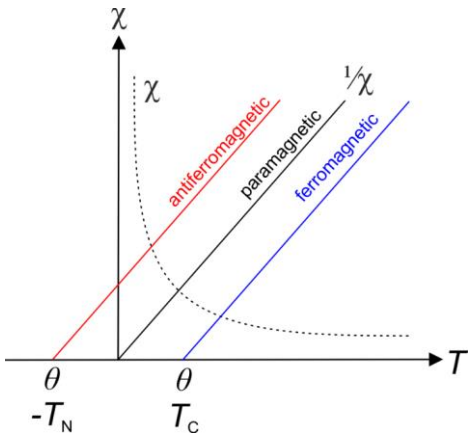


Figure 1.19: Plot of the inverse susceptibility (1/χ) against temperature for a paramagnetic (black), a ferromagnetic (blue) and an antiferromagnet (red). With the temperature intercept showing the respective Curie-Weiss temperature.

1.4.6 Frustration and Spin Glass Behaviour

The most famous example of a magnetically frustrated system is the triangular antiferromagnet lattice shown in Figure 1.20. Here, an antiferromagnetic coupling between all three spins is unattainable. If two spins are antiparallel, the third cannot be antiparallel to both. This leaves the system in a frustrated state, though there can be multiple degenerate frustrated states. The absence of a single preferred arrangement results in metastability, where different states can interchange freely at ambient temperatures, so no single ground state is adopted throughout the entire structure.

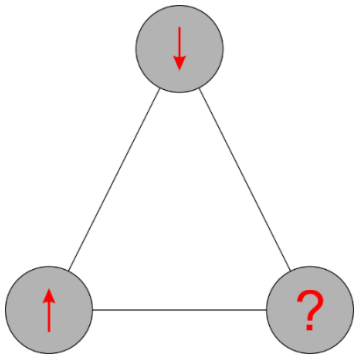


Figure 1.20: The frustrated magnetism in a triangular antiferromagnet. The bottom right spin cannot couple antiferromagnetically to both sites simultaneously.

A spin glass is a magnetic system with mixed interactions characterised by a cooperative yet random freezing of spins at a defined freezing temperature (T_f). Below this temperature, instead of usual long-range magnetic ordering, a metastable frozen state is found. A spin glass is usually a consequence of mixing magnetic frustration with disorder. If there is frustration in an ordered system, introducing disorder results in localised lifting of the frustration and domains in which magnetic order can happen. Disorder can result from several reasons, including vacancies or variations in bond lengths. Several domains will form, but not all spins will have been relaxed by the disorder. These spins external to the domains bridge the interactions between them. When $T \rightarrow T_f$, the interactions between domains and spins gradually becomes more long-range, and the system is in one of its many possible ground states. The appearance of ground states below T_f is said to be 'glassy' in that there is no long-range recurrence. This results in no magnetic Bragg peaks in the neutron diffraction pattern.

1.4.6.1 *A*Ga_2S_4 (A = Fe, Ni)

The *A*Ga_2S_4 system described earlier has been of interest due to the simple two-dimensional exact triangular arrangements of metal cations. Many three-dimensional materials with a triangular magnetic lattice have been investigated, for example, $CuFeO_2$ and Gd_2PdSi_3.[82,83] Experimentally, only a couple of highly two-dimensional examples have been reported such as κ-$(BEDT\text{-}TTF)_2Cu_2(CN)_3$ isosceles triangular lattice.[84] $NiGa_2S_4$ is the first example of a $S = 1$ (Ni^{2+}, $t_{2g}^6\, e_g^2$) two-dimensional bulk antiferromagnet and has been subjected to various macroscopic and microscopic experimental techniques.[85–90] The compound displays strong antiferromagnetic coupling with a Weiss temperature of -80 K. However, no antiferromagnetic or spin-glass-type ordering was found down to 0.35 K. A freezing phenomenon was found at $T_f \sim 10$ K. Inelastic neutron scattering showed incommensurate quasi-elastic short-range magnetic correlation.

For $FeGa_2S_4$, the reported properties show that despite Fe^{2+} possessing spin that is twice as large ($S = 2$, $t_{2g}^4\ e_g^2$) as Ni^{2+}, the main observations are very similar to the Ni variant with a Weiss temperature of 160 K and a $T_f = 16$ K.[91,92] The similarities strongly imply that the two-dimensional coherent behaviour in the frozen spin-disordered state has the same underlying mechanism.

1.5 Magnetic Exchange Mechanism

There are different mechanisms by which magnetic moments can interact. Firstly, there are long-range interactions that occur through space with an r^{-3} dependence. However, these interactions are typically too weak to account for the ordering of magnetic moments and are suppressed by thermal energy even at low temperatures. The other main type of interaction is through bonds. These interactions require the overlap of orbitals and are only as long-range as the orbital overlap permits. The interactions through bonds are much stronger than through space.

1.5.1 Direct Exchange

Direct exchange is through directly overlapping orbitals. Therefore, these interactions are very short-range (r^{-12} dependence). This interaction is only significant between the moments on nearest neighbour ions.

1.5.2 Superexchange

A superexchange interaction is non-direct and proceeds via an intermediate non-magnetic ion and, in insulating compounds, is generally the most important source of metal-metal interactions. The simplest case is three atoms arranged linearly, as shown in Figure 1.21. The filled σ *p* orbital on *X* (oxide, sulfide *etc*.) must have electrons that have opposite spins in each of its lobes resulting in an antiferromagnetic arrangement of the spins in the two

metal σ orbitals. Therefore, *M-X-M* interactions that are 180° are expected to be antiferromagnetic.

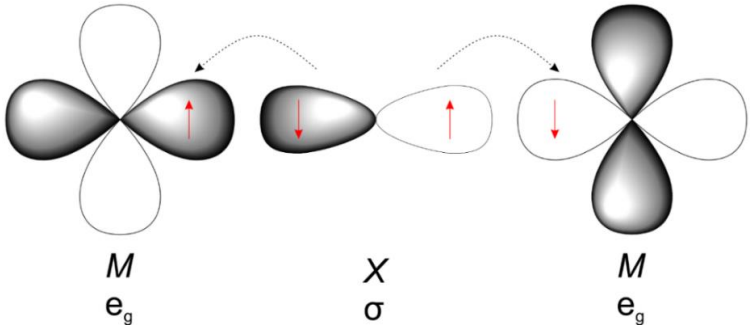


Figure 1.21: Superexchange mechanism in an *M-X-M* 180° bond expected to be antiferromagnetic.

However, when the σ exchange mechanism links two different orbitals, the result can be ferromagnetic ordering. This occurs in cases where the orbitals on the neighbouring metal ions are occupied unequally. An example of this is seen in $CsMnF_4$.[76] The Mn^{3+} ($3d^4$) octahedra are Jahn-Teller distorted, and superexchange involves the half-filled dz^2 and the empty dx^2-y^2.

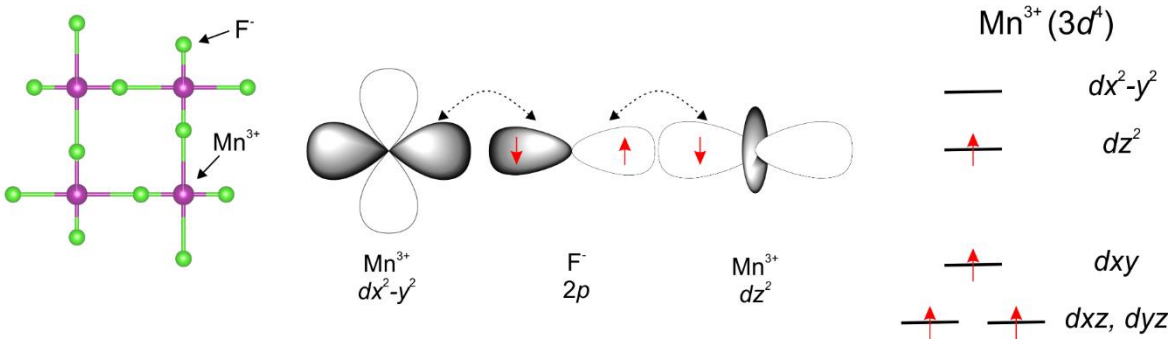


Figure 1.22: Superexchange mechanism in Mn^{3+}-F^--Mn^{3+} 180° bond that is ferromagnetic due to the different orbital involved.

Overlaps that are 90° are possible with metal ion orbitals. The *d*-orbitals couple orthogonally to the *p*-orbitals. This makes it impossible for an electron in one *d*-orbital to reach the *d*-orbital on the other metal site. For the 90° case, superexchange occurs via the coulomb exchange on the connecting *p*-orbital. The exchange interaction for similar metal ions is

expected to be ferromagnetic, but there are instances involving different orbitals where the 90° exchange is antiferromagnetic.

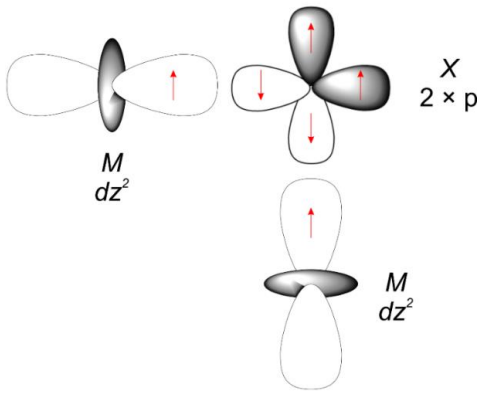


Figure 1.23: Superexchange mechanism in an *M*-*X*-*M* 90° bond expected to be ferromagnetic.

Exchanges can also mediate via second-nearest-neighbour linkages (*M*-*X*-*X*-*M*). An example of this is seen in $Li_3Fe_2(PO_4)_3$.[93]

Factors that affect superexchange mechanisms have been a subject of study. Goodenough-Kanamori-Anderson rules predict that metal-metal superexchange interactions between many common ions through common linkages. Therefore, interactions occurring at ~ 90° and ~ 180° through single neighbours are often easy to predict. However, interactions through longer linkages or significantly differing angles are more difficult to predict.

1.6 Superconductivity

1.6.1 Conventional Superconductivity

In 1911, Kamerlingh-Onnes studied the resistance of solid mercury at low temperatures and observed that resistance rapidly disappeared below 4.2 K.[94] This phenomenon was identified as superconductivity and was found to be exhibited in other systems. It was later shown that a superconducting circuit made from tin or lead allowed current to continue to flow even after the external power supply was removed. Later in 1933, Meissner and Ochsenfeld discovered that

when a superconducting transition happens, extraordinary magnetism is exhibited.[95] When a magnetic field is applied, a sample exhibiting a zero-resistance current near the surface will generate a field equal and opposite to the applied field, causing the complete shielding of the inside of the sample from the external field. As a result, the internal field of a superconductor is always zero, known as perfect diamagnetism. This property was termed the Meissner-Ochsenfeld effect and is much larger than the core diamagnetism described earlier in section 1.4.1.

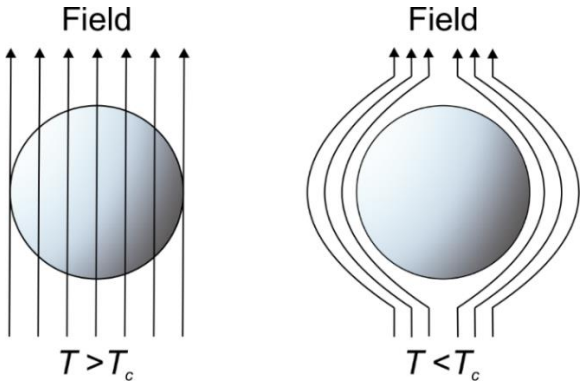


Figure 1.24: The Meissner-Ochsenfeld effect.

Classical theory of conduction could not explain the two properties discovered. Early theories explained the Meissner effect as superconducting electrons that are condensed into a single macroscopic quantum state.[96] But they failed to explain the microscopic properties. Later it was shown that the superconducting transition temperature (T_c) was dependent on isotopes, indicating that electron interaction with the lattice vibrations (phonons) is a significant factor.[97] These three discoveries were later rationalised in 1957 by the Bardeen-Cooper-Schrieffer (BCS) theory.[98]

1.6.2 Bardeen-Cooper-Schrieffer (BCS) Theory

The theory explains that at the Fermi level, there is a small attractive force between conduction electrons caused by phonons, resulting in the electrons binding together below T_c forming ‘Cooper pairs’. These pairs of electrons behave very differently from single

electrons as they act like bosons rather than fermions and therefore are not subject to the Pauli exclusion principle. As bosons, they can condense into the same energy level leaving an energy gap at the Fermi level. This superconducting energy gap (Δ_o) can be related to T_c and T as the energy (E) needed to break apart the Cooper pair and is given by:

$$E = 2\Delta_0 = 3.52 k_B T_c \sqrt{1 - \frac{T}{T_c}} \qquad \text{Equation 1.5}$$

The energy required is twice the energy gap as an electron excited out of the superconducting ground state must also pull its paired partner out of the ground state. From this, an expression of T_c can be derived:

$$T_c = \frac{1.13 E_D e^{\left(-\frac{1}{\lambda}\right)}}{k_B} \qquad \text{Equation 1.6}$$

Where λ is the electron-phonon coupling constant, and E_D is the Debye energy corresponding to the crystal's maximum phonon energy. From this, it shows that T_c correlates positively with λ and E_D. To have a high T_c, the crystal structure should have strong electron-phonon coupling where the phonons are high frequency. The theory predicts that superconductivity cannot easily exceed 40 K. The highest ambient pressure BCS superconductor reported is MgB_2, with a T_c of 39 K.[99] Its light elements result in phonons high in frequency. However, there are recent reports of very high λ and E_D values for light molecules under extreme pressures, such as the sulfur hydride systems giving a T_c of 203 K.[100]

Along with temperature, the strength of the applied external field significantly affects the Cooper pairs. When the strength of the field passes a critical point (H_c), the alignment of Cooper pairs is broken, and superconductivity is destroyed. How the Meissner-effect is broken can happen in two ways, classifying superconductors as type I or II. In a type I superconductor, the material will exclude the field entirely up to H_c. After this point, there

is a sharp transition where the material no longer excludes the field, and the superconductivity is destroyed. Type II behaves similarly to type I up until H_{c1}. However, beyond this, field exclusion is gradually reduced until a second critical field, H_{c2}, where no field is excluded, and superconductivity ceases.

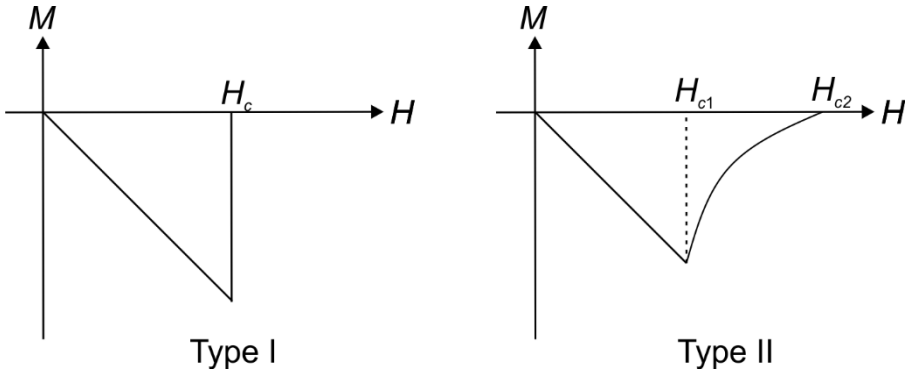


Figure 1.25: Type I (left) and Type II (right) superconductivity.

When an external magnetic field acts on a superconductor, the Cooper pairs are affected in two ways: (i) The orbital-limiting effect and (ii) the Pauli paramagnetic effect.[101,102] The orbital-limiting effect breaks the Cooper pair by inducing momentum, which eventually has enough kinetic energy to exceed the superconducting energy gap and is commonly the dominant effect when approaching T_c. In contrast, the Pauli paramagnetic effect is when the Zeeman splitting energy of electronic spin is large enough to overcome the energy gap resulting in the singlet Cooper pair becoming unstable. This effect is dominant at low temperatures. The maximum upper critical field H_{c2} is given by the paramagnetic breaking effect at $T = 0$ and is referred to as Pauli limit (H_P) and is given by:

$$H_P = \frac{\Delta_0}{\sqrt{2}\mu_B} \approx 1.85 T_c \qquad \text{Equation 1.7}$$

There has been ongoing research to find materials with high T_c that can withstand large fields, particularly for use in superconducting magnets like in MRI machines. Nb_3Sn with a T_c of 18.3 K and withstanding fields of up to 30 T is a good candidate.[103]

1.6.3 Cuprate Superconductors

The search for superconductors with as high a T_c as possible has been ongoing and has made this area extremely rich. A very notable breakthrough came when $YBa_2Cu_3O_{6+x}$ (YBCO) was found to have a T_c of 93 K at ambient pressures.[104] This was remarkable for several reasons. Firstly, it was the first superconductor to have a T_c above 77 K, which is the boiling point of nitrogen. Secondly, it well surpassed the predicted maximum stated by the BCS theory. Up till now, $HgBa_2Ca_2Cu_3O_{8+\delta}$ is the highest reported with T_c = 133 K.[105] Difficulty in turning these compounds into materials ready for applications have limited their use. However, YBCO is starting to be used in the core of the highest field NMR magnets (~ 1 GHz ^{1}H resonance).

BCS theory has no explanation for the extremely high T_c found in these cuprate superconductors. These superconductors show no phonon dependence. The common structural feature in all the cuprate superconductors is two-dimensional CuO_2 planes. There are suggestions that interactions between the magnetic lattice and the electron, known as 'spin-wave' interactions, may be a factor in how Cooper pairs are formed.[106] However, as of now, there is no theory that predicts the unconventional superconductivity observed in this class of compounds.

1.6.4 Chalcogenide and Pnictide Superconductors

Many chalcogenide and pnictide compounds were investigated for superconductivity. There have been multiple reports of chalcogenide-based superconductors, such as $NbSe_2$ and Ta_2Se, with T_c's of 7.2 K and 3.8 K, respectively.[22,107] For many years, attention was focused mainly on the cuprates until 2008, when a family of iron-based superconductors was discovered and became a very active area of study. This started with iron pnictides in 2006, with LaFePO displaying a low T_c of 3.2 K.[108] Two years later, superconductivity was

reported in LaFeAsO systems with a much higher T_c of 26 K, igniting the field.[109] Attention was then shifted to FeSe. As mentioned earlier, the tetragonal polymorph β-FeSe was found to superconduct at ~ 8 K but can be manipulated in multiple ways to increase T_c further.[61] When applying a pressure of 4-6 GPa, T_c was found to increase to 37 K.[110] As mentioned, chemical intercalation of alkali metals between FeSe layers significantly increased the transition temperature. A T_c of 43 K was reported for the phases $Li_x(NH_2)_y(NH_3)_{1-y}Fe_2Se_2$ and $LiFeO_2Fe_2Se_2$.[63,111] Organic molecules can be intercalated such as in $Li_x(C_5H_5N)_yFe_{2-z}Se_2$ resulting in a T_c of 45 K.[112]

The discovery of this family of superconductors suggested that other families of superconductors are yet to be discovered. One family investigated recently is $M_xPd_yCh_z$ (M = Nb, Ta; Ch = S, Se, Te) described earlier. $Nb_2Pd_3Te_5$ and $Nb_3Pd_{0.7}Se_7$ were found to have T_c's of 3.3 K and 2.1 K, respectively.[113,114] $Nb_2Pd_{0.81}S_5$ was reported by Zhang *et al.* to have a T_c of ~ 6.6 K.[115] Although this is comparatively low, the compound displays a remarkably large and anisotropic upper critical field of ~ 37 T, in violation of the Pauli limit by a factor of 3. Later it was found that substituting Nb for Ta and S for Se also resulted in compounds with superconductivity and unusually high upper critical fields. Ta_2PdS_5, Nb_2PdSe_5 and Ta_2PdSe_5 were found to superconduct below 6 K, 5.5 K and 2.5 K receptively.[51,116,117] There is no conclusive theory as to why the M_2PdCh_5 system exhibits such high upper critical fields. Lu *et al.* suggested that the high critical fields are the results of strong spin-orbit scattering from Pd vacancies that are embedded in the lattice of heavy 5*d* Ta and 4*d* Pd.[51]

1.7 Aims of the Thesis

Ceramic synthesis has been the main method of synthesising new solid-state materials, although only thermodynamic products are formed. 'Soft chemistry' allows access to kinetic

products otherwise inaccessible via ceramic synthesis. Many chalcogenide compounds are layered, allowing topotactic manipulation where the original structure remains unchanged.

Although the thesis is titled "Chemical Tuning of Topological Materials" in accordance with the Leverhulme grant project, which has funded this work. The DPhil project has moved away from strictly "topological materials" to a broader topic covering a range of layered chalcogenide materials. This thesis will investigate three different classes of layered chalcogenide compounds with the potential to be topochemically tuned. Chapter 3 will look at the binary chalcogenide $ZrSe_3$. This compound is better expressed as $[Zr]^{4+}[Se]^{2-}[Se_2]^{2-}$ and adopts a structure which is composed of $ZrSe_6$ prisms stacked infinitely along the *b*-axis with $[Se_2]^{2-}$ dimers forming the base of the prism. The dimers are stacked in chains along the *a*-axis with a van der Waals gap between the layers, making it an ideal candidate for intercalation. Zr^{4+} is hard to reduce, although the $[Se_2]^{2-}$ is reducible. There have been reports of Li intercalation in the 1970s when many layered chalcogenides were tested for battery applications.[118] This work will extend this to other alkali metals. There has not been any previous work on topotactic intercalations of $ZrSe_3$. Aside from Li, the other only previous report is of the compounds of the form $A_xZr_2Se_6$ (A = K, Rb, Cs), which are made at high temperatures (850 °C) using A_2Se, Zr and Se and remarkably form structures with a $ZrSe_3$ framework with the alkali metal residing between the layers.[119] This chapter compares and contrasts the structures formed at low temperatures using metal/ammonia intercalation into the host $ZrSe_3$. The intercalation of alkaline earth metal (*e.g.* Ca) will also be explored.

Chapter 4 will examine the $Nb_2Pd_xCh_5$ (*Ch* = S, Se) family, which exhibits superconductivity. This family of compounds also possess a unique structure in that the layers of $NbCh_y$ (y = 6, 7) prisms and $PdCh_4$ are linked by an additional $PdCh_4$. There have

been multiple reports of ways to modify superconductivity through chemical doping, but as of yet, there are no reports in the literature of intercalation.[120,121] Penny Hyde made initial findings of Li intercalation being feasible in $Nb_2Pd_xSe_5$, but more in-depth analysis and characterisation is needed.[122] This chapter will further investigate the effects of Li intercalation on the structure and superconductivity of $Nb_2Pd_xSe_5$ with a detailed analysis of the structure of the intercalate. This will then be extended to $Nb_2Pd_xS_5$. Various methods of Li intercalation will be compared, with electrochemistry also being invoked. Deintercalation of Li will also be explored to see if the process is reversible.

Finally, Chapter 5 will examine the $A_2Ga_2S_5$ (A = Mn, Fe) system, which is the bilayer variant of MGa_2S_4 (M = Fe, Ni). The MGa_2S_4 system has been of interest as the metal cation sits in a triangular lattice which is the simplest form of introducing spin frustration.[85,91] The bilayer $A_2Ga_2S_5$, in theory, with its bipartite honeycomb arrangement of metal cations, can lift that frustration, allowing long-range order. With the aid of neutron diffraction, this work will investigate the magnetism and attempt to model the magnetic ordering. The doping series $Mn_{2-x}Fe_xGa_2S_5$ ($0 < x < 2$) will also be investigated to see how magnetism varies with x.

Chapter 2

2 Experimental Methods

2.1 Synthetic Techniques

2.1.1 Ceramic Synthesis

Traditional solid-state synthesis, also known as 'ceramic synthesis', is the main method of synthesising most solid-state compounds. By performing the reaction at elevated temperatures, the mobility barrier is overcome. This is achieved by grinding together the solid reactants to achieve a uniform distribution and promote grain-to-grain contact, where the reaction occurs. The ground mixture of reactants is often pelletised using a force of 2-5 tonnes, depending on the size of the pellet. Pelletising reduces the inter-particle distance and increases the surface area at the grain contacts. The powder or pellet is typically placed in an inert vessel (usually an alumina crucible) and heated in the furnace at the required temperature for a period ranging from only a couple of hours to over a week. Normally, the furnace is left to naturally cool down to room temperature, although modifying the cooling rate could dictate which products are formed. Some desired products are only metastable and can be trapped by rapidly cooling (quenching) in an ice bath. Slow cooling often favours the formation of crystals.

2.1.2 Air-sensitive Synthesis

When the reactants or products are air/moisture sensitive, an inert atmosphere is needed when conducting solid-state reactions. Handling materials occurs inside an argon-filled dry glovebox. The O_2 and H_2O levels are kept below 1 ppm inside the glovebox. The Ar atmosphere inside the glovebox is not static and is recirculated through a copper catalyst and

a molecular sieve bed which removes O_2 and H_2O in the atmosphere. The catalyst is regenerated frequently using a 20:1 N_2:H_2 gas flow, whilst the sieves are regenerated when heated under a vacuum. An antechamber is connected to the glovebox, allowing materials and equipment to be taken inside. A dynamic vacuum is applied in the antechamber for 20 minutes to remove air and moisture, then filled with Ar before being opened to the glovebox.

Pelletising occurs outside the glovebox, mainly due to the size of the pellet press that would take up too much room inside the glovebox. It is still necessary to maintain an inert atmosphere. This is maintained by tying up the pellet die inside two polyethylene bags, pressing the pellet inside the bag and finally transporting back to the glovebox.

To carry out the reaction under high temperatures, the powder or pellet is placed in a silica ampoule which has been dried at 100 °C. A Young's tap is attached, connecting the ampoule to a vacuum line. The ampoule is evacuated and sealed using a methane/oxygen blowtorch before being placed in the furnace. When highly volatile reactants such as sulfur and iodine are used, the lower part of the ampoule is submerged in liquid N_2 whilst sealing to stop any vapour from being drawn into the vacuum pump, causing potential damage, or changing the composition of the reactants. A slow heating rate during the synthesis is also used to avoid sudden vapour pressure build-up, which may cause the ampoule to explode if the volatile reactant does not react fast enough. Once the reaction is completed, the silica ampoule is scored using a diamond cutter and transported to the glovebox to break inside.

2.1.3 Topotactic Synthetic Methods

Soft chemistry is a technique that uses low temperatures to access kinetic products otherwise inaccessible using high-temperature ceramic methods. This is primarily useful to achieve

topochemical changes (see section 1.2.3) to the material, such as intercalation and deintercalation, in which redox reactions are often the driving force behind them.

To carry out these topochemical changes, it is still necessary to maintain a dry and inert atmosphere. This is achieved by using Schlenk line techniques. First, the desired reactants are placed in a dried Schlenk tube inside the glovebox. The Schlenk tube is then attached to the Schlenk line in a fumehood. A Schlenk line typically possesses a vacuum line for evacuation of air and evaporation of small amounts of solvent, and an N_2 line, allowing solution transfer between reaction vessels via pressure differences. The transfer of solution is achieved by purging both vessels with N_2 and then inserting a cannula between them. Applying an overpressure of nitrogen in the solution vessel allows the solution to be drawn through the cannula into the reaction vessel containing the reactants. The reaction is left to stir for a period, followed by filtering to remove the liquid into a waste vessel using a filter cannula and the overpressure method. The product is washed with the solvent and filtered once more. This is repeated three times. The Schlenk tube is left to dry in a dynamic vacuum for an hour to ensure all solvent vapour is removed before the vessel is transported back into the glovebox.

2.1.3.1 *n*-butyllithium Intercalation

The most common method to intercalate Li into a host material is *n*-butyllithium intercalation (*n*-BuLi). Approximately 10-20 cm^3 of hexane is transferred into the reaction Schlenk tube with the host material. A stoichiometric amount of 1.6 M *n*-BuLi is syringed into the Schlenk tube. The solution is left to stir overnight before the sample is filtered and washed with hexane. The waste-containing Schlenk vessel may contain unreacted *n*-BuLi. Therefore, it is necessary to quench unreacted *n*-BuLi using isopropanol before disposal.

Toluene is initially added to the waste vessel to function as a heat sink, as the reaction of *n*-BuLi and isopropanol can generate a significant amount of heat.

2.1.3.2 Metal/naphthalene Intercalation

Another method to intercalate Li and other alkali metals is using a solution of metal/naphthalene. Firstly, a stoichiometric amount of naphthalene is dissolved in dry tetrahydrofuran (THF). This is then transferred to a vessel containing a slight excess of the alkali metal. The solution is left to stir overnight, where the formation of the naphthalenide radical anion (which will act as the reductant in the intercalation reaction) causes the solution to have an intense green colour. The solution is transferred onto the host material and stirred overnight before the sample is washed and filtered using THF.

2.1.3.3 Metal/ammonia Intercalation

Both alkali and alkaline earth metals can be intercalated using liquid ammonia solution. The Schlenk tube with the host and desired intercalant metal is evacuated on the Schlenk line and cooled to approximately -78 °C using a dry ice and isopropanol bath. Approximately 10 cm^3 of NH_3 is condensed into the Schlenk tube. As the liquid ammonia dissolves the metal, a deep blue solution is formed due to the solvated electrons. The reaction was left to stir for up to 3 hours, then left to naturally warm up to room temperature, during which time the NH_3 evaporates. A dynamic vacuum is then applied to remove any NH_3 vapour or adsorbed NH_3 before transferring the sample to the glovebox.

2.1.3.4 Deintercalation using Iodine

Oxidative deintercalation reactions were conducted using iodine as the deintercalant to remove the intercalated alkali metal from the host structure. Excess iodine was placed in a Schlenk tube outside the glovebox and then purged with nitrogen on the Schlenk line. Dry

acetonitrile (MeCN) was transferred onto the iodine and left to stir for an hour, forming a dark red solution due to the dissolved iodine. The solution was transferred onto the material and left to stir for 2 to 3 days. The sample was washed and filtered using dry MeCN.

2.1.3.5 Electrochemical Intercalation

Electrochemical intercalations were performed by Dr Sunita Dey at the University of Cambridge, UK. The host starting material was assembled in a coin cell in an Ar glovebox. To prepare the cathode, the compound was mixed with Super P Carbon (Timcal) and polyvinylidene fluoride (PVDF) binder in a weight ratio of 80:10:10. The coin cell was assembled with the cathode, a Li counter electrode and a borosilicate glass fibre separator which was soaked in the electrolyte. The electrolyte consists of $LiPF_6$ in ethylene carbonate (EC) and dimethyl carbonate (DMC) in a 1:1 ratio. Galvanostatic charging/discharging was carried out at ambient temperatures using a Lanhe battery cycler. The battery was disassembled inside the Ar glovebox to recover the powder sample for measurements. The cathode mixture was washed thrice using DMC before drying under the glove box ante-chamber vacuum for 30 minutes.

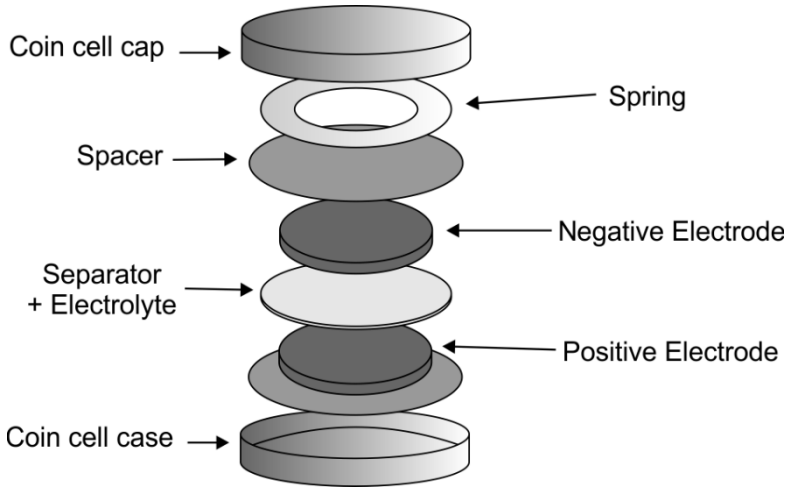


Figure 2.1: Diagram of a typical coin cell assembly.

2.2 Characterisation Techniques

2.2.1 Diffraction

When an incident radiation beam interacts with matter that is liquid, gaseous or amorphous in nature, radiation is scattered in all directions with a broad and featureless distribution with respect to the scattering angle, and an intensity distribution with scattering angle that depends on the form factor of the scattering object (see pages 44 and 54). However, if the material is crystalline (*i.e.* displays a periodic arrangement of atoms) and the radiation wavelength is comparable to interatomic spacing, then the scattering is no longer featureless. When the incident beam interacts with a crystal, the scattered beams can interfere constructively or destructively. Features can be seen as intense signals due to constructive interference occurring in a few special directions and at certain scattering angles for a given material. This provides information on the periodicity (based on the positions) and the relative arrangement of atoms (based on the intensities). Diffraction is a fundamental technique in the structural study of crystalline materials.

2.2.2 X-ray Diffraction

The main type of diffraction used in solid-state chemistry is X-ray diffraction since X-rays are of the wavelength between 0.1-10 Å, which is on the atomic scale. Therefore, a periodic lattice of atoms acts as a diffraction grating. When an X-ray photon interacts with a crystal, an atom's electron can get excited, and the relaxation emits photons (known as fluorescence, which is used in X-ray Absorption Spectroscopy, XAS), or the electron can scatter the X-ray. The scattering occurs as the photon's electric field interacts in a Coulombic manner with the atom's electron.

The first theory of X-ray diffraction was developed by von Laue in 1912. The theory considered crystals as a three-dimensional ordered arrangement of atoms. The theory can be shown using a hypothetical one-dimensional lattice with a row of regularly spaced atoms.

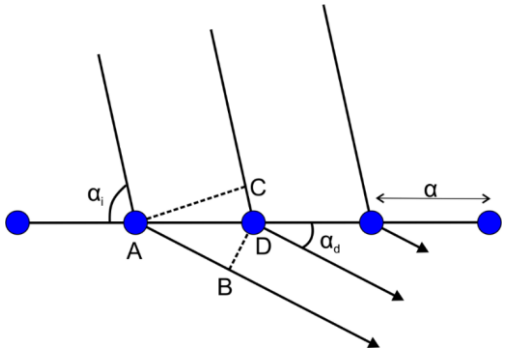


Figure 2.2: Laue scattering of monochromatic radiation by a one-dimensional lattice.

When parallel monochromatic beams of X-rays hit the one-dimensional lattice at angle α_i, for constructive interference, the path difference (AB-CD) must differ by an integer number (n) of wavelengths (λ):

$$AB - CD = a(cos\alpha_d - cos\alpha_i) = n\lambda \qquad \text{Equation 2.1}$$

Three Laue equations can be defined in a three-dimensional crystal, corresponding to the rows of atoms along the orthogonal x, y and z axes. For constructive interference, these three equations must be simultaneously satisfied.

$$b(cos\beta_d - cos\beta_i) = n_y\lambda \qquad \text{Equation 2.2}$$

$$c(cos\gamma_d - cos\gamma_i) = n_z\lambda \qquad \text{Equation 2.3}$$

To calculate the three equations, three lattice spacings, six angles and three integers (12 variables) need to be determined. Although this is a thorough description, a conceptually simpler alternative description was given by W. L. Bragg in which diffraction is now seen as originating from X-rays reflected by planes of atoms known as Miller planes.[123] These

planes are defined by Miller indices *hkl*, which intersect the edges of an $a \times b \times c$ unit cell at $\frac{a}{h}$, $\frac{b}{k}$ and $\frac{c}{l}$.

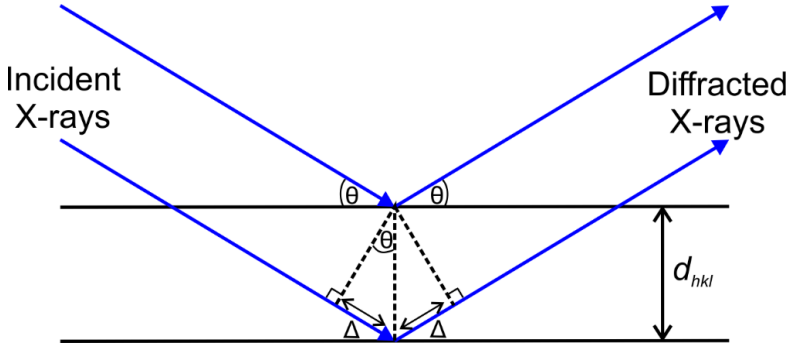


Figure 2.3: Diffraction of X-rays from a Miller plane leading to the derivation of Bragg's law.

As mentioned, constructive interference occurs when the path length (now 2Δ) equals $n\lambda$. Here, the spacing between planes, d_{hkl}, and diffraction angle θ can be related to the wavelength by Bragg's law:

$$2\Delta = n\lambda = 2d_{hkl}\sin\theta \qquad \text{Equation 2.4}$$

The intensity of the diffracted beams is measured in an X-ray diffraction pattern as a function of 2θ. The size and symmetry of the unit cell can be determined from the occurrence and position of these reflections. This is achieved using an indexing process that assigns Miller indices to each observed reflection. The *d*-spacing of the *hkl* layers can be determined via Bragg's Law and related to the unit cell parameters. An example of this for an orthorhombic system with lattice parameters $a \times b \times c$ is given below:

$$\frac{1}{d_{hkl}^2} = \frac{h^2}{a^2} + \frac{k^2}{b^2} + \frac{l^2}{c^2} \qquad \text{Equation 2.5}$$

Translational symmetry within the unit cell results in systematic absences of certain reflections. Using this allows the Bravais lattice type of the crystal to be established, together with the presence of any symmetry elements with a translational component. The intensities

of the reflections give information about the unit cell contents. Reflection intensity, I_{hkl}, is dependent on a few parameters but is mainly governed by the structure factor, F_{hkl}.

$$I_{hkl} \propto |F_{hkl}|^2 \qquad \text{Equation 2.6}$$

The structure factor for a *hkl* reflection accounts for the interference of waves scattered by all the atoms in the unit cell. Therefore, it is dependent on the identity and position of the atoms and is defined as:

$$F_{hkl} = \sum_{n=1}^{N} f_n(\theta)[\cos 2\pi(hx_n + ky_n + lz_n)]\, q + i \sum_{n=1}^{N} f_n(\theta)[\sin 2\pi(hx_n + ky_n + lz_n)]\, q \qquad \text{Equation 2.7}$$

Where N is the number of atoms in the unit cell, $f_n(\theta)$ is the scattering form factor of atom n, x_n, y_n, and z_n are the positional coordinates, and q is the Debye-Waller term which considers the thermal effects of the atom.

The scattering form factor is dependent on the scattering angle and the number of electrons in the atom, Z, and is expressed as:

$$f_n(\theta) \propto \frac{Z}{2}(1 + cos\, 2\theta) \qquad \text{Equation 2.8}$$

Contributions to diffraction intensities are proportional to Z. Therefore, obtaining useful information on light atoms is difficult as X-rays are scattered more weakly than heavy atoms, which contain significantly fewer electrons. Another problem is that atoms of similar electron count, *e.g.* Mn and Fe, cannot be distinguished with X-rays. The angular dependence results in reduced intensity at higher 2θ angles. The electron cloud of an atom is of similar size compared to X-ray wavelength; therefore, X-ray beams travel at different path lengths after being scattered from slightly different regions of the same atom. This results in destructive interference reducing intensity at high 2θ.

At temperatures above absolute zero, atoms are non-stationary and have thermal motion, causing the atoms to be displaced from their average position. The atomic vibrations cause dispersion of the electron density in the atoms, resulting in intensities decreasing with angle as there is now a greater phase difference between scattered X-ray beams, increasing destructive interference. The Debye-Waller factor for thermal isotropic motion q_{iso} is given by:

$$q_{iso} = exp\left[\frac{-8\pi^2 U_{iso} sin^2(\theta)}{\lambda^2}\right] \quad \text{Equation 2.9}$$

Where U_{iso} is the isotropic temperature factor determined experimentally. The term B_{iso} can also be used and is defined as $B_{iso} = 8\pi^2 U_{iso}$

Using the structure factor gives details of the unit cell contents. However, since F_{hkl} is a complex number and the I_{hkl} is proportional to the square of the modulus, only the amplitude and not the phase of F_{hkl} can be extracted. This is known as the 'phase problem'. Computational methods such as direct methods, the Patterson method or charge-flipping have been developed to address this problem.[124–126]

2.2.2.1 Powder X-ray Diffraction

A polycrystalline powder sample consists of many randomly oriented crystallites, where every orientation is represented statistically. Some of these crystallites will be oriented correctly to satisfy Bragg's law, while the other crystallites will not diffract. Diffraction from a set of *hkl* planes can occur at more than one absolute orientation, which results in a cone of diffracted X-rays (known as a Debye-Scherrer cone) being generated around the sample, as shown in Figure 2.4.

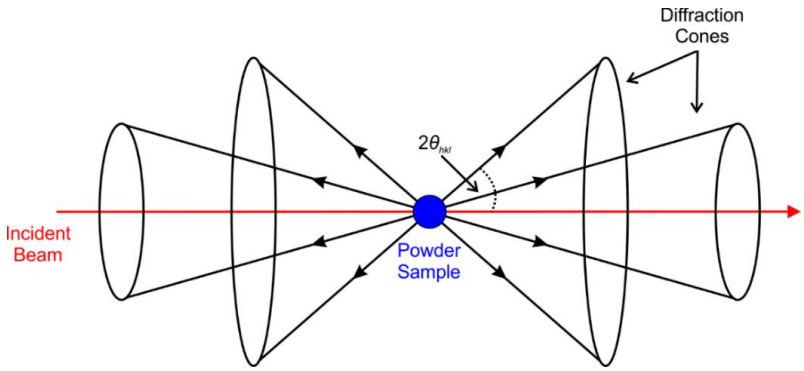


Figure 2.4: Debye-Scherrer cones for powder X-ray diffraction.

In a powder X-ray diffraction experiment, a detector on the X-ray diffractometer can detect these cones and generates a one-dimensional pattern of intensity as a function of diffraction angle 2θ. However, there are disadvantages that come with using powder instead of a single crystal. Reflections with identical d_{hkl} values, *i.e.* 100 and $\bar{1}00$, show as separate points in single crystal diffraction, whereas they will be coincident in a powder pattern. The intensity needs a multiplicity term to account for reflections that are symmetry equivalent. Another problem is that different *hkl* values can have similar d_{hkl} values, leading to partial overlap and increased intensity at that position. An example is seen in a cubic system where perfect overlap is achieved with the 333 and 511 Miller planes. This is also a problem in crystal systems with low symmetry where a larger number of reflections overlap partially.

The phase problem and the peak overlap make it extremely difficult and sometimes impossible to resolve the structure of a material *ab initio* from powder X-ray diffraction. However, powder diffraction is still a very useful and widely used technique. It can be used as a 'fingerprinting' tool to analyse phase purity by comparing it to diffraction patterns of known compounds. Since powder diffraction is a measurement of the bulk sample, it is often a better representative of the bulk than single-crystal diffraction. Using high-resolution instruments such as the synchrotron can reduce the extent of peak overlap and give a higher signal-to-noise ratio.

2.2.2.2 Laboratory Powder X-ray Diffraction

In a typical laboratory powder X-ray diffractometer, X-rays are generated by heating a tungsten element producing electrons which are then accelerated by a 40 kV voltage under vacuum towards a metal anode. This anode is usually a Cu source, which is the case for the diffractometers used in this thesis, although other sources (*e.g.* Mo) can also be used. The electron beam ionises the 1*s* electrons, which are ejected, producing holes in the core orbitals. These vacancies are filled by electrons dropping down from higher energy orbitals. The energy difference is released as an X-ray with a characteristic wavelength (λ). A K_α X-ray emission is a transition between the *L* and *K* shell, and a K_β emission is between *M* and *K* shells. The latter is higher in energy such that $\lambda_\beta < \lambda_\alpha$. However, in a Cu source diffractometer, the intensity is approximately a fifth of the intensity of K_α and therefore, K_α is more frequently used. At high resolutions, the K_α can be seen to be split into $K_{\alpha1}$ and $K_{\alpha2}$ in a 2:1 ratio with a λ of 1.5405 Å and 1.5443 Å respectively. The doublet is a consequence of spin-orbit coupling, which gives two different *J* states, $^2P_{3/2}$ and $^2P_{1/2}$, of the electrons in the 2*p* orbital.

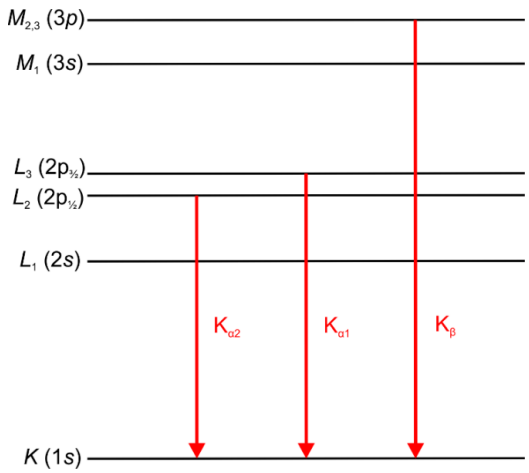


Figure 2.5: $K_{\alpha1}$, $K_{\alpha2}$ and K_β X-ray emissions of Cu source.

For Cu radiation, a Ni filter is used to absorb K_β X-rays. This can also be achieved using energy-discriminating detectors. A monochromator is a crystal that diffracts the beam from

a specified *hkl* plane at a specified angle to give a defined λ. Monochromators can be "broad-band", allowing a wide range of energies ($K_{\alpha 1}$ and $K_{\alpha 2}$), and are typically pyrolytic graphite crystals mounted between the diffracted beam and the detector. A "narrow-band" monochromator only allows a very specific λ and as such, can be used only to isolate $K_{\alpha 1}$. These monochromators are typically Si or Ge crystals and are very sensitive to position and hence are fixed in front of the incident beam. The disadvantage to monochromators is that the isolation of certain wavelengths comes at the expense of intensity.

To prepare samples for laboratory X-ray diffraction, the powder sample was scattered on a glass slide with a thin layer of grease, forming a thin layer of powder. Usually, for air-stable compounds, the slide is placed on a sample holder and allowed to spin to reduce any preferred orientation and improve the powder average. However, for air-sensitive samples, the slide was placed in an air-tight holder with Mylar windows to allow X-rays through but prevent the sample from being exposed to air and decomposing. When the air-tight holders available are used, the sample cannot spin. Typical patterns are collected from $5° \leq 2\theta \leq 70°$. Large doors on the instruments that lock upon the opening of the X-ray shutter keep the user shielded from the X-ray radiation.

Laboratory diffractometers were used for phase-checking, obtaining lattice parameters and preliminary structural analysis. For more accurate analysis, X-ray diffraction patterns were measured using a synchrotron source (section 2.2.3).

2.2.2.3 Bruker D8 Advance Eco Diffractometer

The Bruker D8 Advance Eco diffractometer has a fixed sample position with a rotating X-ray source and detector. The X-ray beam is not monochromated, allowing both $K_{\alpha 1}$ and $K_{\alpha 2}$ radiation which, although it reduces resolution, does allow for increased intensity. Combined with a position-sensitive detector that can measure simultaneously over a 2θ range of 3°, this

results in patterns with a good signal-to-noise ratio to be collected in under half an hour. The detector is energy discriminating, removing K_β and filters out fluorescence. This is useful when analysing samples containing significant amounts of Cr-Co, as these elements emit significant fluorescence when a Cu source is used that contributes to noise in the diffraction pattern.

2.2.2.4 PANalytical Empyrean & PANalytical X'pert Diffractometers

The PANalytical Empyrean is a newer replacement for the PANalytical X'pert, so both diffractometers behave similarly. The diffractometers have a fixed X-ray source with the sample and detector rotating. The fixed X-ray source has a Ge crystal monochromator (*hkl* = 111, angled at 27.6°) fitted, eliminating $K_{\alpha 2}$ radiation which improves resolution and peak shape compared to the Bruker D8 Advance Eco, but the intensity is much lower. The PANalytical instruments collect higher quality data but usually require longer scan times (1-2 hours). However, the biggest drawback is that they do not filter out fluorescence.

2.2.3 Synchrotron X-ray Diffraction

Synchrotrons can produce highly intense but highly collimated and stable electromagnetic radiation beams with tuneable wavelengths. This allows for data collection at a much greater precision than the laboratory instruments due to the better resolution of overlapping peaks and much-improved signal-to-noise ratio. Therefore, more accurate and precise data analysis can be carried out.

The radiation is generated by using magnetic fields to force charged particles travelling near the speed of light to change direction as they accelerate around the ring. For X-ray synchrotrons, electrons are used. Electrons are generated by an electron gun where like

laboratory diffractometers, a tungsten element is heated, emitting electrons. The electrons are accelerated through a linear accelerator (a *linac*) to produce a high-energy beam on the MeV scale. The *linac* consists of a series of electric fields that oscillate from positive to attract electrons, then to negative to repel them onto the next field. A booster synchrotron is used to further energise the beam to the GeV input range of the main storage ring.

The electrons are injected into the storage ring in discrete bunches. A radio-frequency cavity (a kicker magnet) replenishes energy lost in the electron bunches as they emit radiation. A very high vacuum of ~ 10^{-13} bar is used throughout the synchrotron to prevent energy loss of the electron beam. Despite the vacuum, electron bunches will eventually decay over time because of collisions with other molecules. Therefore, the storage ring is typically refilled daily (in modern synchrotrons the refilling is continuous). The storage ring is not a perfect circle. It consists of straight and curved sections. An electron is forced to change direction when it passes through the bending magnets. This change of momentum causes radiation emission, and the radiation's wavelength is determined by the electron energy and the magnetic field.

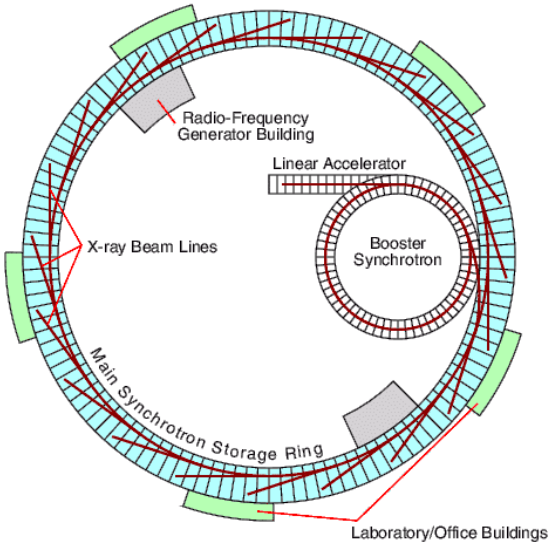


Figure 2.6: Schematic of a synchrotron.[127]

Third-generation synchrotrons use insertion devices in the straight sections to generate radiation in addition to the bending magnets. These devices consist of alternating magnetic poles, producing a series of oscillating electron accelerations, with each oscillation emitting radiation. Two types of insertion devices are used: wigglers and undulators. Wigglers produce directly superimposable radiation, closely mimicking the output of a bending magnet but with higher energy (shorter wavelength) radiation. An undulator produces non-superimposable harmonic radiation where in-phase constructive interference generates very high-intensity beams, whereas lower-intensity beams are generated with out-of-phase radiation.

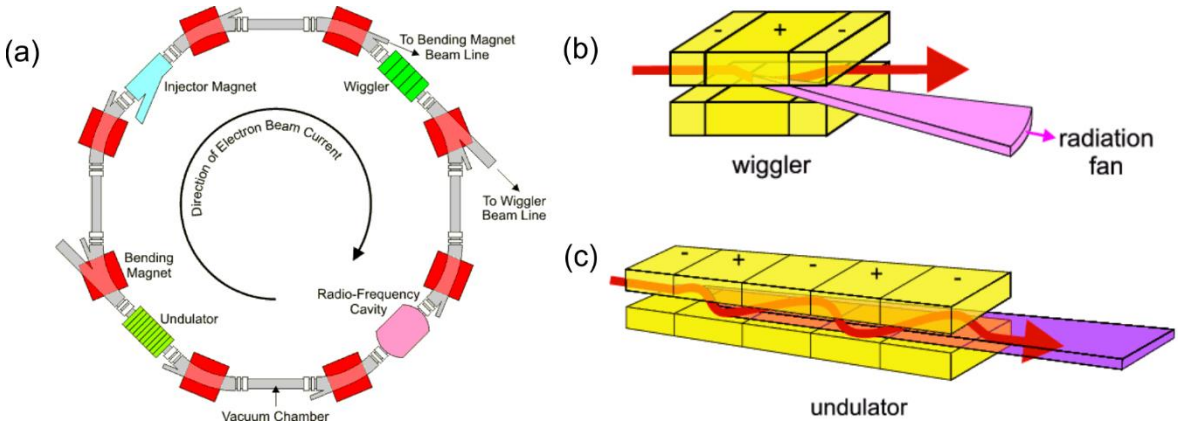


Figure 2.7: (a) Detailed schematic of storage ring showing bending magnets and the insertion device.[127] (b) and (c) show the wiggler and undulator, respectively.[128]

The emitted radiation is directed to the individual beamlines, which are tailored to a specific measurement: diffraction (powder or single-crystal), spectroscopy, imaging, microscopy *etc.*

Synchrotron X-ray diffraction data used in this thesis were collected on the I11 beamline at the Diamond Light Source, Harwell, UK, a third-generation synchrotron with a 3 GeV storage ring.

2.2.3.1 I11 Beamline, Diamond Light Source

The I11 beamline is a high-resolution powder diffraction beamline at the Diamond Light Source.[129,130] I11 uses an undulator source to generate high-intensity radiation with wavelengths of 0.5-2.1 Å (X-ray beams of energy ranging from 6-25 keV), with the optimum range of 0.62-1.1 Å. The wavelength used for all I11 data in this thesis is ~ 0.826 Å, with the precise value obtained on the day of the experiment using a Si calibration experiment. The X-ray beam is monochromated by a double-crystal Si (*hkl* = 111) monochromator.

I11 uses two types of detectors: a Mythen position sensitive detector (PSD) and a MultiAnalyser crystal (MAC) detector. The PSD is a strip detector consisting of 18 linear Si p-n junction strip detection modules arranged in a 90° arc. Approximately 1 mm is left between modules, leaving gaps of uncollected data in the diffraction pattern. To account for this, a second pattern is collected by moving the detector by 0.25° in the 2θ direction, and then the two patterns are merged. PSD is used for very quick powder diffraction measurements (t ~ 1 s) with a high signal-to-noise ratio.

The MAC detector comprises of 45 Si (111) analyser crystals with 9 individual detectors on 5 separate arms. This allows 45 individual 2θ values to be collected simultaneously with slightly higher resolution than the PSD with lower background and reduced sensitivity to sample misalignment. The downside is that the scan requires a much longer time (~ 30 minutes).

I11 is also equipped with a cryostream and hot air blower, which allows variable temperature PSD diffraction data to be collected. The nitrogen cryostream can range from 80 to 500 K with the hot-air blower reaching 1000 °C. Variable temperature experiments are useful in measuring lattice parameters as a function of temperature or observing changes in symmetry, polymorphism, or decomposition.

To prepare a sample for measurement at I11, the samples were prepared in the in-house glovebox by grinding together equal volumes of the sample and glass powder. The dilution reduces absorption and preferred orientation of the sample. The mixture was then packed in 0.5 mm borosilicate capillaries which were sealed using the blowtorch and wax. The capillaries were glued into a glass ferrule that was mounted on a magnetic base at the beamline and loaded onto a carousel. A robotic arm is programmed to select the capillary and load it in the beam's path, thus not requiring a person to access the instrument. This automation significantly reduces downtime and allows more samples to be measured.

2.2.4 Neutron Powder Diffraction

Like X-rays, neutrons are another type of radiation that is extremely useful in the characterisation of materials both structurally and magnetically. Neutrons can be treated like waves using the de Broglie relationship:

$$\lambda = \frac{h}{p} = \frac{h}{mv} = \frac{h}{\sqrt{2mE}} \qquad \text{Equation 2.10}$$

where h is Plank's constant, p is the momentum, m is the mass of the neutron, v is the velocity, and E is the energy. With the appropriate energy, neutrons can therefore have wavelengths on the atomic scale and interact with the material (*e.g.* E = 25 meV corresponds to λ = 1.81 Å). X-rays are scattered by the atom's electron cloud. In contrast, neutrons are scattered by the atom's nucleus via the strong nuclear force. Whereas the X-ray scattering form factor is proportional to the atomic number, the neutron scattering form factor depends on the atom's coherent scattering length, which varies erratically with atomic number. Even isotopes can have significantly different coherent scattering lengths. With neutron diffraction, light elements (H, Li, N *etc.*) that have insignificant contributions in X-ray diffraction can now be detectable. Neutrons are also useful in distinguishing atoms with

similar atomic numbers. Also, in contrast to X-rays, the small size of the nucleus relative to the wavelength results in the neutron scattering form factor having no angular dependence.

Table 2.1: Bound coherent scattering length of elements used in this thesis. Values are taken from Neutron News.[131]

Element	Scattering Length / fm	Element	Scattering Length / fm
H	-3.739(1)	**Fe**	9.45(2)
Li	-1.90(2)	**Ga**	7.288(2)
N	9.36(2)	**Se**	7.970(9)
S	2.847(1)	**Zr**	7.16(3)
Ca	4.70(2)	**Nb**	7.054(3)
Mn	-3.73(2)	**Pd**	5.91(6)

Another characteristic of neutrons that sets them apart from X-rays is that neutrons are spin-½ particles. Therefore, neutrons can interact with magnetic moments in the material. If the material is magnetically ordered, then neutrons can be diffracted by the magnetic lattice. This produces a second diffraction pattern of magnetic Bragg peaks superimposed onto the nuclear diffraction pattern. In this case, the neutrons interact with the unpaired electrons. The wavelength, comparable to the atomic spacing, results in a fall-off in the magnetic form factor with angle, akin to the X-ray form factor but more rapid.

Contrary to X-rays, neutrons interact weakly with the material. Hence, it is necessary to use a much larger amount of sample (> 1 g) and significantly longer measurement times for the collected data to have an acceptable signal-to-noise ratio.

Another drawback of neutron diffraction is that it cannot be performed in-house like X-ray diffraction. Instead, neutron diffraction requires a large and highly specialised facility. This results from how the neutron beam is generated, which is both difficult and expensive.

Neutrons are typically generated using one of two methods: reactor source or spallation source. A reactor source uses nuclear fission to produce neutrons from the radioactive decay of a radioactive source. The neutrons generated have wavelengths associated with the nuclear reaction. Before being directed at the sample, the neutron beam is passed through a monochromator. Like for X-rays, the obtained diffraction pattern shows the intensity as a function of 2θ.

The resolution for a single wavelength diffractometer is θ dependent. It is expressed by the Cagliotti function, which describes how the full width at half maximum (FWHM) of a Bragg reflection varies with the scattering angle.[132]

$$\sigma^2 = \frac{FWHM^2}{8ln2} = Utan^2\theta + Vtan\theta + W \qquad \text{Equation 2.11}$$

Where *U, V* and *W* are all parameters which are instrument and sample dependent.

In a spallation source, hydride ions are generated by an ion source and then accelerated. In the process, the electrons are stripped off to become protons. The protons are accelerated in a synchrotron and then fired at a metal target, generating around ~ 20 neutrons per proton. This produces a "white" beam of neutrons as the neutrons generated have a wide range of wavelengths.

Neutron diffraction data used in this thesis was collected from two facilities: ISIS, Harwell Campus, UK, a spallation neutron source, and the Australian Nuclear Science and Technology Organisation (ANSTO) situated in New South Wales, Australia. ANSTO uses a reactor source.

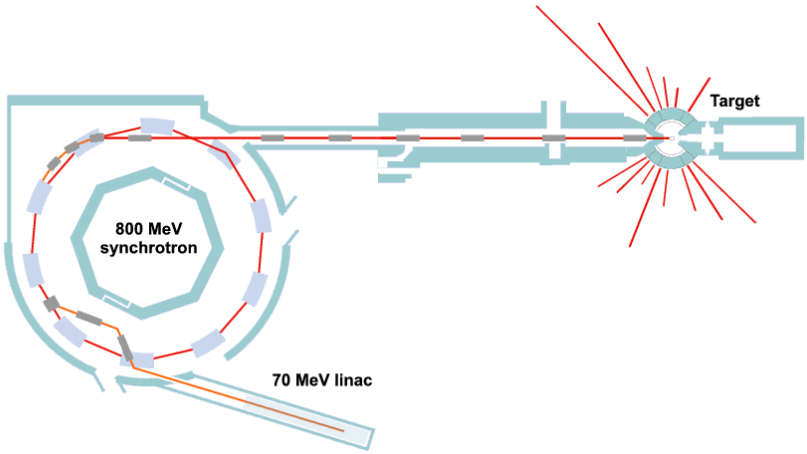


Figure 2.8: Schematic of ISIS Pulsed and Neutron Source.[133]

At ISIS, there are two target stations: target station 1 (TS1) and target station 2 (TS2). Both use a tungsten metal target with proton bunches divided between TS1 and TS2 in a 4:1 ratio. In this way, intense neutron pulses are generated. The generated neutrons are moderated to slower speeds (to obtain the desired wavelength) using hydrogenous moderators. Due to the large distribution of wavelengths, it is wasteful and very inefficient to monochromate the "white" beam of neutrons. Therefore, unlike reactor sources, which measure intensity as a function of 2θ, the intensity is measured as a function of time-of-flight (ToF). Replacing the velocity, v, in Equation 2.10 with L/t where L is distance and t is time relates the time to the wavelength. Instead of a moving detector, multiple fixed-angle detectors are used.

The resolution in a ToF diffractometer is described as the uncertainty in d-spacing (Δd) as a function of d:

$$\frac{\Delta d}{d} = \sqrt{\Delta\theta^2 cot^2\theta + \left(\frac{\Delta t}{t}\right)^2 + \left(\frac{\Delta L}{L}\right)^2} \qquad \text{Equation 2.12}$$

Where the uncertainty in the diffracting angle, ToF and flight path distance is given as $\Delta\theta$, Δt and ΔL, respectively. From this, $\Delta\theta \rightarrow 0$ as $2\theta \rightarrow 180°$ which results in the higher angle detector banks having higher resolution. Resolution can also be increased by increasing the

flight path, which increases the time and reduces Δt and ΔL but at the expense of flux. Low-angle banks measure reflections with high *d*-spacing, which is especially useful in looking at magnetic reflections. Intermediate banks (located at 90°) provide a balance of good *d*-spacing range and good resolution.

The ANSTO facility uses a 20 MW nuclear research reactor (named OPAL) that is submerged in a pool of water. The reactor uses low-enriched uranium (< 20 % ^{235}U) as its fuel source. The reactor core consists of 16 fuel assemblies located 13 m underwater in an open pool. The depth of the water shields the radiation. Light water (normal H_2O) is used as the coolant and moderator. In contrast, heavy water (D_2O) acts as a neutron reflector, maintaining the nuclear chain reaction in the reactor core by reflecting neutrons towards the core, improving neutron flux.

All neutron diffraction data in this thesis were collected on powder samples packed in air-tight 6 mm diameter vanadium cans in an argon glovebox and sealed using an indium wire gasket. Vanadium is used as it has a very low coherent scattering length (-0.38 fm) and therefore has minimal contribution to the diffraction pattern.[131] Low-temperature measurements were measured in a helium cryostat. Details on the individual neutron diffractometers used are described below.

2.2.4.1 POLARIS (ISIS, TS1)

POLARIS is a medium-resolution and high-intensity diffractometer at TS1 at ISIS. This allows for measurement with short counting times or on small samples. The white beam of neutrons passes through a water moderator at ambient temperature with a wavelength distribution of ~ 0.1-6.5 Å. It has a primary flight path of 14 m, and 40 detector modules cover ~ 44 % of the maximum possible 4π steradians. The diffractometer contains 5 detector

banks: 6-14°, 19-34°, 40-67°, 75-113° and 135-168° with *d*-spacing coverage of ~ 0.25-20 Å. The maximum resolution in the backscattering bank is 0.3 % $\Delta d/d$.[134]

2.2.4.2 WISH (ISIS, TS2)

WISH (WIde angle in a Single Histogram) is a long wavelength diffractometer optimised for high resolution at medium-high *d*-spacing, making it suitable for magnetic structure characterisation. High-resolution data is provided in the *d*-spacing range of 0.7-17 Å with a maximum *d*-spacing coverage of up to 50 Å. WISH has a 40 m primary flight path and uses a solid methane moderator at 50 K that generates neutrons with wavelengths of up to 15 Å, considerably larger than POLARIS. A continuous detector array allows for uninterrupted coverage from 10-170°. However, since resolution changes as a function of θ, it is divided into 10 banks, 5 on either side, such that banks 1 and 10, 2 and 9, *etc.*, are at equivalent angles. The measured data from the two sides are combined to improve the signal-to-noise ratio.[135]

2.2.4.3 Echidna (ANSTO)

Echidna (named after the Australian egg-laying mammal) is a high-resolution diffractometer. It has a wavelength range of 0.98-2.53 Å. A Ge monochromator consisting of 23 slabs, which cut along the *hkl* direction, allows a single wavelength to be chosen. Typically, these wavelengths are 1.30 Å (337), 1.62 Å (335). 2.44 Å (331) at a 140° monochromator diffraction angle (take-off angle). The take-off angle is variable from 90-140° and can be fixed at 155°, although the 140° angle, in practice, is optimum between overall resolution and downtime. The diffractometer has 128 cylindrical ^{3}He position-sensitive detector (PSD) tubes. These are arranged vertically and are spaced 1.25° apart around the perimeter of a circle of radius 1.291 m centred around the sample giving a coverage of 158.75° around the sample. Typical scan times range from 1 to 6 hours

depending on sample composition, sample size and instrument configuration, with an average of 2.5 hours. The high resolution ($\Delta d/d \sim 0.1$ %) makes the instrument suitable for structural characterisation.[136,137]

2.2.5 Structural Refinement

2.2.5.1 Rietveld Refinement

To overcome the phase problem that is present when solving the structure of a material from a powder diffraction pattern, the Rietveld method is used.[138,139] First developed by H. M. Rietveld in the 1960s, this method allows the real structure to be approximated by using a starting structural model, that is close to the real structure, to be refined, so that the initial calculated pattern of the starting model matches fairly closely the diffraction pattern observed. For a given point j in the pattern, the calculated intensity y_j^{calc} is determined by combining all the contributions of the Bragg reflection:

$$y_j^{calc} = s \sum_{hkl} L_{hkl} |F_{hkl}|^2 \varphi(2\theta_i - 2\theta_{hkl}) P_{hkl} A + y_j^{back} \qquad \text{Equation 2.13}$$

where s is the scale factor, L_{hkl} is the Lorentz factor, F_{hkl} is the structure factor, φ defines the peak shape, P_{hkl} is the preferred orientation function, A is the absorption factor and y_j^{back} is the background intensity at point j. From this, the residual function S_y which is the difference between the experimental and theoretical pattern, can be obtained:

$$S_y = \sum_j w_j (y_j^{obs} - y_j^{calc})^2 \qquad \text{Equation 2.14}$$

Where y_j^{obs} is the observed experimental intensity at point j, w_j is the statistical weighting factor equal to y_j^{obs}, meaning that each point j has an equal contribution to the refinement. The method uses a least-squares minimisation of S_y. A perturbation is applied to the initially

defined parameters to decrease S_y. A successful perturbation is fed back into the starting model. This is repeated until the model can no longer be improved, and thus a solution is obtained. Starting models were obtained as Crystallographic Information Files (CIFs) from the Inorganic Crystal Structure Database (ICSD), FIZ Karlsruhe.[140] The refinement was carried out using the program TOPAS-Academic version 6.[141] Several parameters can be refined, such as lattice parameters, atomic positions, fractional occupation, and thermal displacement parameters. Other parameters external to the model, such as background, peak profile and instrument corrections, can also be refined. It is important to note that the refinement does not consider how chemically reasonable the structure is. Therefore, care must be taken when conducting a refinement as it is possible that in search of the minimal S_y, the perturbations deviate drastically from the initial values such that the obtained model does not make chemical sense.

As well as assessing the quality of the fit visually, the quality of the refinement can be quantified by using a calculated weighted profile *R* factor, R_{wp}, which is given by:

$$R_{wp} = \sqrt{\frac{S_y}{\sum_j w_j (y_j^{obs})^2}} \qquad \text{Equation 2.15}$$

Here the final R_{wp} should approach the statically expected value R_{exp}:

$$R_{exp} = \sqrt{\frac{N^{obs} - N^{var}}{\sum_j w_j (y_j^{obs})^2}} \qquad \text{Equation 2.16}$$

Where N^{obs} and N^{var} are the number of observables and refined parameters, respectively. In a model that matches perfectly, R_{wp} will be equal to R_{exp}. These two parameters can be related by a "goodness of fit" parameter, χ.

$$\chi = \frac{R_{wp}}{R_{exp}}$$ Equation 2.17

Typically, the smaller these values are, the higher the fit quality. However, these values can be skewed and vary significantly depending on the type of data collected. For example, synchrotron data has much-improved resolution compared to in-house diffractometers. However, in doing so, any imperfections in the pattern become more obvious, resulting in more discrepancies and larger values even though the model obtained is of higher quality.[142]

2.2.5.2 Pawley Refinement

The Pawley refinement, like the Rietveld refinement, is a method to fit a powder diffraction pattern to a starting model.[143] Like the Rietveld method, lattice parameters, background, peak-shape functions, instrument corrections, *etc.*, are all still refinable. However, the Pawley method completely disregards the contents of the unit cell. It assigns arbitrary intensity to the *hkl* reflections, unlike the Rietveld method, which calculates intensity from the structure factor F_{hkl}. This method cannot give you a refined structure. Instead, this method is useful in determining lattice parameters and confirming which space-group gives the best fit for a new compound. TOPAS academic version 6 was also used for Pawley refinements.[141]

2.2.6 SQUID Magnetometry

A Superconducting Quantum Interference Device (SQUID) is an extremely sensitive instrument used to measure a sample's magnetic properties. Measurements were conducted on the Quantum Design SQUID MPMS®3 magnetometer. The main component of the SQUID is a superconducting loop separated into two by thin insulating strips to form two parallel Josephson junctions. Cooper pairs can tunnel through the insulating barrier with no resistance on application of a small current. However, if the current exceeds a critical value,

the superconducting state is broken, and now there is a finite resistance. Therefore, the voltage across the junction can be determined and outputted. An external magnetic field influences the critical current, affecting the obtained voltage. Variations in the applied magnetic field can be seen by monitoring changes in the voltage.[144]

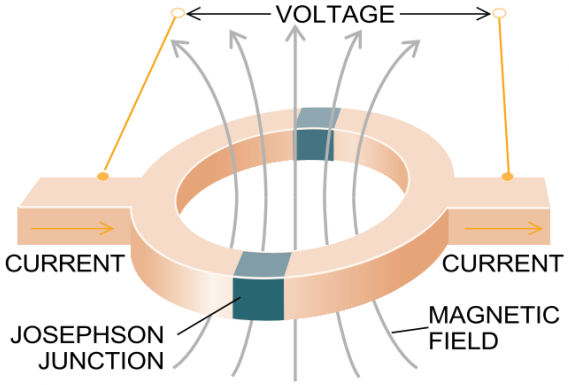


Figure 2.9: Schematic of the Josephson junctions in the SQUID.[144]

The sample is weighed out in a gelatin capsule, placed in a straw, and surrounded by empty capsules. The straw is lowered into a cryostat chamber surrounded by induction coils and magnetised by a He-cooled magnet, making the magnet superconducting. As the sample moves through the coils, a current proportional to the magnetisation is produced. The current travels to the SQUID via superconducting wires, where it is converted into voltage. The SQUID can measure magnetisation as a function of temperature ($1.8 < T < 400$ K) and applied magnetic field ($-7 < H < 7$ T).

2.2.6.1 DC Magnetometry

The use of the SQUID allows multiple types of measurements. The simplest is magnetisation against field (M v H). The gradient of the typically linear plot is the magnetic susceptibly which quantifies the ease with which an applied field may align magnetic moments in the sample. A negative gradient indicates the sample is diamagnet, whereas a positive gradient shows paramagnetism. For a ferromagnet, the M v H plot starts approximately linear but tails

off as the field increases. This is due to the individual ordered domains becoming aligned with the field leading to saturation, and so M v H at high field show a constant flat line. For paramagnets, extremely large fields (not attainable in lab instruments) would be needed for saturation.

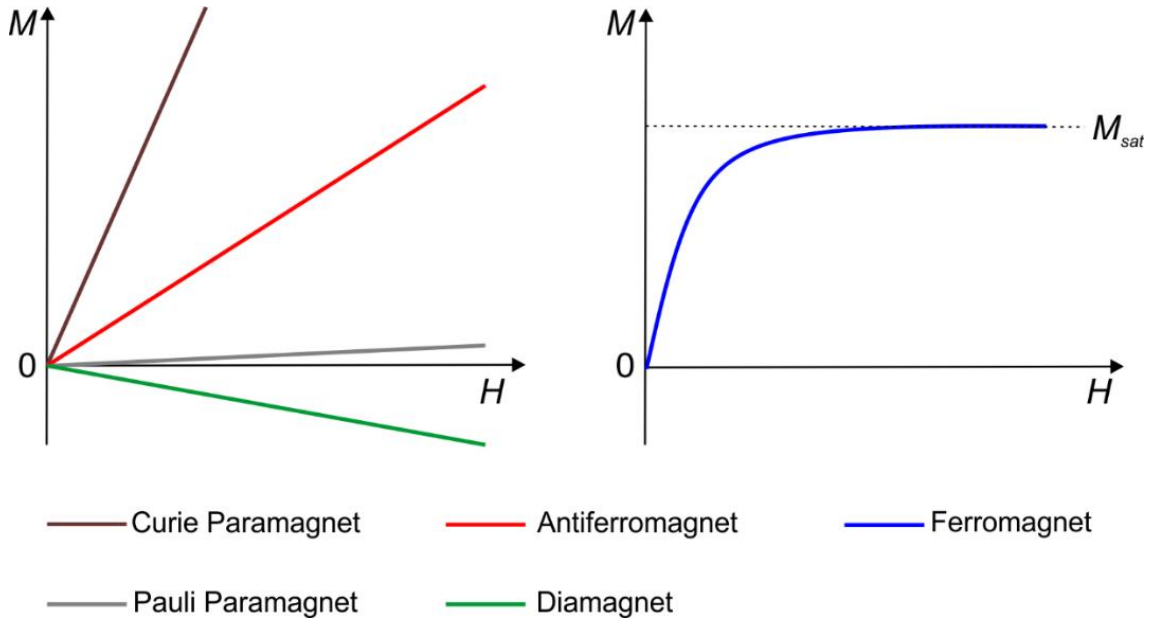


Figure 2.10: Representations of a typical magnetisation vs field graph for the various types of magnetism. Note that for an antiferromagnet below T_N, the direction of the applied field relative to the ordered moment direction determines the size of the induced magnetisation. The response shown is typical for a bulk powder sample of an antiferromagnet in the small magnetic fields normally accessible in the laboratory.

As mentioned in Chapter 1, magnetic moments of different compound classes vary considerably, with ferromagnets being the strongest and diamagnets/Pauli paramagnets being the weakest. There can be a difference of 10^6 in the magnitude of the moment. Therefore, trace amounts of a ferromagnet impurity in a diamagnetic compound can be seen on the SQUID in the form of the M v H not being completely linear. Ferromagnetism dominates at low fields until saturation point. Then, at higher fields, the sample's diamagnetism or paramagnetism is more dominant.

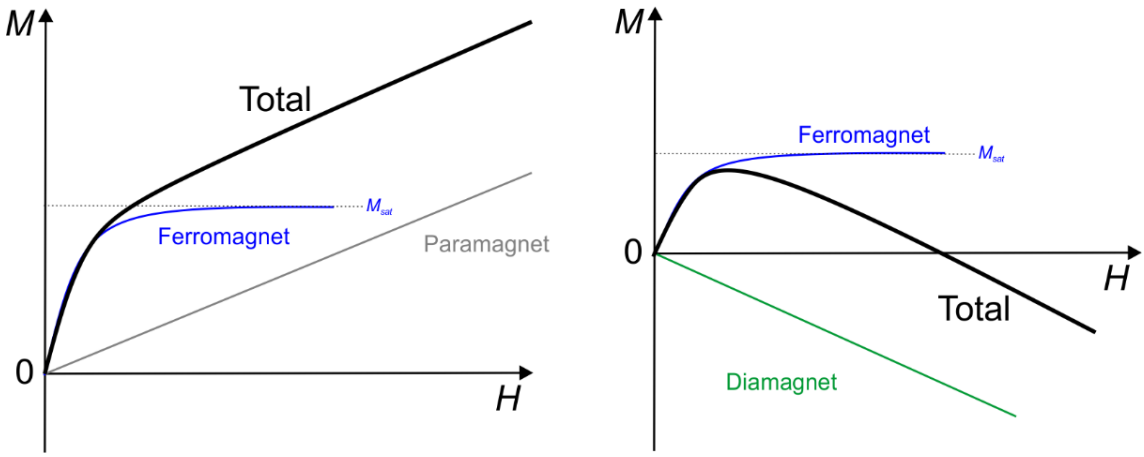


Figure 2.11: Magnetisation vs field graph of a paramagnetic (left) and diamagnetic (right) compound containing ferromagnetic impurity.

If a sample contains ferromagnetic impurities, then it is useful to measure *M* at two fields beyond the saturation of the impurity (in the linear regime), and the gradient between these two points is taken, eliminating the impurity effect.

Measuring a hysteresis loop can give more information about the behaviour of the magnetic system. This involves starting at a high field *H*, measuring the magnetisation when reducing the field then applying the field in the opposite direction *-H*. The field is reduced once more before returning to the initial field *H.* For a paramagnet removing the field will set the magnetisation back to zero. For a ferromagnet, however, when the field is removed, the alignment of the magnetic domains does not completely break, and some remnant magnetisation remains. Applying the field in the opposite direction is now affected by the field applied before. Since the domains are aligned opposite to the new field, the magnitude of the induced magnetisation is lower. The shape of the hysteresis indicates the ease at which a material can be demagnetised. A narrow hysteresis is a property of a soft magnet, whereas a wide hysteresis loop indicates a magnet with high coercivity.

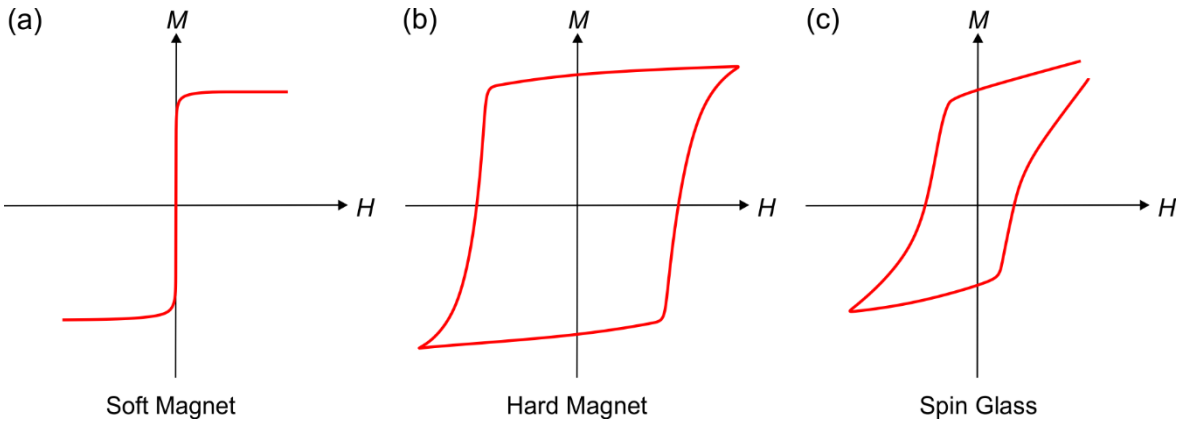


Figure 2.12: Magnetisations versus field isotherms for a soft (a) and hard (b) magnet as well as a spin glass material (c).

In a spin glass, the domains are locked, so they will display a strong hysteresis with respect to the field aligning them. When a negative field is applied, domains may leave the locked state, but the memory of the initial state can remain. This means the magnetisation returns more easily when returning to a positive field. The hysteresis may superficially resemble that of a ferromagnet, although its often not symmetrical about the origin, or the curve may not re-join its starting value.

Measuring magnetisation as a function of temperature can also confirm the magnetic nature described in Chapter 1. Here, the transition temperature can be seen, as well as determining the constants from the Curie-Weiss Law (Equation 1.4) by plotting $\frac{1}{\chi}$ against T. The magnetisation is typically measured twice, once zero-field cooled (ZFC) and once field cooled (FC). ZFC refers to applying no field at a temperature well above the ordering temperature and then cooling to base (1.8 K) before turning on the applied field. The SQUID then measures magnetisation upon warming. Whereas for FC, the field is set before it is cooled to the base temperature. The energy required for the moments to align in the field can differ for ZFC and FC, and the way they contrast can be used to indicate the type of magnetism present. For example, on first viewing, ZFC and FC curves in a spin glass appear like an antiferromagnet. Still, deviations are typically larger due to the locked-in state being

different in the presence or absence of the applied field. In a classical antiferromagnet, the ZFC and FC will overlap. For a spin glass, there may be some deviation at low fields in ZFC and FC above the ordering temperature due to the persistence in the arrangement of local domains above the system's global transition temperature.

2.2.6.2 Superconductivity

Superconductivity in a material is commonly defined when the material exhibits zero resistivity below a critical temperature. However, superconductors additionally show the property of perfect diamagnetism. For simplicity, it is often more convenient to probe the magnetic changes using a contactless measurement rather than electric changes. A superconducting transition can be seen when the susceptibility drops below 0 after a transition temperature due to the Meissner effect, expelling all lines of magnetic flux until perfect diamagnetism is achieved.

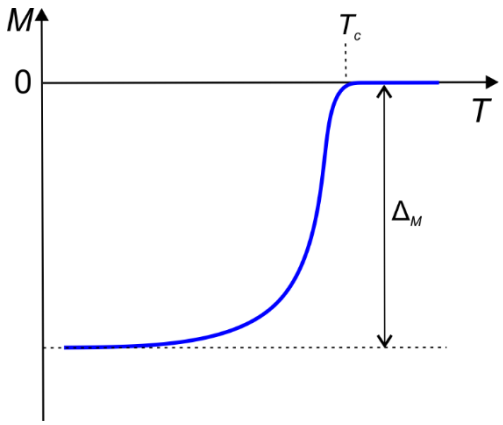


Figure 2.13: A typical magnetisation vs temperature plot of a superconductor.

It is more beneficial to plot the superconducting volume fraction (*SVF*), which indicates what percentage of the material is superconducting. This can be calculated by taking the difference in the measured magnetic moment, denoted here as Δ_M, from the normal state (above T_c) and the magnetic moment at the lowest temperature possible (1.8 K). From this, the dimensionless magnetic susceptibility (χ), can be calculated:

$$\chi = \frac{\rho \Delta_M}{mH}$$ Equation 2.18

Where m is the sample mass (in g), H is the applied field (in Oe), and ρ is the crystallographic density (in g cm^{-3}). The superconducting volume fraction can be expressed as:

$$SVF = 4\pi\chi$$ Equation 2.19

where 4π represents a sample that displays perfect diamagnetism through its entire volume. In an ideal superconductor, $4\pi\chi$ = -1, which is equivalent to a *SVF* of 100 %.

For the superconducting compounds in this thesis, magnetisation was measured in ZFC and FC as a function of temperature (1.8 K ≤ T ≤ 8 K). A field of 10 Oe was used. A small, applied field is important such that it does not exceed the critical field of the material. A large enough field will penetrate the superconductor and thus gives a lower volume fraction.

2.2.6.3 AC Magnetometry

The previous magnetic measurements discussed so far relate to a direct current (DC) field where the applied magnetic field is constant in one direction. However, another less-used technique is applying an alternating current (AC) field where a small field oscillates between the positive and negative directions. The speed at which the field oscillates is known as the frequency, and the magnitude that the field reaches is known as the drive field. The advantage of an AC measurement is that it can provide information about the magnetic system dynamics, as magnetic moments will follow the field with a time dependency.

In AC measurements, a small AC drive field is superimposed on the DC field, causing a time-dependent moment in the sample. At low frequencies, the measurement is similar to a DC measurement. However, at high frequencies, the system dynamics may make the AC moment not follow DC magnetisation. Here, the sample magnetisation may lag behind the

drive field. This results in the AC magnetic susceptibility compromising of two components: the magnitude χ and the phase shift ϕ. The susceptibility, χ, can be seen as having an in-phase (real) component, χ' and an out-of-phase (imaginary) component, χ'', which are related by:

$$\chi' = \cos\phi \qquad \text{Equation 2.20}$$

$$\chi'' = \sin\phi \qquad \text{Equation 2.21}$$

$$\chi = \sqrt{(\chi')^2 + (\chi'')^2} \qquad \text{Equation 2.22}$$

$$\phi = \tan^{-1}\left(\frac{\chi''}{\chi'}\right) \qquad \text{Equation 2.23}$$

For a low frequency, $\phi \sim 0$, therefore, $\chi'' \sim 0$ and $\chi' \sim \chi$(DC). In spin-glasses, relaxation and irreversibility give rise to a non-zero χ''. This can be seen in a shift of the transition peak, as shown below.

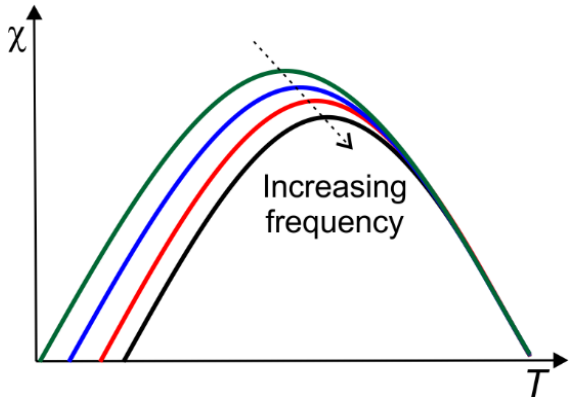


Figure 2.14: AC magnetisation of an antiferromagnetic transition where the peak shifts with frequency.

2.2.7 X-ray Absorption Spectroscopy (XAS)

As mentioned previously, when an X-ray interacts with matter, not only are the X-rays diffracted, but they can be absorbed too. X-ray absorption spectroscopy (XAS) probes the

transition of a core electron (typically 1*s* or 2*p*) from the ground state to the excited state. XAS is useful in providing information on atomic oxidation states, symmetry, and local structure information and does not require long-range order for this technique to be applicable. Therefore, it can be used on liquids and molecular gasses, making this a versatile technique.

The absorption coefficient $\mu(E)$ is the measure of an atom's absorption and, for an atom in isolation, is approximated as:

$$\mu(E) \approx \frac{\rho Z^4}{AE^3} \qquad \text{Equation 2.24}$$

where ρ is the sample density, Z is the atomic number, A is the atomic mass, and E is the photon's energy. $\mu(E)$ has a $1/E^3$ relationship since it decreases as the X-ray becomes more energetic and penetrating. When the energy of the X-ray is high enough to overcome the binding energy of the core electron, $\mu(E)$ increases sharply, and an "absorption edge" arises as the electron has transitioned to an excited state. The absorption edge is labelled *K*-edge, *L*-edge *etc.*, depending on which inner shell the electron transitioned from (*K* for $n = 1$, *L* for $n = 2$ *etc.*).

$\mu(E)$ can be determined experimentally by XAS by rearranging the Beer-Lambert Law to give:

$$\mu(E) = \varepsilon \, ln\left(\frac{I_0}{I}\right) \qquad \text{Equation 2.25}$$

Where ε is the thickness of the sample, I_0 and I the intensity of the incident and transmitted X-rays, respectively. Sample thickness can be removed by normalising $\mu(E)$.

A typical XAS spectrum of normalised $\mu(E)$ is shown below in Figure 2.15. The spectrum has two major components: The X-ray Absorption Near Edge Spectroscopy (XANES) and

the Extended X-ray Absorption Fine-Structure Spectroscopy (EXAFS). XANES consists of (i) The pre-edge, which can provide information on local symmetry, (ii) the absorption edge, which is indicative of the energy gap between the ground and excited state and is useful for determining oxidation states and (iii) the near-edge which includes very local structural information. EXAFS also provides information about the local structure.

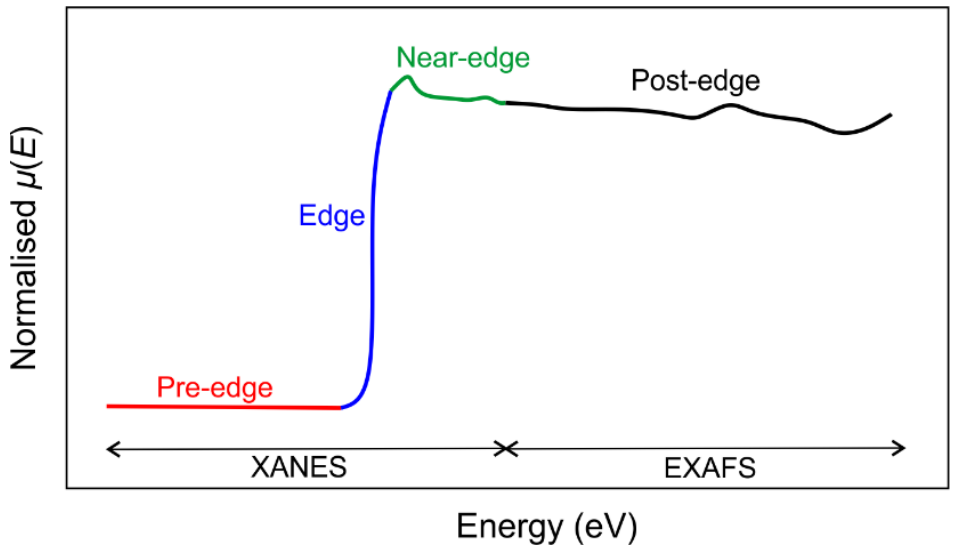


Figure 2.15: Typical XAS plot showing the XANES and EXAFS components.

XAS was carried out on the B18 beamline at the Diamond Light Source.[145] The synchrotron, as stated previously, provides X-rays with very high energies suitable for studying most of the elements. The beamline uses a bending magnet source to provide energies from 2-35 keV. The beam passes through a collimating Si mirror, then either a Si (311) or Si (111) monochromator (depending on the energy required) before being directed at the sample.

To prepare the sample, the sample was diluted with cellulose to reduce beam absorption and then pressed into a 13 mm pellet. The pellet was taped onto a plastic grid using diamagnetic tape before being sealed in an aluminised polyethene bag under an Ar atmosphere. The measurement was carried out without opening the polyethene bag to prevent air exposure. Data processing and normalisation were conducted using the Athena software package.[146]

2.2.8 SEM-EDX

Scanning electron microscopy (SEM) with energy dispersive X-ray spectroscopy (EDX or EDS) is a widely used analytical technique to probe the surface and study the topography of materials. SEM uses a focused beam of electrons instead of light to form an image, which has many advantages over traditional optical microscopes. SEM has a much larger depth of field, allowing more of the material to be in focus at any one time. SEM produces much higher-resolution images since the beam can be focused on a very small spot. Electromagnetic lenses are made up of wire coils inside metal poles that generate a magnetic field upon the passing of a current. Electrons are highly sensitive to the magnetic field, enabling the lenses to control the beam. When the incident electron beam interacts with the sample, electrons and X-rays are ejected. Backscattered electrons are reflected elastically (no loss of electron energy) and originate from deeper areas of the sample. The intensity can be correlated to the atomic number and is highly sensitive to different atomic numbers. Hence very qualitative elemental information can be obtained. Secondary electrons come from the atoms in the sample due to inelastic scattering, whereby the interaction causes a loss of energy, which occurs on the surface. The surface topography of the sample dictates the intensity. An image of the sample surface can be formed by measuring this intensity as a function of the position of the incident electron beam.

When the incident electron beam hits the sample, it can excite an inner shell electron, displacing it. This leaves an electron hole in which a higher energy outer shell electron will drop down to the lower energy inner shell to fill it. The energy difference is released as an X-ray. The energy of this X-ray is unique to the element and the transition. An energy-dispersive spectrometer can measure the number and energy of the X-rays emitted, providing quantitative information on elemental composition. Therefore, combining SEM with EDX

is a method that provides both qualitative and quantitative information in a relatively rapid, inexpensive and non-destructive manner.

Measurements were carried out on the Zeiss EVO MA10 equipped with an Oxford Instruments X-act EDS detector in the David Cockayne Centre for Electron Microscopy, University of Oxford. The powder samples were mounted on an adhesive carbon tape, and then the sample surface was coated with 6 nm carbon layers using a Lecia ACE600 Coater. The technique cannot be used for very air-sensitive samples as air exposure is inevitable during the transfer of the sample to the carbon coater and then to the sample chamber in the SEM. EDS maps were processed using the Oxford Instruments Aztec software.

2.2.9 Nuclear Magnetic Resonance (NMR) Spectroscopy

Nuclear magnetic resonance (NMR) spectroscopy is a powerful and highly sensitive technique to probe chemical structures and study local chemical environments of nuclei that have a nuclear spin. In NMR, nuclei with a non-zero spin placed in an external magnetic field will respond oscillatory to resonant excitation by radiofrequency irradiation. The degeneracy of the nuclear spin states is lifted in a magnetic field, leading to an energy difference ΔE which is given by:

$$\Delta E = \gamma\hbar(1-\sigma)B_0 \qquad \text{Equation 2.26}$$

Where γ is the gyromagnetic ratio, $\hbar$ is the reduced Plank's constant, σ the chemical shielding around the nucleus, and B_0 is the applied magnetic field strength. Typical magnetic fields in NMR experiments can range from 5-28 T with the transition in nuclear spin states in the MHz frequency range. The local field the nucleus experience is not equal to the applied field because of shielding effects from surrounding electron density resulting in slightly different frequencies. The frequency signal produced gives information about the chemical structure.

This is dependent on the applied field; therefore, it is converted to a chemical shift value independent of the field. Chemical shift is the fractional difference between the frequencies of the nuclei in question and a reference compound given in parts per million (ppm).

Chemical shifts can also be affected by other nuclei spin interactions such as spin-spin scalar coupling (depends on covalent bonding), spin-spin dipolar coupling (depends on internuclear distance), and for nuclei with spin > ½, there is quadrupolar coupling (interaction with the electric field gradient). These anisotropic interactions depend on the angle θ between the sample and the applied magnetic field. The frequency difference $\Delta\nu$ is related to θ by:

$$\Delta\nu \propto (1 - 3cos^2\theta) \qquad \text{Equation 2.27}$$

In solution, molecular tumbling averages out these interactions, and typical solution NMR spectra consists of sharp lines.

2.2.9.1 Solid-state ^{7}Li NMR

In the solid state, there is no molecular tumbling to average out these anisotropic interactions. This results in extensive line broadening, which conceals NMR peaks. To overcome this problem, "magic-angle spinning" (MAS) is used where the sample is spun around an axis tilted at a specific angle of 54.74° from the field.[147] At 54.74°, the (1-3cos$^2\theta$) term equals zero. To achieve the complete averaging of these interactions, samples must be spun at a frequency greater than the highest frequency anisotropic interaction. If not, then a manifold of spinning sidebands become visible.

In this thesis, solid-state ^{7}Li MAS NMR was used to probe Li environments in Li intercalates. ^{7}Li has spin of $^3/_2$. NMR measurements were carried out by Dr Sunita Dey, University of Cambridge, UK. Measurements were performed on a Bruker Avance 200 MHz

(4.07 T) spectrometer operating with a ^{7}Li frequency of 77.8 MHz. Samples were packed inside a glovebox into a 1.3 mm ZrO_2 rotor and spun at speeds from 35-60 kHz. LiF was used as the reference (-1 ppm), and Bruker Topspin version 4.0.7 was used to process the raw data.

2.2.10 Computational Methods

2.2.10.1 Density Functional Theory (DFT)

First principles (*ab initio*) methods were developed to model and predict properties of many-body systems without using experiments. The Hartee-Fock (HF) theory, developed in the 1930s, assumes that the many-electron wavefunction is the determinant of single-electron wavefunctions.[148] However, the downside is that electronic correlations are not fully incorporated, and the wavefunctions are a function of 3*N* variables (*x*, *y* and *z* coordinates of the *N* atoms in the system). On the other hand, density functional theory (DFT) bypasses the need for many-electron wavefunction and instead uses functionals (functions of another function) of spatially dependent electron density. The theory is based on the Hohenberg-Kohn theorem developed in the 1960s that states the total energy is a functional of the electron density.[149] Electron density is only dependent on the three spatial coordinates *x*, *y* and *z*, speeding up the calculation, which now requires far less computational power, making it useful for larger systems. The disadvantage is that the exact energy functional of a system is unknown and must be approximated. Traditionally, HF methods were more reliable, but in recent times DFT methods are much more refined, leading to higher accuracy and lower computational expense. DFT has increased in popularity and is frequently used to investigate many compounds' structural, electronic, and magnetic properties.

In this thesis, DFT was used (in Chapter 4) to calculate the electronic density of states and band structure and predict the relative energies of Li sites within a host structure along with their ^{7}Li NMR chemical shift. These computational calculations were carried out by Jiayi Cen at UCL. A detailed description of the method is provided in Appendix I.

2.2.10.2 Monte Carlo Simulations

Monte Carlo simulation is a broad class of computational algorithms that depend on repeated random sampling to obtain numerical results.

In this thesis, Monte Carlo simulation was used to simulate diffuse magnetic scattering (see Chapter 5). In this simulation, a large supercell containing a vast number of spins is set up. A simulated annealing is performed starting from a temperature above the magnetic ordering temperature down to the base temperature where it would be ordered. At each temperature, the program executes 10^n flips per spin using the Metropolis method outlined below.[150]

1. A spin is chosen randomly, and the energy (E) required to flip the spin is calculated.
2. If $E < 0$, flip the spin as the system is now in a lower energy state.
3. However, if $E > 0$, the transition probability $W = e^{\frac{-E}{kT}}$ is calculated.
4. A random number between 0 to 1 is generated, and if smaller than W, flip the spin; otherwise, do not flip the spin.
5. Repeat steps 1 to 4.

This process is repeated many times and coverages on a spin configuration. From this, the spin-spin correlation function and the magnetic structure factor can be derived, allowing the neutron scattering intensity to be calculated and plotted.

2.2.11 Raman Spectroscopy

Raman spectroscopy is a vibrational spectroscopic technique used in studying chemical bonding and chemical structure. The technique relies on light scattering, where the sample scatters incident light from a high-intensity light source, usually a laser in the visible, near-infrared, or near-ultraviolet range. Light can be scattered elastically or inelastically. Elastic scattering is where the scattered light is the same wavelength as the incident light (known as Rayleigh scattering). This constitutes most of the scattering. However, a small fraction of light, typically of the order 10^{-9}, is scattered inelastically at a wavelength not equal to the incident light. This is known as Raman scattering. Raman scattering can be split into Stokes and Anti-Stokes scattering depending on the energy of the photon emitted. In Stokes scattering, the molecule relaxes to a higher vibrational state than originally, emitting a lower energy photon with a higher wavelength. Conversely, for anti-Stokes scattering, the molecule emits a higher energy (lower wavelength) photon when it relaxes to a lower vibrational state than initially. Since anti-Stokes require the molecule to be in a vibrationally excited state before being exposed to the light, this transition is the least common and suffers from a lack of intensity. Therefore, in Raman scattering measurements, photons with incident energy or higher are filtered, and only Stokes scattering is used.

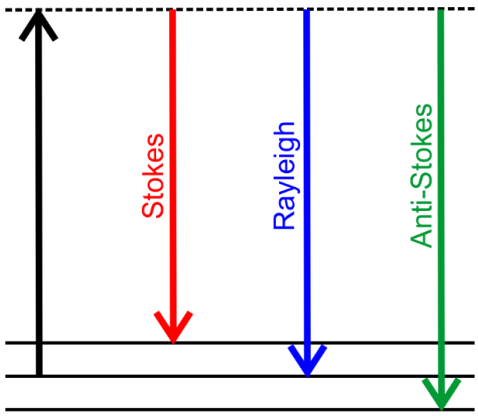


Figure 2.16: Vibrational transitions showing the elastic scattering (Rayleigh) and inelastic scattering (Stokes and anti-stokes).

Raman measurements were carried out in-house on the ThermoScientific™ DXR3 SmartRaman spectrometer, equipped with 532 nm and 785 nm lasers. Laser power was fixed to 100 mW and can obtain a spectrum from 100 cm^{-1} to 3500 cm^{-1}. To prevent air exposure, samples were sealed in a 1.5 mm borosilicate capillary and loaded onto the instrument.

2.2.12 Elemental Analysis

2.2.12.1 ICP-MS

Inductively coupled plasma mass spectrometry (ICP-MS) is a technique used to analyse element composition in a sample. The method is capable of detecting most of the elements in the periodic table at extremely low detection limits, down to even 0.1 part per trillion. ICP-MS requires liquefied samples; therefore, solids are typically dissolved in acid. Ar carrier gas is used to aerosolise the sample sending only small droplets into the chamber. This is then inductively heated using an electromagnetic coil and ionises the argon gas forming the plasma. The extreme temperature of the plasma atomises the sample, and the sample atoms are ionised. Because of the high ionisation energy of Ar, the reaction $Ar^+ + e^- \rightarrow Ar$ is more energetically favourable than $M^+ + e^- \rightarrow M$ in all cases except He, F and Ne. This ensures that the sample remains ionised to be detected by the mass spectrometer, which separates the ions according to their mass-to-charge ratio.

The limitation of ICP-MS is that it cannot be used to measure H, He, O, N, F, Ar and Ne. The mass of H and He are below the range of the mass spectrometer. O, N and Ar are present in high amounts from the plasma and the air. F and Ne cannot be ionised in the argon plasma due to their higher first ionisation energies.

ICP-MS measurements were carried out by Dr Nigel Howard (via Dr Sunita Dey), University of Cambridge, UK. Elemental content was evaluated with Perkin Elmer Nexion

350D quadrupole-based Inductively Coupled Plasma - Mass Spectrometer. The sample was digested in ICP grade aqueous HNO_3 and quantified against calibration points generated from the standard solutions.

2.2.12.2 Dumas Combustion Method

The Dumas combustion method is used to measure N and H content in inorganic materials, which is otherwise impossible using ICP-MS. This elemental analysis technique can indirectly analyse C, H, N, O and S composition in a sample from combustion products. A few milligrams of a sample are combusted at high temperatures in an environment of pure oxygen. This allows the complete combustion into CO_2, N_2, H_2O and SO_2. After combustion, the mixture of gases is passed over copper, removing excess oxygen and reducing nitrogen oxides to elemental nitrogen. Gas chromatography can be used to separate the gases, with the identification of the gas achieved using thermal conductivity detection or infrared spectroscopy. From this, element contents are given as mass percentages of the sample. Elemental analysis was conducted by Elemental Microanalysis, Okehampton, UK.

2.2.13 Specific Heat Capacity

The specific heat capacity (C_p) of a material is the energy required to raise its temperature. C_p of a solid-state material can be represented using the Einstein or Debye model. In the Einstein model, the N vibrating atoms in a crystal are seen as N simple harmonic oscillators with the same frequency. In the Debye model, the harmonic oscillators are coupled with a range of frequencies. Both models correctly give the specific heat capacity at the high-temperature limit (the Dulong and Petit law). However, the Debye model significantly improves on the Einstein model at low temperatures in which it models C_p with a T^3 dependence, in agreement with experimental observation.[151]

For a magnetic compound, a magnetic transition could be seen as a peak or kink in a C_p against T plot. C_p is the sum of a lattice contribution (C_l) and a magnetic contribution (C_m). C_m can be extracted by subtracting C_l from C_p. C_l can be obtained by measuring the C_p of a homologous non-magnetic compound. From this, the magnetic enthalpy and entropy changes can be calculated using the equations below:

$$\Delta H_m = \int_{T_1}^{T_2} C_m \, dT \qquad \text{Equation 2.28}$$

$$\Delta S_m = \int_{T_1}^{T_2} \frac{C_m}{T} \, dT \qquad \text{Equation 2.29}$$

Specific heat capacity measurements were carried out on a Quantum Design PPMS® instrument at the Oxford Physics Department. A 1 mm by 1 mm sintered pellet was cut and glued using thermal paste onto a puck before being placed inside the PPMS.

Chapter 3

3 Intercalation reactions of $ZrSe_3$

The work in this chapter has been published [Elgaml, M., Cassidy, S. J. & Clarke, S. J. Topochemical intercalation reactions of $ZrSe_3$. *J. Solid State Chem*. **314**, 123436 (2022)]

3.1 Introduction

The structure of $ZrSe_3$ was described in section 1.2.1.2. Li intercalation into $ZrSe_3$ was first carried out by Chianelli *et al.* and subsequently followed up by Sourisseau *et al*. and Canadell *et al*.[118,152,153] It was reported that when chemically intercalating Li into $ZrSe_3$, three moles of Li per mole of $ZrSe_3$ were always taken up, corresponding to the full reduction of the chalcogenide to Se^{2-} and reduction of Zr(IV) to Zr(III). The structure appears to have gone through significant change and suffered a substantial loss of crystallinity; hence the structure of this intercalate remains unsolved.

Klepp *et al*. reported partially reduced compounds of the form $A_xZr_2Se_6$ (A = K, Rb, Cs; $0.8 < x < 1.1$) with a $ZrSe_3$ framework similar to that in $ZrSe_3$ being formed with the group I alkali metal ions, A^+, residing between the layers.[119] Two structures were found which are related to each other by the relative shifting of the $ZrSe_3$ layers. These compounds can formally be described as intercalates of $ZrSe_3$. However, they were not formed in topochemical intercalation reactions. Instead, they were obtained by reacting A_2Se (A = K, Rb, Cs), Zr and Se in a 1:4:11 ratio at 850 °C. It is particularly notable that these compounds form a similar framework to that found in the binary $ZrSe_3$.

For $K_{1.1}Zr_2Se_6$ ($K_{0.55}ZrSe_3$), and $Rb_{0.86}Zr_2Se_6$ ($Rb_{0.43}ZrSe_3$), Klepp *et al.* obtained a structure crystallising in *Immm*,[119] whereas for $Cs_{0.80}Zr_2Se_6$ ($Cs_{0.40}ZrSe_3$), the compound crystallised

in *Cmc*2_1. The two structures are related by different relative shifts of adjacent layers in $ZrSe_3$, as shown in Figure 3.1; if the top layer is shifted to the right relative to the bottom layer, then an inversion centre appears, the structure has body-centred symmetry, and the space group is *Immm*. Whereas if the top layer is shifted to the left, there is no inversion centre, the structure only has *C*-centring, and the space group is non-centrosymmetric *Cmc*2_1.

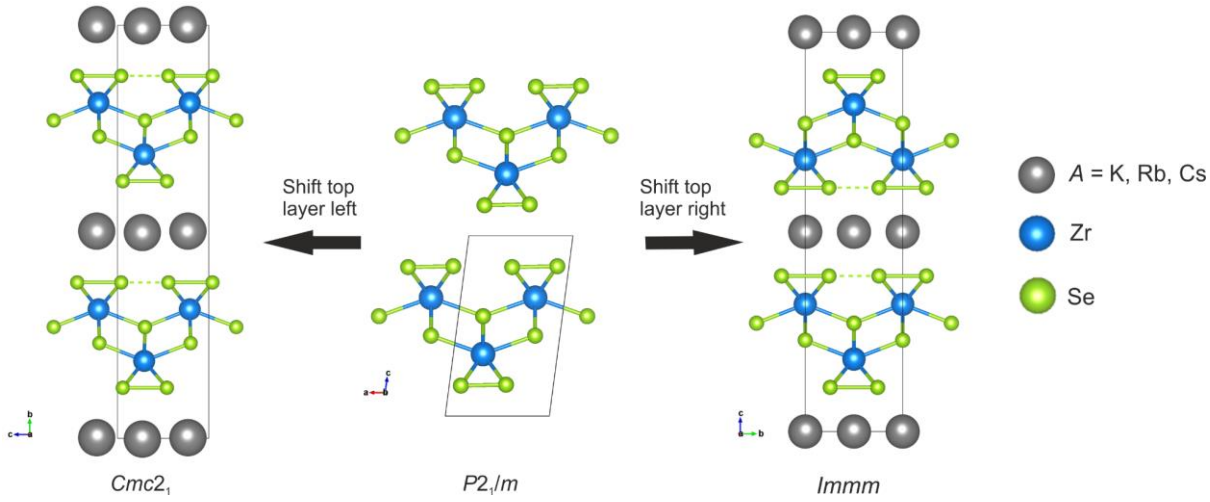


Figure 3.1: The relationship between the structure of $ZrSe_3$ (centre) and the structures of the intercalated polymorphs. The dotted line represents the interaction between neighbouring selenide dimers due to their subsequent reduction.

In this chapter, compositions similar to those obtained by Klepp *et al.*[119] will be shown to also be attainable via topochemical reactions of $ZrSe_3$ using low-temperature soft chemical methods. Here, $ZrSe_3$ is reacted with the metal in liquid NH_3 in the intercalation process described in section 2.1.3.3. The structures of the alkali metal (K, Rb and Cs) intercalates are compared with those reported by Klepp *et al.*[119] with different polymorphs attained at low temperatures. Furthermore, the work described in this chapter will also show that the use of low-temperature intercalation chemistry enables co-intercalation of Ca and ammonia/amide species into this system, leading to a much larger expansion of the interlayer spacing than is found in the alkali metal intercalates.

3.2 $ZrSe_3$

Single-phase crystalline $ZrSe_3$ was synthesised by a direct combination of the elements; Zr foil (Alfa Aesar, 99.8 %) and Se powder (Alfa Aesar, 99.999 %). The starting materials were combined in a dry evacuated silica ampoule and heated at 450 °C at 1 °C/min for 12 hours to ensure reaction of the volatile chalcogen, then heated further at 900 °C (1 °C/min) for 72 hours before being left to cool naturally to room temperature. The product was a black crystalline powder.

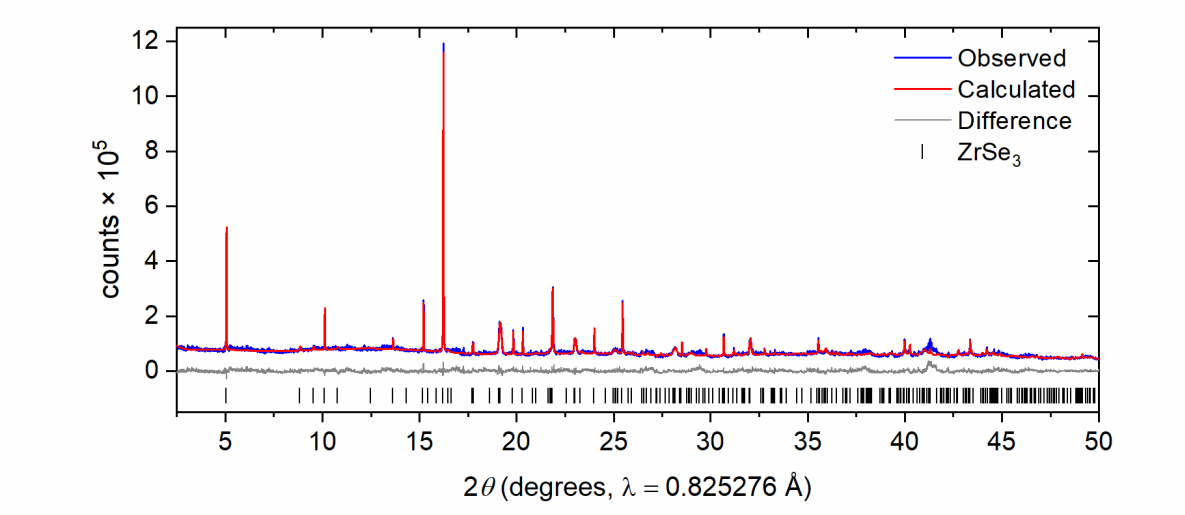


Figure 3.2: Rietveld refinement against I11 (PSD) PXRD pattern of $ZrSe_3$ (ME005). The blue line is the observed experimental pattern, the red line is the calculated pattern of the refined model, and the grey line is the difference between them. The tick marks show the Bragg reflections.

Performing a Rietveld refinement on $ZrSe_3$ was relatively difficult as, despite obtaining accurate lattice parameters, it was not possible to accurately refine the *x* coordinates of the elements in the compound, which resulted in the Se-Se dimer and non-dimer distances deviating from the reported literature values (~ 0.25 Å difference). The layers are free to shift relative to each other along the *a*-axis which results in stacking disorder. This would place the dimer in the crystallographic position of the non-dimer and vice-versa. Therefore, the powder diffraction experiment leads to an averaging of the *x* position resulting in the Se-Se dimer distance being longer than expected and the non-dimer distance being shorter.

As mentioned in Chapter 1, two structural variants (A and B) were initially reported for MCh_3, which were viewed as mirror images, where $x_A = 1\text{-}x_B$.[38] Careful examination using single-crystal diffraction concluded, 20 years later, that only one variant exists.[39] The use of single-crystal diffraction is necessary to obtain accurate positional parameters. For the rest of this chapter, the reported literature values of $ZrSe_3$ shown in the table below from Furuseth *et al.*[38] will be used to compare with the intercalates.

Table 3.1: Comparison of structural parameters of refined $ZrSe_3$.

Compound	**$ZrSe_3$ (ME005)**	**$ZrSe_3$ (Furuseth *et al.*)**[38]
Space Group	$P2_1/m$	$P2_1/m$
***a* / Å**	5.4080(2)	5.4109(12)
***b* / Å**	3.7481(1)	3.7488(9)
***c* / Å**	9.4599(4)	9.444(2)
***β* / °**	98.197(6)	97.48
Volume / Å^3	189.79(1)	189.94
***x*(Zr)**	0.239(1)	0.285
***x*(Se1)**	0.779(1)	0.762
***x*(Se2)**	0.455(1)	0.456
***x*(Se3)**	0.938(1)	0.888
Se-Se (Dimer) / Å	2.593(9)	2.3441(6)
Se-Se (Non-Dimer) / Å	2.827(9)	3.0676(7)

3.3 K Intercalation

Intercalation of K into $ZrSe_3$ using K/NH_3 solution resulted in the black powder turning brown in colour, with the dark blue solution of the solvated electrons in NH_3 decolourising within minutes. The powder X-ray diffraction pattern showed similarities to that obtained by Klepp *et al.*,[119] with the indexing of the pattern showing an approximate 16 % increase in the interlayer separation compared with $ZrSe_3$ itself, and the initial structural model was determined from this literature report. The lattice parameters are in very close agreement

with those of the structure of $K_{0.55}ZrSe_3$ reported by Klepp *et al.*[119] modelled in *Immm*. However, the pattern was fit instead by the *Cmc*2_1 model obtained by them for $Cs_{0.40}ZrSe_3$. This was deduced from the presence of reflections such as 021 and 151, which are symmetry forbidden in *Immm* (as these reflections violate the $h + k + l = 2n$ rule) but allowed in *Cmc*2_1.

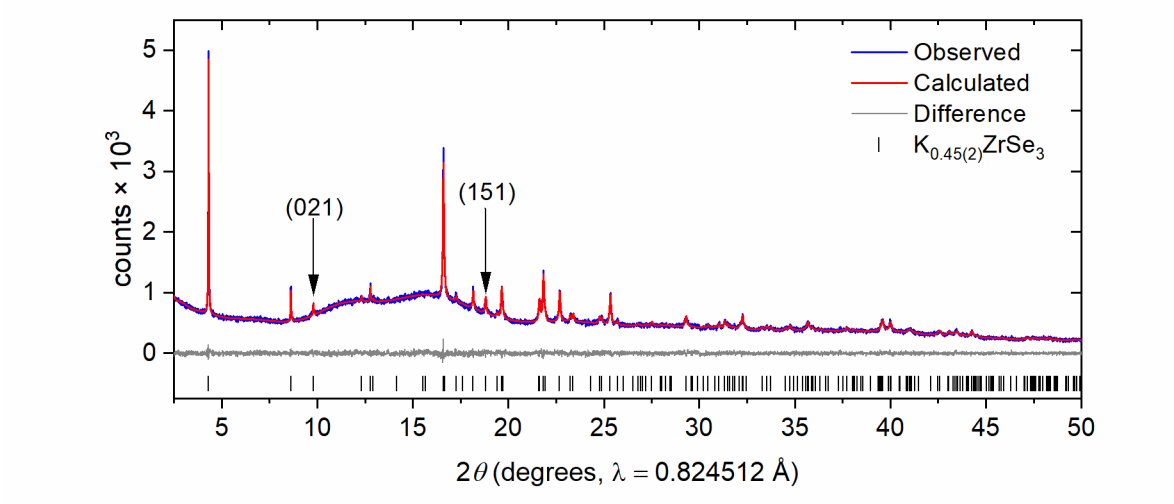


Figure 3.3: Rietveld refinement against I11 (MAC) PXRD pattern of $K_{0.42(2)}ZrSe_3$. The 021 and 151 peaks allowed in *Cmc*2_1 but forbidden in *Immm* are indicated. R_{wp}: 3.05 %

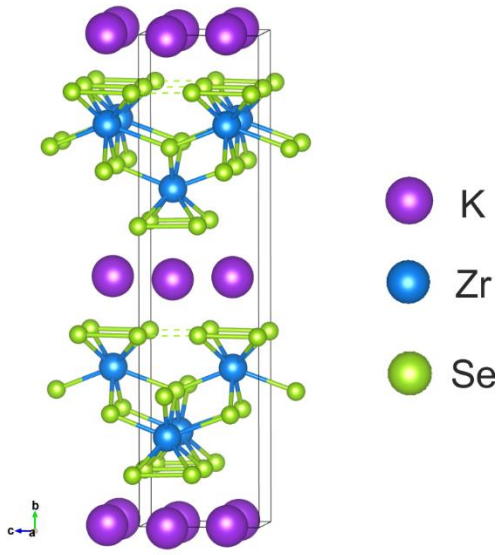


Figure 3.4: *Cmc*2_1 structure of $K_{0.42(2)}ZrSe_3$. The green dotted lines between Se-Se dimers indicate the non-dimer Se-Se interaction.

The K occupancy was refined to 0.45(2), which is 0.1 lower per formula unit than the $K_{0.55}ZrSe_3$ obtained in the high-temperature synthesis. Thermal displacement parameters were constrained to refine to one common value due to the quality of the data, which caused high correlation between parameters. Only about half of the K in the reaction was incorporated into the host, and it is assumed that the excess electrons in the metal/ammonia solution are consumed by side reactions.

Table 3.2: Comparison of structural parameters and distances of $ZrSe_3$, the high-temperature $K_{0.55}ZrSe_3$ and the low-temperature $K_{0.45(2)}ZrSe_3$. ‡ Indicates the crystallographic *b* and *c* axis swapping so that the standard space group symbol is used.

Compound		**$ZrSe_3$**	**$K_{0.55}ZrSe_3$**	**$K_{0.45(2)}ZrSe_3$**
Source		Furuseth *et al.*[38]	Klepp *et al.*[119]	ME005B
Space Group		$P2_1/m$ (No. 11)	$Immm$ (No. 71)	$Cmc2_1$ (No. 36)
***a* / Å**		5.4109(12)	3.746(3)	3.76149(9)
***b* / Å**		3.7488(9)	5.354(8)	21.970(1) ‡
***c* / Å**		9.444(2)	21.929(3)	5.3835(1)
***β* / °**		97.48	90	90
Volume / Å^3		189.94	439.8	444.90(3)
Interlayer Separation / Å		9.444(2)	10.964(2)	10.985(1)
Van der Waals Gap / Å		3.2499(6)	4.845(5)	4.90(4)
Bond Lengths / Å	**Mean Zr-Se**	2.7654(2)	2.763	2.789(7)
	Se-Se (Dimer)	2.3441(6)	2.603(2)	2.663(10)
	Se-Se (Non-Dimer)	3.0676(7)	2.751(2)	2.721(10)

Table 3.3: Positional parameters of $K_{0.45(2)}ZrSe_3$.† the Thermal displacement parameters were refined to one single value due to the quality of the data, which refines to some negative thermal displacement values.

Positional Parameters						
Atom	***x***	***y***	***z***	***Occupancy***	***Wyckoff Symbol***	$B_{eq}(Å^2)^†$
			$K_{0.45(2)}ZrSe_3$			
K(1)	0.5	0.5027(11)	0.268(18)	0.45(2)	4*a*	0.18(9)
Zr(1)	0.5	0.3178(2)	0.265(5)	1	4*a*	0.18(9)
Se(1)	0	0.2286(3)	0.240(7)	1	4*a*	0.18(9)
Se(2)	0.5	0.1126(13)	0.511(2)	1	4*a*	0.18(9)
Se(3)	0	0.3896(13)	0.506(2)	1	4*a*	0.18(9)

Table 3.4: Bond distances in $K_{0.45(2)}ZrSe_3$.

Bond Lengths / Å	
	$K_{0.45(2)}ZrSe_3$
K(1)-Se(2)	3.33(5) x2 3.44(5) x2
K(1)-Se(3)	3.34(5) x2 3.37(5) x2
Zr(1)-Se(1)	2.720(6) x2 2.75(3) 3.00 (3)
Zr(1)-Se(2)	2.783(2) x2
Zr(1)-Se(3)	2.78(2) x2
Se-Se (Dimer)	2.663(12)
Se-Se (Non-Dimer)	2.721(12)

$K_{0.45(2)}ZrSe_3$ was annealed on the I11 synchrotron beamline to test whether the low-temperature $Cmc2_1$ polymorph can transform into the high-temperature *Immm* polymorph. However, upon heating, multiple new peaks at low angles are formed that do not correspond to an *Immm* phase. These new peaks could correspond to decomposition or significant structural rearrangement and could not be indexed. No known phase in the ICSD database constituting the elements could be matched to these new peaks. It is plausible that upon

heating the low-temperature intercalate, other reaction pathways are more favourable than the transformation into the other polymorph.

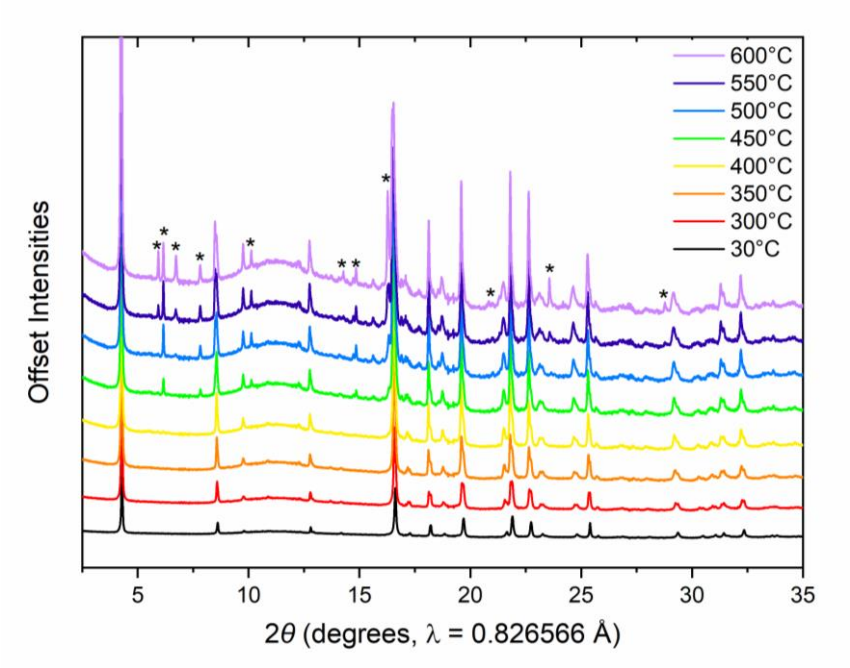


Figure 3.5: Variable temperature PXRD performed on the I11 beamline. * New peaks formed from heating that could not be indexed.

3.4 Rb Intercalation

Rb intercalation using Rb/NH_3 solution proceeded with a similar colour change as the K intercalation and a ~ 20.1 % increase in the interlayer separation compared with $ZrSe_3$. This is a ~ 3.2 % (0.385(6) Å) larger increase compared to $K_{0.45(2)}ZrSe_3$, a difference consistent with the greater size of the Rb^+ ion compared with K^+. In contrast to the K intercalation, the systematic absences in the diffraction pattern do correspond with those for Klepp *et al.*'s $Rb_{0.43}ZrSe_3$ *Immm* compound synthesised at high temperatures (indicated by the presence of 011 and 013 Bragg reflections in Figure 3.6).[119] The lattice parameters of the Rb-containing compounds obtained at high temperatures and by direct intercalation are in very close agreement (see Table 3.5), with only a 0.2 % difference in the unit cell volume.[119] The Rb

occupancy in the topotactic intercalation reaction was refined to be 0.41(1) per $ZrSe_3$ unit, again in agreement with the literature value for the high-temperature synthesis.[119]

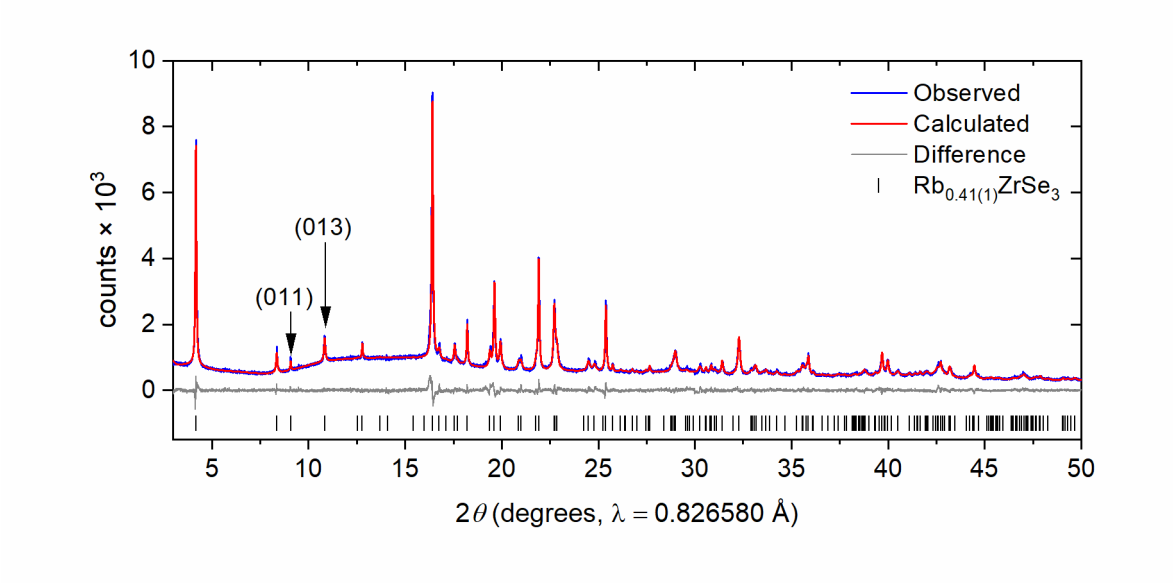


Figure 3.6: Rietveld refinement against I11 (MAC) PXRD pattern of $Rb_{0.41(1)}ZrSe_3$. The 011 and 013 peaks allowed in *Immm* but forbidden in $Cmc2_1$ are indicated. R_{wp}: 4.66 %.

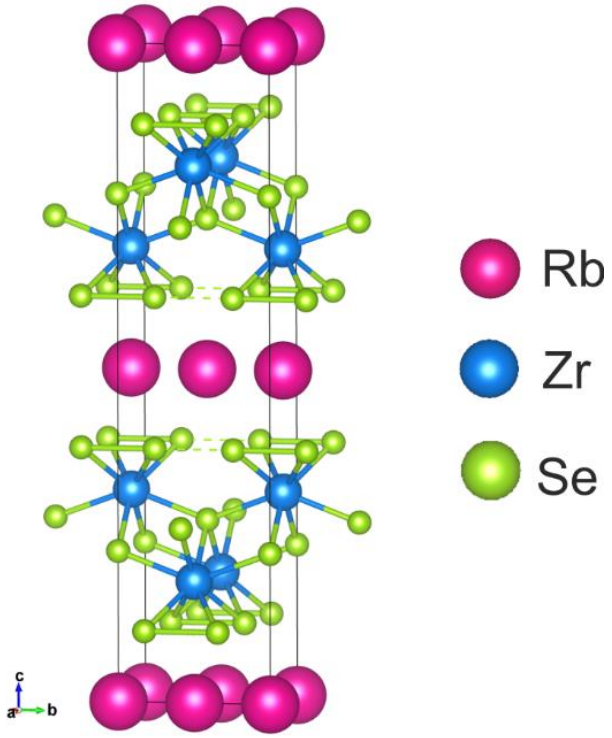


Figure 3.7: *Immm* structure of $Rb_{0.41(1)}ZrSe_3$.

Table 3.5: Comparison of structural parameters and distances of $ZrSe_3$, the high-temperature $Rb_{0.43}ZrSe_3$ and the low-temperature $Rb_{0.411)}ZrSe_3$.

Compound		**$ZrSe_3$**	**$Rb_{0.43}ZrSe_3$**	**$Rb_{0.41(1)}ZrSe_3$**
Source		Furuseth *et al.*[38]	Klepp *et al.*[119]	ME033
Space Group		$P2_1/m$ (No. 11)	*Immm* (No. 71)	*Immm* (No. 71)
***a* / Å**		5.4109(12)	3.756(1)	3.76243(8)
***b* / Å**		3.7488(9)	5.359(4)	5.3673(1)
***c* / Å**		9.444(2)	22.81(1)	22.6882(9)
***β* / °**		97.48	90	90
Volume / Å^3		189.94	459.1	458.17(3)
Interlayer Separation / Å		9.444(2)	11.405(5)	11.344(6)
Van der Waals Gap / Å		3.2499(6)	5.286(4)	5.226(5)
Bond Lengths / Å	**Mean Zr-Se**	2.7654(2)	2.771	2.785(1)
	Se-Se (Dimer)	2.3441(6)	2.602(3)	2.592(4)
	Se-Se (Non-Dimer)	3.0676(7)	2.757(3)	2.775(4)

Table 3.6: Positional parameters of $Rb_{0.41(1)}ZrSe_3$.

Positional Parameters						
Atom	***x***	***y***	***z***	***Occupancy***	***Wyckoff Symbol***	**B_{eq} (Å^2)**
			$Rb_{0.41(1)}ZrSe_3$			
Rb(1)	0.5	0.5	0.5	0.502(8)	2*a*	1.5(2)
Rb(2)	0	0.5	0	0.309(7)	2*d*	0.5(4)
Zr(1)	0.5	0	0.31528(9)	1	4*j*	0.52(6)
Se(1)	0.5	0	0.22859(12)	1	4*i*	1.52(7)
Se(2)	0	-0.2415(3)	0.38483(9)	1	8*l*	0.91(5)

Table 3.7: Bond distances in $Rb_{0.41(1)}ZrSe_3$.

Bond Lengths / Å	
	$Rb_{0.41(1)}ZrSe_3$
Rb(1)-Se(2)	3.506(2) x4
Rb(2)-Se(2)	3.471(2) x4
Zr(1)-Se(1)	2.722(3) x2 2.862(2) x2
Zr(1)-Se(2)	2.777(2) x4
Se-Se (Dimer)	2.592(4)
Se-Se (Non-Dimer)	2.775(4)

3.5 Cs Intercalation

Caesium intercalation into $ZrSe_3$ showed an even greater increase of ~ 24.6 % in the interlayer separation, as expected due to the even greater size of Cs^+. However, comparing this low-temperature intercalate to Klepp's $Cs_{0.4}ZrSe_3$ *Cmc*2_1 compound synthesised at high temperature, the low-temperature intercalate was found to be ~ 2.41 % (0.284(7) Å) smaller. Moreover, the material obtained via intercalation crystallises in *Immm* with the structure adopted by the Rb analogues made at high or low temperatures. Again, this was deduced by the absence of the 021 and 151 reflections allowed in *Cmc*2_1 but not in *Immm*; in addition to the presence of the 011 and 013 reflections allowed in *Immm* but not in *Cmc*2_1 since they violate the $k = 2n$ reflection condition for 0*kl* reflections. The Cs content was refined to 0.42(2), in good agreement with the literature value for the high-temperature phase.[119] Due to the difficulty in handling Cs metal, not all the parent $ZrSe_3$ was consumed. Furthermore, a Cs_2Se_3 side product was detected in small amounts, possibly due to competing reactions.

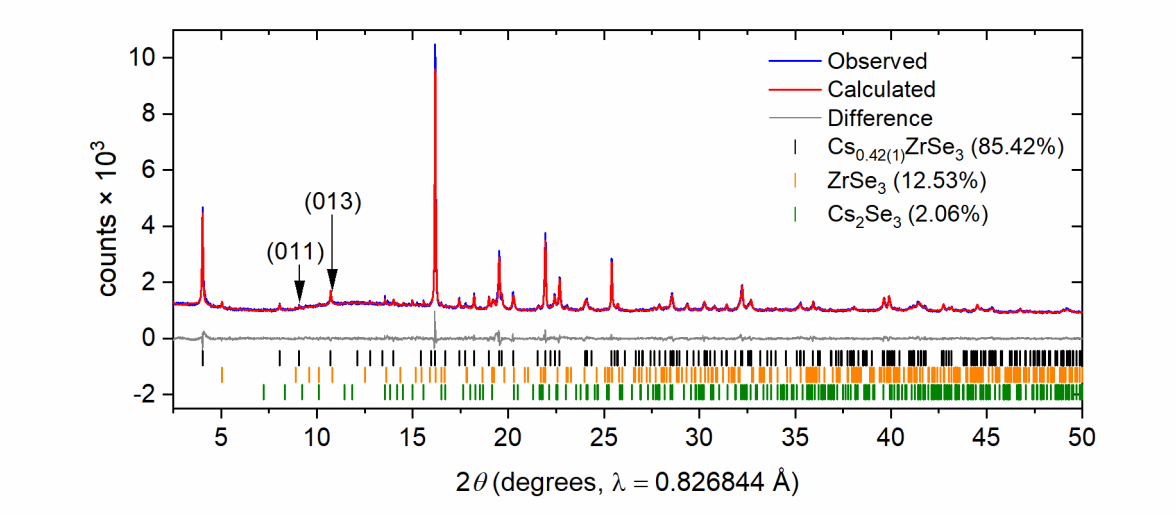


Figure 3.8: Rietveld refinement against I11 (MAC) PXRD pattern of $Cs_{0.42(1)}ZrSe_3$. The 011 and 013 peaks allowed in *Immm* but forbidden in *Cmc*2_1 are indicated. R_{wp}: 6.33 %.

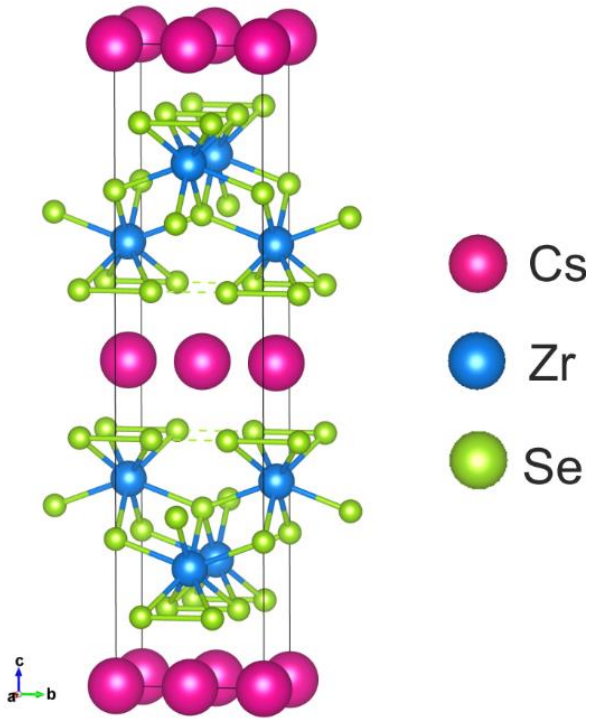


Figure 3.9: : *Immm* structure of $Cs_{0.42(1)}ZrSe_3$.

Table 3.8: Comparison of structural parameters and distances of $ZrSe_3$, the high-temperature $Cs_{0.40}ZrSe_3$ and the low-temperature $Cs_{0.42(1)}ZrSe_3$. ‡ Indicates the crystallographic *b* and *c* axis swapping to enable the standard space group setting to be used.

Compound		**$ZrSe_3$**	**$Cs_{0.40}ZrSe_3$**	**$Cs_{0.42(1)}ZrSe_3$**
Source		Furuseth *et al.*[38]	Klepp *et al.*[119]	ME050
Space Group		$P2_1/m$ (No. 11)	$Cmc2_1$ (No. 36)	*Immm* (No. 71)
***a* / Å**		5.4109(12)	3.747(1)	3.76225(7)
***b* / Å**		3.7488(9)	24.102(5) ‡	5.3616(1)
***c* / Å**		9.444(2)	5.332(2)	23.5341(9)
***β* / °**		97.48	90	90
Volume / Å^3		189.94	481.5	474.73(3)
Interlayer Separation / Å		9.444(2)	12.051(3)	11.767(7)
Van der Waals Gap / Å		3.2499(6)	5.906(4)	5.580(5)
Bond Lengths / Å	**Mean Zr-Se**	2.7654(2)	2.776	2.796(2)
	Se-Se (Dimer)	2.3441(6)	2.572(4)	2.605(5)
	Se-Se (Non-Dimer)	3.0676(7)	2.760(4)	2.757(5)

Table 3.9: Positional parameters of $Cs_{0.42(1)}ZrSe_3$.

Positional Parameters						
Atom	***x***	***y***	***z***	***Occupancy***	***Wyckoff Symbol***	***B_{eq}* (Å^2)**
			$Cs_{0.42(1)}ZrSe_3$			
Cs(1)	0.5	0.5	0.5	0.508(7)	2*a*	3.6(2)
Cs(2)	0	0.5	0	0.325(6)	2*d*	3.0(4)
Zr(1)	0.5	0	0.31370(12)	1	4*j*	0.28(7)
Se(1)	0.5	0	0.22887(12)	1	4*i*	0.57(8)
Se(2)	0	-0.2429(4)	0.38145(10)	1	8*l*	0.55(6).

Table 3.10: Bond distances in $Cs_{0.42(1)}ZrSe_3$.

Bond Lengths / Å	
	$Cs_{0.42(1)}ZrSe_3$
Cs(1)-Se(2)	3.636(2) x4
Cs(2)-Se(2)	3.608(2) x4
Zr(1)-Se(1)	2.743(4) x2 2.862(2) x2
Zr(1)-Se(2)	2.789(3) x4
Se-Se (Dimer)	2.605(5)
Se-Se (Non-Dimer)	2.757(5)

3.6 Discussion and Comparison

In the intercalation reactions, the average Zr-Se distances show no significant change with the values ranging from 2.785(1) to 2.796(2) Å, in good agreement with the 2.7654(2) Å found in $ZrSe_3$. This indicates that the oxidation state of Zr remains at +4. The main change that has occurred is the elongation of the Se-Se dimer distance due to the partial reduction of $[Se_2]^{2-}$. This leads to the subsequent contraction in the distance between neighbouring dimers such that the structures can now be seen as a move away from formal discrete dimers towards a poly-selenide chain with alternating Se-Se distances. For $Rb_{0.41(1)}ZrSe_3$ and $Cs_{0.42(1)}ZrSe_3$ crystallising in *Immm*, the selenide dimer bond length has increased from 2.34 Å in $ZrSe_3$ to 2.592(4) Å and 2.605(5) Å for $Rb_{0.41(1)}ZrSe_3$ and $Cs_{0.42(1)}ZrSe_3$ respectively with the between-dimer distance decreasing from 3.07 Å to 2.775(4) Å and 2.757(5) Å for the Rb and Cs intercalates respectively. The Se-Se distances in these cases with similar electron counts are very similar for both the reported high-temperature[119] and the low-temperature syntheses.

On the other hand, in $K_{0.45(2)}ZrSe_3$ prepared by intercalation and crystallising in $Cmc2_1$, the selenide dimer bond length has seen an increase to 2.66(1) Å, 0.06(2) Å greater than the

distance reported for the *Immm* phase synthesised at high temperatures by Klepp *et al.*[119] Since the high-temperature product $K_{0.55}ZrSe_3$ compound contains slightly more K, which one would expect would cause a larger expansion of the Se-Se dimer distance, it is likely not solely the number of electrons that controls the change of Se-Se dimer length but most likely the different structure as well. In the *Cmc*2_1 phase reported here, the between-dimer Se-Se distance is reduced significantly compared to the value in $ZrSe_3$ and is only an extra 0.06(2) Å longer than the dimer bond length.

In contrast to Klepp *et al.*'s high-temperature structures,[119] which are produced under thermodynamic control, these reactions here were carried out at -78 °C. Therefore, there is kinetic control over which structure is obtained. One can attempt to explain why, at low temperatures, $Cs_{0.42(1)}ZrSe_3$ crystallises in *Immm* similarly to $Rb_{0.41(1)}ZrSe_3$ by taking into account the coordination environment of the alkali metal in the two distinct symmetries.

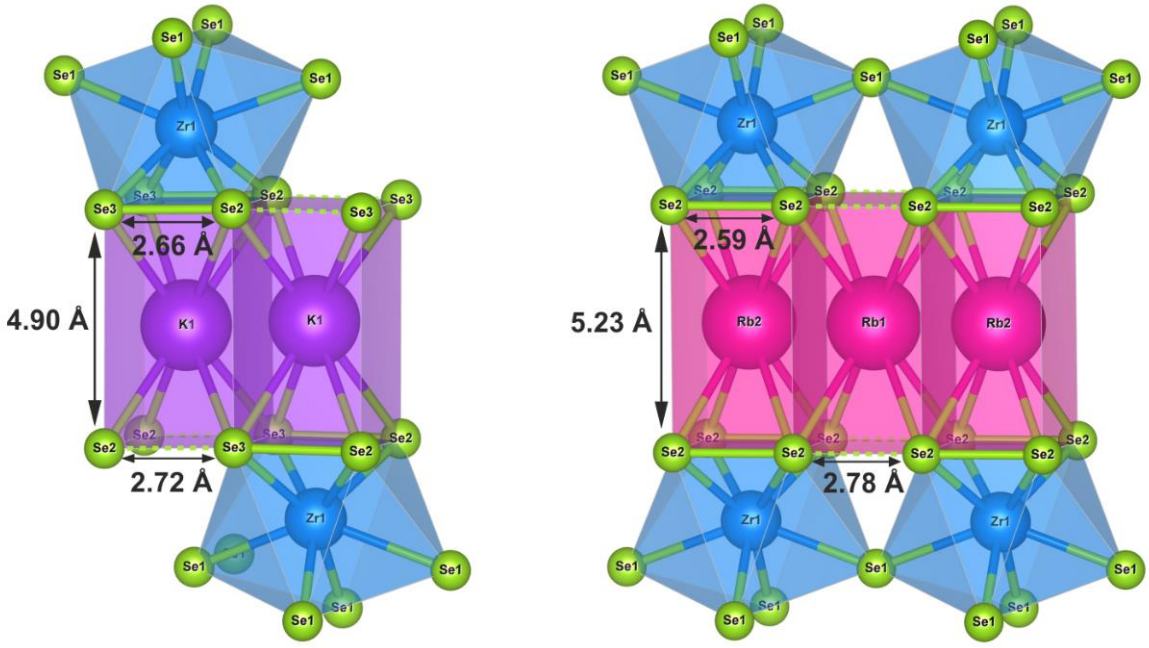


Figure 3.10: Comparison of the crystallographic sites in *Cmc*2_1 (left) and *Immm* (right) symmetry.

In the *Immm* structure of $Rb_{0.41(1)}ZrSe_3$, there are two crystallographically distinct alkali metal sites. For Rb(1), the ends of the prism are made up of neighbouring selenide dimers

contacts of length 2.78 Å whereas, for Rb(2), the ends of the prism are made up of the selenide dimers themselves (length 2.59 Å). The different size prisms are reflected in the Rb fractional occupation of the two sites where Rb(1) and Rb(2) are approximately 0.50 and 0.31 occupied, respectively, giving an average of 0.41 (similar case for the Cs intercalate). These two sites cannot be simultaneously fully occupied since the repulsion between them will be high. The distance between the sites is ~ 2.7 Å, whereas typical Rb-Rb distances in rubidium chalcogenides and halides such as Rb_2Se and RbCl are 4 Å and 4.65 Å, respectively.[154,155] It is likely that there are large regions within the alkali metal layers where there is a checkerboard-type arrangement of alkali metal ions within a particular layer which would give inter-ion distances of about 4.62 Å and would be consistent with the mean occupancy of the two sites being below 0.5. However, the absence of any superstructure reflections indicates that there is no full long-range ordering of the alkali ions and vacancies.

In the *Cmc*2_1 structure of $K_{0.45(2)}ZrSe_3$, there is only one crystallographic alkali metal site. One end of the prism is made from the selenide dimer, and the other end is made from neighbouring selenide dimers, which are not too dissimilar in length, perhaps to minimise prism distortion. The *Immm* structure, therefore, contains the largest alkali metal site, and this may explain why under kinetic control, it is favoured by the large Rb^+ and Cs^+ cations, whereas for K^+, this preference is less. In the high-temperature *Immm* structure of $K_{0.55}ZrSe_3$, the large cation site allows significantly more K^+ occupation (0.64), giving a mean occupancy for the two sites of slightly above 0.5, according to Klepp *et al.*[119]

3.7 Ca Intercalation

The intercalation reaction with a Ca/NH_3 solution resulted in no colour change to the black solid. By modifying the ratio of the reactants and analysing the resultant powder X-ray diffraction pattern, it was observed that only 0.2 equivalents of the metal were needed to

consume the starting material fully. This is approximately half required by the alkali metal intercalates, indicating a similar number of electrons donated to form this product. The complexity of the diffraction pattern will be discussed shortly. Still, an initial assessment of the structure can be made by observing the position of the 1st 00*l* diffraction peak, which is indicative of the interlayer separation. The interlayer separation of this product of nominal composition '$Ca_{0.2}ZrSe_3$' is 10 % greater than that of the $K_{0.45(2)}ZrSe_3$ intercalate, which strongly suggests that co-intercalation of the solvent has also occurred. Chemical analysis using the Dumas combustion method (described in section 2.2.12.2) confirmed the presence of ammonia/amide species with an N:H ratio of 1:2.77(8) and gave 0.596(7) N per formula unit, which suggests a formula of $Ca_{0.2}(NH_3)_{0.45(7)}(NH_2)_{0.15(7)}ZrSe_3$. Using this approximation, the $[Se_2]^{2-}$ dimer would be slightly less reduced compared to the alkali intercalates as only 0.25(7) electrons (instead of ~ 0.4) are used in the reduction with the remaining electrons used to form H_2 during the reduction of NH_3 to form NH_2^-.

Table 3.11: Elemental analysis results.

Elemental Microanalysis Results		
	N	**H**
Average	2.41 %	0.48 %
Uncertainty	0.025 %	0.009 %

Compared with the alkali metal intercalates, the structure was much less straightforward to characterise. An initial model was based on the *Immm* structure of $K_{0.55}ZrSe_3$ with expanded lattice parameters, which accounted well for the peak positions and gave a satisfactory fit to the powder X-ray diffraction if a suitably broad and anisotropic peak shape model was used. However, this model struggled to account for the intensities of low *d*-spacing reflections, which is particularly evident in the powder neutron diffraction measured at POLARIS, where these reflections are better resolved (see section 2.2.4). Since 0.2 equivalents of Ca^{2+} per

$ZrSe_3$ were used in the synthesis and chemical analysis suggests 80 % occupancy overall of the two sites occupied by alkali metals. Therefore, in the *Immm* model, Ca was modelled with an occupancy of 0.2 on one of the cation sites, with an N occupancy of 0.6 on the other site. This would give a Ca-N distance of ~ 2.67 Å, which is reasonable as a typical Ca-N distance, such as in calcium imide is 2.57 Å.[156] In the refinement of the PXRD data, the H positions can be neglected due to their insignificant scattering compared to Zr and Se. However, with neutron diffraction, H and N are significant contributors to the scattering (H = -3.74 fm, N = 9.36 fm, Zr = 7.16 fm, Se = 7.97 fm)[131]. In the *Immm* model, the hydrogen positions were approximated to have square prismatic coordination around N with a bond length ~ 1 Å giving 8 potential N-H...Se hydrogen bonds with a distance of 2.7-2.8 Å as seen in other metal/ammonia intercalates.[63,65] The H content calculated from the elemental analysis was split across the 8 sites. Allowing the occupancies to refine resulted in unrealistic values and no improvement to the visual fit.

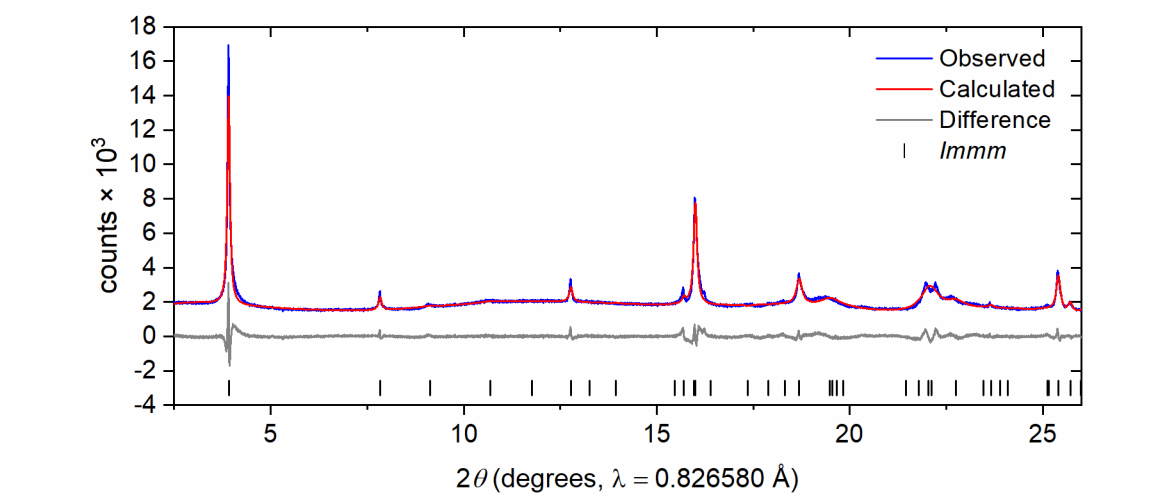


Figure 3.11: Preliminary Rietveld refinement against I11 (MAC) PXRD pattern of $Ca_{0.2}(NH_3)_{0.45(7)}(NH_2)_{0.15(7)}ZrSe_3$ using the *Immm* model. R_{wp}: 8.76 %.

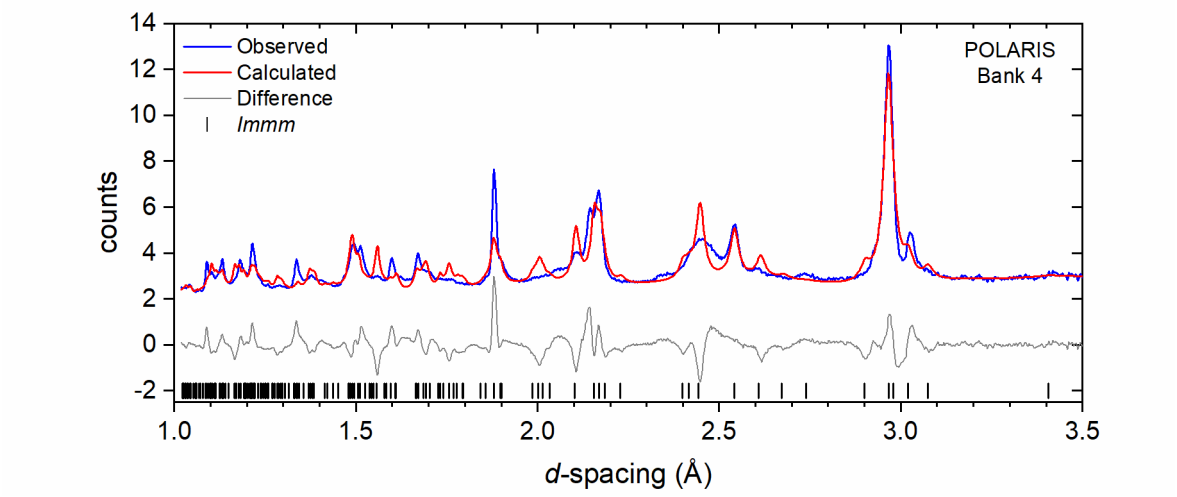


Figure 3.12: Preliminary Rietveld refinement against ToF PND pattern (measured on POLARIS bank 4 (90° bank)) of $Ca_{0.2}(NH_3)_{0.45(7)}(NH_2)_{0.15(7)}ZrSe_3$ using the *Immm* model. R_{wp}: 7.14 %.

Table 3.12: Comparison of lattice parameters of $Ca_{0.2}(NH_3)_{0.45(7)}(NH_2)_{0.15(7)}ZrSe_3$ and the *Immm* structure of $K_{0.55}ZrSe_3$ showing the much larger expansion.

	$Ca_{0.2}(NH_3)_{0.45(7)}(NH_2)_{0.15(7)}ZrSe_3$	**$K_{0.55}ZrSe_3$** [119]
Space Group	*Immm*	*Immm*
***a* / Å**	3.7630(1)	3.746(3)
***b* / Å**	5.3496(3)	5.354(8)
***c* / Å**	24.210(3)	21.929(3)
***Volume* / Å^3**	487.36(7)	439.8

3.7.1 Stacking Fault Refinement

Although the uncertainty in the occupancies and positions of N and H may contribute to the severe intensity mismatch, a combination of sharp and broad peaks in both the synchrotron X-ray and neutron diffraction patterns are consistent with significant stacking disorder, akin to the stacking disorder seen in the parent $ZrSe_3$. However, in the case of $ZrSe_3$, single-crystal X-ray diffraction was used to determine the structure. In this case, single-crystal analysis is not a viable method. Microscopy techniques, such as HAADF-STEM imaging in principle, provide insight into the types of stacking disorder present, but ammonia-intercalated layers are typically unstable with respect to an electron beam. Therefore, the

capability available in Topas Academic Version 6 onwards was used to account for this. Without a clear knowledge of the types of stacking disorder involved, it was not feasible to construct a model based on a small number of additional parameters such as those previously reported in the literature.[14,157,158]. The stacking disorder present in $Ca_{0.2}(NH_3)_{0.45(7)}(NH_2)_{0.15(7)}ZrSe_3$ is modelled without any existing knowledge of the type of stacking disorder present in the following way. The initial *Immm* structure giving the fits shown in Figure 3.11, was separated into $ZrSe_3$ and Ca/NH_3 subunits, with the divide between the blocks chosen to be at the centre of the van der Waals gap. The *Immm* structure may thus be regenerated by a stacking model containing two of the $ZrSe_3$ and Ca/NH_3 subunits, with a ½, ½ offset in the *ab* plane applied to the second pair of subunits to account for the body-centring in the *Immm* structure. The supercell was generated by stacking 100 $ZrSe_3$ subunits with 100 intervening Ca/NH_3 subunits, with suitable offsets to mimic the body-centring. Structural parameters of the subunits are given in Appendix II.

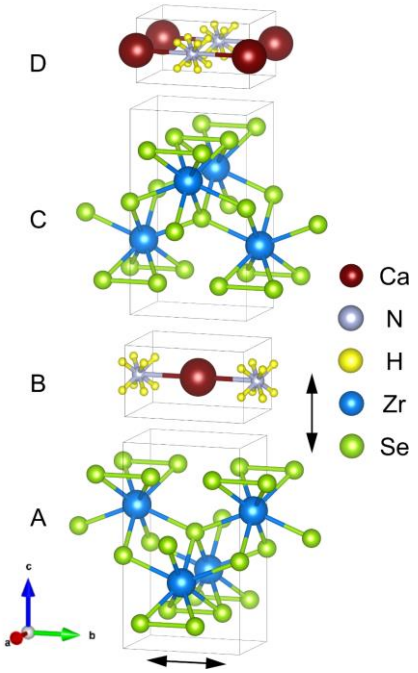


Figure 3.13: Subunits (A-D) of $Ca_{0.2}(NH_3)_{0.45(7)}(NH_2)_{0.15(7)}ZrSe_3$ with the arrows indicating the directions the subunits were allowed to refine.

This initial large supercell thus corresponds exactly to the *Immm* structure. Instead of refining this model using anisotropic peak broadening, a simple symmetric peak shape was used based on isotropic crystallite size broadening of the peaks and the relative positions of the subunits were then refined, with the 1st $ZrSe_3$ subunit remaining fixed as an anchor. This positional refinement of the subunits was first attempted by only allowing them to vary position in the *ab* plane – modelling turbostratic disorder/variation in the structure. Refinements of the relative shifts in the *a*-direction (*i.e.* along the axis of the $ZrSe_6$ prisms) always led to negligible shifting. In contrast, the shifting in the *b* direction (parallel to the axis of the Se-Se dimers) was significant. Allowing both the $ZrSe_3$ and Ca/NH_3 subunits to refine their position in just the *b*-direction (Figure 3.14) leads to R_{wp} for the neutron diffraction improving from 7.1 % to 4.6 % in the 90° bank, and the visual fit is greatly improved.

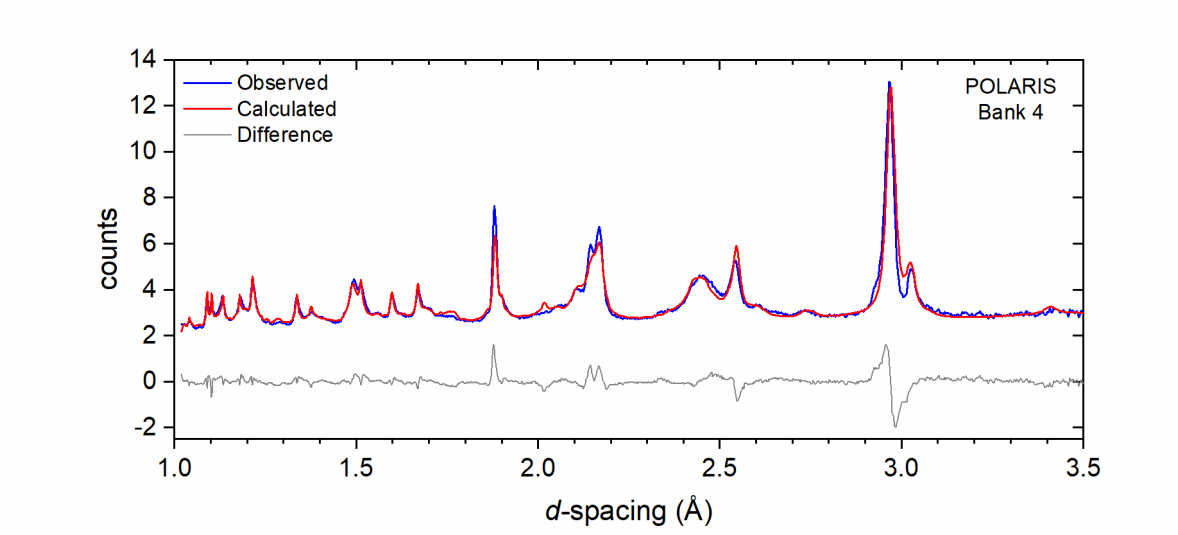


Figure 3.14: Stacking fault refinement against PND pattern of $Ca_{0.2}(NH_3)_{0.45(7)}(NH_2)_{0.15(7)}ZrSe_3$ allowing to only refine in the *b*-axis. R_{wp}: 4.6 %.

Due to the size of the refinement and the number of peaks calculated, it was only practically possible to refine against one bank of the neutron data at a time for the stacking model. Here the 90° bank (bank 4) at POLARIS was chosen since it has the best balance of resolution

and *d*-spacing. It is reasonable to be suspicious of a model that allows hundreds of freely refining parameters, and indeed many different absolute configurations of the supercell can give equivalent fits to the data. However, all solutions of equivalent R_{wp} give the same distribution of relative shifts from one $ZrSe_3$ subunit to the next (Figure 3.15), which is reproduced across both the X-ray and neutron diffraction refinements as shown in Figure 3.16 and 3.18.

The consequence of this result can be understood by relating it to the *Cmc*2_1 and *Immm* models, shown in Figure 3.1. For the pure *Immm* model, the distribution of relative shifts in Figure 3.16 would have a single sharp peak at 0, whereas for the pure *Cmc*2_1 model, there would be symmetric sharp peaks at ±0.5. The model produced by the stacking fault analysis has a large degree of variability in the *b*-direction shift, with a broad peak centred around 0 and no secondary maxima at ±0.5, suggesting that on average, the $ZrSe_3$ subunits remain in the body-centred *Immm* configuration, consistent with the initial indexing of the pattern.

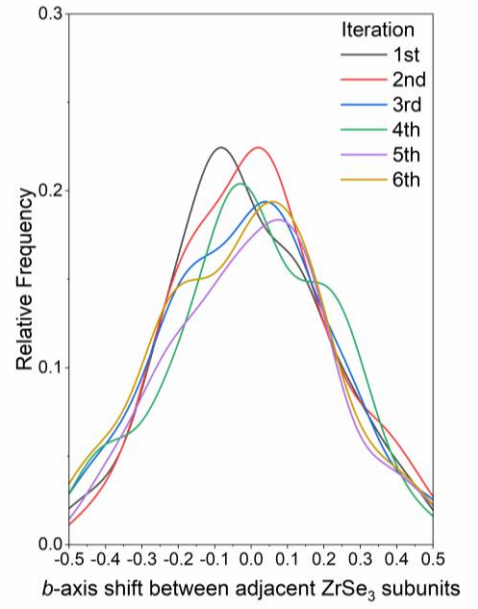


Figure 3.15: Distribution of shifts between adjacent $ZrSe_3$ subunits with multiple iterations of the refinement showing the refinement is consistent and reproducible.

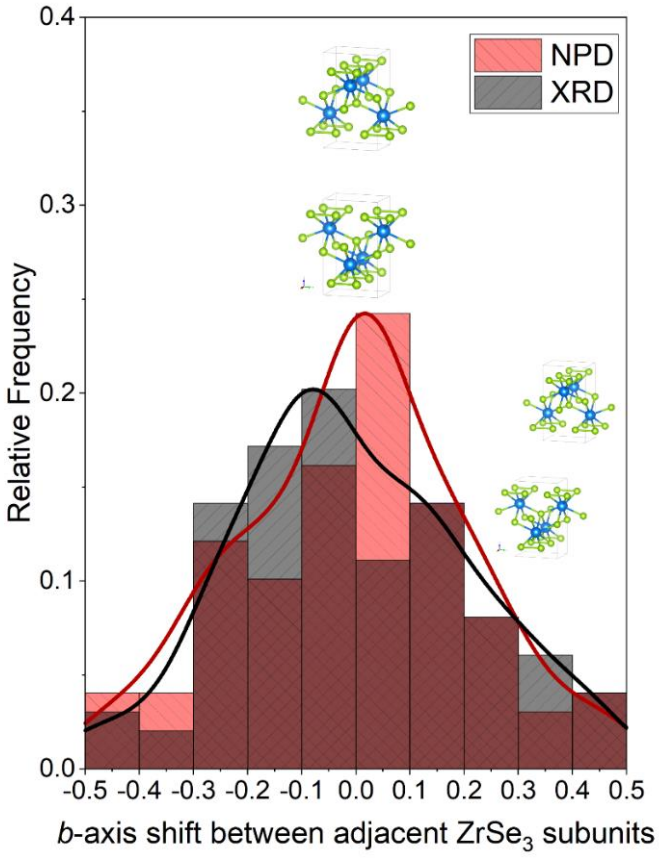


Figure 3.16: Distribution of shifts between adjacent $ZrSe_3$ subunits. A shift of 0 shows an *Immm* arrangement and shifts of ±0.5 indicates a *Cmc*2_1 arrangement.

To consider how the Ca/NH_3 subunits shift, The density plot in Figure 3.17 below shows the Ca/NH_3 subunit *b*-axis shift relative to the $ZrSe_3$ subunits above and below it. The density plot shows a clear preference for shifts of (0, 0), (±0.5, ±0.5), (0, ±0.5) and (±0.5, 0). This is summarised in the distribution diagram in Figure 3.18, showing the average of the modulus of the shifts.

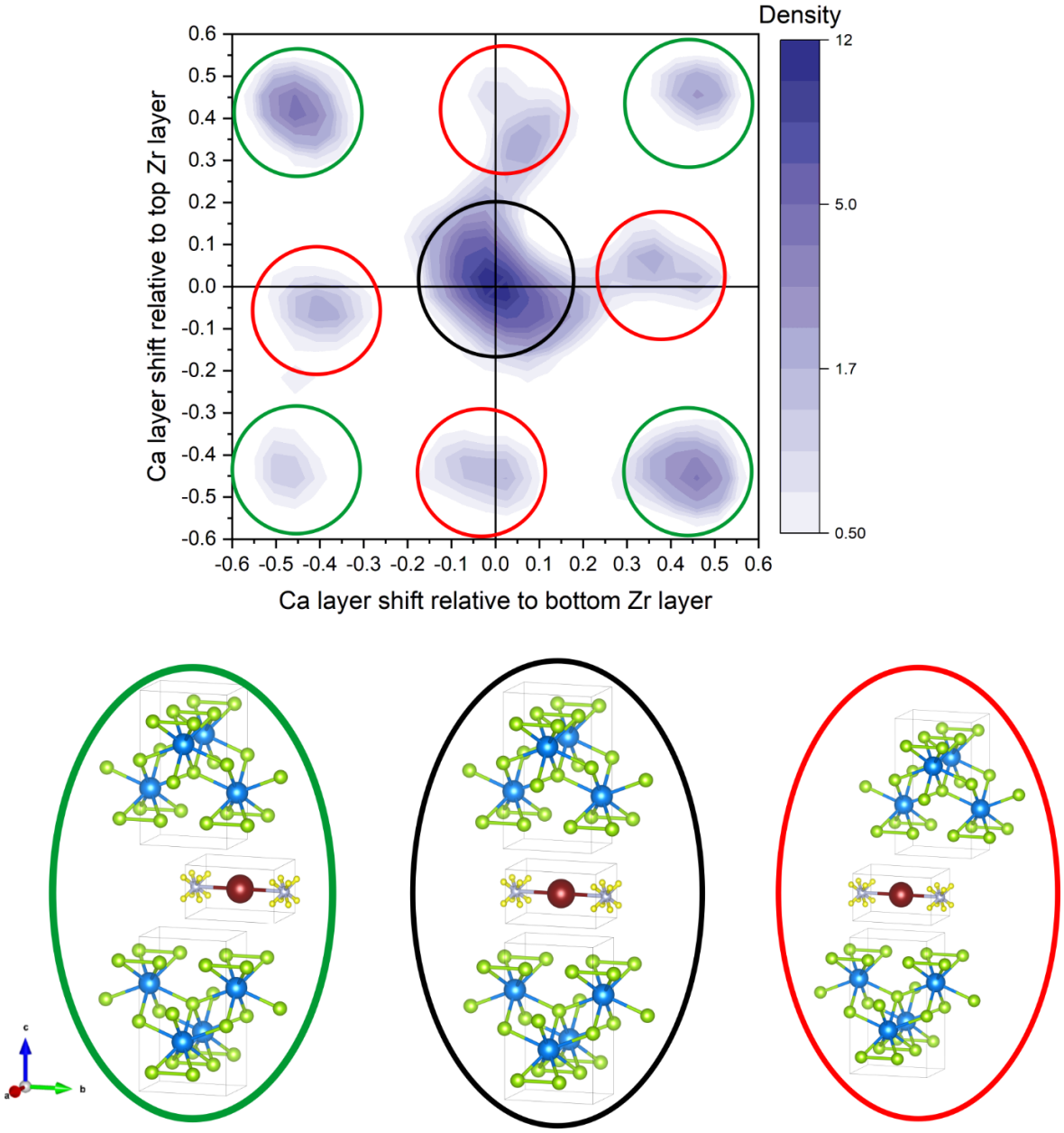


Figure 3.17: Density plot of Ca/NH_3 layer shifts relative to the adjacent $ZrSe_3$ layer below (*x*-axis) and above (*y*-axis). The density plot is made of the combination of values from both X-ray and neutron refinement data. The different density regions are circled in different colours to show what type of arrangement they correspond to. Both green and black circles correspond to an *Immm* arrangement where the green has the Ca/NH_3 shifted by 0.5 a unit cell along the *b*-axis. The red circles correspond to a $Cmc2_1$ arrangement.

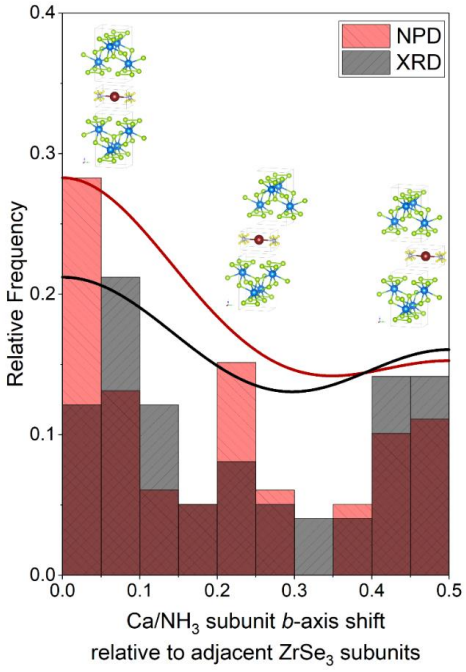


Figure 3.18: Distribution of Ca/NH_3 *b*-axis shifts relative to adjacent $ZrSe_3$ subunits. This plot was generated by taking the average of the modulus of the shifts seen in Figure 3.17.

A shift of 0 indicates that the arrangement of Ca/NH_3 and $ZrSe_3$ subunits remains unmoved from the initial *Immm* model. A 0.5 shift suggests the Ca/NH_3 subunit shifting by half a unit cell such that the Ca and the NH_3 have swapped positions whilst the $ZrSe_3$ subunits remain unchanged. A shift of 0.25, an average of 0 and 0.5, suggests that one of the $ZrSe_3$ subunits either above or below the Ca/NH_3 subunit has shifted by half a unit cell. The two adjacent $ZrSe_3$ subunits, therefore, take up a $Cmc2_1$ arrangement. Both X-ray and neutron distributions show peaks at 0 and 0.5, indicating the majority preference for the *Immm* arrangement. Both the X-ray and neutron models show a higher frequency of 0 shifts than 0.5 shifts, indicating the Ca and NH_3 have a higher preference for their assigned positions, as shown in Figure 3.13, rather than being interchanged. The distribution in the X-ray model shows a lower preference for Ca/NH_3 ordering than the neutron. As an approximation, if one groups all Ca/NH_3 subunit *b*-axis shifts < 0.1 as 'unshifted' and groups all Ca/NH_3 subunit shifts > 0.4 as 'shifted'. The ratio of 'unshifted' to 'shifted' for the neutron model is ~ 1.95,

whereas for the X-ray model is ~ 1.18. This is expected due to the lower contrast between the X-ray form factors of 0.2 Ca and 0.6 N with respect to the neutron scattering lengths (Ca: 4.70 fm, H: -3.74 fm, N: +9.36 fm)[131]. This result supports the initial, intuitive assignment of the two sites, in which NH_3 has a closer proximity to Se to allow for increased Se...H hydrogen bonding.

A further improvement to the fit can be achieved by allowing the subunits to move relative to one another in the stacking direction, *c*. The bond lengths and contents of the layers were kept constant. Still, their relative positions along *c* were refined, effectively increasing or decreasing the van der Waals gaps between them. This provides a rough modelling of interstratification (*i.e.* the variation/disorder between alternate layers) in a structure. In this case, the modelling accounts for different amounts of intercalation leading to different interlayer separations from one layer to the next. The $ZrSe_3$ subunit *c* shifts were refined while the Ca/NH_3 *c* shifts were constrained such that each subunit stayed in the centre of the van der Waals gap of the $ZrSe_3$ subunits above and below it. The R_{wp} of the neutron fit improves significantly from 4.6 to 1.7 on inclusion of this variation, providing the fit to the data shown below in Figure 3.19.

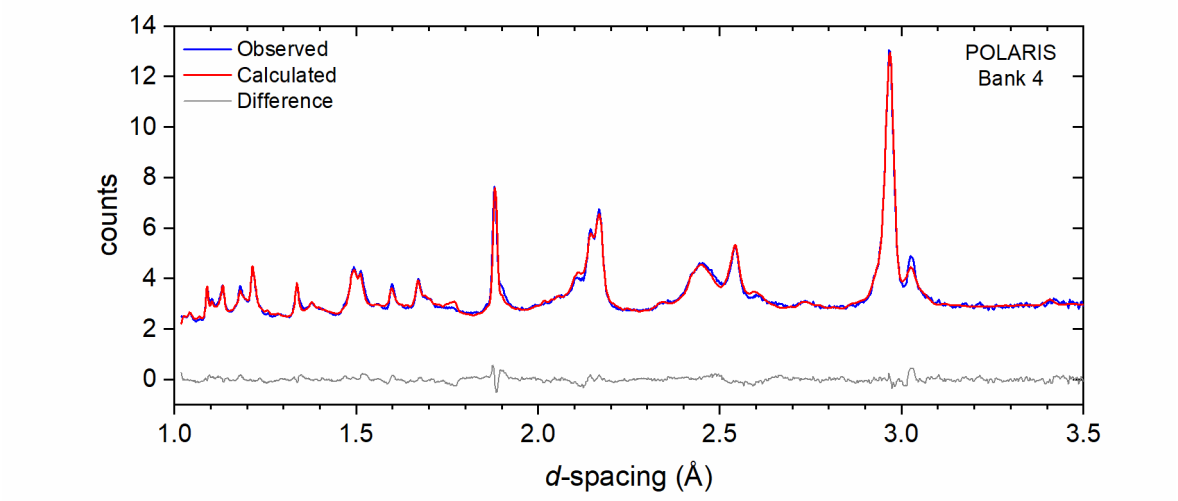


Figure 3.19: Stacking fault refinement against PND pattern of $Ca_{0.2}(NH_3)_{0.45(7)}(NH_2)_{0.15(7)}ZrSe_3$, where the subunits were allowed to refine in both the *b* and *c* axis. R_{wp}: 1.70 %.

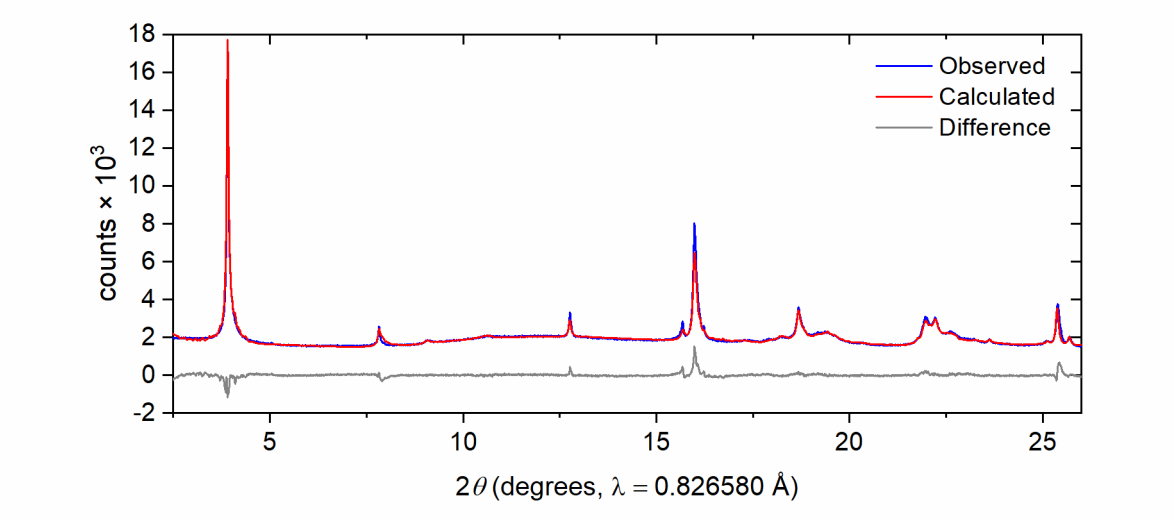


Figure 3.20: Stacking fault refinement against I11 (PSD) PXRD pattern of $Ca_{0.2}(NH_3)_{0.45(7)}(NH_2)_{0.15(7)}ZrSe_3$ where the subunits were allowed to refine in both the *b* and *c* axis. R_{wp}: 7.51 %.

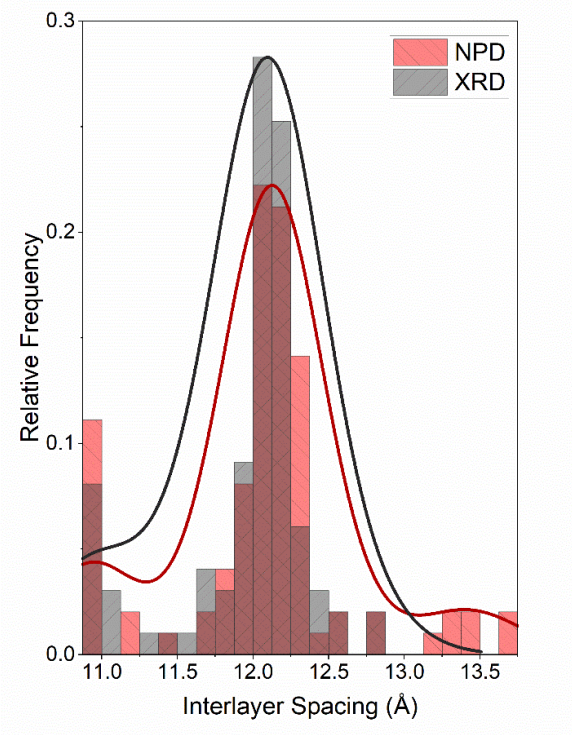


Figure 3.21: Distribution of interlayer separations.

The improvement of the fit on the addition of interstratification to the model clearly shows that the distribution of the Ca-ammonia/amide co-intercalant between the $ZrSe_3$ layers is non-uniform across the crystallites. Some variation of this kind is plausible and again is reproduced by separate models to both the X-ray and neutron diffraction data, as shown in

Figure 3.21, giving similar distributions of different interlayer separations. There is a secondary maximum seen < 11 Å. For reference, the interlayer spacing for the $K_{0.45(2)}ZrSe_3$ intercalate is 10.985(1) Å. Therefore, this suggests that some layers are solvent free and only contain the Ca^{2+} ion. Values larger than the average could suggest possible extra solvent between the layers or differing NH_3/NH_2^- ratio. In the Li/NH_3 intercalate of Bi_2Se_3, the difference in interlayer spacing between the intercalate and the ammonia-rich phase is ~ 2.5 Å.[65] The difference in the interlayer spacing, in this case, is not as big, so it is unlikely that ammonia-rich layers are present.

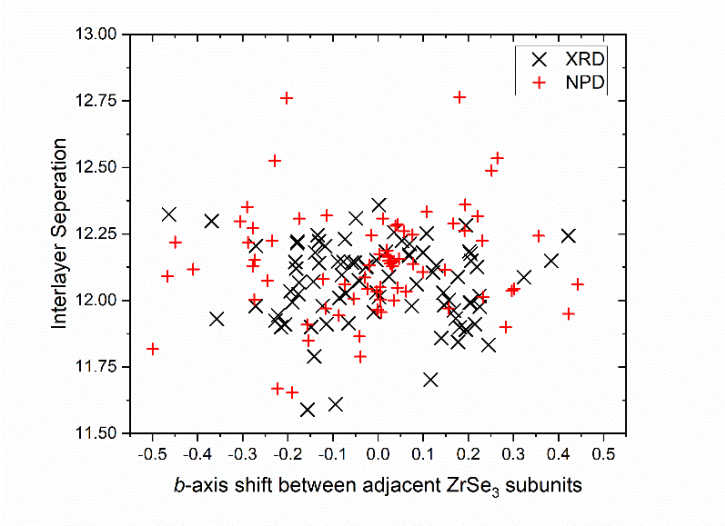


Figure 3.22: A scatter plot of the relative shifts in the *b*-axis of adjacent $ZrSe_3$ subunits compared to its corresponding interlayer separation showing a seemingly random distribution.

There were no obvious correlations between turbostraticity and interstratification, as seen in Figure 3.22, but correlations may be present outside the detection limits of the model.

This method of stacking fault refinement provides insight into the type and degree of disorder in the structure, but the model does come with limitations. The method of modelling interstratification is limited by the constraint that for every expanded layer, there must be a contracted layer to match. So it is plausible that the true distribution of interlayer spacings is not perfectly represented. While it is possible to refine the bond distances and atomic site

occupancies, these are realistically likely to be too correlated to the shifting parameters to be confidently extracted. So it is necessary to fix them to sensible values. To best approximate these bond distances, the atomic coordinates for the layers were taken from the initial refinement based on the *Immm* model. This gave a Se-Se distance in the $ZrSe_3$ layer of ~ 2.52 Å and ~ 2.83 Å for the dimer and non-dimer distances, respectively, consistent with the fact that the selenide dimer was less reduced compared to the alkali intercalates due to the presence of amide species. As mentioned earlier, in the initial *Immm* model, the occupancies of Ca, N and H were fixed at 0.2, 0.6 and 0.205, respectively. These constraints were necessary to implement the stacking fault modelling, but some are expected to be approximations. For example, it is plausible that the Se-Se distances take a range of values rather than just two, and it is expected that the Ca/NH_3 occupancies will vary with the differing interlayer separations, whereas they are all taken to be identical in the model. Nevertheless, the necessity to include both turbostratic and interstratification disorders to fit the diffraction data accurately allows one to be confident that both types of stacking disorders are present.

The variation in the *b*-axis shift seen in this intercalate but not in alkali metals intercalates might be explained by the role of ammonia/amide. Unlike in the alkali metal variants, the interlayer spacing is too large for the small Ca^{2+} intercalant to be involved in any significant bonding interaction with the selenide ions. The highly charged Ca^{2+} ions remain solvated by the ammonia and amide moieties which interact with the selenide ions, presumably by N H...Se hydrogen bonding interactions as found in other metal/ammonia intercalates.[63,65] The $ZrSe_3$ layers are thus not 'locked' in position by bonding to the intercalant cation, and there is more freedom in their relative arrangement compared with the alkali intercalates.

3.7.2 Low-temperature Structure

Powder neutron diffraction was also measured at 5 K at POLARIS to assess how the stacking faults would vary with temperature and compare to the refinement at ambient temperatures (~ 300 K) described above. The lower temperature should also reduce thermal displacement parameters. There is no significant change to the diffraction pattern apart from lattice contraction, which is expected at lower temperatures. The lattice parameters of the contracted cell were obtained from a Pawley refinement of the neutron diffraction pattern and are listed below.

Table 3.13: Lattice parameters of $Ca_{0.2}(NH_3)_{0.45(7)}(NH_2)_{0.15(7)}ZrSe_3$ at 300 K and 5 K.

	***a* / Å**	***b* / Å**	***c* / Å**	***Volume* / Å^3**
300 K	3.7630(1)	5.3496(3)	24.210(3)	487.36(7)
5 K	3.749(1)	5.334(3)	24.077(11)	481.5(4)

The stacking fault refinement at 5 K was carried out similarly to the refinement at 300 K allowing the blocks to refine in the *b* and *c* axes. This led to a reasonably good fit with the R_{wp} of 2.40 %

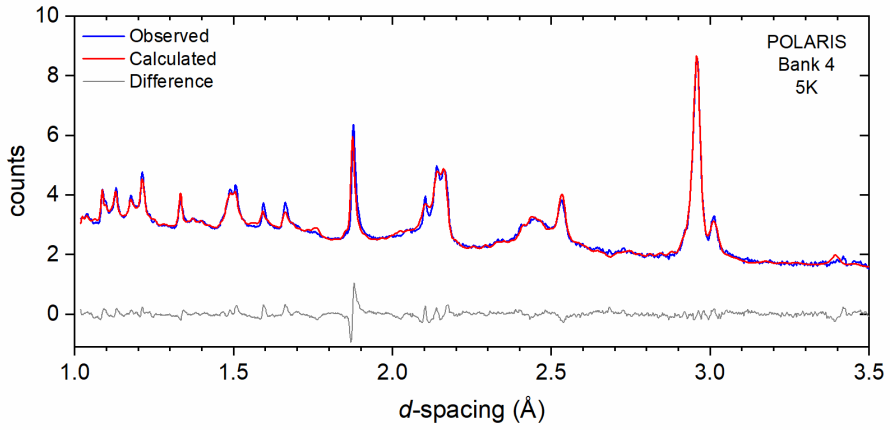


Figure 3.23: Stacking fault refinement against PND pattern (at 5 K) of $Ca_{0.2}(NH_3)_{0.45(7)}(NH_2)_{0.15(7)}ZrSe_3$ where the subunits were allowed to refine in both the *b* and *c* axis. R_{wp}: 2.40 %.

The *b*-axis shifts between adjacent $ZrSe_3$ layers were calculated in a similar manner to the previous refinement. Comparing to the room temperature refinement showed a similar distribution with the maxima at 0, indicating the majority of the $ZrSe_3$ units remain in the initial *Immm* arrangement with no secondary maxima at 0.5 or -0.5. However, the distribution at 5 K overall has a greater degree of variability compared to 300 K, with the maximum at 0 being broader and less pronounced.

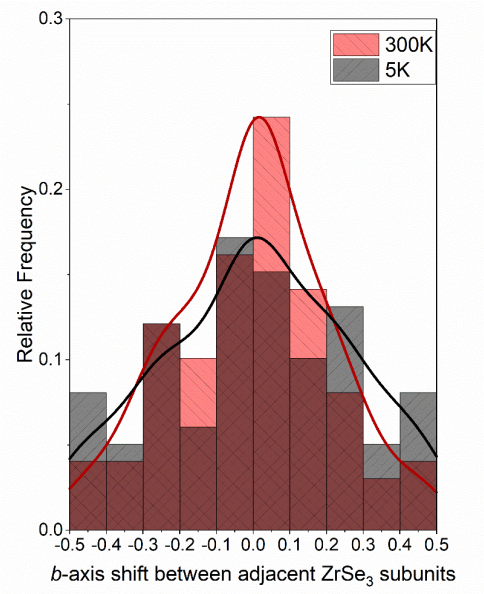


Figure 3.24: Comparison of $ZrSe_3$ subunit shifts from neutron stacking fault refinement at 300 K and 5 K.

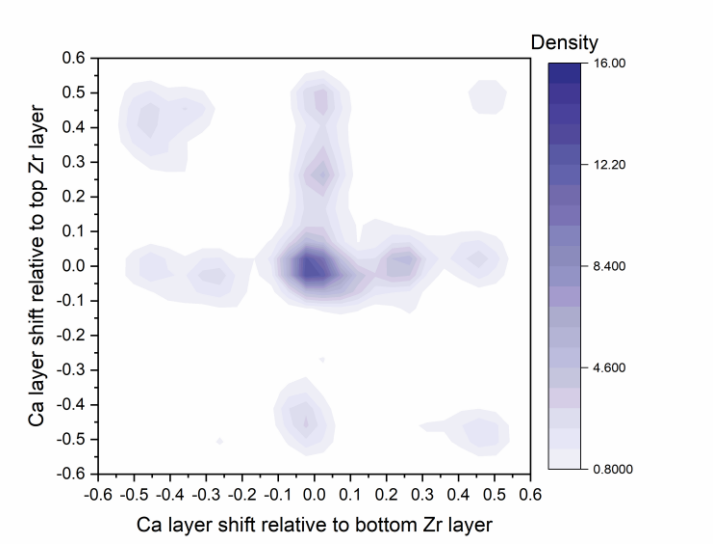


Figure 3.25: Density plot of the Ca/NH_3 layer shifts from the stacking fault neutron refinement at 5 K.

Comparing the shifting in the *b* axis of the Ca/NH_3 subunits relative to the $ZrSe_3$ subunits above and below, a similar trend in the density plot is also seen compared to ambient temperatures. The distribution is also not random, and there is density seen at the distinct points (0, 0), (0, ±0.5), (±0.5, 0) and (±0.5, ±0.5), with the majority of density seen at the original unchanged point (0, 0) and less at (±0.5, ±0.5). Some extra density is seen at the points (±0.25, 0) and (0, ±0.25), which relate to the greater variability of the $ZrSe_3$ subunits shift in Figure 3.24.

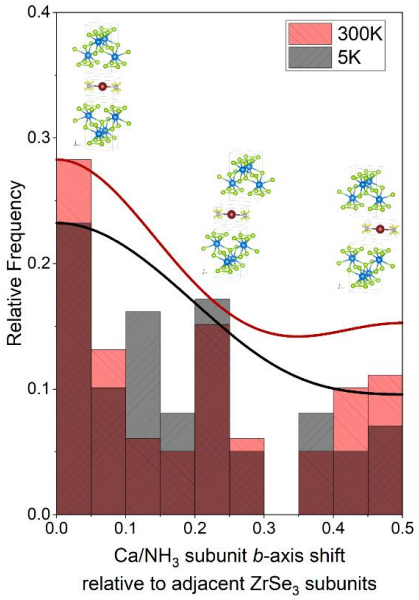


Figure 3.26: Comparison of Ca/NH_3 distributions from stacking fault neutron refinement at 300 K and 5 K.

When plotting the distribution of Ca/NH_3 subunit shifts similar to Figure 3.18, the difference between the unshifted Ca/NH_3 and the Ca/NH_3 subunits shifted by 0.5 becomes more apparent. Earlier, it was mentioned that for the neutron model at 300 K, the ratio of unshifted to shifted Ca/NH_3 subunits was ~ 1.95. At 5 K, this ratio is larger at ~ 2.78. This may result from the decreasing thermal effects upon cooling to 5 K, which reduces the effects of averaging. It is also possible that there is no real change and what is observed is a spread of values due to intrinsic uncertainties. To be sure of this, a number of different samples would need to be measured.

Interstratification was also modelled. The distributions at both temperatures are similar, with the maxima at 5 K slightly shifted to smaller interlayer spacing values, as expected with the thermal contraction upon cooling. Similarly, the secondary maximum seen below 11 Å, due to solvent-free layers, has also seen a slight shift to lower interlayer spacing values.

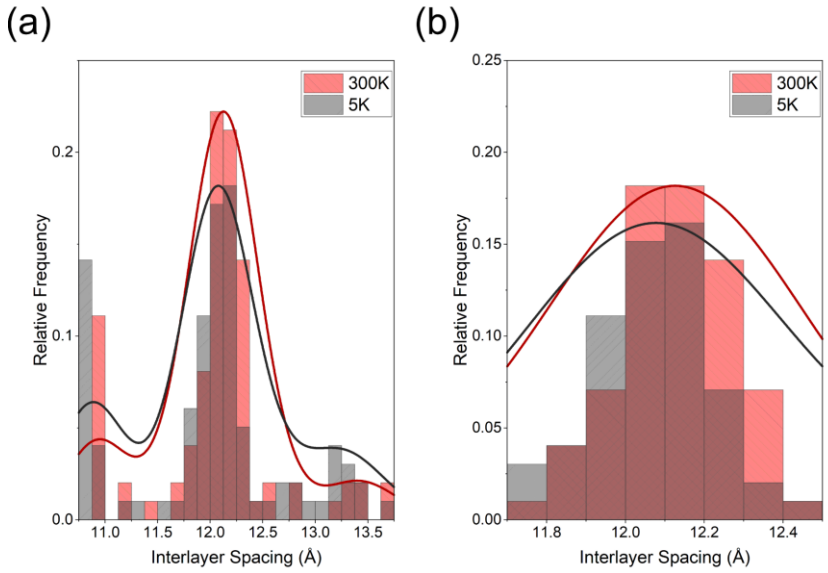


Figure 3.27: Comparison of interlayer separation at 300 K and 5 K. (b) is a close-up of (a) showing how the mode of the interlayer spacing is reduced at 5 K.

3.7.3 Variable Temperature XRD

The Ca intercalate was heated *in situ* to 600 °C at the I11 beamline to test temperature effects on the NH_3 and whether the NH_3 can be thermally deintercalated from the intercalate, forming only Ca_xZrSe_3. It was found that at approximately 400 °C, the compound decomposes into the parent $ZrSe_3$ with no indication of any intermediate phase. Rietveld refinement on the phase at 600 °C fits well to $ZrSe_3$, with a 2 % increase in volume compared to ambient temperatures, likely due to thermal expansion. The diffraction pattern shows no sign of any side products from Ca/NH_3. It is possible that they have formed amorphous products and cannot be seen.

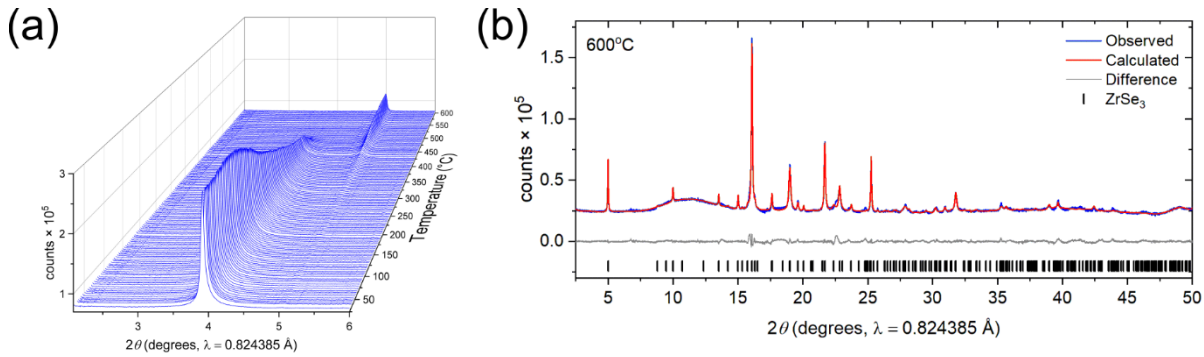


Figure 3.28: (a) Variable temperature PXRD for the low angle reflection, showing how the intercalate decomposes at around 400 °C. (b) Rietveld refinement against I11 (PSD) PXRD pattern of the phase at 600 °C showing that it decomposed back to $ZrSe_3$.

3.8 Magnetometry

The magnetisation was measured against a magnetic field from 0-5 T at 300 K. The parent $ZrSe_3$ shows a clear diamagnetic signal with a molar susceptibility (χ_{mol}) of -8.17(1)×10^{-5} emu mol^{-1}. The intercalates also remain diamagnetic with χ_{mol} varying only by ±2×10^{-5} emu mol^{-1}, confirming that in the reduction, the Zr^{4+} oxidation state remains unchanged. Therefore, the reduction is taking place in the $[Se_2]^{2-}$ dimers. Figure 3.29 shows the plot of the magnetisation against the field of $ZrSe_3$ and the intercalates. Some of the intercalates show an initial increase in susceptibility due to some trace ferromagnetic impurity, as described before in section 2.2.6.1. The susceptibilities were taken from only fitting the linear part of the plot.

Table 3.14: Molar susceptibility values for $ZrSe_3$ and the intercalates.

Compound	**χ_{mol} at 300 K (×10^{-5} emu mol^{-1})**
$ZrSe_3$	-8.17(1)
$K_{0.45(2)}ZrSe_3$	-7.33(1)
$Rb_{0.41(1)}ZrSe_3$	-9.67(1)
$Cs_{0.42(1)}ZrSe_3$	-7.76(2)
$Ca_{0.2}(NH_3)_{0.45(7)}(NH_2)_{0.15(7)}ZrSe_3$	-8.15(2)

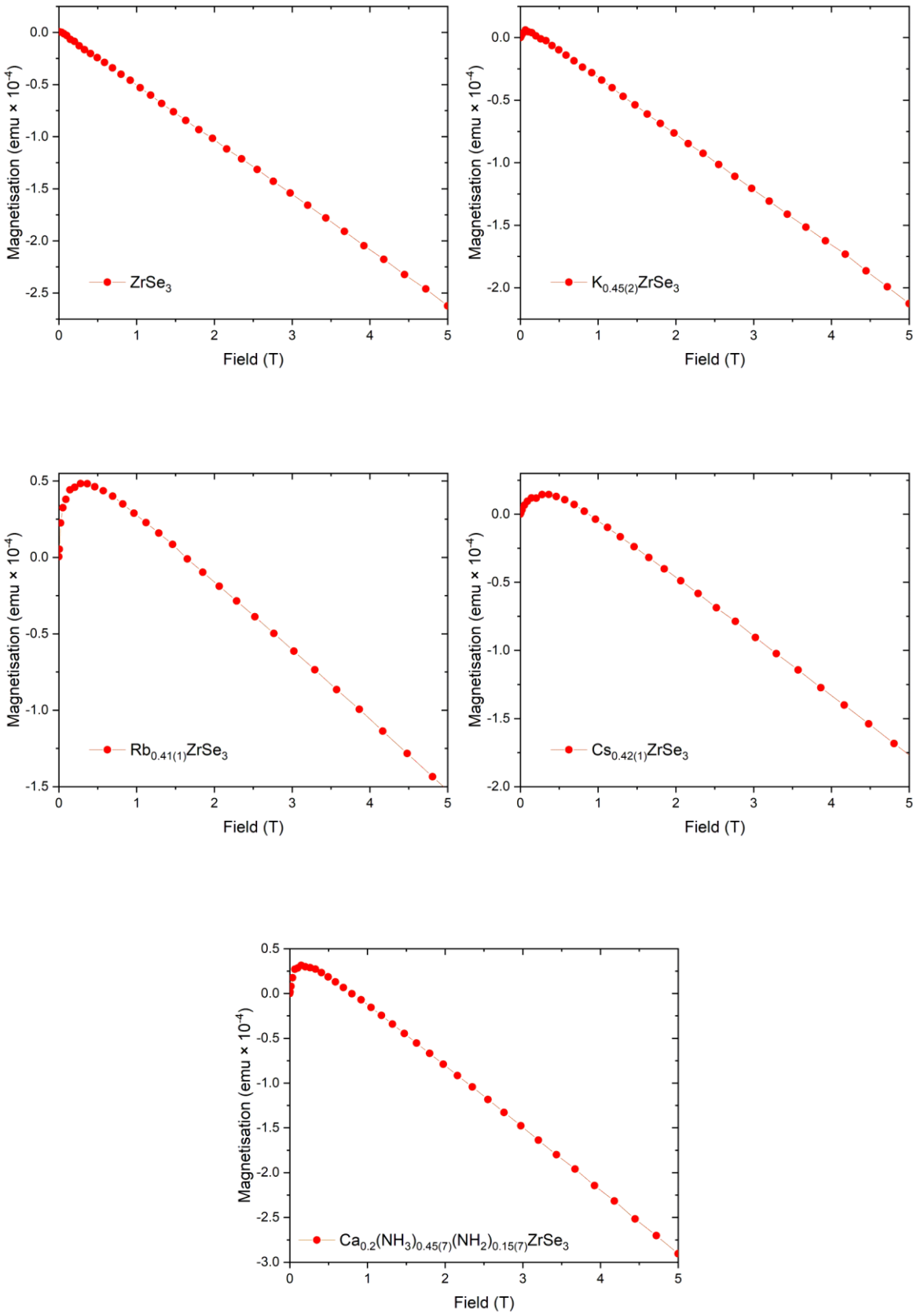


Figure 3.29: Magnetisation vs field plot of $ZrSe_3$ and the intercalates showing diamagnetism for all compounds.

Upon intercalation, if the $[Se_2]^{2-}$ dimers are being partially reduced and the $[Se_2]^{2-}$ antibonding bands are being partially filled, then paramagnetic behaviour would be expected. However, it is evident from the χ_{mol} values, which do not deviate significantly from parent $ZrSe_3$, that this is not the case. It is likely that perhaps only a fraction of the dimers are being fully reduced to Se^{2-}. If one approximates the stoichiometry of the alkali metal intercalates to $A_{0.5}ZrSe_3$, then for every $[Se_2]^{2-}$ dimer, there are 0.5 electrons available for reduction. Since two electrons are needed to reduce $[Se_2]^{2-}$ to Se^{2-}. Therefore, for every four $[Se_2]^{2-}$ dimers, one is reduced to Se^{2-} ($4[Se_2]^{2-} + 2e^- \rightarrow 3[Se_2]^{2-} + 2Se^{2-}$). In the powder diffraction, it is likely that an averaging is observed.

In theory, for diamagnetic compounds, the diamagnetic susceptibility, χ_D, can be calculated using tabulated numbers obtained from Bain *et al*.[159] The susceptibility can be found by summing the individual diamagnetic component for each ion. Although for $ZrSe_3$, there is an added complication due to the $[Se_2]^{2-}$ dimer. There is no tabulated value for the $[Se_2]^{2-}$ dimer. One can give an estimate of the χ_D of $[Se_2]^{2-}$ by subtracting the tabulated χ_D values of Zr^{4+} and Se^{2-} (-1×10^{-5} emu mol^{-1} and -4.8×10^{-5} emu mol^{-1}, respectively) from the χ_{mol} obtained from the *M* vs *H* plot ($-8.17(1)\times10^{-5}$ emu mol^{-1}). This would give a χ_D value for $[Se_2]^{2-}$ of approximately -2.4×10^{-5} emu mol^{-1}, suggesting that the $[Se_2]^{2-}$ is less diamagnetic compared to Se^{2-}.

3.9 Raman Spectroscopy

Raman spectroscopy measurements were carried out to investigate the effects of intercalation on the Raman modes. The parent $ZrSe_3$ displays the main modes as previously reported.[160] Only the A_g^8 mode is exclusive to the $[Se_2]^{2-}$ dimer (Figure 3.30) with the A_g^3, A_g^5 and A_g^6 modes involving the Zr and the Se^{2-} as well. It is important to note that in a crystalline material, unlike with molecules, the atoms are interacting with neighbours, and

therefore, these modes cannot be taken individually but rather as a collective. In crystalline materials, these vibration modes are quantised as phonons.

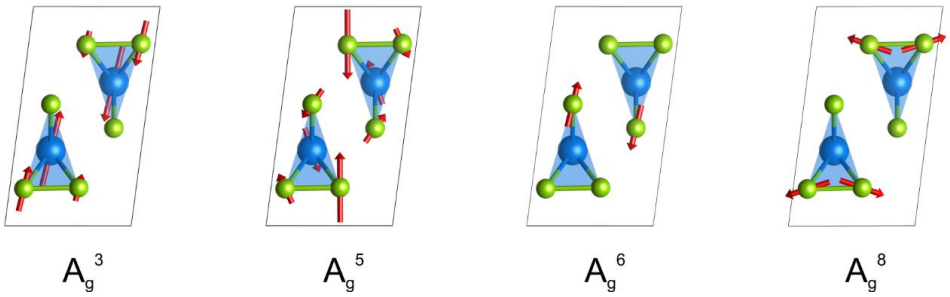


Figure 3.30: Schematic of the Raman modes present in $ZrSe_3$. The A_g^8 is exclusive to the Se-Se dimer.

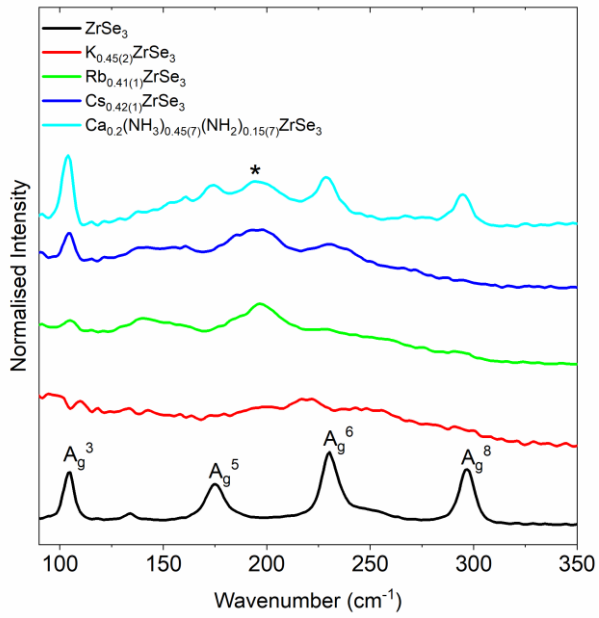


Figure 3.31: Raman spectrum of $ZrSe_3$ and the intercalates. The asterisk indicates the new mode seen.

Comparing the Raman spectra of the intercalates, it is evident that intercalation and the consequent reduction of the $[Se_2]^{2-}$ dimer has a significant effect on the modes. This is especially seen when looking at the A_g^8 mode, which disappears when intercalating alkali metals. From the magnetism discussed earlier, it is likely there is a fraction of the $[Se_2]^{2-}$ dimer being reduced. This reduction would be enough to disrupt the phonon modes, and perhaps a clear signal is not seen due to the disorder. A new peak is seen at 200 cm^{-1}, although a more in-depth Raman spectroscopy study would be needed to assign this mode.

In the Ca/NH_3 intercalate, the presence of both this new peak and the original A_g^8 mode would suggest that there are slabs where the $[Se_2]^{2-}$ dimers are being reduced (like with the alkali metal intercalates) and regions where the slabs are completely non-reduced (like with parent $ZrSe_3$). This would be consistent with the overall reduced reduction in the Ca/NH_3 intercalate (0.25(7) electrons available for reduction based on elemental analysis) compared to the alkali metal intercalates (~ 0.4 electrons). This is also consistent with the stacking disorder and the ~ 2.52 Å average Se-Se dimer length used in the stacking fault refinement being shorter than the ~ 2.6 Å average Se-Se dimer length in the alkali metal intercalates.

Using 2.6 Å as an approximate value corresponding to reduction taking place in all the slabs (based on the alkali intercalates) and 2.34 Å as the value corresponding to all slabs being completely non-reduced (based on parent $ZrSe_3$). A value of 2.52 Å would correspond to 69 % of the slabs that are being reduced. Given that for the alkali metal intercalates, ~ 0.4 electrons would achieve reduction in all the slabs, the 0.25(7) electrons available for reduction would correspond to 45-80 % of the slabs being reduced; hence 69 % falls within this range.

The presence of regions with non-reduced dimers would support the theory that some of the Se-Se dimers do not have any significant bonding interaction with the Ca^{2+} intercalant, resulting in the layers being free to move, leading to significant stacking disorder in this system. This, however, does not rule out the possibility of some hydrogen bonding of the NH_3/NH_2^- species to Se (H-Se distance of 2.7-2.8 Å from *Immm* model) as seen in the Li/NH_3 intercalation of FeSe.[63]

3.10 Conclusion

The work presented here in this chapter has shown that the low-temperature intercalation into $ZrSe_3$ occurs with differing polymorphs to that previously reported in a high-

temperature synthesis. Under these conditions, the reactions are under kinetic control. Therefore, the polymorphs found for the Rb and Cs intercalates are likely dictated by the large size of the cations, preferring to occupy the largest site possible, found in the *Immm* structure. Annealing the low-temperature *Cmc*2_1 K intercalate appeared to favour other reaction pathways than the transformation into the high-temperature *Immm* polymorph.

The intercalation with Ca proceeds with the co-intercalation of the ammonia solvent. This results in an expansion greater than that of the Cs intercalate. Elemental analysis confirms the presence of the solvent species and suggests a formula of $Ca_{0.2}(NH_3)_{0.45(7)}(NH_2)_{0.15(7)}ZrSe_3$. The co-intercalation resulted in large interlayer separations such that the compound suffers from severe stacking disorder due to the alkaline earth metal ion having little bonding interaction with the Se. The diffraction patterns cannot be simply modelled with either the *Immm* or *Cmc*2_1 models. Therefore, a stacking fault model based on the *Immm* model was used where multiple rigid blocks of $ZrSe_3$ and Ca/NH_3 were allowed to refine independently. This model significantly improved the fit to the observed X-ray and neutron diffraction patterns, with the body-centred *Immm*-type arrangement of $ZrSe_3$ layers having the largest probability. Ca/NH_3 layer shifts in the neutron refinement show a clear favourability of the NH_3 being in closer proximity to the Se, presumably to facilitate hydrogen bonding. The refinement was also carried out on neutron diffraction data measured at 5 K. Aside from expected lattice contraction, the pattern shows no significant difference to ambient temperature. There is a slight variation in the *b*-axis shifting, likely due to decreasing thermal effects or uncertainties intrinsic to the refinement.

Magnetometry measurements confirmed that the Zr^{4+} oxidation state remains unchanged as the intercalates remain diamagnetic, and therefore the reduction is occurring on the Se-Se dimers, and there is no indication that Zr^{4+} is being reduced. However, it is likely that a

fraction (approximately a quarter) of the $[Se_2]^{2-}$ are being fully reduced to Se^{2-} rather than a partial reduction, as then paramagnetism would be expected to be observed.

Raman spectroscopy on the Ca/NH_3 intercalate showed the presence of the non-reduced selenide dimer (A_g^8) mode and a new peak at lower wavenumbers, which may correspond to regions where the slabs are being reduced. This would suggest that in this system, there is a mixture of regions where slabs are reduced and non-reduced, consistent with the stacking faults.

$ZrSe_3$ powder is black in colour with a reported direct and indirect bandgap of 1.1 and 1.47 eV, respectively.[161] Intercalation with alkali metal was found here to change the powder colour from black to brown. This is likely due to increases in the band gap upon intercalation through chemical and structural changes. It supports the observation that some of the diselenide ions are reduced, and the compounds remain insulating diamagnets. The band gap measurements and computational calculations of the density of states and band structures can be an area for potential future work.

Chapter 4

4 Li Intercalation of $Nb_2Pd_xCh_5$ (*Ch* = S, Se)

4.1 Introduction

The majority of transition metal chalcogenides that have been well-studied are binary compounds. However, with the improvement in air-sensitive synthesis and characterisation methods, the 1980s saw a wave of synthesis of new ternary chalcogenides. The extra element provides an additional degree of freedom giving rise to novel structure types such as the case seen in $M_2Pd_xCh_5$ (*M* = Nb, Ta; *Ch* = S, Se). $Nb_2Pd_{0.71}Se_5$ was the first of this family to be synthesised in 1985 by Keszler *et al*.[49] The structure (as shown in Figure 4.1) was found to be monoclinic crystallising in the *C*2/*m* space group and consists of MCh_6 triangular prisms [*M*(1)], MCh_7 monocapped triangular prisms [*M*(2)] and PdCh_4 square planar [Pd(1)] units arranged in layers. The layers are linked with an additional PdCh_4 [Pd(2)]. This second Pd site was reported to be deficient, with the site being ~ 40 % occupied.

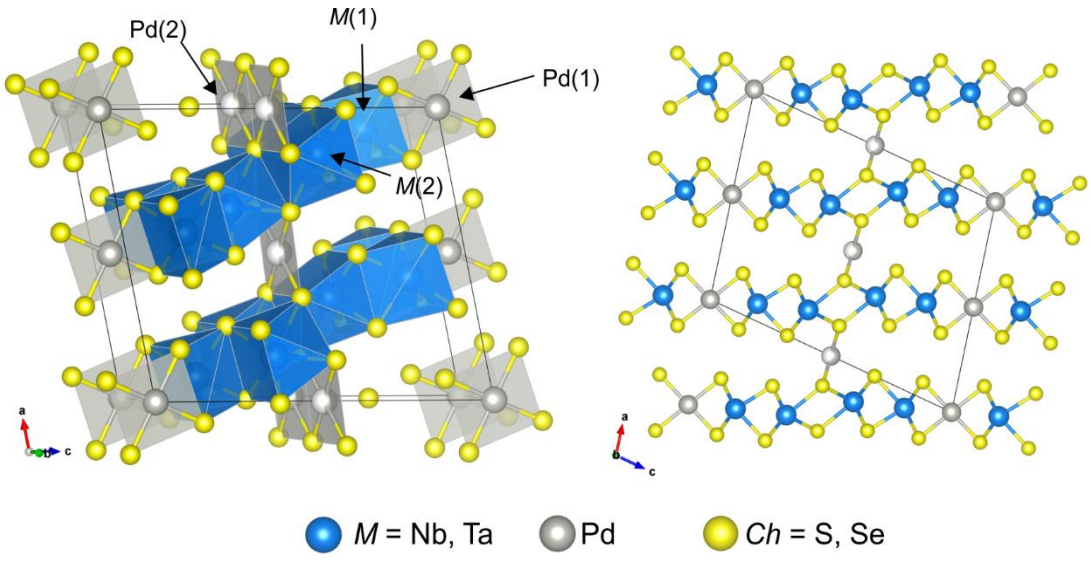


Figure 4.1: Structure of $M_2Pd_xCh_5$ (*M* = Nb, Ta; *Ch* = S, Se).

At the time, it was only reported to be a metallic conductor, however in 2013, superconductivity was discovered by Khim *et al.* occurring at T_c = 5.5 K.[116] They found that there is a positive correlation between Pd occupancy and T_c, with T_c ranging from 3.4 - 5.5 K for $0.8 < x < 1.3$ although, the composition of the reported $Nb_2Pd_{1.2}Se_5$ phase with T_c = 5.5 K must be doubtful because the maximum possible Pd site occupancy for the Pd(1) and Pd(2) sites is exceeded. The authors obtained a cell volume that is 0.3 % larger than that reported for the phase $Nb_2Pd_{0.891}Se_5$,[162] suggesting that although it is unlikely the Pd occupancy is 1.2, the Pd(2) site is close to full occupancy of 1. It has also been reported that for $0.67 < x < 0.7$, T_c ranges from 0.3 - 1 K.[114] The first report of superconductivity was earlier in 2013 when the sulfide $Nb_2Pd_{0.81}S_5$ was reported by Zhang *et al*. with a T_c of 6.6 K which ignited the research in this area.[115] The superconductivity was of interest not primarily for the relatively low transition temperature but rather the remarkably large and anisotropic upper critical fields these compounds possess, in violation of the Pauli limit (section 1.6.2) by a factor of 3 and which, to date, has no conclusive explanation.

Following the work of Keszler *et al.* in 1985, Squattrito *et al.* synthesised the phase $Ta_2Pd_{0.89}S_5$.[163] Similarly, superconductivity was reported in 2013 with T_c = 6 K.[51] The fourth and final member of this family, Ta_2PdSe_5 was first reported in 2015. The compound contained some impurities but was reported with a T_c of ~ 2.5 K.[117]

Research on the modification of the superconductivity has been mainly achieved by substitutional hole or electron doping by making substitutions at the Pd site. Shen *et al.* reported $Nb_2(Pd_{1-y}R_y)_{0.76}S_5$ (*R* = Ir, Ag).[164] It was found that superconductivity can be enhanced by partial substitution of Pd by Ir with a maximum T_c of ~ 8 K when $y = 0.4$, but upon further hole-doping, T_c is suppressed. When electron doping is carried out with Ag, T_c decreases until it is completely suppressed when doped to 40 % Ag. Superconductivity is

also completely suppressed when 15 % of the Pd is exchanged for Ni in an isoelectronic substitution.[121] By doping Nb_2PdS_5 with Se, T_c decreases with increasing Se content until there is complete suppression (at least down to the 1.8 K detection limit of the instrument) at 50 % Se substitution.[165] However, its upper critical field remained immune to the effects of Se doping.

No intercalation chemistry has been reported on these compounds. However, the van der Waals gap between the layers makes this material a promising candidate for the intercalation of small ions. Even though the layers are linked by the interlayer Pd ions, as shown in Figure 4.1, there are large channels in the structure. Penny Hyde, in her master thesis, made some initial findings that intercalation using *n*-BuLi was possible in $Nb_2Pd_xSe_5$;[122] however, detailed structure characterisation was needed.

In this chapter, Li intercalation via chemical and electrochemical methods into $Nb_2Pd_xS_5$ and $Nb_2Pd_xSe_5$ will be described with a comparison of the various lithiation methods. This chapter will show the complete suppression of the superconductivity upon intercalation, with deintercalation partially restoring it, with a structural study using a combination of X-ray diffraction, neutron diffraction, solid-state NMR, and computational analysis.

4.2 $Nb_2Pd_xS_5$

4.2.1 Synthesis and characterisation of $Nb_2Pd_xS_5$

Polycrystalline samples of $Nb_2Pd_xS_5$ were synthesised by a direct combination of elements. Nb powder (Alfa Aesar, 99.99 %), Pd powder (Alfa Aesar, 99.95 %) and S powder (Alfa Aesar, 99.999 %) were ground together in a Nb:Pd:S ratio of 2:0.85:6. The mixture was pelletised and heated to 850 °C at a rate of 1 °C/min and held for 24 hours then left to furnace cool. A significant excess of S was used, as was reported by Zhang *et al.*[115] Using

stoichiometric amounts of S led to the formation of binary Nb-S side phases. Using a non-stoichiometric amount of Pd was found to be optimal for the synthesis. Using a Pd stoichiometry of 1 (*i.e.* to give full occupancy of both Pd sites) produced a PdS side phase at ~ 5 % by mass. Lowering the Pd stoichiometry to 0.85 makes the formation of PdS less favourable, and the impurity is reduced to < 3 % by mass. The variation in Pd content has no significant effect on the superconducting nature in contrast to what was reported for $Nb_2Pd_xSe_5$.[114,116] Yu *et al.* synthesised $Nb_2Pd_xS_{5-\delta}$ ($0.6 < x < 1$; $0 < \delta < 0.62$) single crystal fibres with T_c ranging from 4.67 K to 7.43 K, but no reliable trend in the T_c with composition was observed.[166] With a starting stoichiometry of 0.85, the site occupancy of Pd(2), the strongest X-ray scatterer in the system, refined to 0.496(3), giving an overall Pd occupancy of 0.748(2). Structural parameters from the Rietveld refinement are provided in Table 4.1. SEM imaging shows a homogenous distribution of the elements with EDX mapping on five points on the crystallite in Figure 4.4(a), giving an average stoichiometry of $Nb_2Pd_{0.78(1)}S_{4.9(1)}$, in line with the independent result from the Rietveld refinements. The plot of the magnetic susceptibility against temperature shown in Figure 4.3 for zero-field cooled and field cooled at 10 Oe shows $Nb_2Pd_{0.748(2)}S_5$ exhibiting bulk superconductivity with a T_c of 6.5 K and a *SVF* of ~ 80 %.

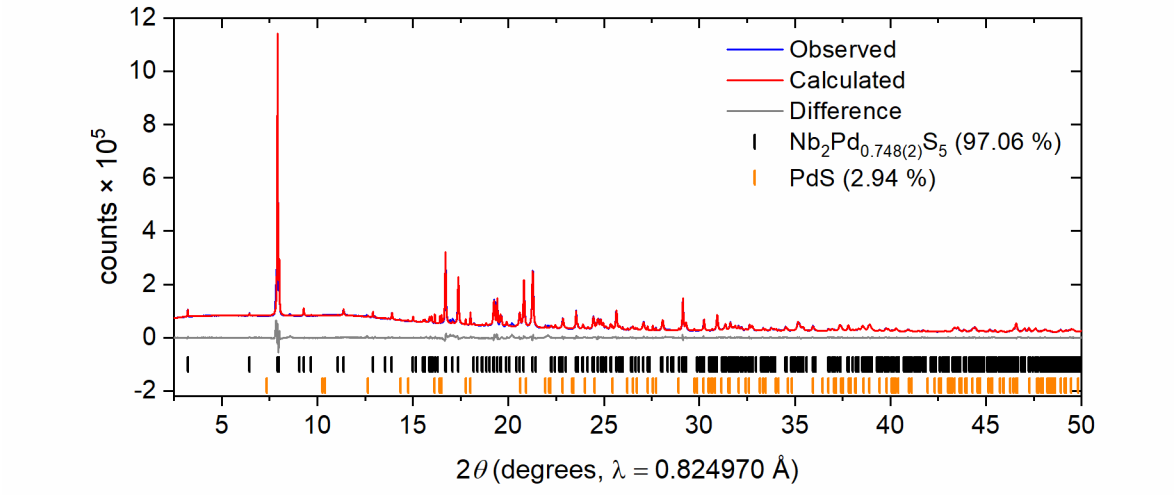


Figure 4.2: Rietveld refinement against I11 (PSD) PXRD pattern of $Nb_2Pd_{0.748(2)}S_5$ (ME174). R_{wp}: 3.73 %

Table 4.1: Structural parameters obtained from refinement of $Nb_2Pd_{0.748(2)}S_5$.

$Nb_2Pd_{0.748(2)}S_5$ (ME174)					
Space Group	***a* / Å**	***b* / Å**	***c* / Å**	**Volume / Å^3**	***β* / °**
C2/m (No. 12)	12.1448(1)	3.27971(2)	15.0798(1)	585.04(1)	103.161(9)
***Mean Bond Length* / Å**					
	Nb(1)-S			2.469(3)	
	Nb(2)-S			2.523(3)	
	Pd(1)-S			2.358(5)	
	Pd(2)-S			2.403(5)	
Positional Parameters					
Atom	***x***	***y***	***z***	***Occupancy***	***Wyckoff Symbol***	***U_{iso}* / Å^2**
Nb(1)	0.0752(2)	0.5	0.1817(2)	1	4*i*	0.0044(6)
Nb(2)	0.1532(2)	0	0.3781(2)	1	4*i*	0.0044(6)
Pd(1)	0	0	0	1	2*a*	0.0022(9)
Pd(2)	0	0	0.5	0.496(3)	2*c*	0.0022(9)
S(1)	0.3538(5)	0	0.4917(5)	1	4*i*	0.0043(7)
S(2)	0.2511(5)	0.5	0.3032(5)	1	4*i*	0.0043(7)
S(3)	0.1789(5)	0	0.1032(5)	1	4*i*	0.0043(7)
S(4)	0.4276(5)	0.5	0.1319(5)	1	4*i*	0.0043(7)
S(5)	0.4995(4)	0	0.3191(4)	1	4*i*	0.0043(7)

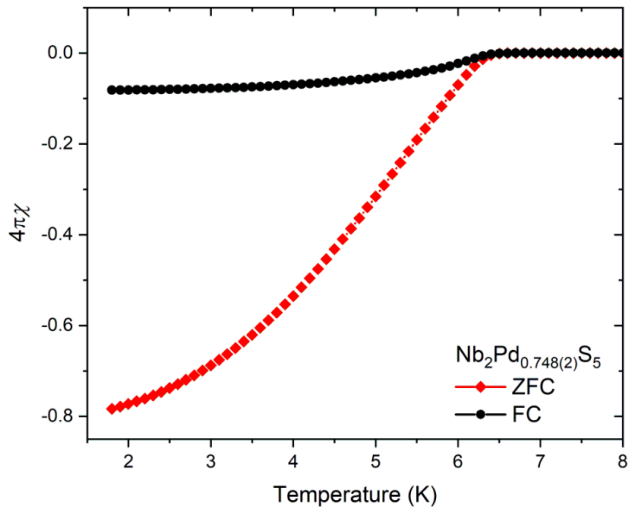


Figure 4.3: Zero-field cooled (red) and field cooled (black) plot of the magnetic susceptibility against temperature measured at 10 Oe showing a T_c of 6.5 K and *SVF* of ~ 80 %.

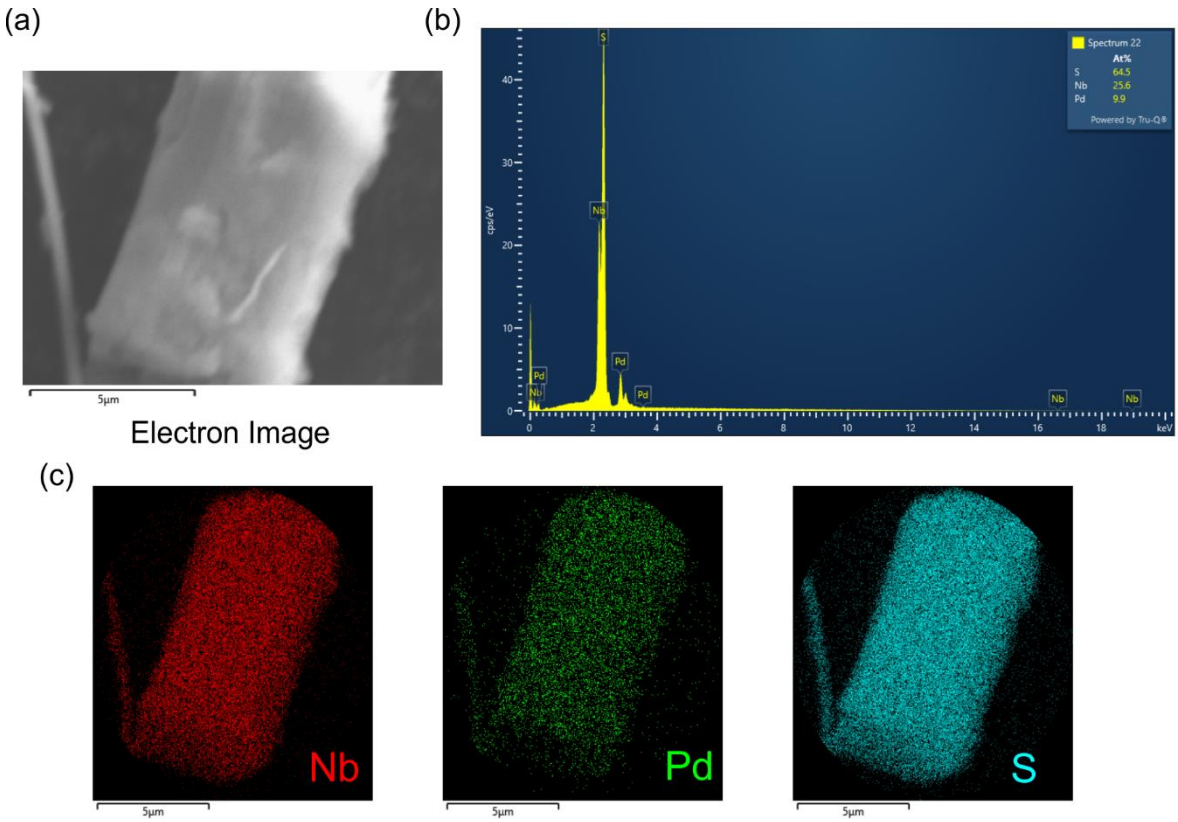


Figure 4.4: (a) SEM image of $Nb_2Pd_{0.74(1)}S_5$ with (c) showing the homogenous spread of the elements. (b) EDX spectrum giving a stoichiometry of $Nb_2Pd_{0.78(1)}S_{4.9(1)}$.

The density of states and electronic band structure were calculated by Jiayi Cen, UCL, using density functional theory (a detailed description of the procedure is provided in Appendix I), confirming the metallic nature with no gap at the Fermi level (E_f), consistent with previous reports.[115,167] For the calculations, the stoichiometric Nb_2PdS_5 composition was assumed. With partially occupied sites, a large supercell would be required with ion/vacancy ordering. This would result in the large supercell having too many possible configurations making the calculations extremely time-consuming. The change in Pd(2) site occupancy is not expected to modify the topology of the band structure but may cause a slight shift in the Fermi level (Energy = 0) to lower energies. Therefore, fully occupied Nb_2PdS_5 was deemed sufficient to display the important features of the electronic structure. The valence band (where the Energy < 0) is dominated by strongly hybridised Pd(4*d*) and S(3*p*) states. Around the Fermi

level, the bands mainly consist of Nb(4*d*) and S(3*p*) hybridised states, which also form the majority of the conduction band.

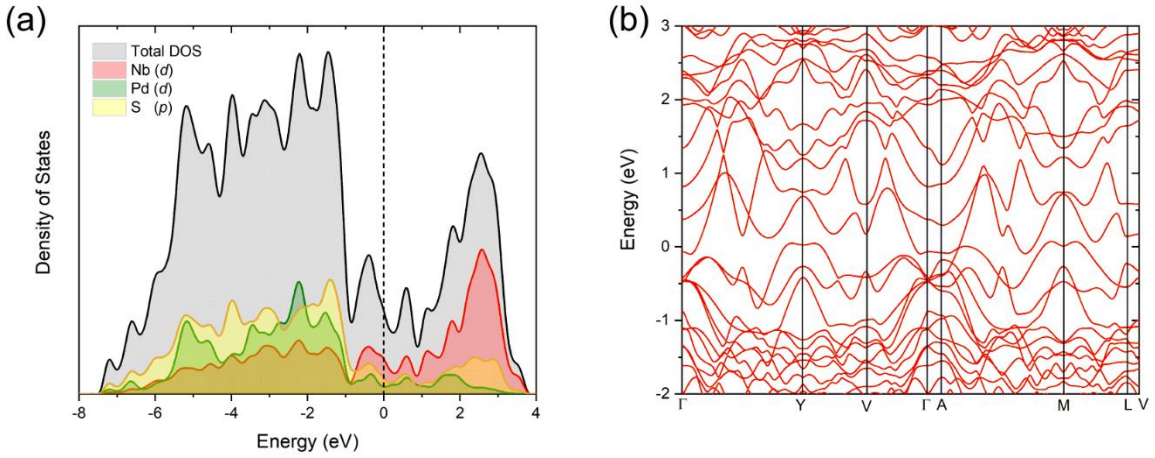


Figure 4.5: (a) Electronic density of states and (b) electronic band structure of Nb_2PdS_5 showing the metallic nature and the hybridisation of the bands.

4.2.2 Chemical Intercalation

$Nb_2Pd_{0.74(1)}S_5$ was chemically intercalated using three different methods of intercalation; *n*-BuLi, Li in ammonia solution and Li in naphthalene solution with varying stoichiometries. It can be seen from Figure 4.6(a) that intercalation using 0.5, 1 and 2 molar equivalents of *n*-BuLi, does not produce a single intercalated phase. Instead, multiple phases were seen, with a significant reduction in crystallinity.

Intercalation using a 1:1 molar ratio of the Li/ammonia reagent resulted in the powder remaining black, with the dark blue colour of the solvated electrons decolourising in minutes. This produced an expanded intercalated phase. However, as seen in Figure 4.6 (b), a side phase appears to form with a small side peak at a slightly lower angle than the main peak ($20\bar{1}$ Bragg reflection). This peak diminishes when less Li is used and was not present when a 0.6:1 Li : $Nb_2Pd_{0.74(1)}S_5$ ratio was used in a Li/ammonia reaction.

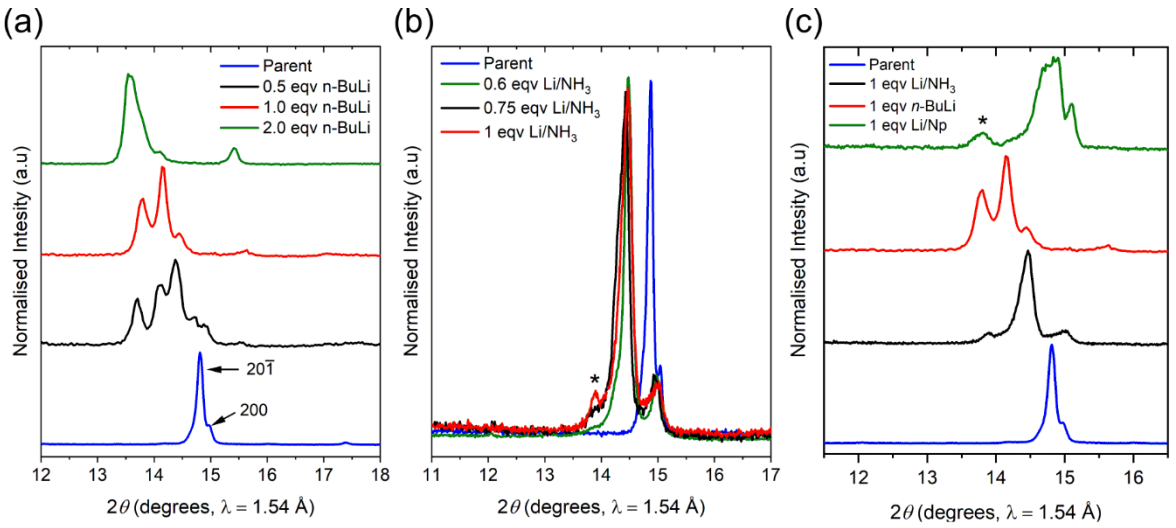


Figure 4.6: Comparison of the main 20$\bar{1}$ and 200 Bragg reflection using different intercalation methods and varying Li stoichiometries for (a) n-BuLi, (b) Li in ammonia and (c) Li in naphthalene. The plot at (c) compares the three reagents using a 1:1 molar ratio. The asterisk indicates the peak corresponding to the side phase.

Intercalation was also carried out using a 1:1 molar ratio of the Li/naphthalene reagent. However, this also produced multiple phases. The parent material had not been fully consumed, as evident in the broad peak in Figure 4.6(c). Despite it not going to completion, the side phase at higher *d*-spacing is still forming, as seen when using other reagents.

4.2.3 Lithium Intercalate

4.2.3.1 Powder X-ray Diffraction

From these intercalation methods, it was evident that Li/NH_3 was the best reagent producing a single crystalline intercalated phase with no additional side phases. The intercalated phase was measured on the I11 beamline, Diamond Light Source, with the Rietveld refinement determining that the unit cell expanded by approximately 0.2 Å, 0.01 Å and 0.26 Å in the *a*, *b* and *c* directions, respectively, with an increase of ~ 3.3° in the monoclinic angle and the *C*2/*m* space group being maintained. Comparing the mean bond lengths shown in Table 4.2, there appears to be no significant change reflecting the small increase in unit cell dimensions.

Table 4.2: Comparison of structural parameters of $Nb_2Pd_{0.748(2)}S_5$ (ME174) and $Li_xNb_2Pd_{0.743(2)}S_5$ (ME176).

Compound	**$Nb_2Pd_{0.748(2)}S_5$**	**$Li_xNb_2Pd_{0.743(2)}S_5$**
	Parent (ME174)	Intercalate (ME176)
***a* / Å**	12.1448(1)	12.3390(5)
***b* / Å**	3.27971(2)	3.2933(1)
***c* / Å**	15.0798(1)	15.3447(6)
Volume / Å^3	585.04(1)	598.03(4)
***β* / °**	103.161(9)	106.444(1)
Mean Bond Lengths / Å		
Nb(1)-S	2.469(3)	2.463(3)
Nb(2)-S	2.523(3)	2.545(3)
Pd(1)-S	2.358(5)	2.373(6)
Pd(2)-S	2.403(5)	2.390(6)

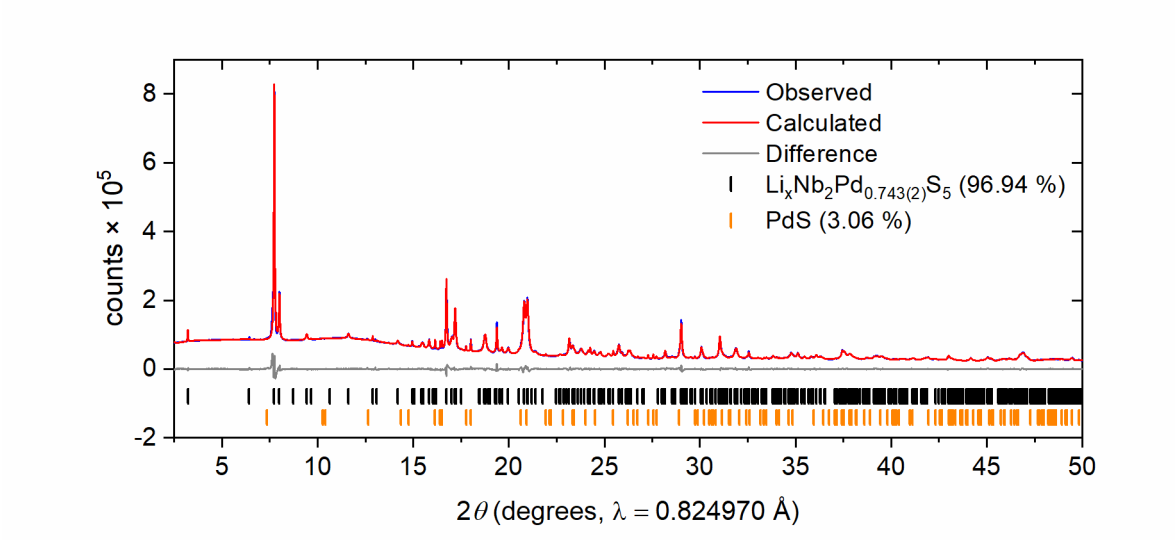


Figure 4.7: Rietveld refinement against I11 (PSD) PXRD pattern of $Li_xNb_2Pd_{0.743(2)}S_5$. R_{wp}: 2.79 %. The Li content here is labelled as *x* as Li cannot be refined from the X-ray data, although it is refined in the neutron diffraction data.

4.2.3.2 Powder Neutron Diffraction

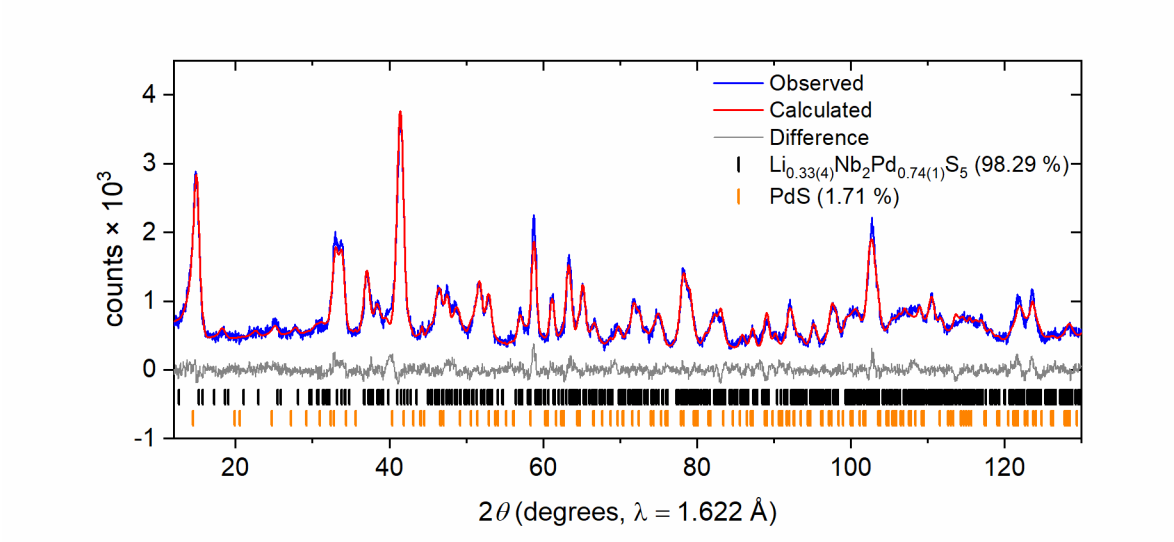


Figure 4.8: Rietveld refinement against PND pattern of $Li_{0.33(4)}Nb_2Pd_{0.74(1)}S_5$. R_{wp}: 3.26 %.

Powder neutron diffraction measured on Echidna, ANSTO (data collected by Max Avdeev via the mail-in service) was used to determine Li positions since it is not possible with X-ray diffraction due to the X-ray scattering factor scaling with electron count. Therefore, the contribution of the light Li atom is very weak compared to the much heavier 4*d* metals. Refinement against PND data confirmed the expansion of the unit cell of the intercalated phase, with the lattice parameters in agreement with those determined from the synchrotron PXRD data. Li is the only negative scatter in the system with a coherent scattering length of -1.9 fm (for reference: Nb = 7.05 fm; Pd = 5.91 fm; S = 2.85 fm).[131] A negative scattering centre was located using a difference Fourier map (where the calculated structure factors are subtracted from the observed structure factors) at (0.208(5), 0.5, 0.002(3)), corresponding to a triangular prismatic site. The rectangular base of the prism consists of two adjacent $Pd(1)S_4$ in the *b* direction. A detailed discussion of the Li site will be presented in section 4.2.3.4. Li was refined with an occupancy of 0.33(4) Li per formula unit. ICP-MS was attempted to confirm the Li occupancy; however, the compound could not be dissolved in the aqueous HNO_3/HCl solution. The Pd(2) occupancy was refined to 0.47(2), which was similar to the

consistent occupancies of 0.496(3) and 0.485(3) obtained from the PXRD refinement of the parent and intercalate, respectively. Allowing for the uncertainty in the refined parameters and the approximately 1:3 ratio of the magnitude of the scattering lengths of Li and Pd, this suggests that the Li is not intercalated into the vacant Pd(2) linkage sites above the 5 % level.

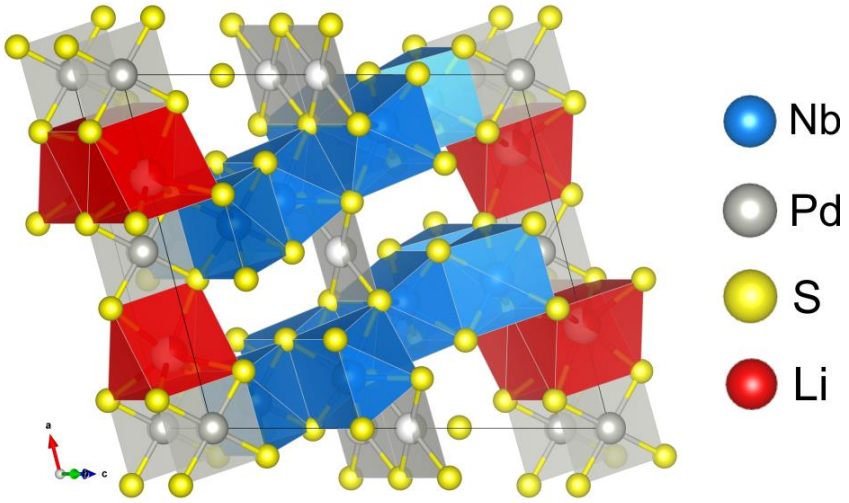


Figure 4.9: Structure of $Li_{0.33(4)}Nb_2Pd_{0.74(1)}S_5$ obtained from PND refinement. The red site shows the Li triangular prismatic environment. A more detailed description is provided in section 4.2.3.4.

Table 4.3: Structural parameters of the Li intercalate obtained from synchrotron PXRD refinement and PND. The values from PND are given in [ ].

$Li_{0.33(4)}Nb_2Pd_{0.74(1)}S_5$: *C*2/*m* (No.12)						
***a* / Å**		***b* / Å**	***c* / Å**	**Volume / Å^3**		***β* / °**
12.3390(5) [12.3428(12)]		3.2933(1) [3.2914(2)]	15.3447(6) [15.3390(15)]	598.03(4) [597.5(1)]		106.444(1) [106.489(7)]
Positional Parameters						
Atom	***x***	***y***	***z***	***Occupancy***	***Wyckoff Symbol***	***U_{iso}* / Å^2**
Nb(1)	0.0737(2) [0.0779(6)]	0.5	0.1852(2) [0.1868(4)]	1	4*i*	0.0022(8) [0.0042(8)]
Nb(2)	0.1475(2) [0.1443(5)]	0	0.3768(2) [0.3777(4)]	1	4*i*	0.0019(7) [0.0042(8)]
Pd(1)	0	0	0	1	2*a*	0.0031(8) [0.0042(8)]
Pd(2)	0	0	0.5	0.485(3) [0.470(17)]	2*c*	0.0031(8) [0.0042(8)]
S(1)	0.3579(6) [0.3594(10)]	0	0.4949(5) [0.5031(9)]	1	4*i*	0.0011(7) [0.0086(16)]
S(2)	0.2517(6) [0.2506(14)]	0.5	0.3116(5) [0.3054(11)]	1	4*i*	0.0011(7) [0.0086(16)]
S(3)	0.1701(6) [0.1612(11)]	0	0.1140(5) [0.1155(9)]	1	4*i*	0.0011(7) [0.0086(16)]
S(4)	0.4165(6) [0.4214(13)]	0.5	0.1256(5) [0.1201(10)]	1	4*i*	0.0011(7) [0.0086(16)]
S(5)	0.4953(6) [0.4981(12)]	0	0.3075(5) [0.3155(9)]	1	4*i*	0.0011(7) [0.0086(16)]
Li	[0.208(5)]	0.5	[0.002(4)]	[0.33(4)]	4*i*	[0.0042(8)]
Mean Bond Lengths / Å						
Nb(1)-S				2.463(3) [2.433(7)]		
Nb(2)-S				2.545(3) [2.528(7)]		
Pd(1)-S				2.373(6) [2.286(11)]		
Pd(2)-S				2.390(6) [2.401(11)]		
Li-S				[2.66(3)]		

Structural information is provided in Table 4.3. Thermal displacement parameters were constrained to be isotropic and equal for similar elements and sites to avoid excessive parameter correlation, particularly in refinements against the lower-resolution neutron powder diffraction data. The Li position and occupancy have a higher degree of uncertainty, most likely due to its weak scattering length relative to the other elements (Nb = 7.05 fm;

Pd = 5.91 fm; S = 2.85 fm),[131] its relatively low occupancy and the possibility that Li can be mobile in the space between the layers.

4.2.3.3 ^{7}Li NMR Spectroscopy and DFT Calculations

Solid-state ^{7}Li NMR spectroscopy measurements produced a single peak centred at around 4 ppm (referenced to LiF at -1 ppm). This would suggest Li occupies a single site, consistent with the one negative scattering centre found in the neutron diffraction refinement, or was exchanging rapidly between sites on the NMR timescale. The peak, however, with a Full-Width-at-Half-Maximum (FWHM) of 10.8 ppm is significantly broader than the 2 ppm found in the comparable ^{7}Li MAS NMR spectrum of Li_2S,[168] suggesting that although it may be one Li environment, the cation is likely to be mobile between sites within the layers. This is consistent with the fact that there is a higher degree of uncertainty in the refined Li position and occupancy.

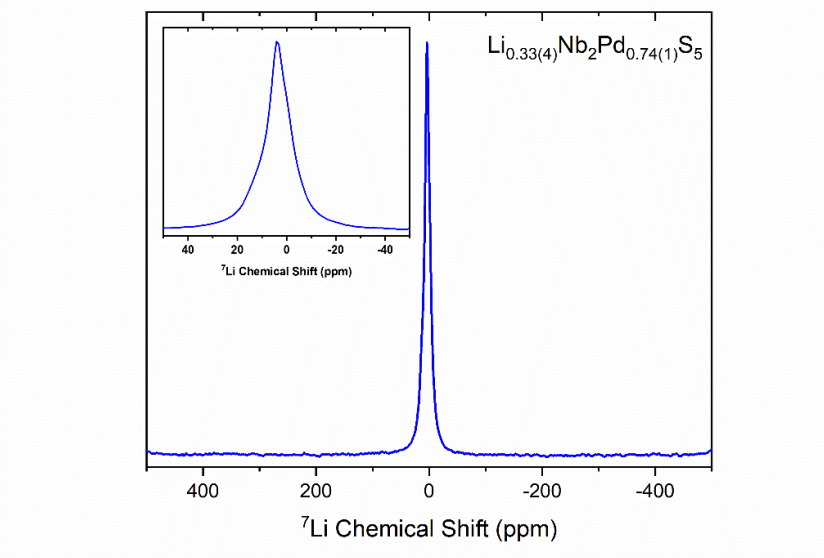


Figure 4.10: Solid state ^{7}Li NMR of $Li_{0.33(4)}Nb_2Pd_{0.74(1)}S_5$ showing one peak indicating one Li site. Inset shows how the peak is broad, suggesting Li is mobile.

DFT calculations were performed using the stochiometric *C*2/*m* Nb_2PdS_5 model to locate all possible Li sites within the compound and to calculate their relative energies. One Li atom

was placed in the 32-atom supercell with four formula units of Nb_2PdS_5, corresponding to a composition of $Li_{0.25}Nb_2PdS_5$, similar to that deduced experimentally. Twenty-two unique interstitial sites were identified, and each Li interstitial structure was allowed to relax. All Li interstitials were relaxed to five distinct possible sites. The calculated lattice parameters of $Li_{0.25}Nb_2PdS_5$ show a smaller volume compared to the experimental structure. A diagram showing the locations of the five Li sites calculated after optimisation is shown below in Figure 4.11, with structural information of the sites given in Table 4.5.

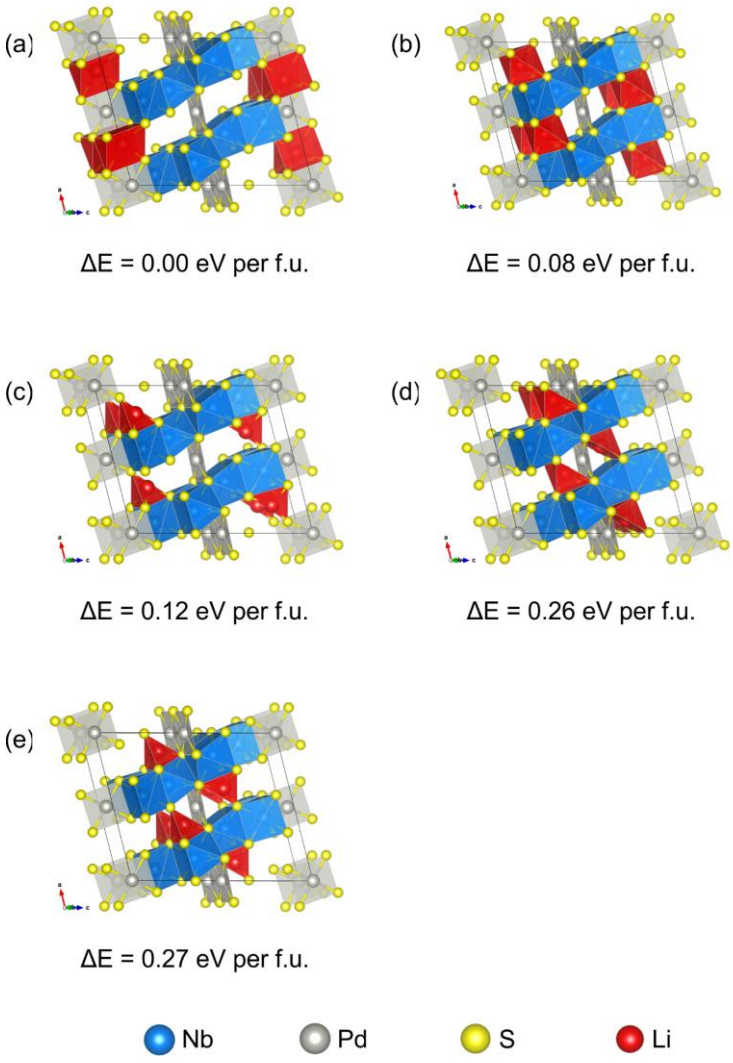


Figure 4.11: Schematic of the Li sites (a-e) determined from DFT ranked from lowest energy to highest.

Table 4.4: Lattice parameters of $Nb_2Pd_{0.748(2)}S_5$, the experimentally determined intercalated phase and the calculated $Li_{0.25}Nb_2PdS_5$.

Compound	**$Nb_2Pd_{0.74(1)}S_5$**	**$Li_{0.33(4)}Nb_2Pd_{0.74(1)}S_5$**	**$Li_{0.25}Nb_2PdS_5$**
	Experimental Parent	Experimental Intercalate	Calculated Intercalate
***a* / Å**	12.1448(1)	12.3390(5)	12.1897
***b* / Å**	3.27971(2)	3.2933(1)	3.2825
***c* / Å**	15.0798(1)	15.3447(6)	15.3662
Volume / Å^3	585.04(1)	598.03(4)	590.1944
***β* / °**	103.161(9)	106.444(1)	106.2761

Table 4.5: Description of the Li sites (a)-(e).

Site		**(a)**	**(b)**	**(c)**	**(d)**	**(e)**
Δ*E* / eV		0.00	0.32	0.50	1.03	1.09
Site		4*i*	4*i*	4*i*	4*i*	4*i*
Li Site Energy / eV f.u.$^{-1}$		0.00	0.08	0.12	0.26	0.27
Site Co-ordinates	***x***	0.2208	0.1621	0.1852	0.0937	0.1266
	y	0.5	0.5	0	0	0.5
	z	0.9941	0.7991	0.8087	0.6179	0.6366
Mean Li-S Bond length / Å		2.596	2.457	2.326	2.435	2.242
Description of Coordination environment		Triangular prism	Octahedral	Seesaw	Square pyramidal	Seesaw

The lowest energy site (site (a)) calculated was the triangular prismatic site which was identified independently from the neutron refinement. This site has a calculated mean Li-S bond length of ~ 2.6 Å. Typical Li-S distances seen for 6-coordinate Li sites in intercalates such as $Li_{0.63}NbS_2$, and $LiIrS_2$ have been reported to be 2.55 Å and 2.67 Å, respectively.[169,170]

Therefore, the calculated bond distances are in line with previous reports. Note that the calculated energies using a composition similar to that deduced from experiment avoid close Li-Li contacts. If the site in Figure 4.11(a) were to be fully occupied, adjacent Li ions would be in very close proximity to each other (~ 1.8 Å), which would be electrostatically unfavourable.

The second lowest energy site (site (b)) calculated is an octahedral environment. The octahedra share a face with the $Nb(1)S_6$ prisms in the adjacent layers. The average bond length of this site is 2.46 Å, which is more in line with typical Li-S distances seen for Li_2S consisting of tetrahedral Li environments with bond lengths of 2.48 Å.[171] Site (c) can be viewed as a seesaw-like environment with smaller-than-expected Li-S distances of ~ 2.33 Å. The shorter bond lengths and the strained geometry increases the energy of this site. Although site (d) is a square-based pyramid site with a reasonable mean bond length, the distance of Li to the linkage Pd(2) is only 1.9 Å. The proximity of the two positive charge centres causes repulsion; hence the energy is much higher. Finally, site (e) is also a see-saw-like coordination with smaller bond lengths of 2.24 Å and proximity to Pd(2) of ~ 2.8 Å; the combination of these factors makes this site the highest in energy.

4.2.3.4 Lithium Site

Occupancy of the triangular prismatic Li site, shown in Figure 4.11(a), is evident from the neutron refinement and is corroborated by the computation. This is consistent with the observation of a single NMR resonance. Before intercalation, the empty triangular prismatic site is distorted with the prism being distorted such that the angles between the rectangular face, approximately perpendicular to the *a* axis, and the triangular faces deviate by ±14.1(3)° from the undistorted 90°. After intercalation, the layers undergo a relative motion which involves a rotation of the $Pd(1)S_4$ square planar units about a direction parallel to the *b* axis

so that the triangular prisms become less distorted with the interfacial angle deviating by only ±3.2(3)° and ±1.0(5)° from the ideal 90° in the X-ray and neutron models respectively.

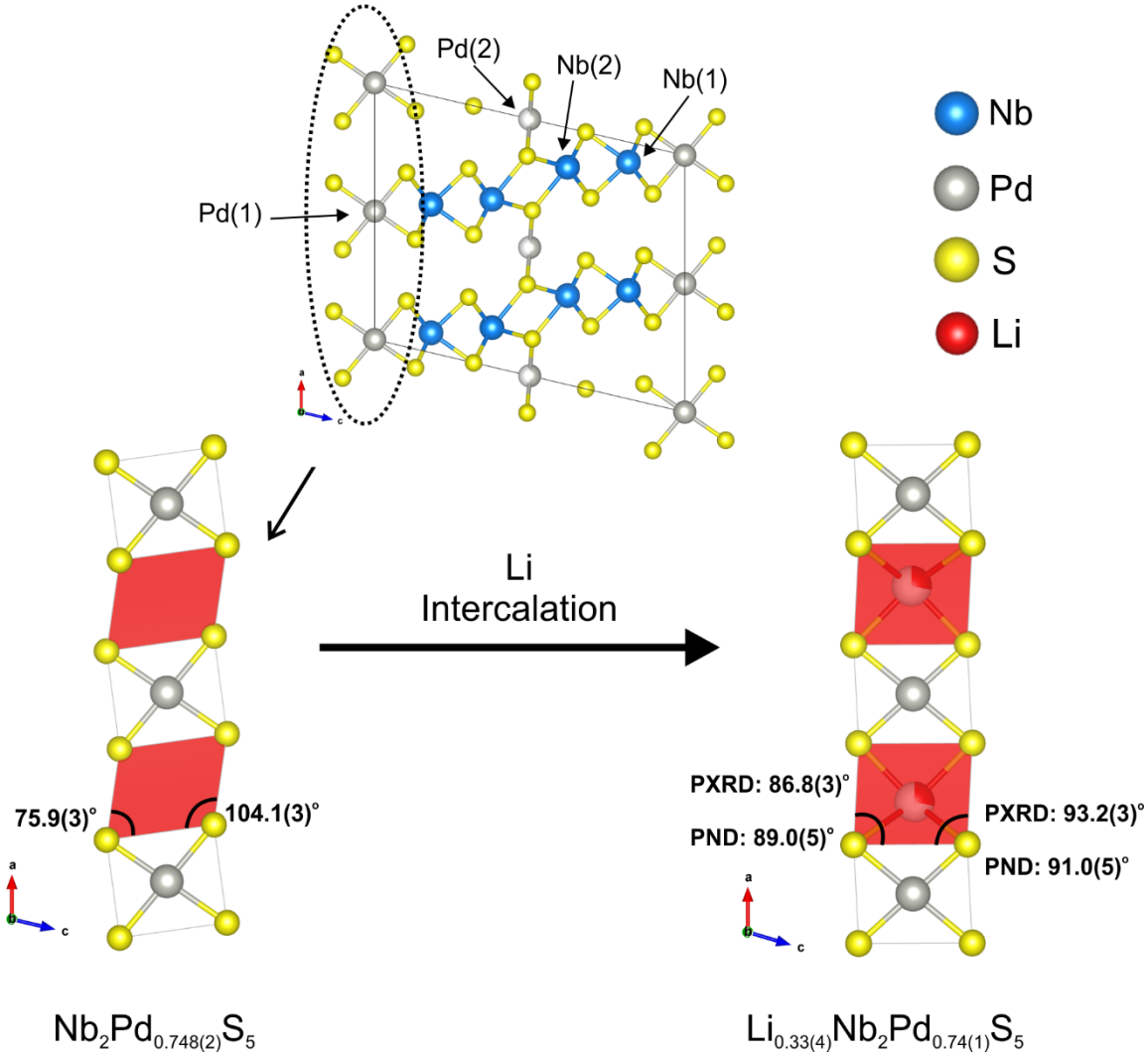


Figure 4.12: Schematic of the Li site before and after intercalation showing the rotation of the $Pd(1)S_4$ units leading to the triangular prism becoming less distorted after the Li is intercalated.

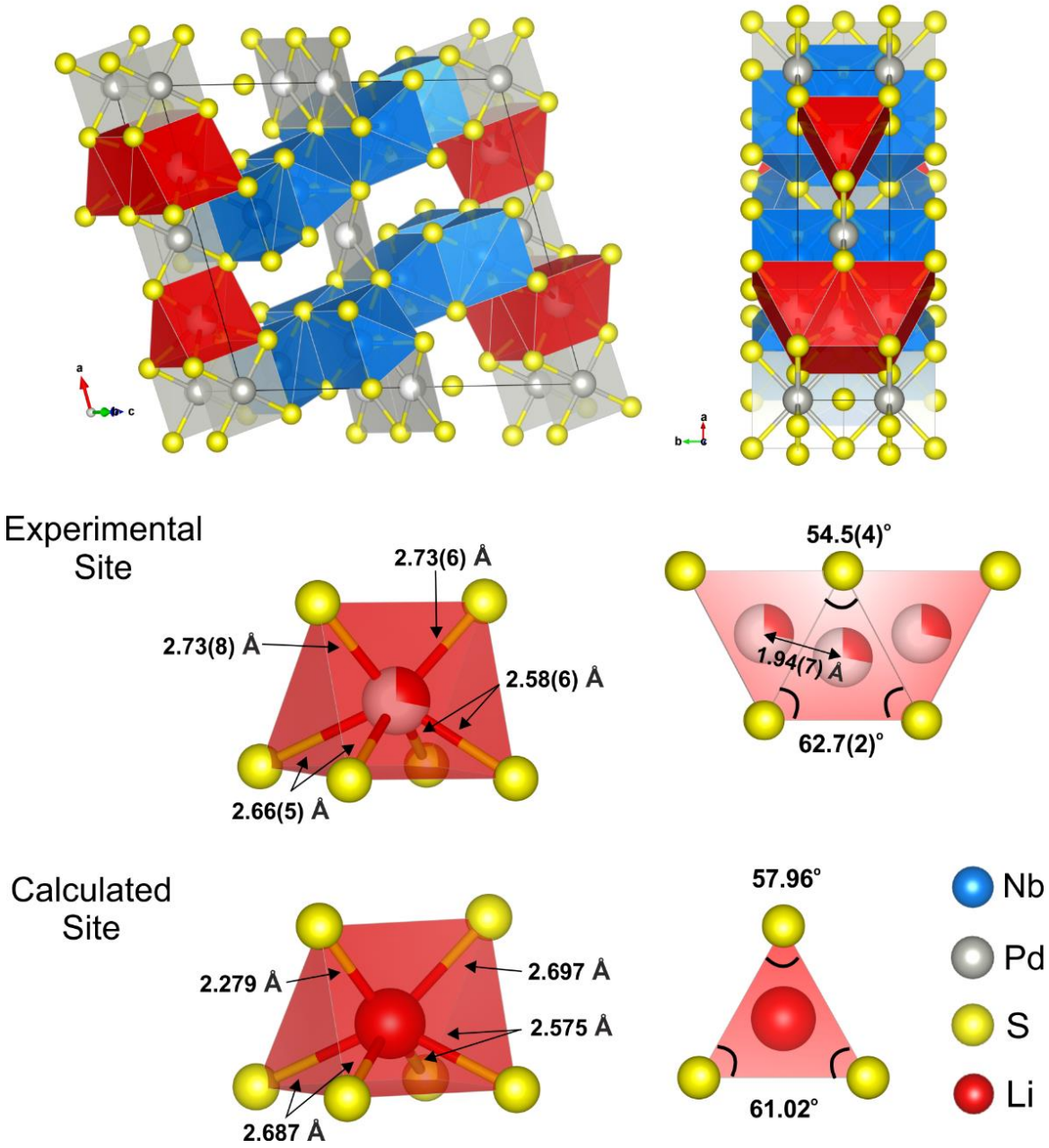


Figure 4.13: Schematic of the triangular prismatic Li site obtained experimentally from the refinement of neutron diffraction data and obtained theoretically from DFT calculations.

A closer examination of the Li site is shown in Figure 4.13; the Li coordination is distorted within the prism with Li-S bond lengths ranging from 2.58(6) Å to 2.73(8) Å giving a mean bond length of 2.66(3) Å. Although this is slightly larger than typical Li-S distances reported (*e.g.* 2.55 Å for $Li_{0.63}NbS_2$),[169] it is in line with that reported for $LiIrS_2$ (2.67 Å).[170] A bond valence sum (BVS) calculated for Li resulted in a value of 0.88(8), in line with the oxidation

state of Li^+ being +1 (see Appendix I for BVS calculations). The triangular prisms are stacked face-sharing in the *b*-direction, which can explain the off-centre position of Li and the larger uncertainty, as Li can be very mobile between triangular prism sites. This may be the reason for the broadness of the NMR resonance. The stacking of the prisms results in adjacent Li sites being in close proximity to one another with Li-Li distances of 1.94(7) Å. Therefore, while the occupation of this site is favoured over the occupation of other sites in the calculations, full occupancy may be difficult to obtain experimentally due to the Li-Li repulsions, which is consistent with the sub-stoichiometric amount of Li needed in the synthesis to avoid the formation of impurity phases and the 0.33(4) occupancy obtained from the neutron refinement is also reasonable to minimise repulsion.

4.2.3.5 Deintercalation

Deintercalation of the intercalated Li was achieved by reacting with an excess of I_2 in an MeCN solution. The deintercalated phase has similar lattice parameters to the original parent compound. Still, the unit cell volume is approximately 0.5 % larger than the original parent compound (compared to ~ 2.2 % in the intercalated phase), perhaps suggesting there remains some Li present which is not deintercalated. Assuming volume is linear with composition, this would be equivalent to ~ 0.07 Li per formula unit. The presence of broader peaks in the diffraction pattern suggests that the crystallinity of the compound is reduced compared to the starting parent material. For example, for the main 200 Bragg reflection, the FWHM increases by 150 % compared to the original $Nb_2Pd_{0.74(1)}S_5$ phase (for comparison, the FWHM increased by 25 % upon intercalation). It is possible that there may be regions that are Li-rich and that the broader peaks could suggest a range of lattice parameters. Repeated treatment with iodine was found to have no effect on the cell parameters.

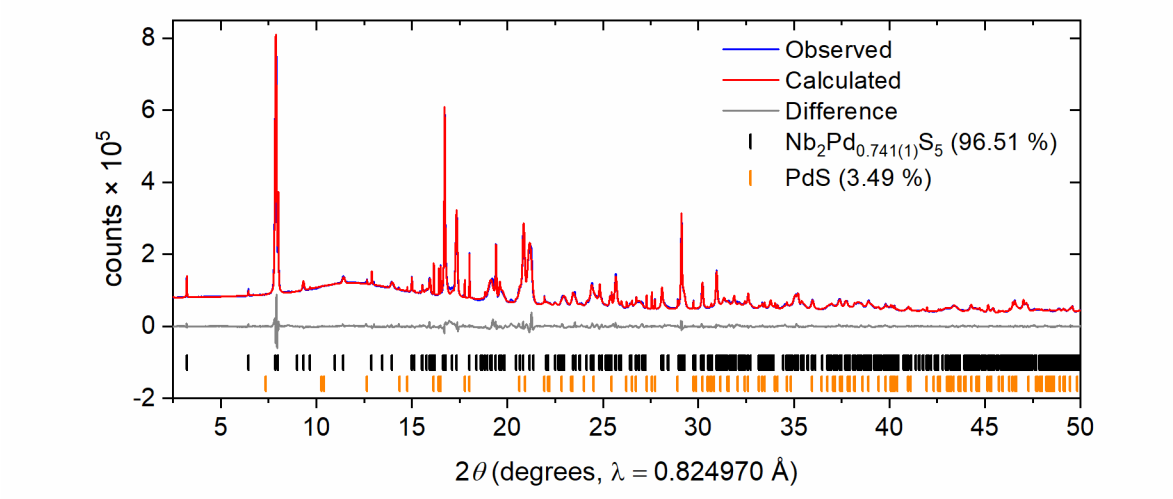


Figure 4.14: Rietveld refinement against I11 (PSD) PXRD pattern of deintercalated $Li_{0.33(4)}Nb_2Pd_{0.74(1)}S_5$ back to $Nb_2Pd_{0.74(1)}S_5$ (ME177). R_{wp}: 3.14 %.

4.2.4 Magnetometry

Li intercalation causes suppression in the superconductivity with no observable superconducting transition evident down to 2 K. Superconductivity is observed again upon deintercalation back to the original parent phase. However, it is only partially restored, consistent with the observation that the original lattice parameters are not fully recovered. The onset transition temperature is lower (T_c ~ 5.5 K), and the superconducting volume fraction is much reduced (~ 7 % compared to 80 % in the original host material prior to lithiation). This could be potentially due to a trace amount of Li still in the phase. From the diffraction pattern of the deintercalated phase, the broader peaks could suggest regions that still contain Li and would reduce the superconducting volume fraction.

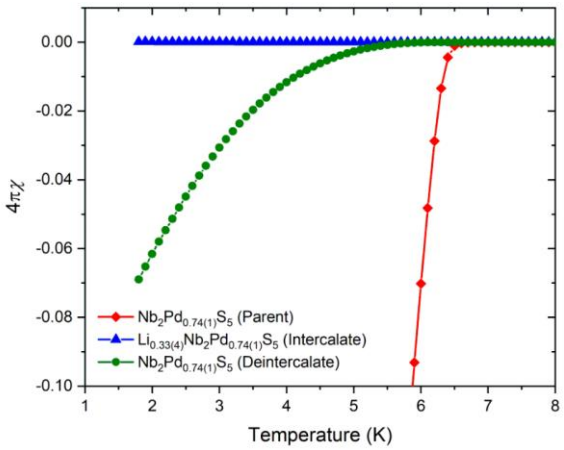


Figure 4.15: Magnetic susceptibility against temperature for zero-field cooled measurements at a field of 10 Oe for parent $Nb_2Pd_{0.74(1)}S_5$, the intercalate and deintercalated phases.

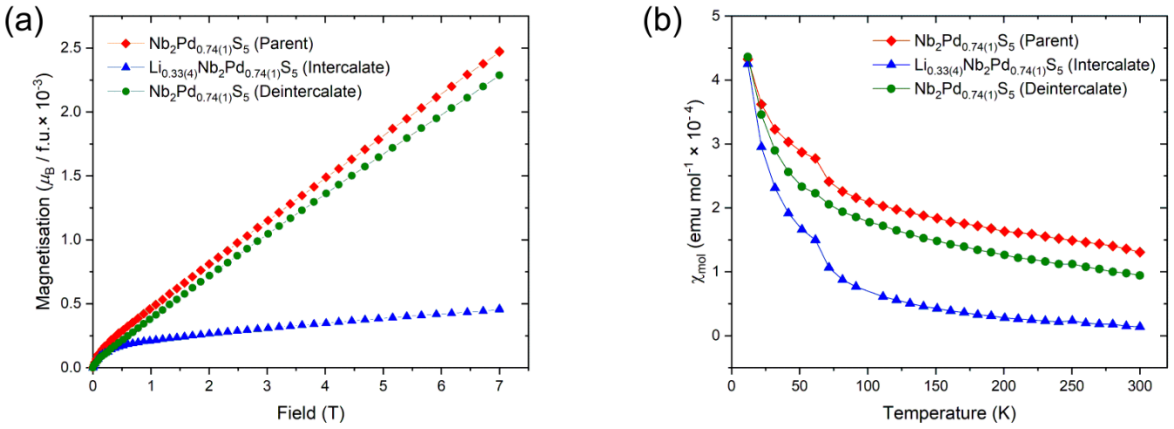


Figure 4.16: (a) Magnetisation against field (at 300 K) and (c) Molar susceptibility (χ_{mol}) against temperature of parent $Nb_2Pd_{0.74(1)}S_5$, the intercalate and deintercalated phase. Molar susceptibility was measured at 3 T and 4 T with the difference taken to eliminate ferromagnetic impurities evident at a low field in (a).

The parent $Nb_2Pd_{0.74(1)}S_5$ compound is paramagnetic with a room-temperature molar susceptibility (χ_{mol}) of $1.865(3)\times10^{-4}$ emu mol^{-1}. Variable temperature measurements (measured at 3 T and 4 T with the difference taken between them to eliminate ferromagnetic impurities) showed that the susceptibility does not obey the Curie-Weiss law. The curves could instead be fitted by a temperature-independent contribution (arising from Pauli paramagnetism and core diamagnetism) and a small Curie-Weiss-type contribution. The susceptibility plot can be fitted to the equation:

$$\chi = \chi_0 + \frac{C}{T - \theta} \qquad \text{Equation 4.1}$$

Where χ_0 is the temperature-independent susceptibility and $\frac{C}{T - \theta}$ is the Curie-Weiss contribution arising from impurity or localised spin states. χ_0 consists of a Pauli paramagnetic contribution and a second temperature-independent component, χ_D, arising from the diamagnetism of the core electrons. For $Nb_2Pd_{0.74(1)}S_5$, χ_D is calculated to be approximately $-1.865(3)\times10^{-4}$ emu mol^{-1} by summing the individual diamagnetic components of each ion with the values obtained from Bain *et al.*[159] Subtracting χ_D from χ_0 gives the Pauli paramagnetic susceptibility χ_P. The χ_P values are given in Table 4.6.

Upon intercalation, χ_{mol} decreases to $2.03(2)\times10^{-5}$ emu mol^{-1}, a reduction by an order of magnitude. χ_P decreases from $2.75(4)\times10^{-4}$ to $1.60(3)\times10^{-4}$, a reduction of approximately 40 %. This, therefore, shows that the density of states at the Fermi level, which is proportional to the Pauli susceptibility, is reduced. This is consistent with the calculations, which show that the density of states decreases just above E_F. This may also explain the suppression of the superconductivity since T_c increases with increasing density of states at E_F in the BCS theory. Shen *et al.* reported on the doping of $Nb_2Pd_{0.76}S_5$ with Ag and Ir and concluded that doping with Ir (hole doping) increases T_c with a maximum at 40 % doping and then is suppressed with increasing Ir content.[164] Conversely, doping with Ag (electron doping) decreases T_c with $T_c < 2$ K at 20 % Ag doping and is completely suppressed with 40 % doping. This would appear consistent with navigating the peak in the DOS found in the calculations (Figure 4.5(a)) and in previous reports.[167] A phase diagram showed a superconducting dome in which Shen *et al*. drew similarities to that seen for the cuprate and iron pnictide superconductors.[106,172] Li intercalation mimics Ag doping, in which the system is injected with electrons. A Li content of 0.33(4) would therefore be analogous to 30-40 % Ag doping, resulting in full suppression of superconductivity.

Deintercalation is shown to increase the χ_{mol} and χ_P back to values similar to the initial host material with values of $1.775(9)\times10^{-4}$ emu mol^{-1} and $2.50(4)\times10^{-4}$ emu mol^{-1}, respectively. χ_P is ~ 10 % smaller for the deintercalated phase, corresponding to a reduction in the density of states at the Fermi level and is consistent with the partial restoration of the superconductivity at lower T_c and volume fraction, as seen in Figure 4.15. Assuming χ_P follows a linear trend with composition, a χ_P of $2.50(4)\times10^{-4}$ emu mol^{-1} would correspond to a Li content of ~ 0.07, consistent with the unit cell volume changes. A Li content of ~ 0.07 can be approximated to 10 % Ag doping reported by Shen *et al*., in which they report a T_c of ~ 4 K. Therefore, all the experimental results are consistent with one another.

The sample intercalated using 2 molar equivalents of *n*-BuLi was measured to assess whether adding additional Li navigates E_F to the adjacent peak in the DOS (Figure 4.5) with higher density of states. However, no superconducting transition was observed. Susceptibility vs temperature measurements gave a χ_0 value of $-3.4(3)\times10^{-5}$ emu mol^{-1}, resulting in a χ_P value of ~ 1.5×10^{-5} emu mol^{-1}, lower in value than $Li_{0.33(4)}Nb_2Pd_{0.74(1)}S_5$ and suggesting that E_F still lies on the negative gradient of the peak.

Table 4.6: Susceptibility values of $Nb_2Pd_{0.74(1)}S_5$ host material and the intercalated and deintercalated phases. χ_D values obtained from Bain *et al.*[159]

	$Nb_2Pd_{0.74(1)}S_5$	**$Li_{0.33(4)}Nb_2Pd_{0.74(1)}S_5$**	**$Nb_2Pd_{0.74(1)}S_5$**
	Parent	Intercalate	Deintercalate
χ_{mol} / emu mol^{-1} (at 300 K)	$1.865(3)\times10^{-4}$	$2.03(2)\times10^{-5}$	$1.775(9)\times10^{-4}$
χ_0 / emu mol^{-1}	$8.8(4)\times10^{-5}$	$-2.7(3)\times10^{-5}$	$6.3(4)\times10^{-5}$
χ_D / emu mol^{-1}	$-1.865(3)\times10^{-4}$	$-1.868(3)\times10^{-4}$	$-1.865(3)\times10^{-4}$
χ_P / emu mol^{-1}	$2.75(4)\times10^{-4}$	$1.60(3)\times10^{-4}$	$2.50(4)\times10^{-4}$

4.2.5 Electrochemical Intercalation

$Nb_2Pd_{0.74(1)}S_5$ was intercalated with Li electrochemically for comparison with the chemically lithiated material, allowing more control on the extent of the intercalation and attempting to achieve a higher Li content without forming side phases. The potential vs specific capacity graph below in Figure 4.17(a) initially shows a continuous change in potential, characteristic of a single phase continuously changing in composition and its chemical potential. However, a step in the discharge curve is seen around 25-30 mAh/g, indicating new phase formation. The parent compound was discharged to three distinct points: 12 mAh/g, 25 mAh/g and 50 mAh/g, corresponding to theoretical Li contents (*x*(Li)) of 0.19, 0.4 and 0.79, respectively. Here, a theoretical Li content of 1 would be achieved when discharging to 63 mAh/g. The Li content of 0.33(4) obtained chemically from the PND refinement is analogous to a specific capacity of 18.3-23.3 mAh/g (indicated in Figure 4.17(a)), corresponding to the region prior to the step in the discharge curve.

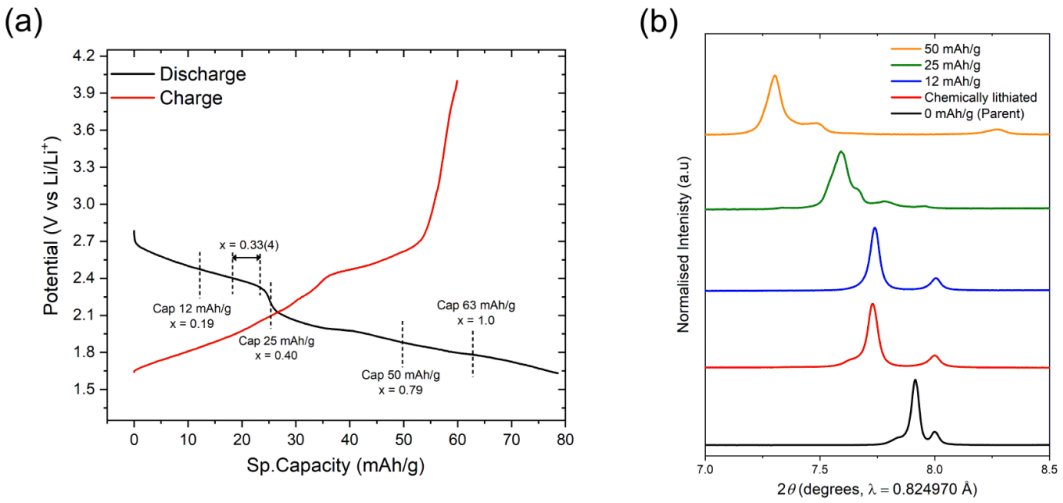


Figure 4.17: (a) Potential against specific capacity plot with specific capacities of 12, 25 and 50 and 63 mAh/g indicated corresponding to a theoretical Li content of 0.19, 0.4, 0.79 and 1, respectively. The Li content of 0.33(4) obtained from refinement is shown as a reference. (b) PXRD pattern of the main $20\bar{1}$ and 200 Bragg reflection with varying starting Li stoichiometries.

The three intercalated samples were measured on the I11 beamline. Figure 4.17(b) shows that the $20\bar{1}$ Bragg reflection moves to higher *d*-spacing with greater degree of intercalation as expected. The sample discharged to 12 mAh/g produced a single crystalline phase with structural parameters similar to those of the chemically intercalated phase with a difference in the unit cell volume of only ~ 0.1 %.

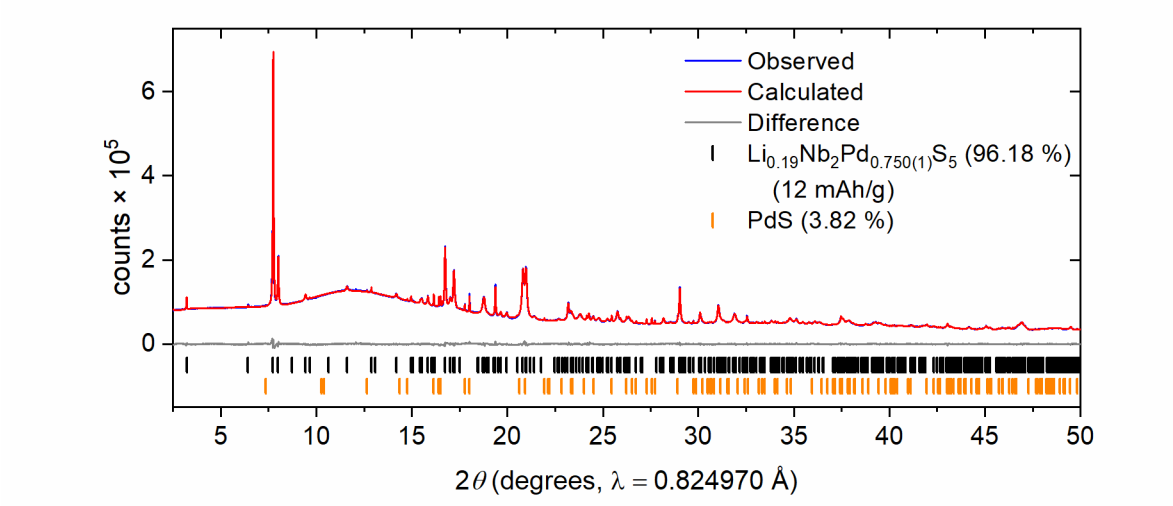


Figure 4.18: Rietveld refinement against I11 (PSD) PXRD pattern of the electrochemical intercalate, $Li_{0.19}Nb_2Pd_{0.75(1)}S_5$ (ME178), the sample discharged to 12 mAh/g R_{wp}: 1.23 %.

Table 4.7: Lattice parameters of the chemical intercalate, and the electrochemical intercalates discharged to 12 and 25 mAh/g.

	Parent (ME174)	**Intercalate (Li/NH_3) (ME176)**	**Intercalate (Electrochemical 12 mAh/g) (ME178)**	**Intercalate (Electrochemical 25 mAh/g) (ME179)**
***a* / Å**	12.1448(1)	12.3390(5)	12.3266(3)	12.6208(4)
***b* / Å**	3.27971(2)	3.2933(1)	3.29196(6)	3.30577(8)
***c* / Å**	15.0798(1)	15.3447(6)	15.3412(7)	15.2049(4)
Vol / Å^3	585.04(1)	598.03(4)	597.32(3)	611.61(3)
***β* / °**	103.161(9)	106.444(1)	106.360(9)	105.396(1)
		Mean Bond Lengths / Å		
Nb(1)-S	2.469(3)	2.463(3)	2.463(3)	2.461(3)
Nb(2)-S	2.523(3)	2.545(3)	2.530(3)	2.556(4)
Pd(1)-S	2.358(5)	2.373(6)	2.377(4)	2.363(6)
Pd(2)-S	2.403(5)	2.390(6)	2.423(3)	2.470(6)

From the discharge curve in Figure 4.17(a), a step in the curve is seen around 20-30 mAh/g. Examining the diffraction pattern of the intercalated sample discharged to 25 mAh/g (x(Li) = 0.4), at the step in the discharge curve, the compound has expanded significantly but has also undergone phase separation. The pattern can be fit as two intercalated phases, as shown in Figure 4.20.

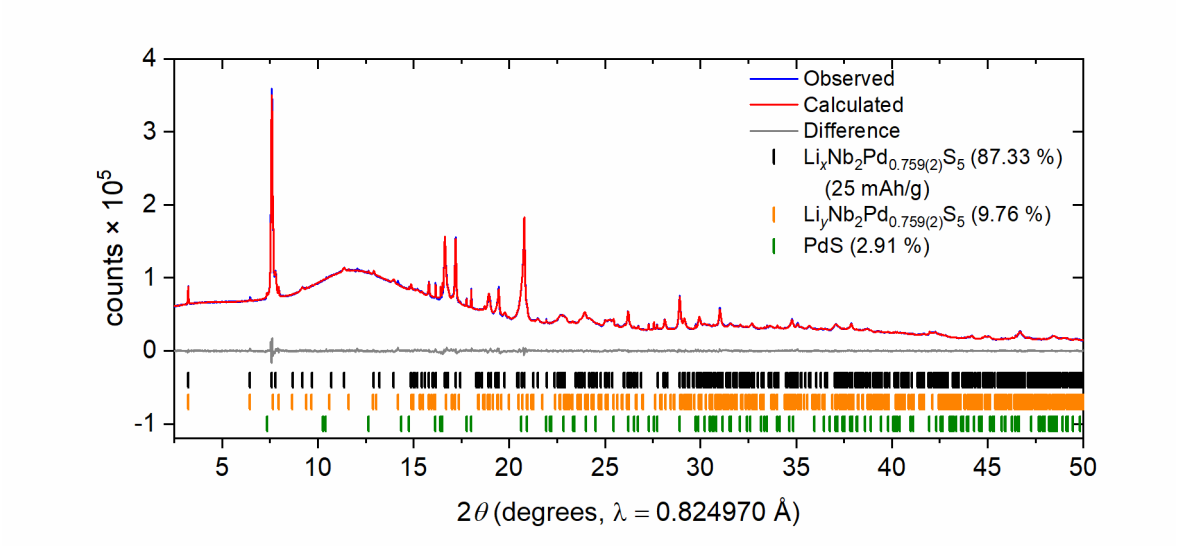


Figure 4.19: Rietveld refinement against I11 (PSD) PXRD pattern of the electrochemical intercalate, $Li_xNb_2Pd_{0.75(1)}S_5$ (ME179), the sample discharged to 25 mAh/g. R_{wp}: 1.00 %.

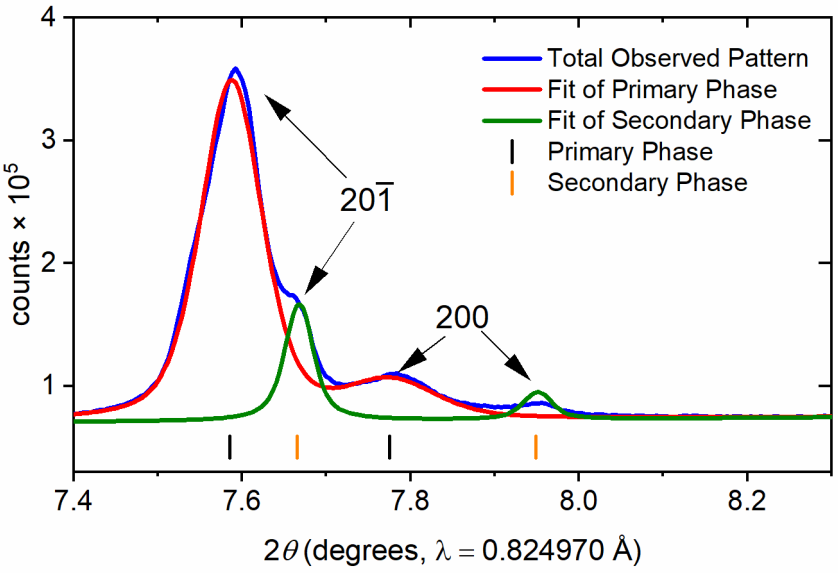


Figure 4.20: The main 20$\bar{1}$ and 200 Bragg reflections from the refinement in Figure 4.19.

The main phase (~ 87 % by mass) has expanded by approximately 0.48 Å, 0.03 Å and 0.13 Å in the *a*, *b* and *c* axes, respectively, compared to the parent with a 2.2° increase in the monoclinic angle. Compared to the intercalate discharged at 12 mAh/g, and the chemical intercalate, the volume has increased by 2.4 %. The main expansion compared to the sample discharged to 12 mAh/g is in the *a*-axis with an ~ 0.27 Å increase which is reflected in the 0.05 Å increase in the Pd(2)-S bond length. The *c*-axis has seen a contraction of ~ 0.14, with the monoclinic angle also reducing by ~ 1°. The smaller secondary intercalated phase has lattice parameters a = 12.4318(5) Å, b = 3.3003(2) Å, c = 15.3627(9) Å and β = 106.780(4)°, therefore this phase is more akin to the sample discharged to 12 mAh/g but with a ~ 1 % volume increase. As stated earlier, due to the proximity of the Li triangular prism sites, they cannot be occupied with high Li content. It is likely that the 0.33(4) Li content obtained from the neutron refinement is the upper limit to the occupancy of the triangular prism site before it becomes energetically unfavourable. This is consistent with x(Li) = 0.33(4) corresponding to the region just before the step in the discharge curve and that using higher starting stoichiometries of Li in the chemical intercalation reactions, as shown in Figure 4.6(b), results in an emerging side phase.

This significant change in the structure at x(Li) = 0.4 suggests extra Li occupying another site. When examining the changes in the triangular prismatic site upon intercalation, it can be seen in Figure 4.21 that at low Li content (x(Li) = 0.19), the site becomes less distorted, similarly to the chemically intercalated compound. However, at higher Li content (x(Li) = 0.4), the site becomes distorted again, indicating that the layers shift relative to one another to perhaps accommodate Li in another site.

From the DFT calculations, the triangular prism site was calculated as the lowest energy for $Li_{0.25}Nb_2PdS_5$; However, the Li site energies can change upon inserting more Li into the

structure, as Li ions can no longer be considered to be independent of another. It is possible that the octahedral site could become more favourable, and therefore the reduction in the monoclinic angle may result from the layers readjusting for Li in the new site. The octahedral sites are edge-sharing along the *b*-axis, with the Li-Li distance between adjacent sites being ~ 3.3 Å (*b*-axis). Therefore, this site can accommodate a higher Li occupancy with minimal electrostatic repulsion. However, neutron diffraction on the electrochemically synthesised phases would be required to explore this further, but this is challenging on account of the volume of sample needed and the inevitable background arising from the additives (binder *etc.*) mixed with the phase for the electrochemical synthesis.

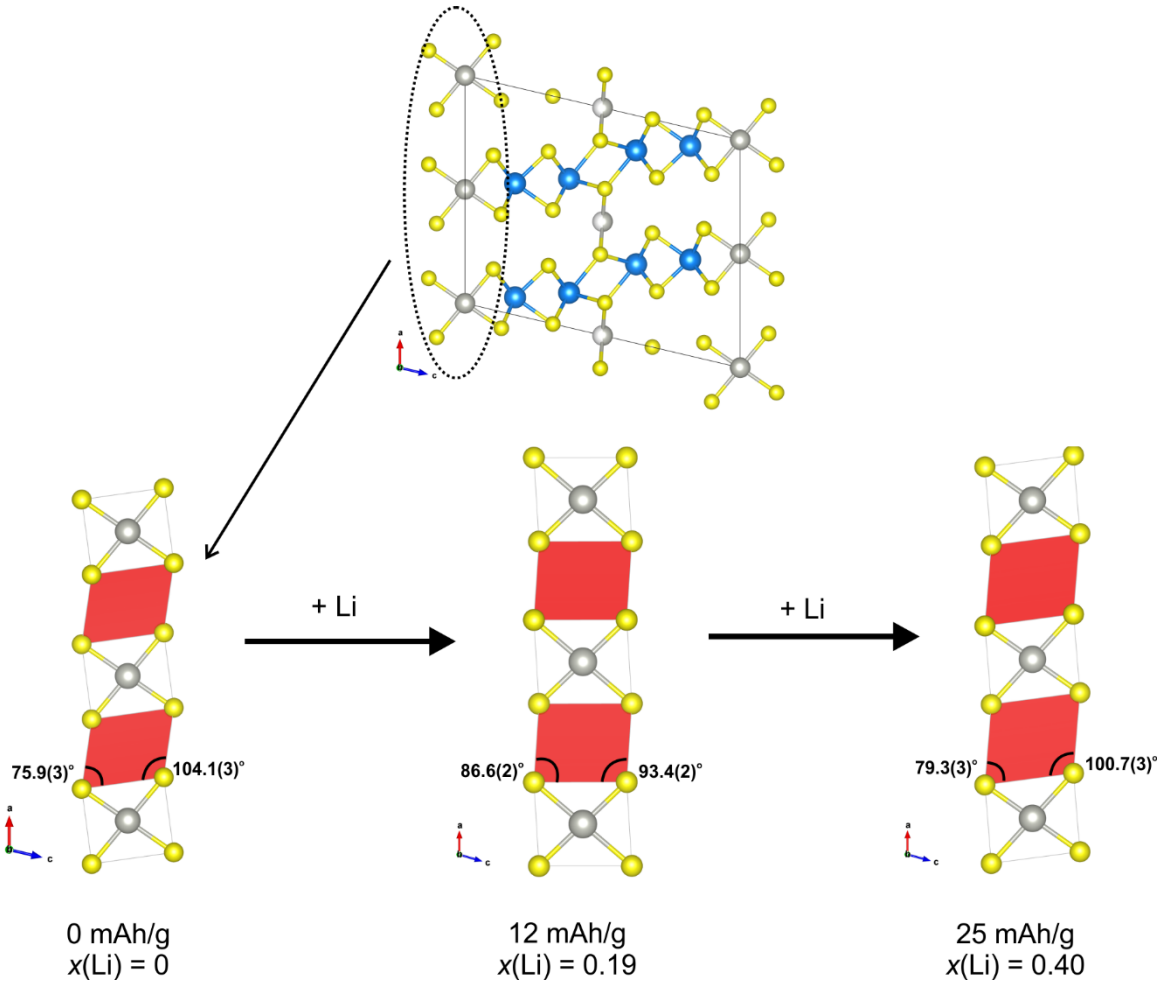


Figure 4.21: Schematic of the Li triangular prism site before and after intercalation showing how at low Li content, the site becomes less distorted, but at higher Li content, the site distorts again, suggesting the layers are shifting to accommodate Li in another site.

Table 4.8: Lattice parameters of the electrochemical intercalates.

	Parent (ME174)	**12 mAh/g *x*(Li) = 0.19 (ME178)**	**25 mAh/g *x*(Li) = 0.4 (ME179)**	**50 mAh/g *x*(Li) = 0.79 (ME180)**
***a* / Å**	12.1448(1)	12.3266(3)	12.6208(4)	13.0426(10)
***b* / Å**	3.27971(2)	3.29196(6)	3.30577(8)	3.3295(1)
***c* / Å**	15.0798(1)	15.3412(7)	15.2049(4)	15.5651(8)
Vol / Å^3	585.04(1)	597.32(3)	611.61(3)	640.05(7)
***β* / °**	103.161(9)	106.360(9)	105.396(1)	108.751(4)

The phase separation remains when discharged to 50 mAh/g (*x*(Li) = 0.79). The main phase was indexed to lattice parameters *a* = 13.042(1) Å, *b* = 3.3295(1) Å, *c* = 15.5651(8) Å and *β* = 108.751(4)°; an even greater increase in the unit cell compared to the parent of approximately 0.89 Å, 0.05 Å and 0.48 Å in the *a*, *b* and *c* axes, respectively, and 5.6° in the monoclinic angle. This expansion is significantly larger than the one seen in the sample discharged to 25 mAh/g (a further volume increase of ~ 4.6 % and an increase of ~ 9.4 % over the original $Nb_2Pd_{0.74(1)}S_5$ host phase). The increase in the unit cell volume follows a linear trend with increasing Li content, as shown in Figure 4.22.

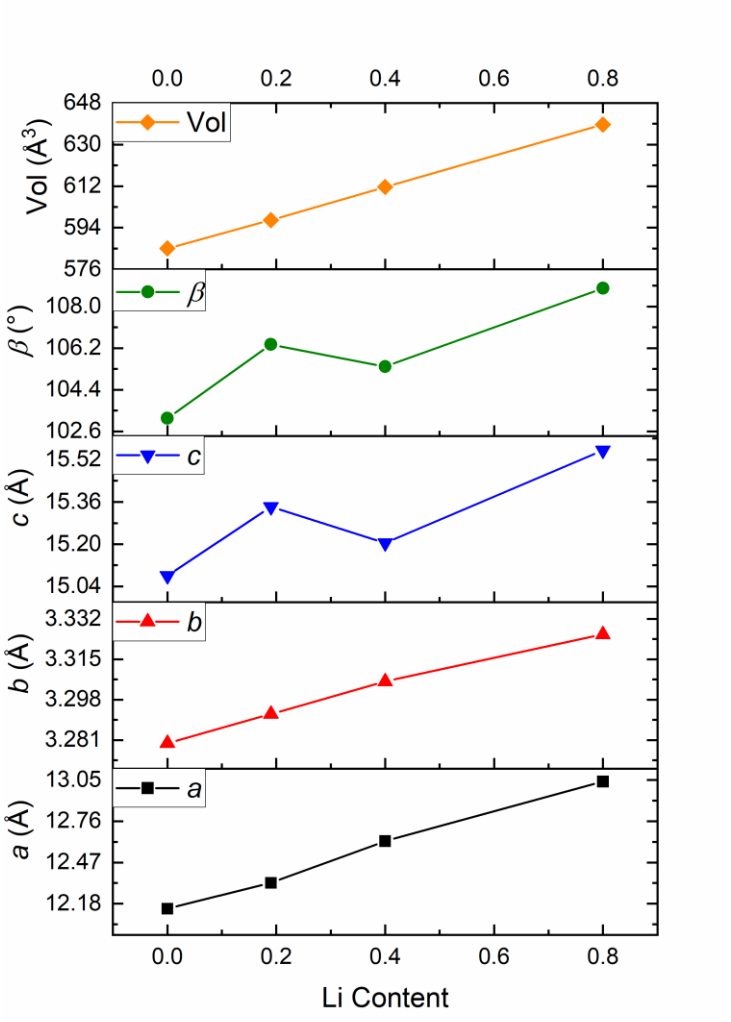


Figure 4.22: Lattice Parameters of the electrochemical intercalates.

The secondary phase was indexed to lattice parameters a = 12.858(1) Å, b = 3.269(1) Å, c = 15.296(3) Å and β = 105.441(4)°, which is more akin to the sample discharged to 25 mAh/g but with a ~ 1.3 % volume increase. The crystallinity is reduced, with the peaks having a lower resolution. Therefore, with the dual-phase nature and the complexity of the unit cell, causing many of the peaks to overlap, it was difficult to carry out a reliable Rietveld refinement on the PXRD pattern. Lattice parameters were obtained from a Pawley refinement with the fit shown in Figure 4.23. Further work is required to get a more definitive picture.

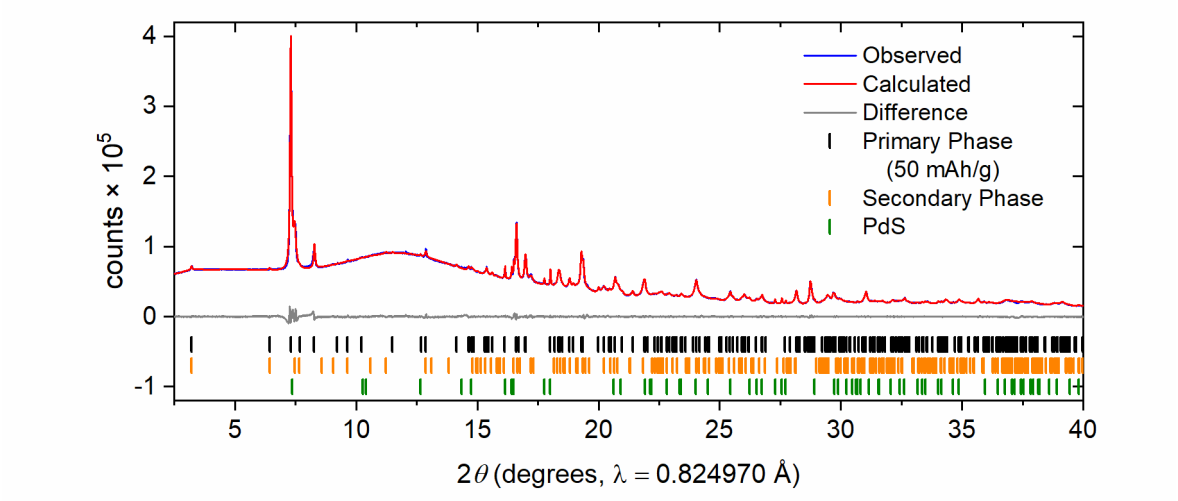


Figure 4.23: Pawley refinement against I11 (PSD) PXRD pattern of the sample discharged to 50 mAh/g (ME180).

The sample discharged to 50 mAh/g can be compared to the intercalation using a 2:1 molar ratio of *n*-BuLi shown in Figure 4.6(a). The PXRD patterns are similar, with the *n*-BuLi intercalant being less crystalline (the sharp peaks at higher angles in the pattern are from the PdS side phase). The chemical intercalate can also be fitted to two phases with the lattice parameters shown in Table 4.9, with the difference in volume between the main phases being < 1 %. This would suggest that at higher Li content, chemical and electrochemical intercalation behave similarly.

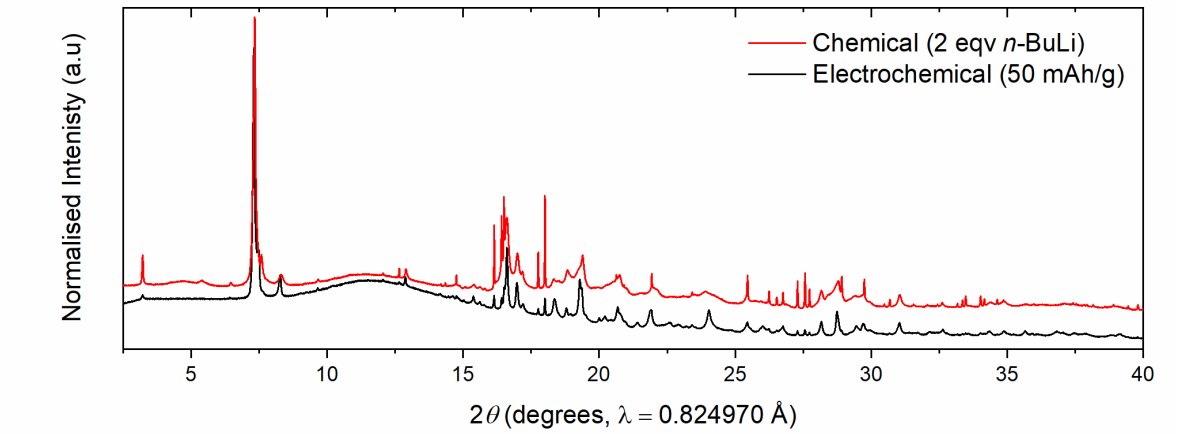


Figure 4.24: Comparison of the I11 (PSD) PXRD patterns of ME180 (50 mAh/g) to ME060 (2 eqv n-BuLi).

Table 4.9: Comparison of the two phases found in ME180 and ME060.

		Electrochemical (50 mAh/g) ME180	**Chemical (2 eqv *n*-BuLi) ME060**
Main Phase	*a* / Å	13.0426(10)	12.9845(6)
	b / Å	3.3295(1)	3.323(1)
	c / Å	15.5651(8)	15.505(2)
	Vol / Å^3	640.05(7)	634.1(2)
	β / °	108.751(4)	108.62(1)
Secondary Phase	*a* / Å	12.858(1)	12.908(2)
	b / Å	3.269(1)	3.285(1)
	c / Å	15.296(3)	15.261(3)
	Vol / Å^3	619.7(2)	624.8(3)
	β / °	105.441(4)	105.09(2)

4.3 $Nb_2Pd_xSe_5$

4.3.1 Synthesis and characterisation of $Nb_2Pd_xSe_5$

Polycrystalline samples of $NbPd_xSe_5$ were also synthesised by a direct combination of elements; Nb powder (Alfa Aesar, 99.99 %), Pd powder (Alfa Aesar, 99.95 %) and Se powder (Alfa Aesar, 99.999 %). A 2:*x*:5 ($0.8 < x < 1$) ratio of Nb:Pd:Se was ground thoroughly before being pelletised and placed in a dry evacuated silica ampoule. The ampoule was heated to 850 °C for 58 hours and quenched in ice/water. Although the compound can be formed without the need for quenching, it was found that quenching leads to slight improvements in sample purity.

Synthesis of parent $Nb_2Pd_xSe_5$ was not trivial. Like the sulfide variant, varying the Pd content affected the purity. In this case, a starting Pd content of $x = 1$ (which refines to $x = 0.88(1)$ in the X-ray Rietveld refinement) resulted in the formation of a more Pd-rich $Nb_2Pd_3Se_8$ side phase at ~ 7 % by mass. Lowering the value of *x* in the starting stoichiometry reduces the formation of the Pd-rich impurity. However, as a consequence, T_c is also reduced, in line

with the report by Khim *et al.*[116] For $Nb_2Pd_{0.88(1)}Se_5$, a T_c of 5 K was observed, whereas for $Nb_2Pd_{0.70(1)}Se_5$ (achieved from a starting Pd content of $x = 0.8$) superconductivity is either suppressed or falls below the 1.8 K limit of the SQUID magnetometer, again in agreement with previous reports.[114]

For polycrystalline powder samples, both superconductivity and sample purity seem to be affected by the composition of the starting material. It is difficult to target the actual stoichiometry as the Pd stoichiometry of the main phase always seems to be lower than the starting composition, and there is a Pd-rich side phase that competes. Using a starting Pd content of $x = 0.95$ was found to be optimal, with a balance of a relatively high T_c (4.4 K) and a low percentage impurity (~ 2 %). The refined Pd(2) site occupancy was 0.652(3), giving an overall Pd content of 0.826(2) (referred to in the text as $Nb_2Pd_{0.82}Se_5$). Structural information is provided in Table 4.10.

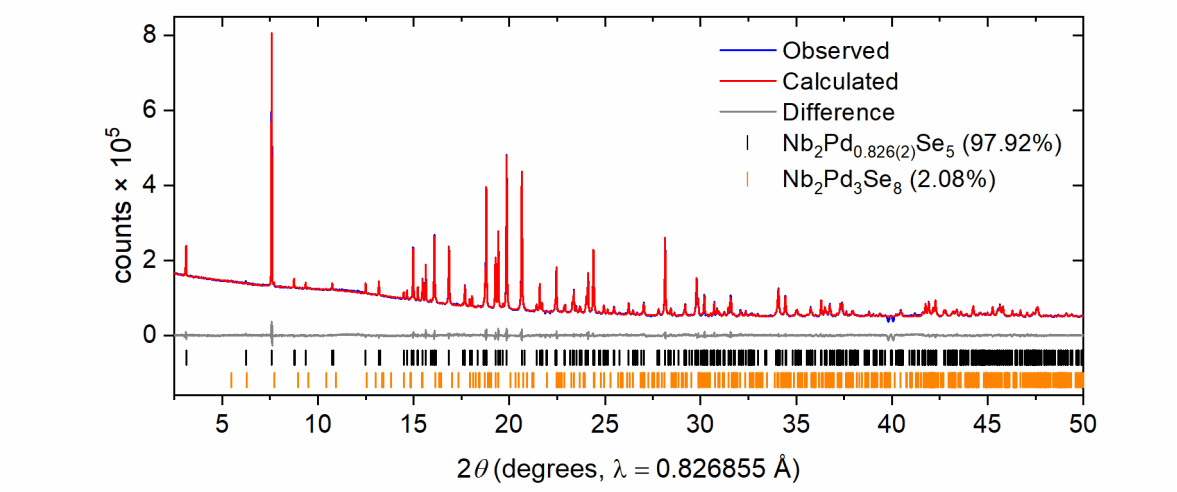


Figure 4.25: Rietveld refinement against I11 (PSD) PXRD pattern of $Nb_2Pd_{0.826(2)}Se_5$ (ME111). R_{wp}: 0.95 %. Taking the impurity into account accounts for a starting Pd content of 0.85, which is 0.1 lower than the actual starting Pd content of 0.95. It is possible that the extra Pd is formed as nanoparticles, not detectable in the diffraction pattern.

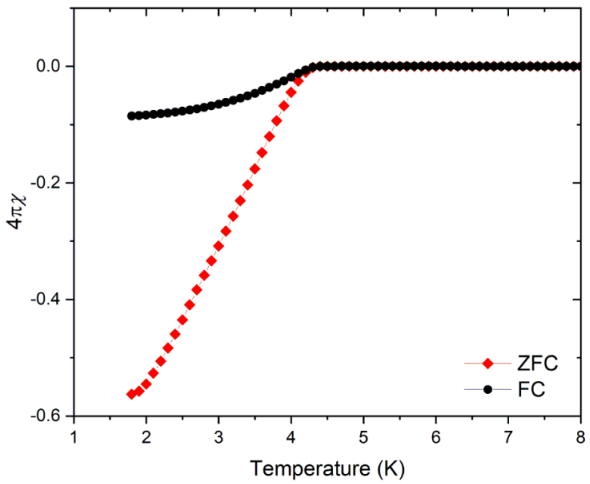


Figure 4.26: Zero-field cooled (red) and field cooled (black) plot of the magnetic susceptibility against temperature measured at 10 Oe showing a T_c of 4.4 K and *SVF* of ~ 58 %.

Table 4.10: Structural parameters of $Nb_2Pd_{0.826(2)}Se_5$.

$Nb_2Pd_{0.826(2)}Se_5$ (ME111)						
Space Group	***a* / Å**	***b* / Å**	***c* / Å**	**Volume / Å^3**	***β* / °**	
C2/m (No. 12)	12.77455(7)	3.39971(1)	15.51532(8)	660.142(6)	101.5569(3)	
***Mean Bond Length* / Å**						
Nb(1)-Se				2.586(1)		
Nb(2)-Se				2.654(1)		
Pd(1)-Se				2.445(2)		
Pd(2)-Se				2.530(2)		
Positional Parameters						
Atom	***x***	***y***	***z***	***Occupancy***	***Wyckoff Symbol***	**U_{iso} / Å^2**
Nb(1)	0.0755(2)	0.5	0.1799(1)	1	4*i*	0.0016(8)
Nb(2)	0.1525(2)	0	0.3761(1)	1	4*i*	0.0072(7)
Pd(1)	0	0	0	1	2*a*	0.0083(9)
Pd(2)	0	0	0.5	0.652(3)	2*c*	0.0015(12)
Se(1)	0.3516(2)	0	0.4913(2)	1	4*i*	0.0016(5)
Se(2)	0.2535(2)	0.5	0.2950(2)	1	4*i*	0.0016(5)
Se(3)	0.1758(2)	0	0.0992(2)	1	4*i*	0.0071(8)
Se(4)	0.4232(2)	0.5	0.1315(2)	1	4*i*	0.0041(8)
Se(5)	0.4991(2)	0	0.3209(2)	1	4*i*	0.0040(8)

SEM imaging on $Nb_2Pd_{0.82}Se_5$ shows a homogenous distribution of the elements with EDX mapping on eight points on the crystallite in Figure 4.27(a), giving an average stoichiometry of $Nb_2Pd_{0.83(1)}S_{4.97(2)}$, in agreement with the Rietveld refinement.

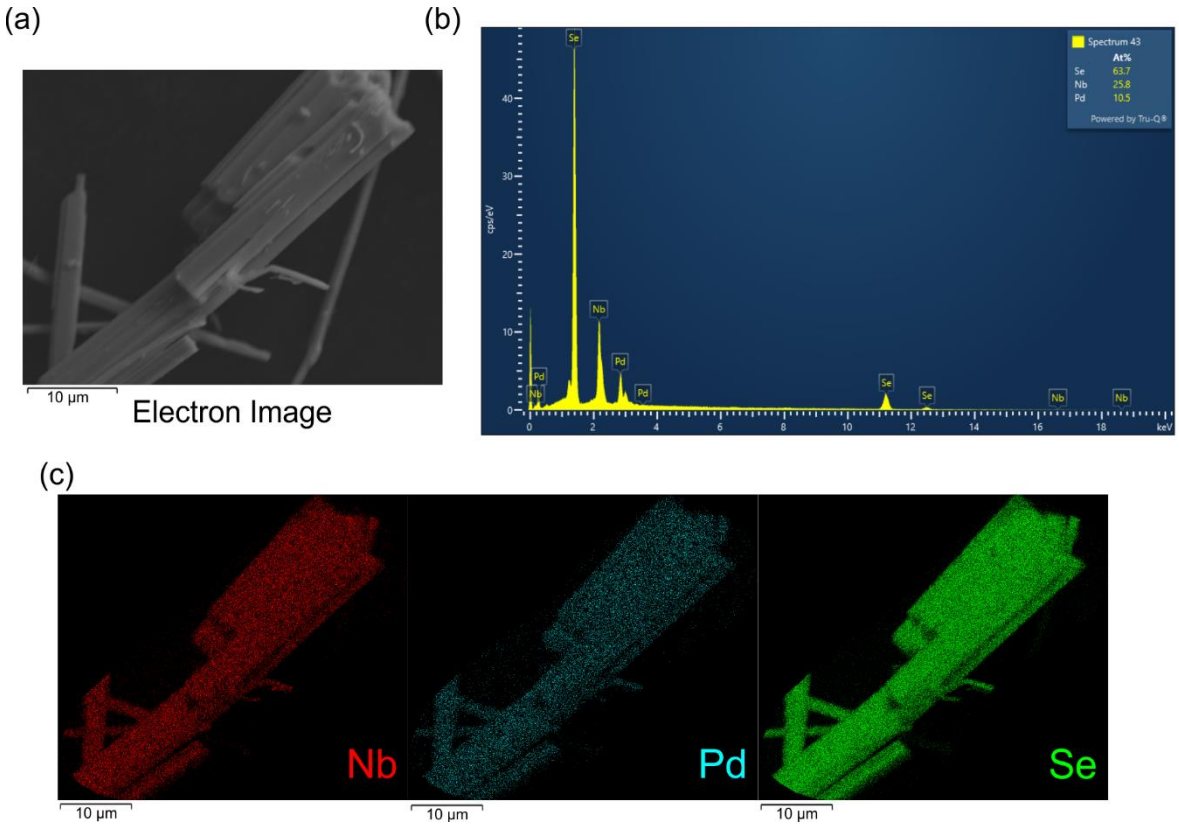


Figure 4.27: (a) SEM image of $Nb_2Pd_{0.82}Se_5$ with (c) showing the homogenous spread of the elements. (b) EDX spectrum gives a stoichiometry of $Nb_2Pd_{0.83(1)}S_{4.97(2)}$.

The band structure and electronic density of states were calculated in a similar manner to Nb_2PdS_5, where it is assumed to be fully stoichiometric. Like Nb_2PdS_5, the DOS shows no gap at the Fermi level (E_F), confirming the metallic nature of the compound as first reported by Keszler *et al.*[49] and is also consistent with previous reports.[167] Similar to Nb_2PdS_5, the valence band (where the Energy < 0) is dominated by strongly hybridised Pd(4*d*) and Se(4*p*) states. Around E_F, it is now mainly consisting of Nb(4*d*) and Se(4*p*) hybridised states which also form the majority of the conduction band. In contrast to Nb_2PdS_5, in which the gradient at E_F is negative, for Nb_2PdSe_5, the gradient is positive. This is in agreement with the DOS

reported by Lohani *et al.*,[167] where both Nb_2PdS_5 and Nb_2PdSe_5 have opposite gradients at the Fermi level.

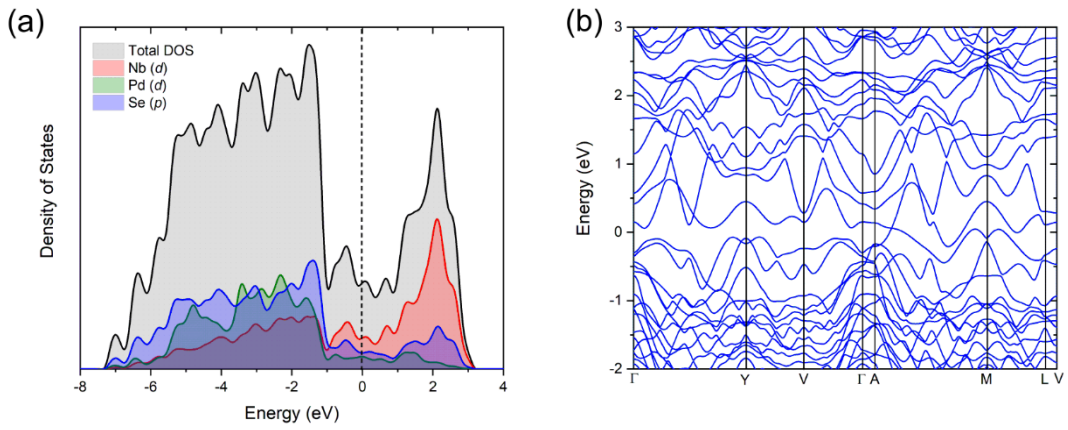


Figure 4.28: (a) Electronic density of states of Nb_2PdSe_5 with (b) a close-up image of the region around the Fermi level. (c) Electronic band structure of Nb_2PdSe_5 shows the metallic nature.

Neu *et al.* conducted a study on single crystals varying the Pd content from $0.68 < x < 0.95$.[162] A Pd(2) occupancy of 0.368(7) (corresponding to $x = 0.68$ in $Nb_2Pd_xSe_5$) was concluded to be the minimum Pd(2) occupancy required to stabilise the structure. They found that full occupancy of the Pd(2) site could not be reached, in line with the findings here. From resistivity measurements, superconductivity was reported to start from Pd(2) = 0.586 ($x \sim 0.79$) with a maximum T_c of 4.5 K at Pd(2) contents between approximately 0.62-0.7 ($0.81 < x < 0.85$). Interestingly they report lower T_c values at higher Pd content with $T_c \sim 3$ K at Pd(2) ~ 0.75 ($x \sim 0.88$). From their single crystal diffraction study,[162] the authors observed only about a 1 % change in lattice parameters with no clear trend in the unit cell volume seen, commenting that the Pd(2) occupancy has no significant effect on the structure (see Appendix III for a plot of their lattice parameters).

Here, the changes in lattice parameters were investigated by measuring five samples with refined Pd contents, *x*, of 0.70(1), 0.73(1), 0.78(1), 0.82(1) and 0.88(1). As shown in Figure 4.29, it is apparent that the unit cell volume increases almost linearly with Pd occupancy.

Synchrotron PXRD would typically give lattice parameters at a much greater precision compared to the single-crystal XRD of Neu *et al.*[162] However, a larger sample size would be required to conclude if a clear trend is seen. The *a* lattice parameter actually decreases initially before increasing again. However, the changes in the *a* parameter are countered by the changes in the *c* lattice parameter such that overall the volume is seen to increase with Pd occupancy with a ~ 0.5 % increase in volume going from $x = 0.70(1)$ to 0.88(1).

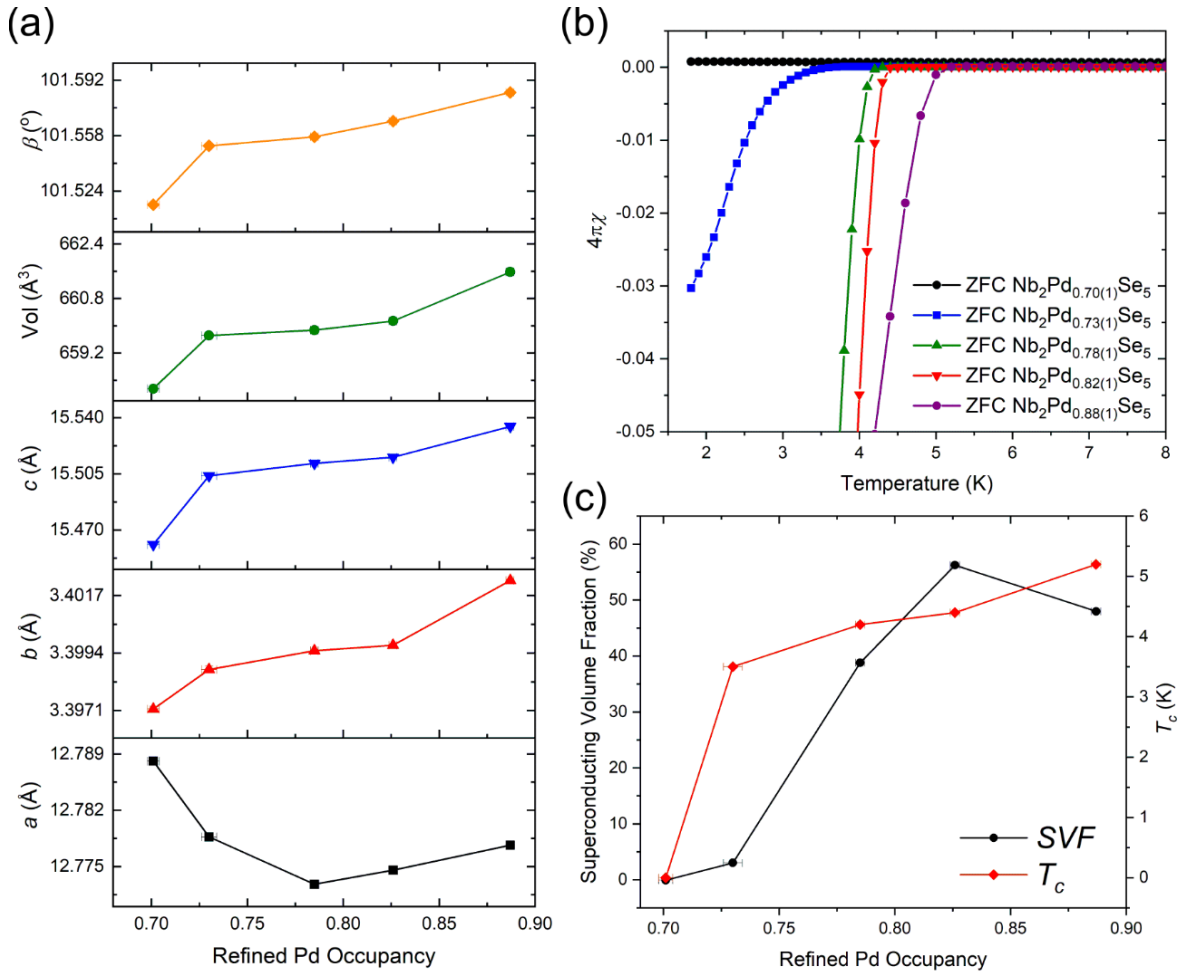


Figure 4.29: (a) Plot of lattice parameters with varying refined Pd occupancy, (b) *SVF* against temperature for zero-field cooled measurements at a field of 10 Oe and (c) variation of T_c and *SVF* with varying refined Pd occupancy

T_c is also observed to increase with Pd occupancy with a maximum T_c of 5 K for $x = 0.88(1)$. A superconducting transition at 3.5 K was observed at $x = 0.73(1)$, albeit at a much-reduced volume fraction (3 %). This Pd content is lower than the report by Neu *et al.*,[162] where they

commented that superconductivity is first observed at $x \sim 0.79$. The positive correlation in T_c with Pd content is consistent with navigating the positive gradient of the density of the state around the Fermi level (Figure 4.30). As mentioned previously, according to BCS theory, T_c increases with increasing density of states at E_F. From the calculated DOS for Nb_2PdSe_5, reducing the Pd content in the system results in the E_F shifting to lower energies, corresponding to lower density of states and, therefore, a reduction in superconductivity.

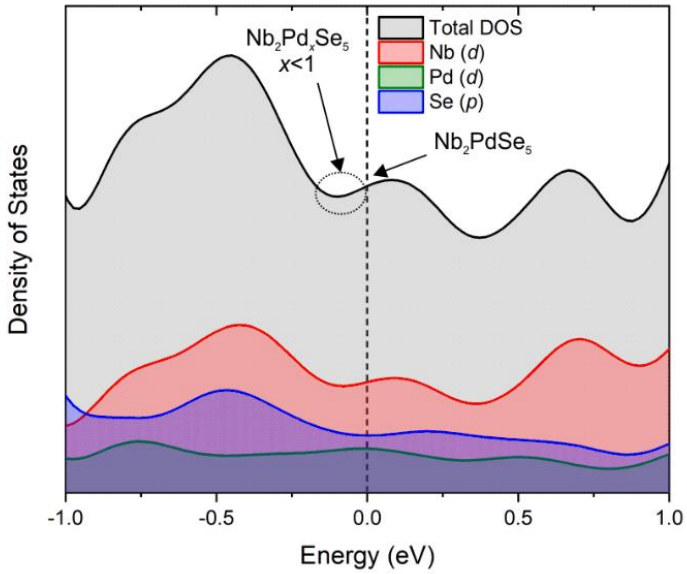


Figure 4.30: Closeup of the DOS of Nb_2PdSe_5. The dotted line shows the E_F for fully occupied Nb_2PdSe_5. The circle shows the lower energy region the E_F is likely to shift to with decreasing Pd content as the electron count decreases.

4.3.2 Chemical Intercalation

$Nb_2Pd_xSe_5$ was intercalated with Li in a similar way to $Nb_2Pd_xS_5$, using the three methods mentioned previously to compare and determine the most suitable reagent to produce the most suitable bulk sample for neutron diffraction. When intercalating using *n*-BuLi as the lithiating reagent, it was found that only a small amount of the reagent (~ 0.4 equivalents) was needed to consume the parent compound.

However, with this method, the crystallinity significantly decreases. It was found, as shown in Figure 4.31(a), that increasing the stoichiometry of the reagent leads to a formation of a low angle shoulder peak on the $20\bar{1}$ reflection Bragg reflection, which grows into a prominent peak when using a 1:1 molar ratio (*i.e.* target stoichiometry of $LiNb_2Pd_{0.82}Se_5$). This peak corresponds to a *d*-spacing of 6.71 Å, which would match the 002 Bragg reflection of an expanded (*i.e.* intercalated) $NbSe_2$ phase with c = 13.23 Å and 13.38 Å reported for $Li_{0.33}NbSe_2$ and $Li_{0.50}NbSe_2$ respectively.[173] It is possible that excess intercalation causes the compound to begin to decompose. Lattice parameters against *n*-BuLi content show an almost linear increase in volume. The *c* parameter contracts at higher stoichiometries, but this is countered by the increase in the *a* parameter.

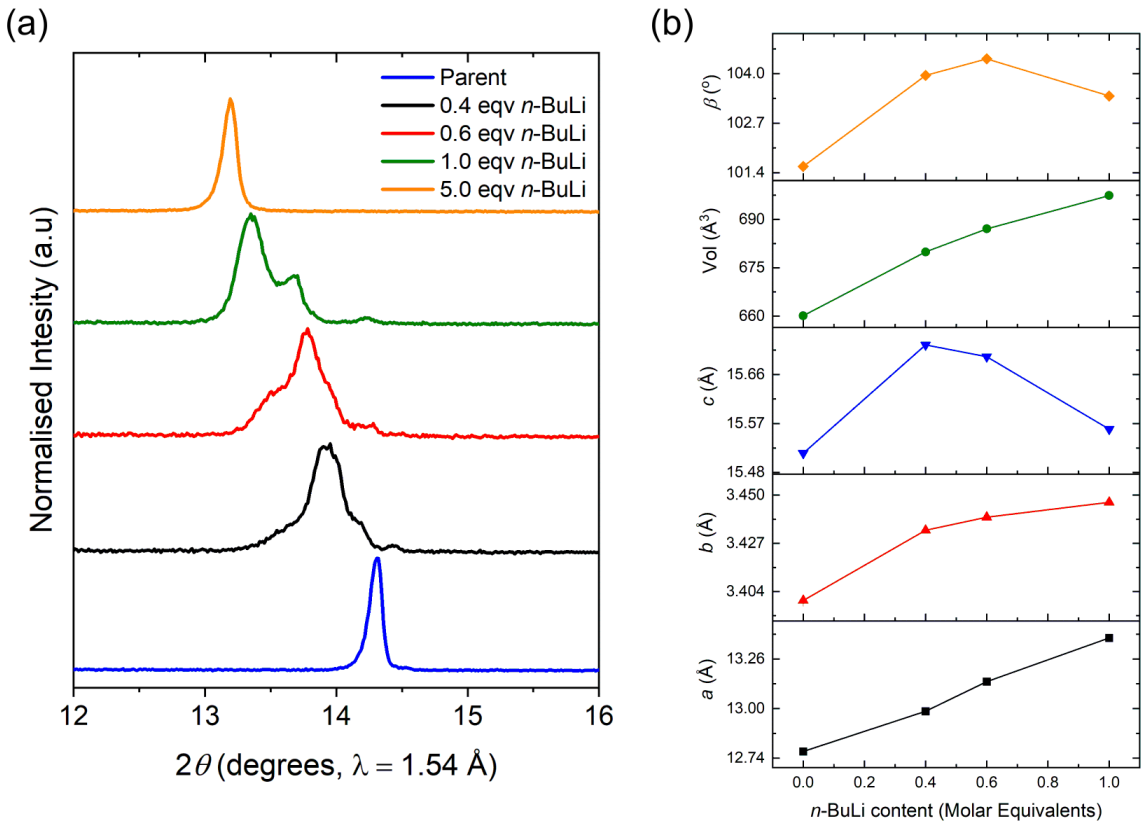


Figure 4.31: (a) Comparison of the main $20\bar{1}$ Bragg reflection and (b) lattice parameters with varying the *n*-BuLi content.

When $Nb_2Pd_xSe_5$ is treated with an excess of *n*-BuLi (5:1 molar ratio), the crystallinity is significantly reduced such that it was difficult to carry out a refinement and establish a structural model. It is unclear whether the main peak at $2\theta = 7°$ corresponds to the decomposition product or some highly intercalated phase. However, when treated with excess iodine, it can be seen from Figure 4.32 that the intercalated phase is recoverable, and the deintercalated cell was found to have a volume ~ 2 % larger than the parent cell. The peak at $2\theta = 7°$ is still evident, although now much broader. If the peak is from the decomposition phase, then the intercalated phase in Figure 4.32(a) is very poorly crystalline and iodine treatment restores crystallinity to the degree that the pattern can be refined. The bump in Figure 4.32(c) at $2\theta = 7°$ could be the remains of the decomposition product.

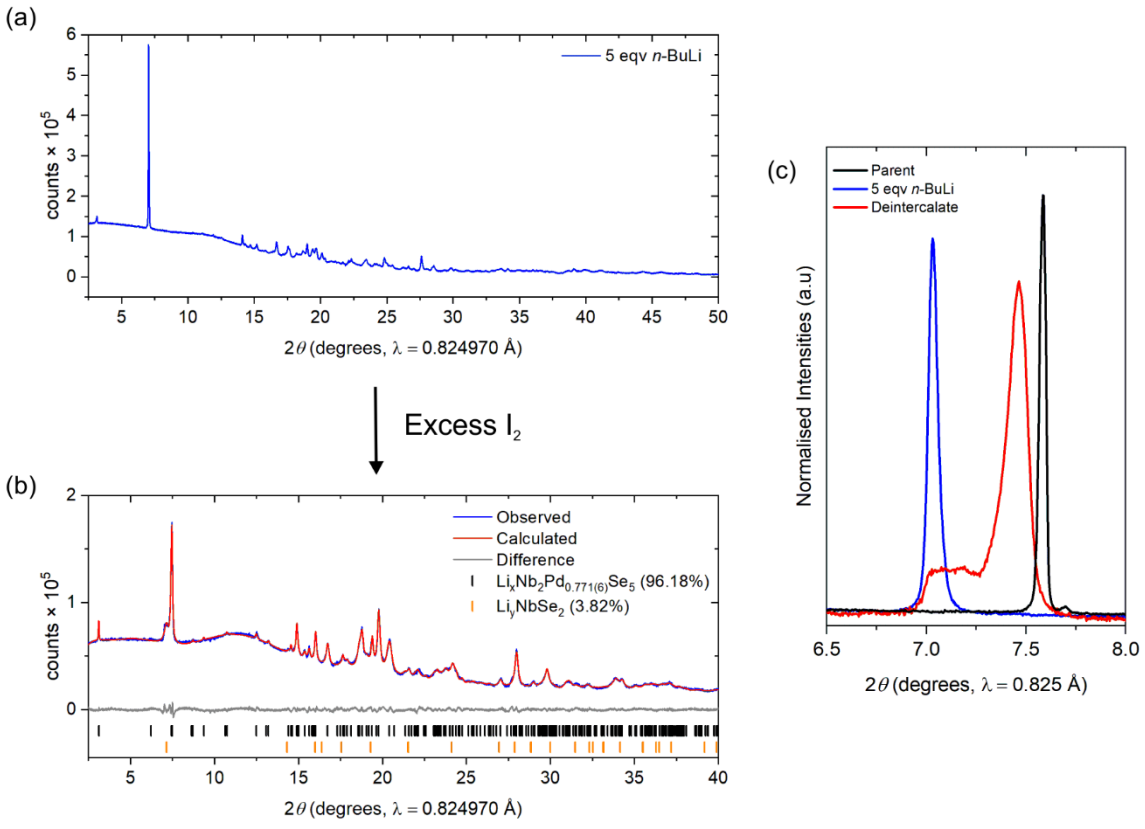


Figure 4.32: (a) I11 (PSD) PXRD pattern of $Nb_2Pd_xSe_5$ when treated with an excess (5 molar equivalence) of *n*-BuLi. (b) Rietveld refinement against I11 (PSD) PXRD pattern of when the intercalate (a) is treated with iodine. R_{wp}: 0.71 % (c) Comparison of the main $20\bar{1}$ Bragg reflections of the parent, intercalated and deintercalated phases.

When intercalating $Nb_2Pd_xSe_5$ with Li in NH_3, unlike with *n*-BuLi, a 1:1 molar ratio was not enough to entirely consume the starting material, and the product was biphasic. This is also in stark contrast with $Nb_2Pd_xS_5$, in which the intercalated phase was formed using a 0.6:1 molar ratio. Using a 2:1 molar ratio consumed the starting material, as seen in Figure 4.33, although a small peak appears at a *d*-spacing of ~ 9.4 Å (see inset of Figure 4.33). This peak is not seen when using *n*-BuLi or Li/naphthalene and cannot be attributed to any phase consisting of the parent elements. It is possible there is some co-intercalation of ammonia molecules or amide ions. This makes this method unsuitable for the preparation of a sample for proposed neutron powder diffraction, as any protons present will result in a large incoherent background.

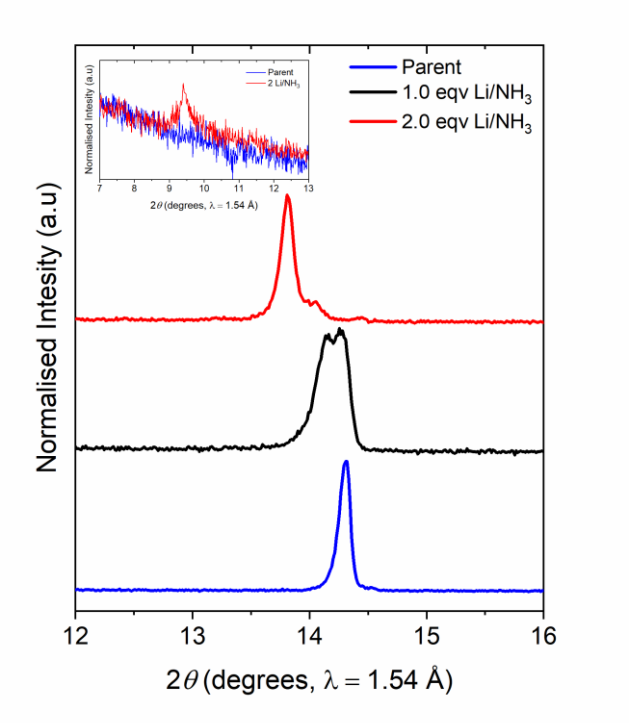


Figure 4.33: Comparison of the main $20\bar{1}$ Bragg reflection when varying the molar ratio of Li/NH_3 reagent. Inset shows the unidentifiable peak at a *d*-spacing of ~ 9.4 Å.

$Nb_2Pd_xSe_5$ was intercalated with Li in a solution of naphthalene/THF. Like the Li/NH_3 reagent, a 1:1 molar ratio did not fully consume the starting material and a two-phase product

is seen. This may be due to the THF not being completely dry, and hence some of the reactant was already used up. Using a 2:1 molar ratio fully consumed the parent compound, although the emergence of the small side peak, at a slightly lower angle than the main $20\bar{1}$ Bragg reflection, is seen (indicated by the arrow in Figure 4.34(a)). This peak is similar in *d*-spacing to the side peak seen when intercalating with *n*-BuLi and could be attributed to decomposition to a Li_yNbSe_2 phase (see inset of Figure 4.34(a)). It was found that using a 1.2:1 molar ratio was the minimum amount needed to fully consume the parent compound whilst minimising the side phase.

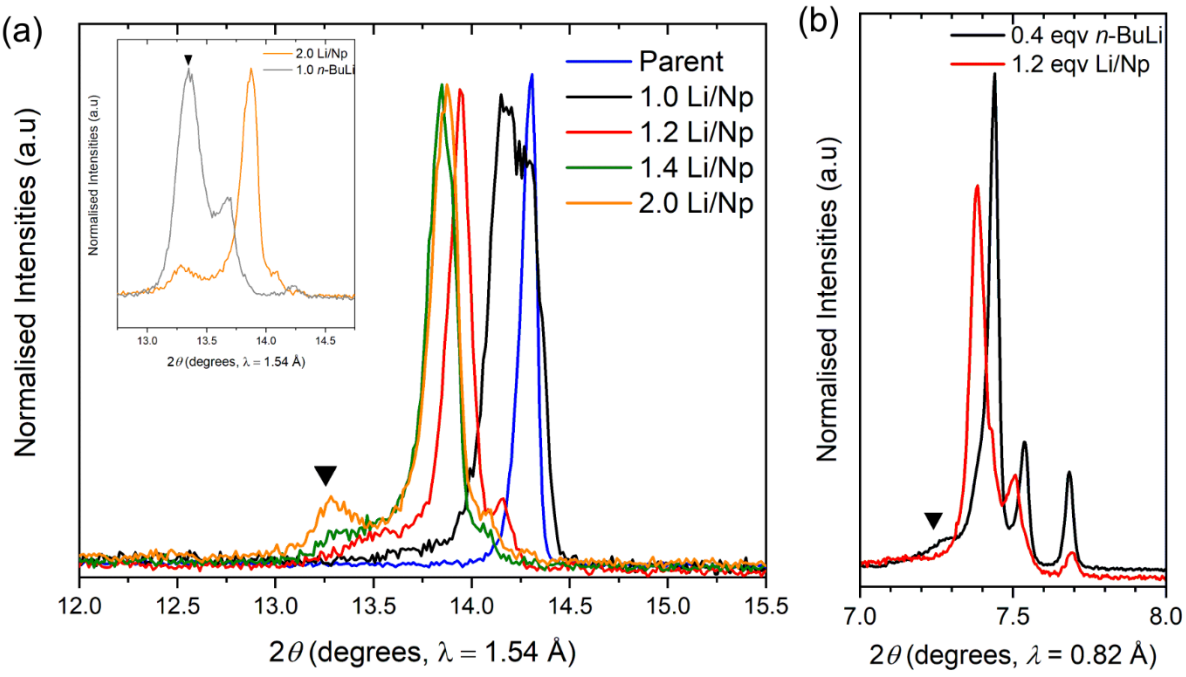


Figure 4.34: (a) Comparison of the main $20\bar{1}$ Bragg reflection when varying the molar ratio of Li/naphthalene reagent with the inset showing how increasing molar ratios lead to side phases as seen with *n*-BuLi intercalation. (b) Comparison of the main $20\bar{1}$ Bragg reflection for 0.4 eqv n-BuLi and 1.2 eqv Li/naphthalene.

A comparison of the $20\bar{1}$ Bragg reflection of the intercalated using 1.2:1 molar ratio of Li/naphthalene and 0.4:1 molar ratio of *n*-BuLi (Figure 4.34(b)) shows how intercalation using Li/naphthalene can achieve a higher Li content whilst minimising decomposition/emerging side phases. This, combined with the fact that there is no risk of

the formation of an amide side phase, resulted in this intercalated phase being the ideal candidate for structural analysis using synchrotron PXRD and PND.

4.3.3 Powder X-ray and Neutron Diffraction

Synchrotron PXRD at I11 shows the unit cell has expanded by approximately 0.24 Å, 0.03 Å and 0.18 Å in the *a*, *b* and *c* directions, respectively, with a 2.4° increase in the monoclinic angle and with no indication that the *C*2/*m* space group was not maintained. Comparing the mean bond lengths, the main significant change was the elongation of the Pd-Se linkage reflecting the increases in the *a* lattice parameter.

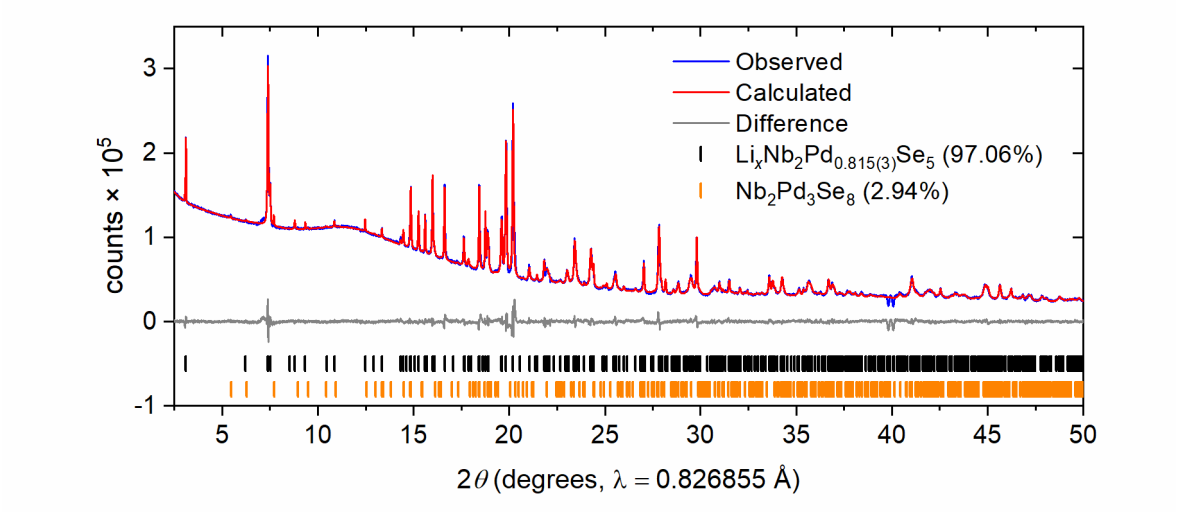


Figure 4.35: Rietveld refinement against I11 (PSD) PXRD pattern of $Li_xNb_2Pd_{0.81(1)}Se_5$ (ME113) intercalated with 1.2 molar equivalents of Li/naphthalene. R_{wp}: 1.10 %.

Table 4.11: Comparison of structural parameters of $Nb_2Pd_{0.826(2)}Se_5$ (ME111) and $Li_xNb_2Pd_{0.813(3)}Se_5$ (ME113).

Compound	**$Nb_2Pd_{0.826(2)}Se_5$**	**$Li_{0.87}Nb_2Pd_{0.815(3)}Se_5$**
	Parent (ME111)	Intercalate (ME113)
Instrument	I11 Beamline	I11 Beamline
***a* / Å**	12.77455(7)	13.0180(3)
***b* / Å**	3.39971(1)	3.43717(4)
***c* / Å**	15.51532(8)	15.6954(2)
Volume / Å^3	660.142(6)	681.39(2)
***β* / °**	101.5669(3)	104.0153(9)
	Mean Bond Lengths / Å	
Nb(1)-Se	2.586(1)	2.584(4)
Nb(2)-Se	2.654(1)	2.660(3)
Pd(1)-Se	2.445(2)	2.458(4)
Pd(2)-Se	2.530(2)	2.582(4)

Powder neutron diffraction measured at POLARIS confirmed the expansion with lattice parameters in agreement with the I11 data. Like for $Li_{0.33(4)}Nb_2Pd_{0.74(1)}S_5$, PND was anticipated to determine Li occupancy and positions in the unit cell. However, attempts at reliably refining Li were not successful. This likely reflects the different scattering lengths of the chalcogen. S has a scattering length of 2.85 fm and is the weakest neutron scatterer in Nb_2PdS_5.[131] In contrast, Se has a scattering length of 7.97 fm, making it the strongest scatterer in the system. Therefore, although Li is a negative scatterer (-1.9 fm), it is still relatively weak compared to Se making it difficult to locate and reliably refine. Another possibility is that Li could be distributed over more than one site. As a result, ICP-MS was used to determine a Li content of 0.87 per formula unit, whereas ^{7}Li NMR spectroscopy and DFT calculations were used to determine Li positions. It should be noted that the value obtained from ICP-MS should be taken be caution, as this technique measures the bulk composition, including any light or amorphous impurities. Similar to $Li_{0.33(4)}Nb_2Pd_{0.74(1)}S_5$,

there is no indication of any significant intercalation of Li on the vacant Pd(2) linkage sites. The Pd(2) occupancy in the PND refinement was refined to 0.63(2), consistent with the occupancies of 0.652(3) and 0.629(3) obtained from the PXRD refinements of the parent and intercalate, respectively.

Table 4.12: Structural parameters of $Li_{0.87}Nb_2Pd_{0.81(1)}Se_5$ (ME113) obtained from synchrotron PXRD refinement and PND. The values from PND are given in [ ].

$Li_{0.87}Nb_2Pd_{0.81(1)}Se_5$: *C*2/*m* (No.12)						
***a* / Å**		***b* / Å**	***c* / Å**	**Volume / Å^3**		***β* / °**
13.0180(3) [13.0281(3)]		3.43717(4) [3.44152(5)]	15.6954(2) [15.6940(3)]	681.38(2) [682.86(2)]		104.0159(9) [103.9662(14)]
Positional Parameters						
Atom	***x***	***y***	***z***	***Occupancy***	***Wyckoff Symbol***	***U_{iso}* / Å^2**
Nb(1)	0.0744(5) [0.0735(4)]	0.5	0.1864(3) [0.1858(3)]	1	4*i*	0.0028(9) [0.0020(5)]
Nb(2)	0.1475(2) [0.1510(3)]	0	0.3751(3) [0.3733(3)]	1	4*i*	0.0028(9) [0.0020(5)]
Pd(1)	0	0	0	1	2*a*	0.0029(16) [0.0108(16)]
Pd(2)	0	0	0.5	0.629(6) [0.636(12)]	2*c*	0.0029(16) [0.0106(16)]
Se(1)	0.3506(5) [0.3513(3)]	0	0.4948(4) [0.4944(2)]	1	4*i*	0.0052(11) [0.0041(6)]
Se(2)	0.2517(6) [0.2507(3)]	0.5	0.3009(4) [0.2999(3)]	1	4*i*	0.0052(11) [0.0041(6)]
Se(3)	0.1703(5) [0.1672(4)]	0	0.1071(4) [0.1063(3)]	1	4*i*	0.0028(16) [0.0056(8)]
Se(4)	0.4234(5) [0.4280(3)]	0.5	0.1301(3) [0.1292(2)]	1	4*i*	0.0047(19) [0.0043(10)]
Se(5)	0.4953(5) [0.4940(3)]	0	0.3198(4) [0.3203(3)]	1	4*i*	0.0067(17) [0.0017(9)]
***Mean Bond Length* / Å**						
Nb(1)-Se				2.584(4) [2.571(3)]		
Nb(2)-Se				2.660(3) [2.673(3)]		
Pd(1)-Se				2.458(4) [2.417(3)]		
Pd(2)-Se				2.582(4) [2.577(3)]		

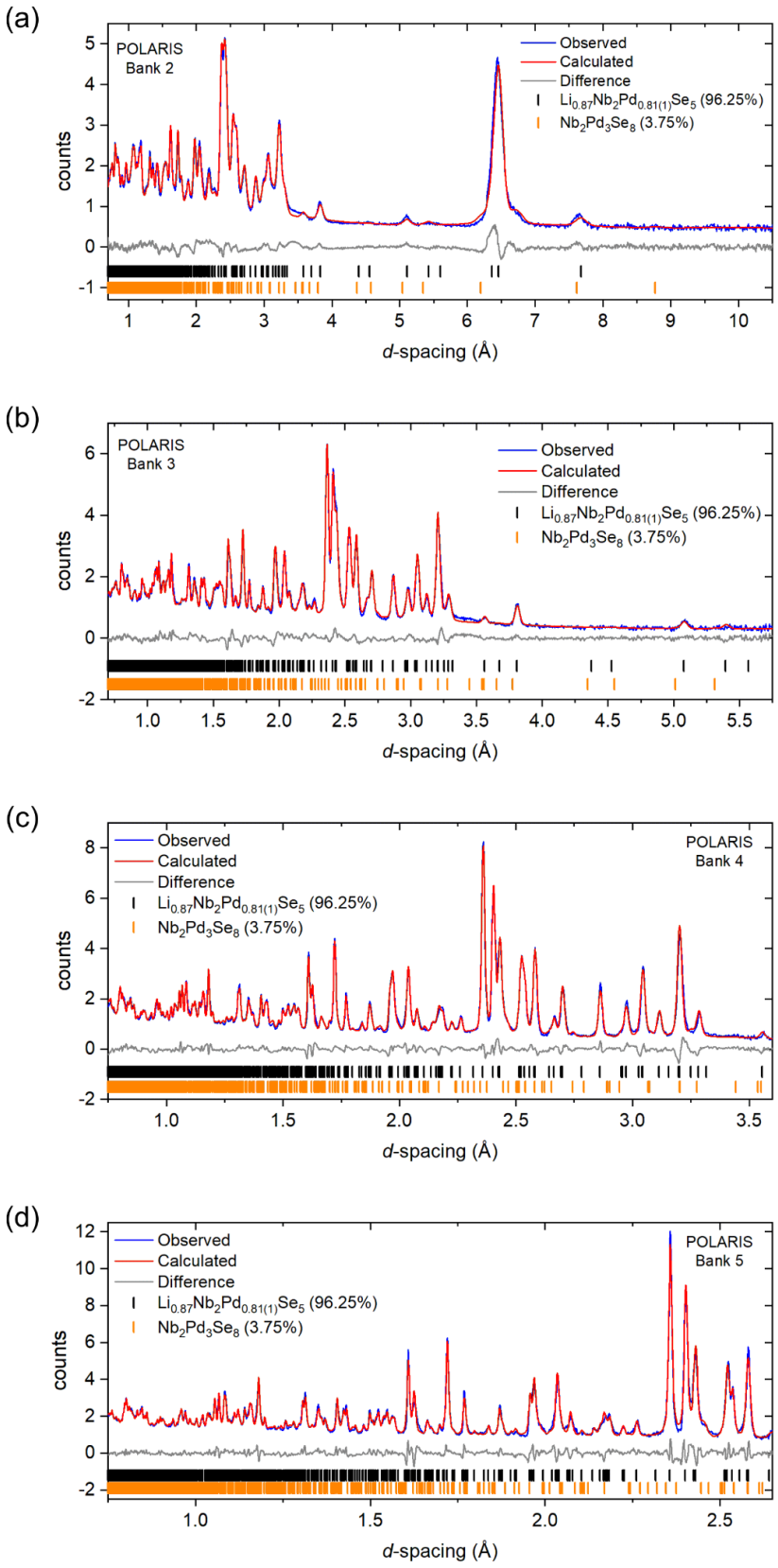


Figure 4.36: Rietveld refinement against the multi-bank (banks 2-5) TOF PND patterns of $Li_{0.87}Nb_2Pd_{81(1)}Se_5$ (ME113). Bank 1 was omitted from the refinement due to the low resolution. Li occupancy was not determined from refinement but rather from ICP-MS. R_{wp}: 5.19 %.

4.3.4 Electrochemical Intercalation

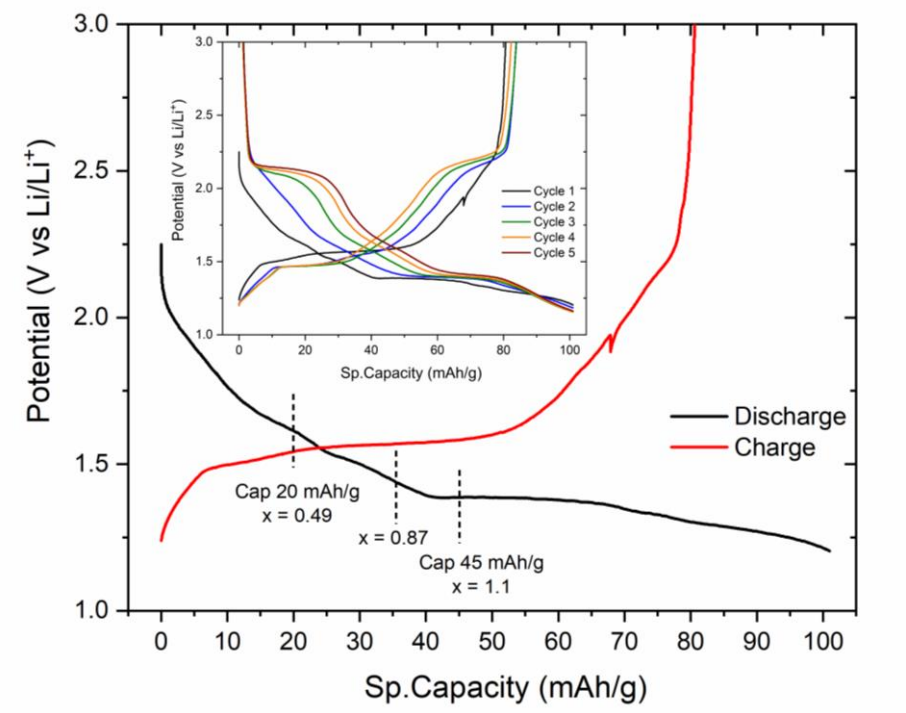


Figure 4.37: Potential against specific capacity plot with specific capacities of 20 and 45 mAh/g indicated corresponding to a theoretical Li content of 0.49 and 1.1, respectively. The Li content of 0.87 obtained from ICP-MS is shown as a reference. The inset shows multiple cycling.

$Nb_2Pd_{0.82}Se_5$ was intercalated electrochemically to allow more control over the extent of intercalation and for comparison with the chemical intercalation. The electrochemistry was stopped at specific capacities of 20 and 45 mAh/g corresponding to a Li content, *x*(Li), of 0.49 and 1.1, respectively. From the potential vs specific capacity graph (Figure 4.37), the plateau in the first cycle after 40 mAh/g (*x*(Li) ~ 1) indicates the formation of a two-phase sample. This would be consistent with a full occupancy of a Li site with excess intercalation leading to phase separation. The Li occupancy of 0.87 (obtained from ICP-MS on the chemically lithiated sample) is also shown, which is equivalent to a specific capacity of ~ 35 mAh/g. This would correspond to the point on the discharge curve just before the plateau. ICP-MS was measured on the sample discharged to 20 mAh/g, confirming the Li content of 0.48, in agreement with the theoretical amount. $Nb_2Pd_{0.82}Se_5$ could be cycled vs

Li multiple times showing good reversibility (although this would unlikely be a battery material candidate due to the heavy metals involved). However, capacities higher than 45 mAh/g (*i.e.* more than 1.1 mol of Li intercalation) could result in a phase separation rather than limited to simple intercalation. Comparing the lattice parameters, it is evident, given the smaller unit cell (~ 1 % smaller in volume), that less intercalation occurred when discharged at 20 mAh/g compared to the chemically intercalated sample. However, when discharged to 45 mAh/g capacity, the unit cell has a greater expansion (~ 1.5 % larger in volume), in-line with the Li content of the samples. The unit cell volume shows an almost linear trend with Li content (Figure 4.38(b)), akin to that observed with $Nb_2Pd_{0.74}S_5$. However, at x(Li) = 1.1, the monoclinic angle and the *c* parameter are reduced, an observation similar to that seen for $Nb_2Pd_{0.74}S_5$ when going from x(Li) = 0.19 to 0.4. From the mean bond lengths, the main significant change is the increase of ~ 0.9 Å in the Pd(2)-Se linkage bond, which follows a similar trend to the change in the *a* parameter.

Table 4.13: Lattice parameters of $Nb_2Pd_{0.82}Se_5$, the chemical intercalate, and the electrochemical intercalates.

	$Nb_2Pd_{0.82(1)}Se_5$	**$Li_{0.87}Nb_2Pd_{0.81(1)}Se_5$**	**$Li_{0.49}Nb_2Pd_{0.81(1)}Se_5$**	**$Li_xNb_2Pd_{0.77(1)}Se_5$**
	Parent	Intercalate (Chemical 1.2 Li/Np)	Intercalate (Electrochemical 20 mAh/g)	Intercalate (Electrochemical 45 mAh/g)
Instrument	I11 Beamline	I11 Beamline	I11 Beamline	I11 Beamline
***a* / Å**	12.77451(7)	13.0180(3)	12.8971(1)	13.2236(4)
***b* / Å**	3.39970(1)	3.43717(4)	3.42535(2)	3.44471(7)
***c* / Å**	15.51529(8)	15.6954(2)	15.6948(3)	15.6011(3)
Vol / Å^3	660.138(6)	681.39(2)	674.06(1)	692.27(3)
***β* / °**	101.5669(3)	104.0153(9)	103.5490(5)	103.237(1)
		Mean Bond Lengths / Å		
Nb(1)-Se	2.586(1)	2.584(4)	2.587(2)	2.554(4)
Nb(2)-Se	2.654(1)	2.660(3)	2.661(2)	2.619(4)
Pd(1)-Se	2.445(2)	2.458(4)	2.475(2)	2.481(5)
Pd(2)-Se	2.530(2)	2.582(4)	2.544(2)	2.621(5)

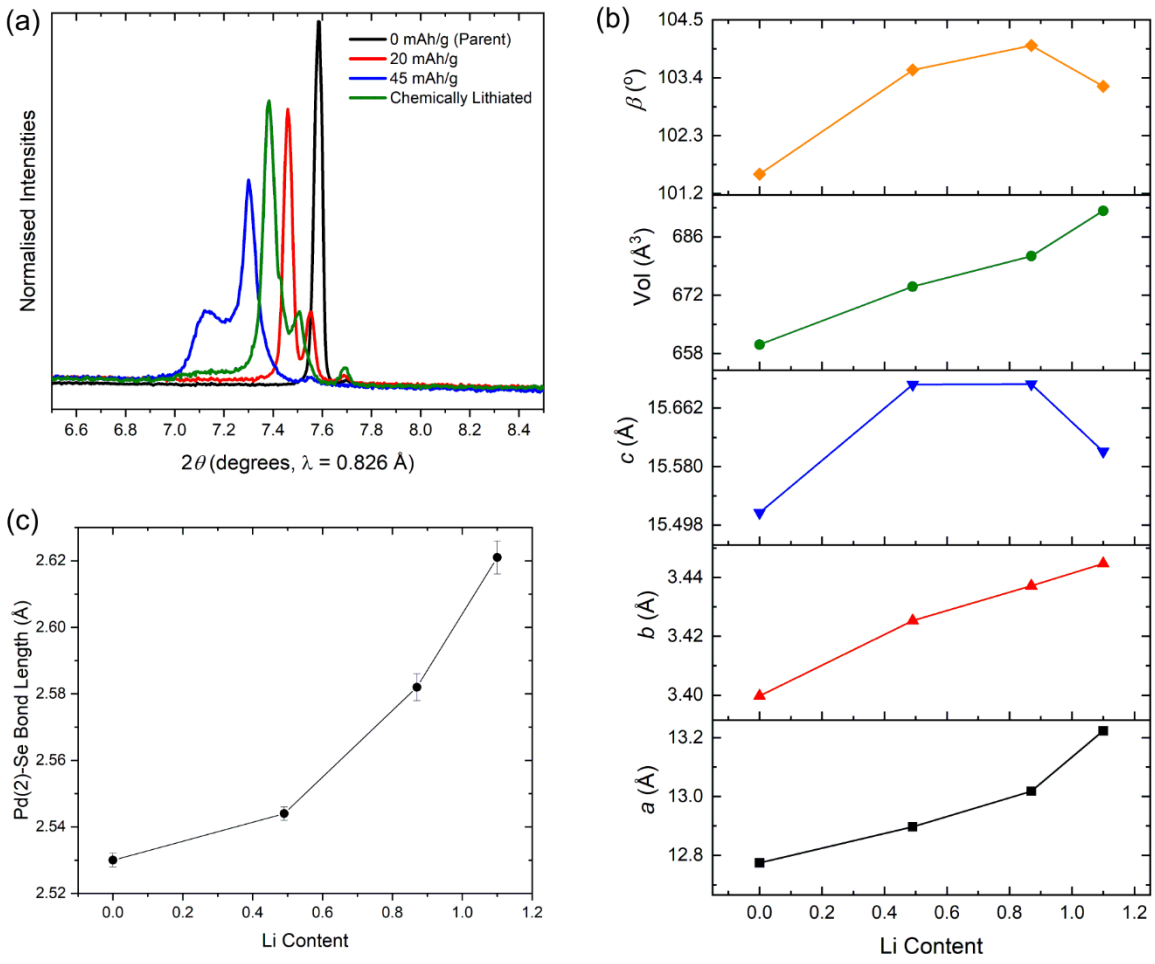


Figure 4.38: (a) PXRD pattern of the main $20\bar{1}$ and 200 Bragg reflection with varying starting Li stoichiometries. (b) Lattice parameters of the electrochemical intercalated phases. (c) Change in Pd(2)-Se bond length with increasing Li content.

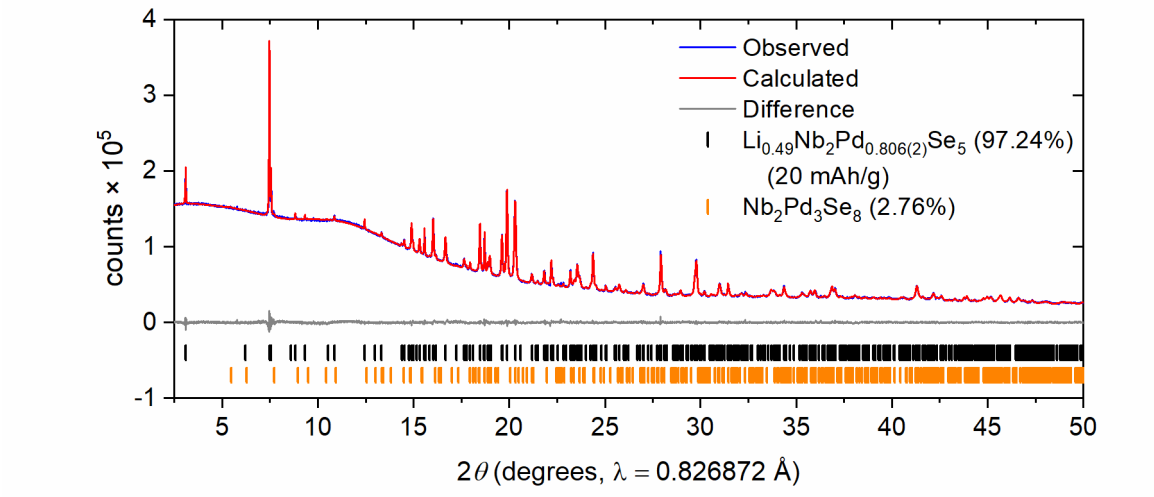


Figure 4.39: Rietveld refinement against I11 (PSD) PXRD pattern of $Li_{0.49}Nb_2Pd_{0.81(1)}Se_5$ (ME142). R_{wp}: 0.65 %.

When discharged to 20mAh/g, the intercalate is very crystalline with no other side phases formed. Whereas when discharged to 45 mAh/g, the sample has similar lattice parameters to the intercalation using a 1:1 molar ratio of *n*-BuLi, with less than one cubic angstrom (~ 0.1 %) difference in unit cell volume. More similarities include the extra peak seen at a *d*-spacing of 6.65 Å matching the 002 Bragg reflection of an expanded (*i.e.* intercalated) $NbSe_2$ phase with c = 13.23 Å, and 13.38 Å reported for $Li_{0.33}NbSe_2$ and $Li_{0.50}NbSe_2$ respectively.[173] Therefore, the plateau in the first cycle after 40 mAh/g indicates the formation of an additional phase, which is probably due to conversion product formation (such as Li_xNbSe_y + Pd metal), and is well known in chalcogenide electrochemistry.[174,175] The Pd(2) site occupancy decreases by ~ 0.1. However, Pd was not detected in the PXRD data, as it is plausible that it is formed as nanoparticles. Therefore, intercalation, whether via chemical or electrochemical routes, produce similar products, and excess intercalation indicates that the compound begins to decompose.

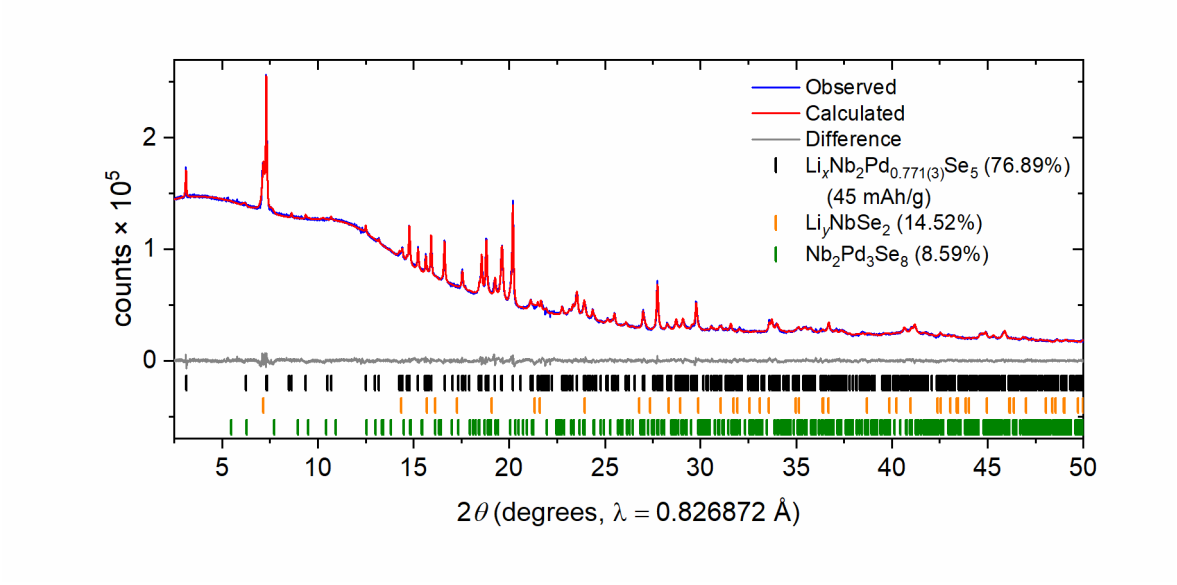


Figure 4.40: Rietveld refinement against I11 (PSD) PXRD pattern of the electrochemical intercalate discharged to 45 mAh/g (ME143). R_{wp}: 0.74 %.

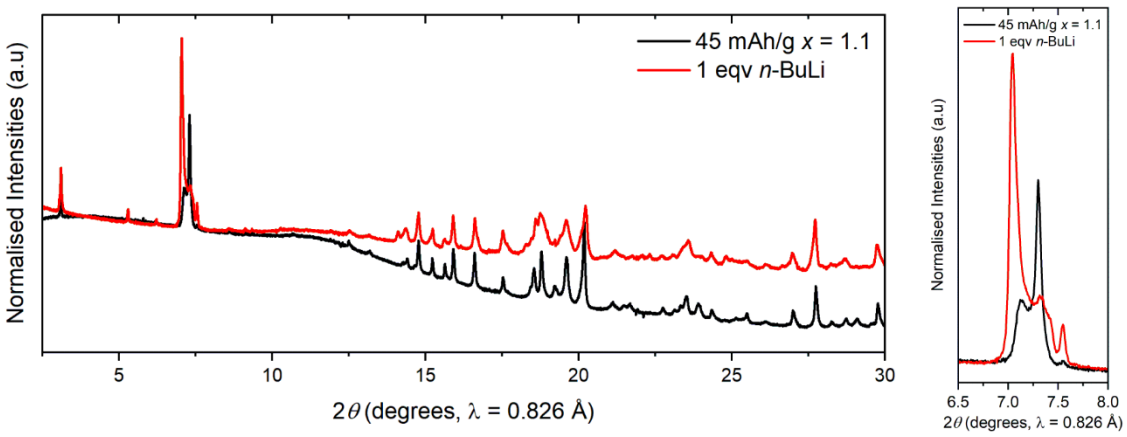


Figure 4.41: Comparison of the I11 PXRD data of the electrochemical intercalate discharged to 45 mAh/g and the intercalate formed using 1 molar equivalent of *n*-BuLi.

4.3.5 DFT Calculations and ^{7}Li NMR Spectroscopy

Since attempts to locate Li sites from neutron diffraction were unsuccessful, to identify the Li sites from the ^{7}Li NMR data, DFT calculations on fully occupied Nb_2PdSe_5 were used to determine the possible Li sites within the compound and calculate their relative energies, similar to the process used for Nb_2PdS_5 (section 4.2.3.3). For each site, the predicted ^{7}Li chemical shift (referenced at -1 ppm) was calculated in the process described in Appendix I. The predicted chemical shifts will then be compared to the experimental NMR data.

The calculated unit cell relaxes to a cell larger in lattice parameters than the $Li_{0.87}Nb_2Pd_{0.82}Se_5$ with an increase of ~ 0.28 Å and 0.2 Å in the *a* and *c* axis, respectively (giving an ~ 3.5 % increase in volume). A diagram showing the locations of the Li sites calculated after optimisation is shown below in Figure 4.42, with structural information of the site given in Table 4.15.

Table 4.14: Comparison of lattice parameters of $Nb_2Pd_{0.82}Se_5$, the intercalates and the calculated unit cell.

	$Nb_2Pd_{0.82(1)}Se_5$	**$Li_{0.87}Nb_2Pd_{0.81(1)}Se_5$**	**$Li_xNb_2Pd_{0.77(1)}Se_5$**	**$Li_{0.25}Nb_2PdSe_5$**
	Parent	Intercalate (Chemical 1.2 Li/Np)	Intercalate (Electrochemical 45 mAh/g)	Calculated Intercalate Cell
***a* / Å**	12.77451(7)	13.0180(3)	13.2236(4)	13.29166
***b* / Å**	3.39970(1)	3.43717(4)	3.44471(7)	3.43089
***c* / Å**	15.51529(8)	15.6954(2)	15.6011(3)	15.86974
Vol / Å^3	660.138(6)	681.39(2)	692.27(3)	705.642
***β* / °**	101.5669(3)	104.0153(9)	103.237(1)	102.82529

Table 4.15: Description of the Li sites (a)-(e).

Site		**(a)**	**(b)**	**(c)**	**(d)**	**(e)**
Δ*E* / eV		0.00	0.35	0.68	0.81	1.13
Site		4*i*	4*i*	4*i*	4*i*	4*i*
Li Site Energy / eV f.u.$^{-1}$		0.00	0.09	0.17	0.20	0.28
Site Co-ordinates	***x***	0.1785	0.1671	0.2105	0.0960	0.1350
	y	0.5	0.5	0	0	0.5
	z	0.9781	0.7963	0.8374	0.6170	0.6493
Mean Li-Se Bond length / Å		2.609	2.573	2.279	2.495	2.240
Description of Coordination environment		Square pyramidal	Octahedral	Seesaw	Square pyramidal	Seesaw
Chemical Shift / ppm		15.28	7.48	9.95	33.52	17.96

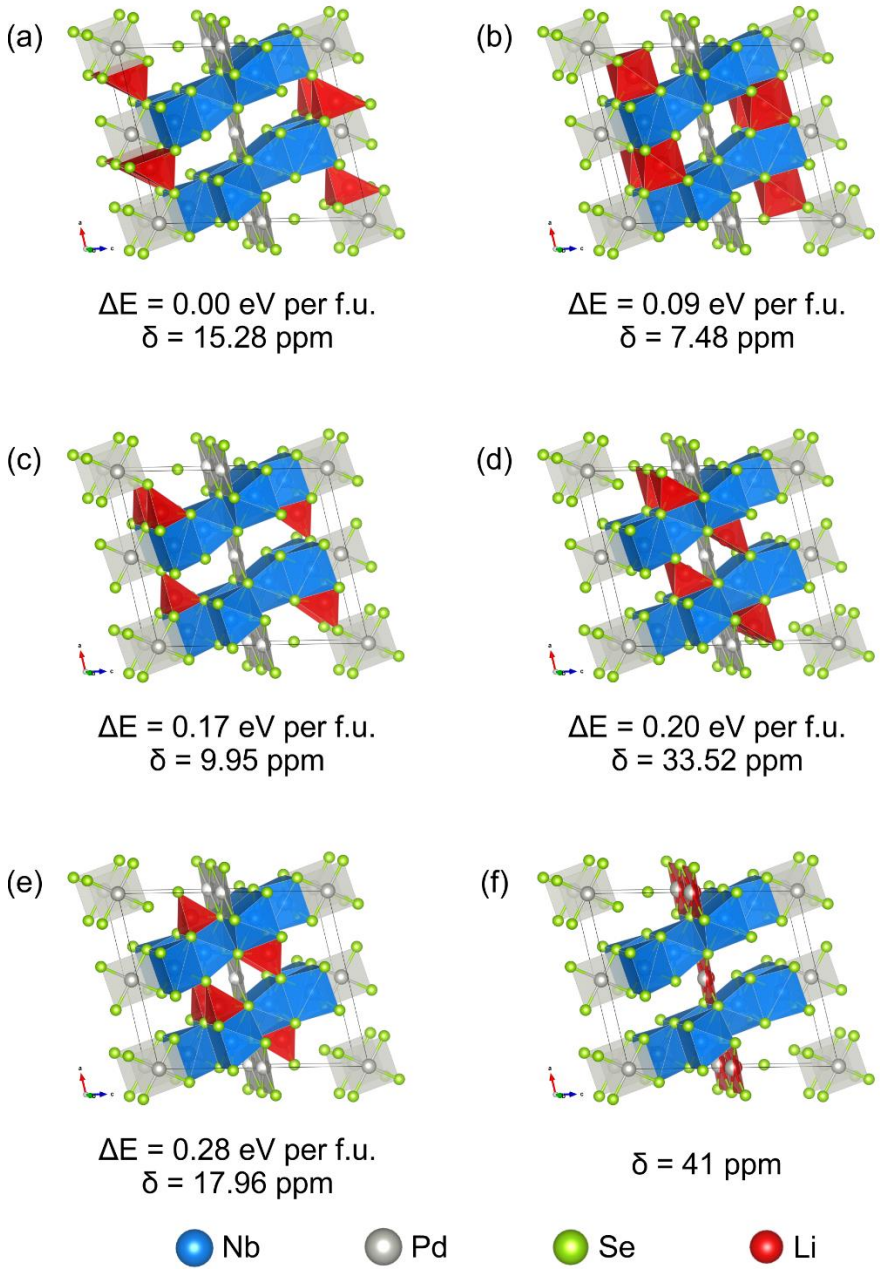


Figure 4.42: Schematic of the Li sites (a-e) determined from DFT ranked from lowest energy to highest with the ^{7}Li chemical shift for each site. Site (f) has no relative energy as the Pd(2) site was assumed to be fully vacant for calculations and thus cannot be compared directly.

The Li positions and energy ordering calculated for the Li sites are analogous to that calculated for Nb_2PdS_5 (section 4.2.3.3), and the justification for the differing energies is also identical. The only significant difference is instead of the lowest energy site being a 6-coordinate triangular prismatic environment found for the sulfide variant; here, this site has morphed into a 5-coordinate distorted square-based pyramid. The mean bond length in

the 5-coordinate site is 2.609 Å which is in line with distances found in Li_2Se and $LiTiSe_2$ of 2.6 Å and 2.63 Å, respectively.[176,177] The distance between Li and the 6th Se anion is ~ 3.6 Å which is likely to be too large of a distance for bonding. Like for the sulfide variant, the Li cations in this site are in close proximity to each other with Li-Li distances of ~ 2.4 Å, which again would likely cause unfavourable electrostatic repulsion. In the PND refinement, Li was tested at both sites (a) and (b) with a fixed Li occupancy of 1 and fixed to reasonable thermal displacements parameters. However, changes in the R_{wp} were small (5.19 % to 5.11 %), indicating the insensitive nature of the data to the Li position. Allowing the Li occupancy to refine resulted in drastic deviation of the Li positions from their initial positions such that they are unreasonable.

Solid-state ^{7}Li MAS NMR spectroscopy measurements were carried out on the chemically lithiated sample as well as the two samples obtained from electrochemical lithiation in a similar manner to $Li_{0.33(4)}Nb_2Pd_{0.75}S_5$ (referenced to LiF at -1 ppm). For the sample discharged to 20 mAh/g (where $x = 0.49$), a single peak was seen at a chemical shift of 7.6 ppm, suggesting, like with $Li_{0.33(4)}Nb_2Pd_{0.75}S_5$, either a single environment or rapid exchange between sites on the NMR timescale. However, in contrast to the sulfide variant, the peak does not have a significant degree of broadness with a FWHM of 2.3 ppm (in contrast to 10.8 ppm found for $Li_{0.33(4)}Nb_2Pd_{0.75}S_5$). Literature on ^{7}Li MAS NMR measurements on Li-Se systems is scarce. For comparison, the side phase Li_xNbSe_2 was synthesised from the intercalation of $NbSe_2$, and the NMR gave a single peak at 6.5 ppm with a FWHM of 19.5 ppm (see Appendix III). Li_2Se was also measured, which gave a single peak at 2.4 ppm and a FWHM of 4.6 ppm (see Appendix III).

When the Li content increases, extra peaks emerge, as seen in the chemically lithiated (Figure 4.43(c)) and the sample discharged to 45 mAh/g (Figure 4.43(a)). Peaks below

0 ppm are weak and come from diamagnetic impurities, including residual $LiPF_6$ salt from the electrolyte. For the chemically lithiated, besides the sharp peak at 8 ppm, two more peaks are seen around 2.2 and 5.1 ppm, suggesting extra Li environments. For the sample discharged to 45 mAh/g (x = 1.1), a broader peak is seen centred at a shift of 6.5 ppm as well as shoulder peaks at 2.2 and 13.7 ppm.

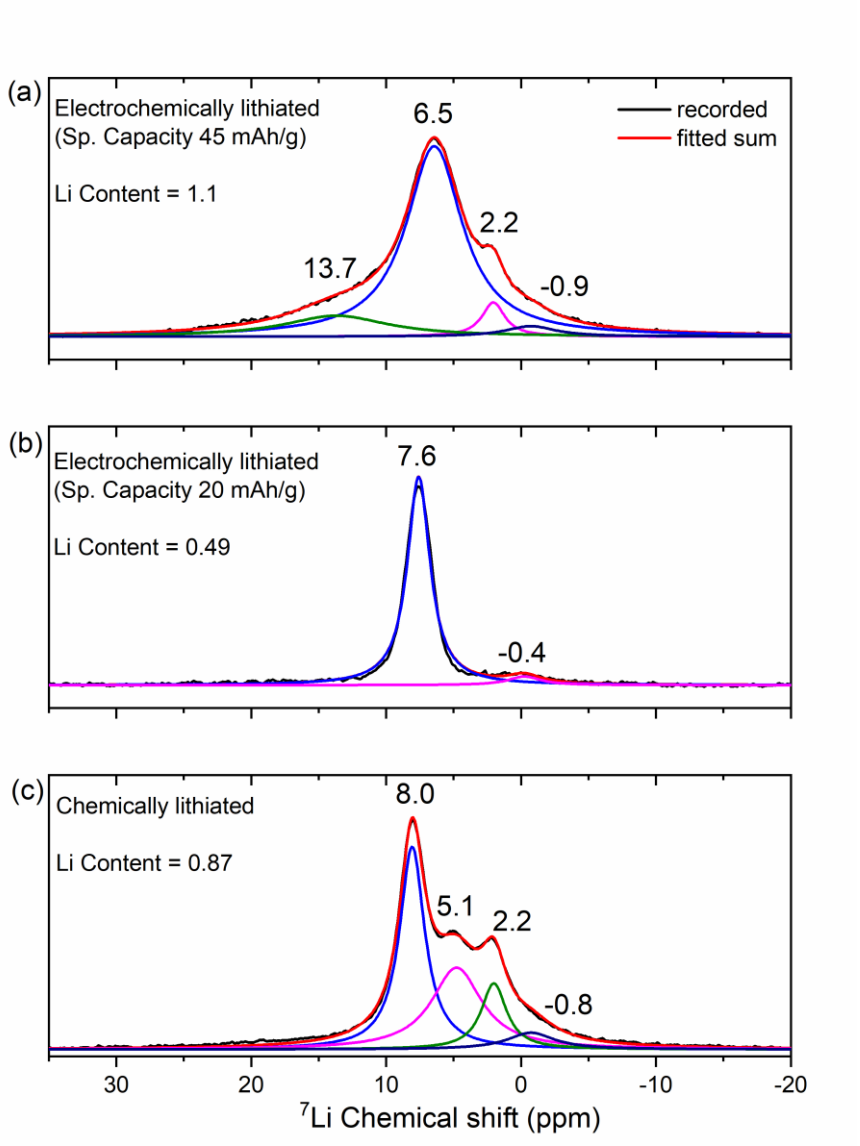


Figure 4.43: Solid-state ^{7}Li NMR of the electrochemical intercalate discharged at 45 mAh/g (a) and 20 mAh/g (b) with (c) showing the spectra for the chemical lithiated $Li_{0.87}Nb_2Pd_{0.81}Se_5$. The coloured lines show how the spectra (a) and (c) consist of multiple signals.

For the ^{7}Li NMR chemical shifts calculated for each possible Li site, the octahedral site (b) was calculated with a chemical shift of 7.48 ppm, in very good agreement with the single peak seen in the electrochemical sample discharged to 20 mAh/g and the main peak at 8 ppm in the chemically lithiated sample. Therefore, the evidence would suggest that upon intercalation, the octahedral site is occupied first despite it not being the lowest energy site available. The lowest energy site, like that seen in $Li_{0.33(4)}Nb_2Pd_{0.75}S_5$, results in Li cations in close proximity to each other. For the selenide, occupancy of two neighbouring sites would result in Li-Li distances of ~ 2.4 Å, which again would cause unfavourable electrostatic repulsion. The octahedral site would allow higher occupation with minimal repulsion. From the discharge curve, before 40 mAh/g (x(Li) ~ 1), there is no obvious kink or step in the curve that would suggest Li perhaps occupies a different site at higher occupancy (like that seen for the sulfide variant in Figure 4.17(a)). This is consistent with Li just intercalating into the octahedral site.

For the sample discharged to 45 mAh/g, excess intercalation causes decomposition, as seen from the PXRD. Therefore, the broad peak consists of the main peak due to Li in the octahedral site and the signal from the Li_yNbSe_2 side phase (6.5 ppm). The peak at 2.2 ppm can be attributed to Li_2Se (2.4 ppm), which would be another product of decomposition not detectable by PXRD (either due to very small amounts or poor crystallinity) but detectable by NMR.

In the chemically lithiated sample, the peak at 5.1 ppm cannot be attributed to any of the sites (a-f). A possibility is that it may be from Li_yNbSe_2 with perhaps different Li content. It is likely that, as seen with intercalation using Li/naphthalene (Figure 4.34(a)) that the sample is at the beginning of decomposition, and the trace side phase is not detectable by PXRD but is in the NMR. The 2.2 ppm peak is also seen, indicating that decomposition has started.

The chemical shift for Li on the Pd(2) site (site (f) in Figure 4.42) was calculated to be 41 ppm. The absence of this resonance in the NMR is suggestive of no Li on the vacant Pd(2) site, consistent with the PND refinement in which the Pd(2) occupancy shows no significant change. A direct comparison of energies is not possible as, in this case, the Pd(2) site was assumed to be fully vacant, whereas, for sites (a-e), it was calculated assuming full occupancy. Therefore, the comparison of site (f) with the other sites is unreasonable due to the differing energies of the whole system.

4.3.6 Deintercalation

Deintercalation of Li from $Li_{0.87}Nb_2Pd_{0.81(1)}Se_5$ by reacting with an excess of iodine in an acetonitrile solution restored the parent compound with similar lattice parameters to the original parent compound. The unit cell volume is approximately 0.3 % larger than the original parent compound (compared to ~ 3.3 % in the intercalated phase). ICP-MS detected a Li content of 0.096, suggesting a trace amount of Li may still be present within the structure. Assuming volume is linear with composition, this would be equivalent to ~ 0.08 Li per formula unit, consistent with ICP-MS results.

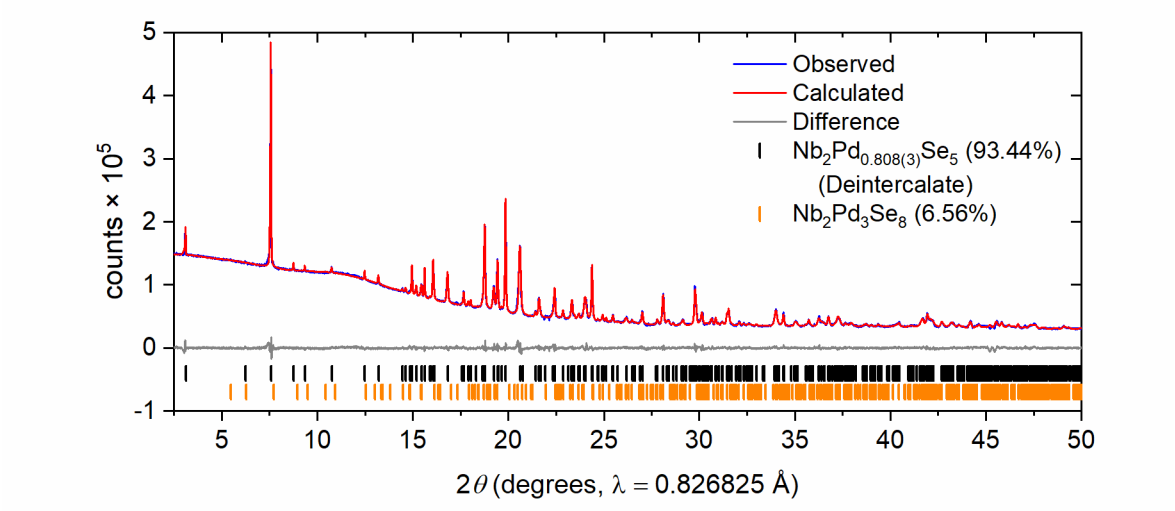


Figure 4.44: Rietveld refinement against I11 (PSD) PXRD pattern of the deintercalated $Li_{0.87}Nb_{0.81(1)}Se_5$ (ME116). R_{wp}: 0.88 %.

Table 4.16: Lattice parameters of parent $Nb_2Pd_{0.82}Se_5$, the chemically intercalated and deintercalated phases.

Compound	*a* / Å	*b* / Å	*c* / Å	Volume / Å^3	*β* / °
Parent	12.77455(7)	3.39971(1)	15.51532(8)	660.142(6)	101.5669(3)
Chemical Intercalate	13.0180(3)	3.43717(4)	15.6954(2)	681.39(2)	104.0153(9)
Deintercalate	12.7897(2)	3.40440(3)	15.5367(2)	662.14(2)	101.7920(9)

^{7}Li NMR spectroscopy showed no observable signal in the 0-10 ppm range, suggesting Li has been deintercalated from the octahedral site. However, two signals are observed at 52 and 66 ppm, which may result from side products or residue in the reaction process with iodine.

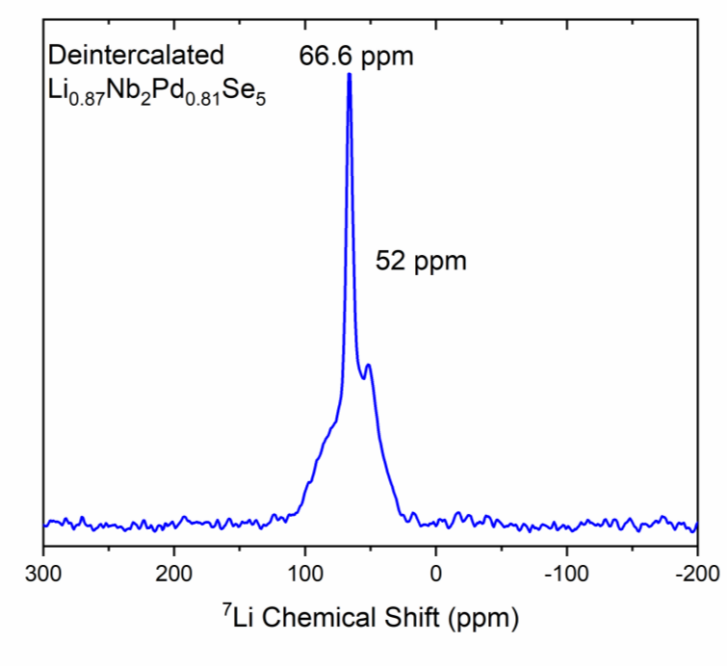


Figure 4.45: Solid-state ^{7}Li NMR spectroscopy of the deintercalated phase.

4.3.7 Magnetometry

Zero-field cooled measurements at 10 Oe on the $Nb_2Pd_xSe_5$ system show a very close resemblance to the $Nb_2Pd_xS_5$ system discussed earlier in section 4.2.4, whereby Li intercalation causes suppression of superconductivity with no observable onset T_c, with

deintercalation partially restoring the superconductivity. The transition temperature of the deintercalated phase is lower with a $T_c \sim 3.9$ K (4.5 K in parent $Nb_2Pd_{0.82}Se_5$). The superconducting volume fraction is also significantly reduced (1.2 % compared to 60 % in the original parent), again likely due to trace amounts of Li still present in the phase.

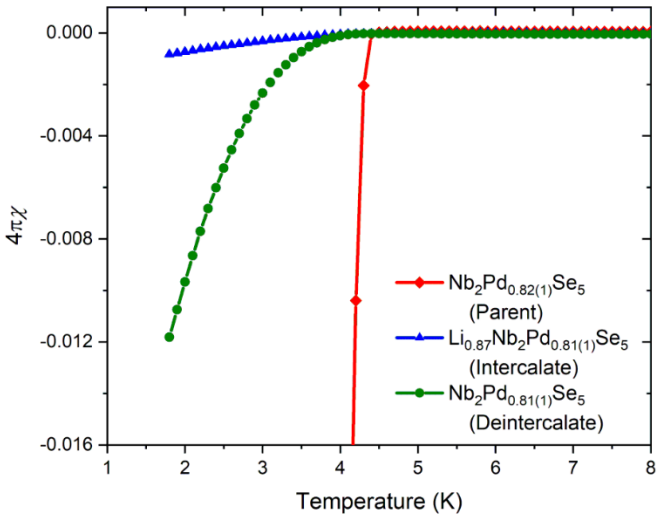


Figure 4.46: Magnetic susceptibility against temperature for zero-field cooled measurements at a field of 10 Oe for parent $Nb_2Pd_{0.82(1)}Se_5$, the intercalate and deintercalated phases.

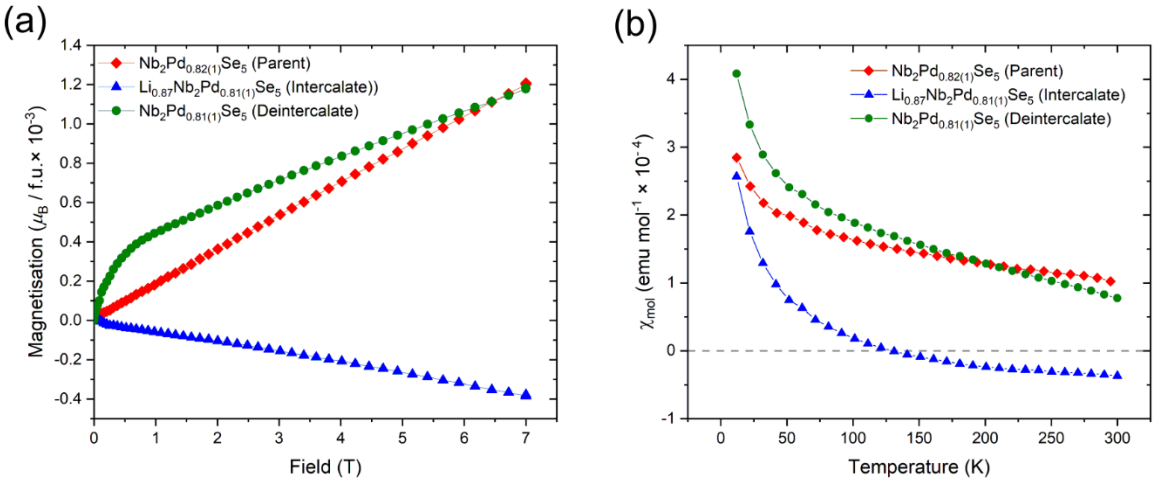


Figure 4.47: (a) Magnetisation against field and (c) Molar susceptibility (χ_{mol}) against temperature of parent $Nb_2Pd_{0.82(1)}Se_5$, the intercalate and deintercalated phases. χ_{mol} was measured at 3 T and 4 T with the difference taken between them to eliminate ferromagnetic impurities that are evident at a low field in (a).

Like $Nb_2Pd_{0.74}S_5$, $Nb_2Pd_{0.82}Se_5$ is paramagnetic with a room-temperature molar susceptibility (χ_{mol}) of $9.56(2)\times10^{-5}$ emu mol^{-1}. Measurement of susceptibility against temperature does not follow the Curie-Weiss law, and the curve can be fitted to Equation 4.1 described in section 4.2.4. For $Nb_2Pd_{0.82(1)}Se_5$, the susceptibility arising from the core diamagnetism, χ_D, was calculated to be $-2.787(1)\times10^{-4}$ emu mol^{-1} (by summing the individual values for each ion from Bains *et al.*[159]), an approximate 50 % increase over the sulfide equivalent reflecting the increase in the number of core electrons going from S to Se. The values of χ_0, χ_D and χ_P are listed below in Table 4.17.

Table 4.17: Susceptibility values of $Nb_2Pd_{0.82(1)}Se_5$ host material and the intercalated and deintercalated phases. χ_D values obtained from Bain *et al.*[159]

	$Nb_2Pd_{0.82(1)}Se_5$	**$Li_{0.87}Nb_2Pd_{0.81(1)}Se_5$**	**$Nb_2Pd_{0.81(1)}Se_5$**
	Parent	Intercalate	Deintercalate
χ_{mol} / emu mol^{-1} (at 300 K)	$9.56(2)\times10^{-5}$	$-3.05(3)\times10^{-5}$	$6.72(4)\times10^{-5}$
χ_0 / emu mol^{-1}	$7.1(5)\times10^{-5}$	$-6.96(8)\times10^{-5}$	$2.5(9)\times10^{-5}$
χ_D / emu mol^{-1}	$-2.787(1)\times10^{-4}$	$-2.793(3)\times10^{-4}$	$-2.782(1)\times10^{-4}$
χ_P / emu mol^{-1}	$3.50(5)\times10^{-4}$	$2.10(1)\times10^{-4}$	$3.0(1)\times10^{-4}$

The increase in the core diamagnetism is more apparent when looking at the susceptibility of $Li_{0.87}Nb_2Pd_{0.81(1)}Se_5$. The sulfide equivalent had a weak paramagnetic room-temperature susceptibility of $2.03(2)\times10^{-5}$ emu mol^{-1} (a reduction by an order of magnitude from $Nb_2Pd_{0.74}S_5$). For $Li_{0.87}Nb_2Pd_{0.81(1)}Se_5$, due to the increase in χ_D, the room-temperature susceptibility becomes diamagnetic with $\chi_{mol} = -3.05(3)\times10^{-5}$ emu mol^{-1}. This is also seen in the variable temperature susceptibility in Figure 4.47(b), where the curve has negative susceptibility when $T > 130$ K. χ_P decreases from $3.50(5)\times10^{-4}$ emu mol^{-1} in the parent to $2.10(1)\times10^{-4}$ emu mol^{-1} in the intercalate, a reduction of approximately 40 % which is similar to the percentage reduction seen with the sulfide variant. This is consistent with the

suppression of superconductivity and the reduced Pauli susceptibility both due to the decrease in the density of states at the Fermi level, E_F.

Deintercalation is shown to increase the χ_{mol} and χ_P back to values almost similar to the initial host material with values of $6.72(4)\times10^{-5}$ emu mol^{-1} and $3.0(1)\times10^{-4}$ emu mol^{-1}, respectively. χ_P is ~ 15 % smaller for the deintercalated phase, which corresponds to a reduction in the density of states at E_F and is consistent with the partial restoration of the superconductivity at a lower T_c and volume fraction, as seen in Figure 4.46. Assuming χ_P follows a linear trend with composition, a χ_P of $3.0(1)\times10^{-4}$ emu mol^{-1} would correspond to a Li content of ~ 0.3. This is an overestimate by ~ 0.2 compared with ICP-MS and the unit cell volume changes, suggesting that perhaps the trend is not linear.

From the density of states calculated for Nb_2PdSe_5 (Figure 4.30), E_F lies on a positive gradient. Increasing the Pd content increases the electron count and navigates E_F to higher density of states, corresponding to an increase in the superconductivity. It might be expected, therefore, that the intercalation of Li would also result in similar behaviour. Measurements on intercalated samples with lower Li content also did not result in any superconducting transition. It is a possibility that the topology of the density of states changes upon intercalation with the significant expansion of the structure upon insertion of Li. To investigate this, DOS was calculated for the lithiated compound, assuming that the octahedral site (site (b) in Figure 4.42) is fully occupied, giving a stoichiometry of $LiNb_2PdSe_5$, a reasonable approximation to $Li_{0.87}Nb_2Pd_{0.81(1)}Se_5$. The intercalated compound remains metallic with no gap at E_F, with the Fermi level shifting to higher energies, as shown in Figure 4.48, as expected with the addition of electrons. However, the region around the Fermi level has a slightly different topology compared to Nb_2PdSe_5, as shown in Figure 4.48(c). For $LiNb_2PdSe_5$, the density of states below E_F is significantly reduced, with the

region above E_F having an increase in the density of states. Since the formula, $LiNb_2PdSe_5$ is an overestimate of the number of electrons compared to $Li_{0.87}Nb_2Pd_{0.81(1)}Se_5$, it's a possibility that E_F resides in that region of reduced density of states and therefore explains the reduced Pauli susceptibility and the suppression of superconductivity.

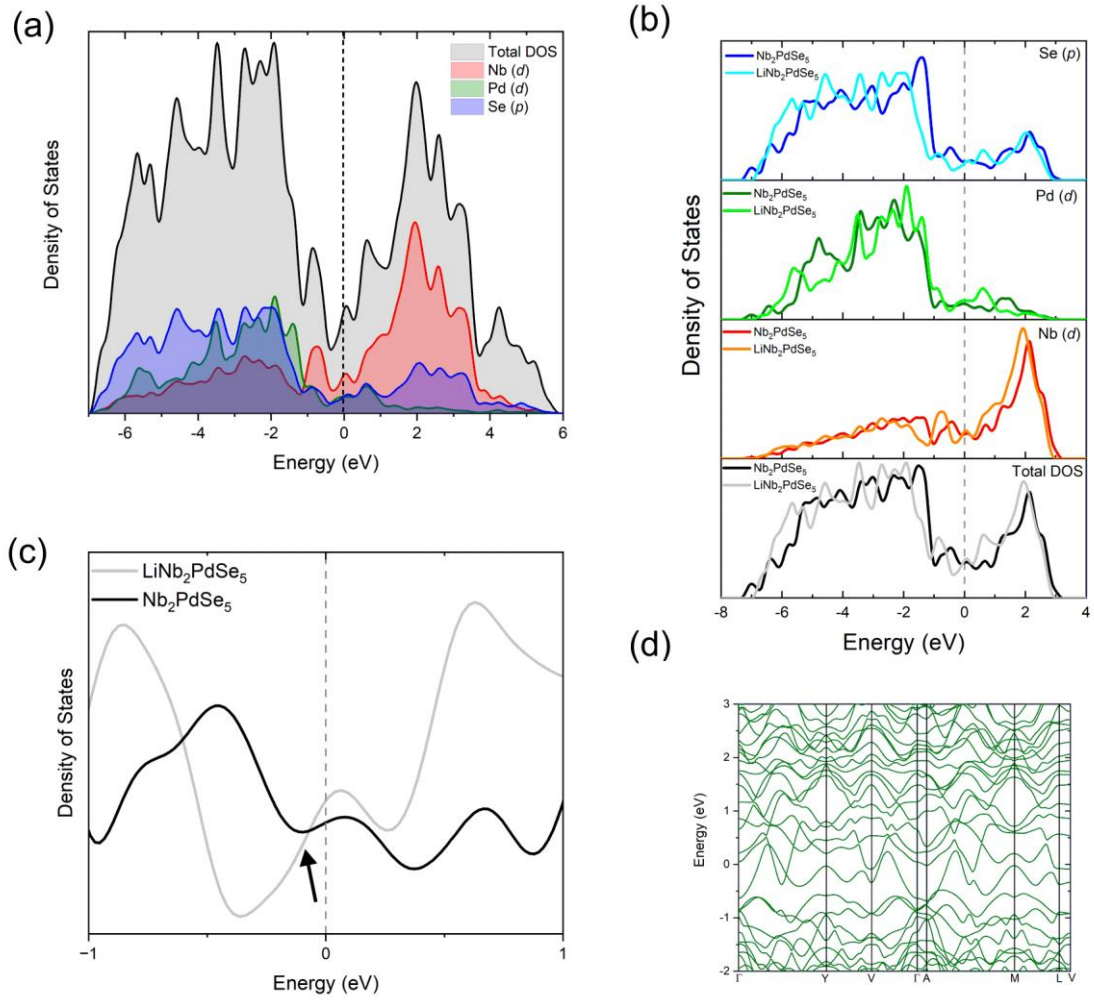


Figure 4.48: (a) Electronic density of states and (d) band structure for $LiNb_2PdSe_5$ assuming the octahedral site is fully occupied. (b) and (c) show a comparison of $LiNb_2PdSe_5$ to Nb_2PdSe_5. The arrow in (c) indicates the possible location of E_F for $LiNb_2Pd_xSe_5$ with lower DOS compared to $Nb_2Pd_xSe_5$.

4.3.8 XANES

XANES on the Nb *K*-edge was measured on the parent and chemically intercalated phase to probe changes in the Nb oxidation state. For stoichiometric Nb_2PdSe_5 with a fully occupied

Pd(2) site, the oxidation of Nb is +4. However, given the ~ 0.6 Pd(2) site occupancy by Pd^{2+} ions, then the formal oxidation of Nb is expected to be approximately +4.2. $NbSe_2$ was also measured as a reference for the Nb^{4+} oxidation state. All three samples show similar edge features with some very subtle variations around the post-edge region, which provides information on the local structure. This suggests that there is no change to the Nb oxidation upon intercalation, in agreement with the mean Nb-Se distances, which do not change significantly. However, due to the metallic nature and the strong delocalisation of the Nb states, it may be difficult to see changes in Nb oxidation, and it is possible that reduction is spread across both Nb and Pd.

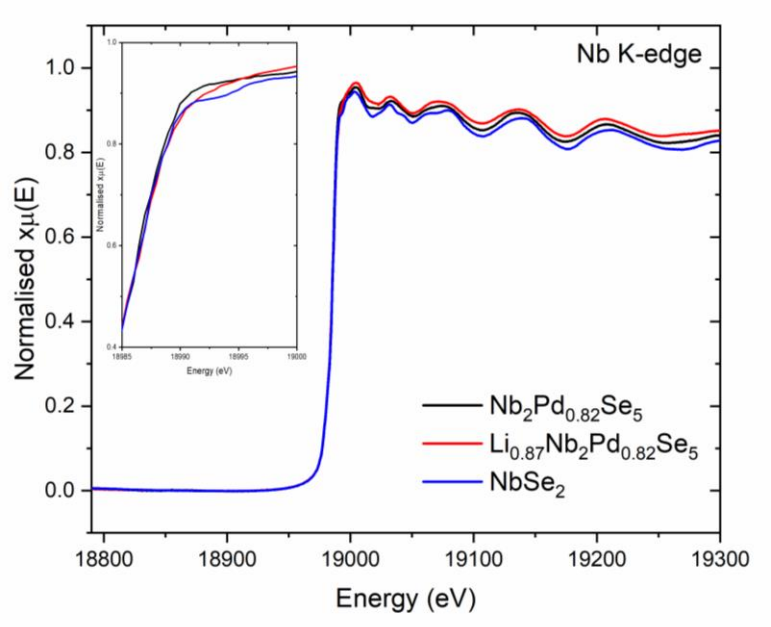


Figure 4.49: XANES on the Nb *K*-edge of $Nb_2Pd_{0.82}Se_5$, $Li_{0.87}Nb_2Pd_{0.81}Se_5$ and $NbSe_2$. $NbSe_2$ is shown here as a reference for the Nb^{4+} oxidation state.

4.4 Conclusions

This chapter has shown the Li intercalation in the isostructural $Nb_2Pd_xS_5$ and $Nb_2Pd_xSe_5$ superconductors. For $Nb_2Pd_{0.74}S_5$, single-phase intercalation was achieved using Li/NH_3 solution. The structure expanded in the unit cell mainly in the *a* and *c* directions with an increase in the monoclinic angle with the *C*2/*m* space group being maintained. The structure

of the intercalate was confirmed using synchrotron PXRD and PND, with Li found to occupy a triangular prismatic site with an occupancy of 0.33(4) obtained by refinement against PND data. Solid-state ^{7}Li NMR gave a single peak indicating that the Li occupies one site or was exchanging rapidly on the NMR timescale. The NMR resonance has a degree of broadness, suggesting Li is mobile. DFT calculations calculated the energies of the possible Li sites, with the triangular prismatic site being the lowest in energy in agreement with the neutron diffraction refinement.

The intercalated phase was deintercalated using iodine back to the parent phase with the lattice parameters suggesting trace amounts of Li potentially remaining. Superconductivity was suppressed upon intercalation but was partially restored upon deintercalation. The onset transition temperature decreased from 6.5 K to 5.5 K with a significant drop in volume fraction from 80 % to 7 %, possibly due to trace amounts of Li present. The injection of electrons into the delocalised system raised the Fermi level and, in accord with the computed density of states, decreased the density of states at the Fermi level and therefore reduced the Pauli susceptibility by ~ 40 %, consistent with the suppression of superconductivity.

Intercalation was also shown to be feasible using electrochemical methods. $Nb_2Pd_{0.74}S_5$ was discharged to specific capacities of 12 mAh/g, 25 mAh/g and 50 mAh/g, which gave a theoretical Li content of 0.19, 0.4 and 0.79, respectively. A step in the discharge curve was seen around 25-30 mAh/g. $Li_{0.19}Nb_2Pd_{0.75}S_5$ is a pure crystalline phase with similar lattice parameters to that obtained via chemical methods. For the sample discharged to 25 mAh/g, phase separation occurred into two intercalated phases. The main phase showed an expansion in the *a*-axis but a contraction in the *c* axis and monoclinic angle compared to the sample discharged to 12 mAh/g. The significant change in structure indicates that additional Li occupies a different site. The triangular prismatic site cannot be highly occupied due to

the proximity of the Li, causing electrostatic repulsion. The 0.33(4) Li content obtained from the refinement may perhaps be the upper limit of the site occupancy as it corresponds to the region just before the step in the discharge curve. The octahedral site is a probable position as it was calculated to be the second lowest in energy and can be fully occupied with minimal electrostatic repulsion. However, further neutron diffraction experiments on bulk samples synthesised electrochemically are needed to conclude this. The phase separation continues when the sample is discharged to 50 mAh/g. The unit cell expands significantly, with the increase in the volume following a linear trend with increasing Li content. However, due to the dual-phase nature of the intercalation, the lower resolution peaks and the complexity of the unit cell resulting overlap of peaks, it was challenging to reliably carry out a Rietveld refinement and deduce the detailed structural changes from the PXRD pattern.

For $Nb_2Pd_{0.82}Se_5$, Li/naphthalene solution was found to be the best reagent for intercalation. However, the compound appears to be prone to decomposition, especially when intercalating using *n*-BuLi. Like with the sulfide variant, the intercalated phase also showed expansion in the *a* and *c* axis with an increase in the monoclinic angle and no indication of a change in the *C*2/*m* symmetry. However, attempts at refining Li position and occupancy from PND were unsuccessful, most likely due to the low scattering lengths of Li compared to the other elements, especially Se. A possibility is that Li could be distributed over more than one site. ICP-MS analysis determined a Li occupancy of 0.87. DFT calculations were used to calculate the lowest energy Li sites, with predicted ^{7}Li NMR chemical shift which was compared with the experimental NMR. The calculated Li sites energy ordering was analogous to that found for the sulfide variant. The main difference is that the lowest energy triangular prismatic site is, for the selenide, off-centre and better represented as a 5-coordinate distorted square-based pyramid. In contrast to the sulfide, the calculated and experimental NMR resonance suggests Li occupies the octahedral site between the layers

despite it being the second lowest energy site calculated, consistent with higher Li occupation being achievable in this site than the lowest energy site calculated without unfavourable electrostatic repulsion. Additional peaks seen in NMR spectroscopy can be attributed to the decomposition products, Li_yNbSe_2 and Li_2Se.

$Nb_2Pd_{0.82}Se_5$ was discharged to specific capacities of 20 and 45 mAh/g, which gave a Li content of approximately 0.49 and 1.1, respectively. The unit cell volume increased linearly with Li content and is consistent with the composition of the chemically intercalated sample. $Li_{0.49}Nb_2Pd_{0.81}Se_5$ is isolated electrochemically as a phase pure crystalline phase. A single peak was seen in the NMR spectroscopy, which matched the main peak in $Li_{0.87}Nb_2Pd_{0.81}Se_5$. In the potential vs specific capacity graph, a plateau is seen at x(Li) ~ 1, in contrast to the sulfide where a step is seen at x(Li) ~ 0.4. This would be consistent with the filling up of one Li site before two-phase separation at x(Li) > 1. For the sample discharged at 45 mAh/g (x(Li) = 1.1), like when using *n*-BuLi, the compound begins to decompose with the Li_yNbSe_2 side phase detected in PXRD and NMR.

Magnetometry measurements are analogous to the sulfide variant with intercalation suppressing superconductivity with partial restoration upon deintercalation. The suppression and restoration of superconductivity can be similarly justified with the changes in the Pauli susceptibility. However, the calculated DOS of both systems are contrasting. For Nb_2PdS_5, E_F lies on a negative gradient, and therefore injecting electrons shifts E_F to a lower density of states. On the other hand, for Nb_2PdSe_5, E_F lies on a positive gradient, and it would be expected injecting electrons would shift E_F to a higher density of states. DOS calculated for $LiNb_2PdSe_5$ showed a change in topology compared to Nb_2PdSe_5, with a significant reduction in the density of states below E_F. Due to the overestimation in the electron count of $LiNb_2PdSe_5$ compared to $Li_{0.87}Nb_2Pd_{0.82}Se_5$, it is possible that E_F resides in that region of

reduced density of states. This could explain the reduction of the Pauli susceptibility and the suppression of superconductivity.

Despite the identical structures of $Nb_2Pd_xS_5$ and $Nb_2Pd_xSe_5$, the chemistry of both compounds has shown significant differences. Extending this further to the other member of this isostructural superconducting family: $Ta_2Pd_xS_5$ and $Ta_2Pd_xSe_5$, would be a good avenue of pursuit to investigate whether both these compounds show similar differences to their Nb counterpart.

Chapter 5

5 Magnetic Behaviour of $A_2Ga_2S_5$ (A = Mn, Fe)

5.1 Introduction

As mentioned in Chapter 1, much of the research on this ternary chalcogenide family focused on MGa_2S_4 (M = Fe, Ni) as the system consists of an exact triangular arrangement of the metal cations which leads to frustration and spin glass behaviour. In the bilayer $A_2Ga_2S_5$ (A = Mn, Fe), the metal cations form a buckled honeycomb-like lattice. The extra metal sulfide layer could, in theory, lift the frustration and allow for long-range magnetic ordering. Previous reports have mainly focused on $Fe_2Ga_2S_5$, drawing comparisons to its single-layer variant.

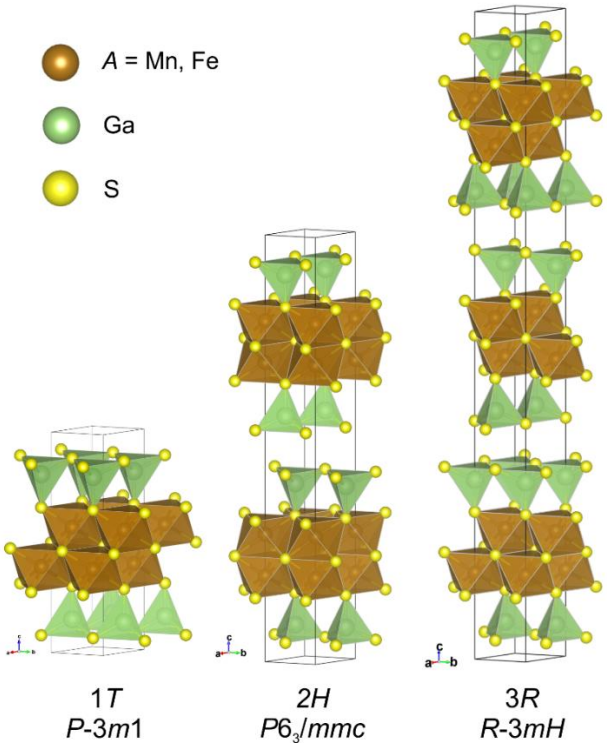


Figure 5.1: Structures of the three polytypes reported for $A_2Ga_2S_5$ (A = Mn, Fe).

First reports of $Fe_2Ga_2S_5$ were made in the early 1980s by Pardo and Dogguy-Smiri when studying the FeS-Ga_2S_3 phase diagram.[56,178] Three polytypes were reported, which are referred to as 1*T*, 2*H* and 3*R* crystallising in the *P*-3*m*1, *P*6$_3$/*mmc* and the *R*-3*mH* space groups, respectively, as shown in Figure 5.1. The number refers to the number of slabs in the units, with the letter corresponding to trigonal (*T*), hexagonal (*H*) or rhombohedral (*R*). This type of polytypism is not uncommon and is seen in some transition metal dichalcogenides such as TaS_2.[179] The 1*T* and 3*R* polytypes consist of the two metal layers edge sharing octahedra, leading to the buckled honeycomb arrangement. For 2*H*, these octahedra are face-sharing, resulting in the two triangular lattices being superimposed. In the 3*R* polytype, each slab is translated by (⅔, ⅓) in the *ab* plane relative to the layer below.

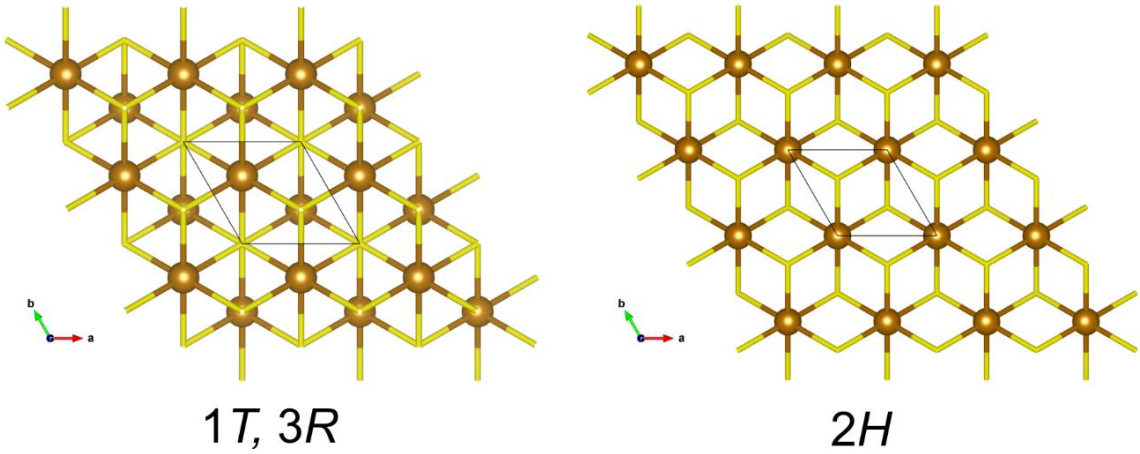


Figure 5.2: View along the stacking axis *c* showing how the 1*T* and 3*R* polytypes have a buckled honeycomb lattice, whereas, for the 2*H*, triangular lattices are superimposed on each other. The non-magnetic ions are excluded.

The 3*R* polytype is the most common and is obtained at a temperature of 1000 °C, whereas below that temperature, a mixture of the 2*H* and 3*R* is reported. $Mn_2Ga_2S_5$, on the other hand, was first reported in 1975 and is exclusively found as the 1*T* polytype crystallising in *P*-3*m*1.[180]

For $Fe_2Ga_2S_5$, Nakatsuji *et al.* reported 3D antiferromagnetic (AFM) ordering with SQUID magnetometry and specific heat capacity indicating a Néel temperature (T_N) of 113 K.[91]

Figure 5.3 shows the different *A*-S-*A* superexchange interactions for $A_2Ga_2S_5$. In the single layer variant, $FeGa_2S_4$, only J_1, which is a near-rectangular (~ 90°) nearest neighbour intralayer interaction, is present. In contrast, the bilayer $A_2Ga_2S_5$ has two additional interlayer coupling interactions, J_2 and J_3. J_2 is also a near-rectangular (~ 90°) nearest neighbour interaction, similar to J_1. J_3 is the second-nearest-neighbour interaction at a path of 180°.

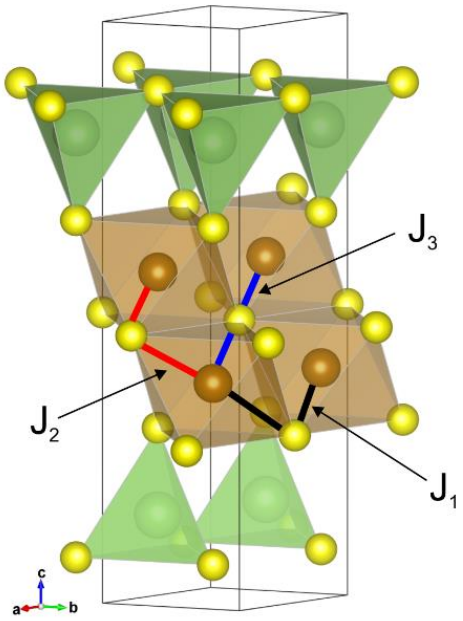


Figure 5.3: The three different coupling interactions seen in $A_2Ga_2S_5$.

Liao *et al.* carried out first-principles calculations on $Fe_2Ga_2S_5$.[181] Four different magnetic configurations were considered: Ferromagnetic (FM), AFM-Néel, AFM-zigzag and AFM-stripy, as shown below in Figure 5.4. The zigzag configuration was calculated to be the lowest in energy in the in-plane direction with T_N of 160 K. It was reported that for 3D magnetism, T_N was calculated to be 176 K, with the interaction between slabs being very weakly ferromagnetic and therefore the magnetism is likely to be 2D. These four magnetic

configurations were also a subject of study for the ABX_3 compounds (A = Mn, Cr; B = P, Si, Ge; X = S, Se, Te) with non-buckled honeycomb lattices, whereby a magnetic phase diagram of these four configurations was constructed.[182]

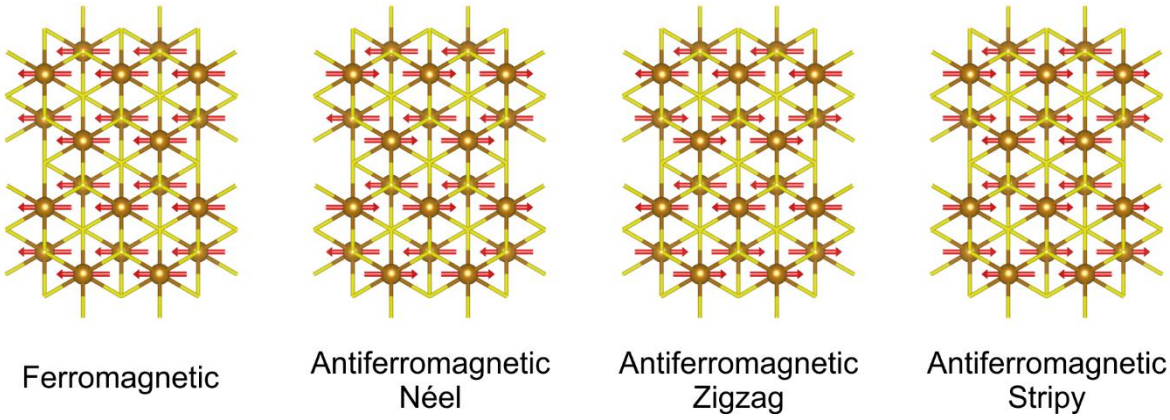


Figure 5.4: Different magnetic configurations of the buckled honeycomb lattice of $A_2Ga_2S_5$.

Since its first observation in the 1970s, the only study so far carried out on $Mn_2Ga_2S_5$ was in 2022, where Shen *et al.* reported magnetic susceptibility measurements showing antiferromagnetic-like behaviour with a Weiss temperature, θ_w, of approximately -260 K.[183] However, the authors reported no long-range magnetic ordering and observed a spin freezing transition at 12 K, well below θ_w.

Work in this chapter began before the report by Shen *et al.*[183] Prior to this work, no neutron diffraction measurements were carried out on these compounds. This chapter presents a study of $Mn_2Ga_2S_5$ and $Fe_2Ga_2S_5$ using X-ray and neutron powder diffraction, SQUID magnetometry and heat capacity. The solid solution $Mn_{2-x}Fe_xGa_2S_5$ will also be investigated.

5.2 Synthesis and Characterisation

5.2.1 $Mn_2Ga_2S_5$

Samples of $Mn_2Ga_2S_5$ were synthesised using a combination of the binary sulfides as was reported in the literature.[180] A 2:1 ratio of MnS (Alfa Aesar 99.9 %) and Ga_2S_3 (Alfa Aesar

99.999 %) powders were ground together, forming a pale green powder mixture, then pressed into a pellet using a force of 5 tonnes. The samples were heated to 900 °C at a rate of 2 °C/min for 12 hours. The powder turned brown in colour. From the synchrotron PXRD pattern collected using the MAC detector, small quantities of the MnS starting material (1.69 % by mass) and Ga_2O_3 (5.45 %) were detected. The starting material MnS had no presence of any oxides, whereas, Ga_2S_3 had a small amount (~ 2 %) of Ga_2O_3. Additional Ga_2O_3 could result from a reaction with the silica ampoule/alumina crucible or small amounts of O_2 or H_2O present in the ampoule. Flaming the ampoule using the blowtorch prior to synthesis was attempted to eliminate this, but it was found to have little effect. Attempts were made to synthesise this compound straight from the elements. However, these attempts were unsuccessful, with green MnS and metallic Ga present in the ampoule after heating.

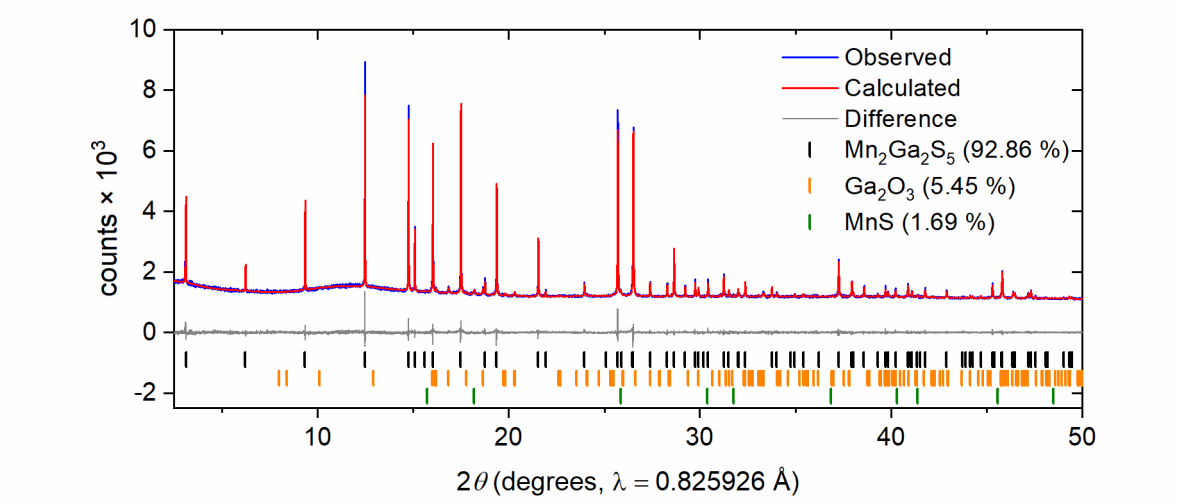


Figure 5.5: Rietveld refinement against I11 (MAC) PXRD pattern of $Mn_2Ga_2S_5$. R_{wp}: 7.04 %

A slight improvement in the fit of the model to the PXRD pattern was achieved by refining the occupancies of Mn and Ga. The Mn octahedral site was refined to a full occupancy of 1. However, the Ga tetrahedral site was refined to 0.966(8), indicating ~ 3.4 % vacancy on the Ga site. The R_{wp} reduced from 7.14 % to 7.04 %. This was probed further using PND data

collected on the WISH diffractometer at ISIS. Diffraction patterns were collected at 200 K, well above any magnetic ordering. Refining the site occupancies resulted in an Mn occupancy of 0.953(9) and a Ga occupancy of 0.801(4). The discrepancy between the PXRD and PND values, especially for the Ga site, indicates mixed-site occupancy. Implementing mixed sites in the PXRD refinement gave unreliable values, most likely due to the not-too-dissimilar electron count of Mn^{2+} and Ga^{3+}. However, the subtle changes can be highlighted well in the PND due to the stark contrast in the scattering lengths of Mn and Ga (Mn = -3.73 fm, Ga = +7.29 fm).[131] The R_{wp} of the PND refinement improves slightly from 6.78 % to 6.76 %

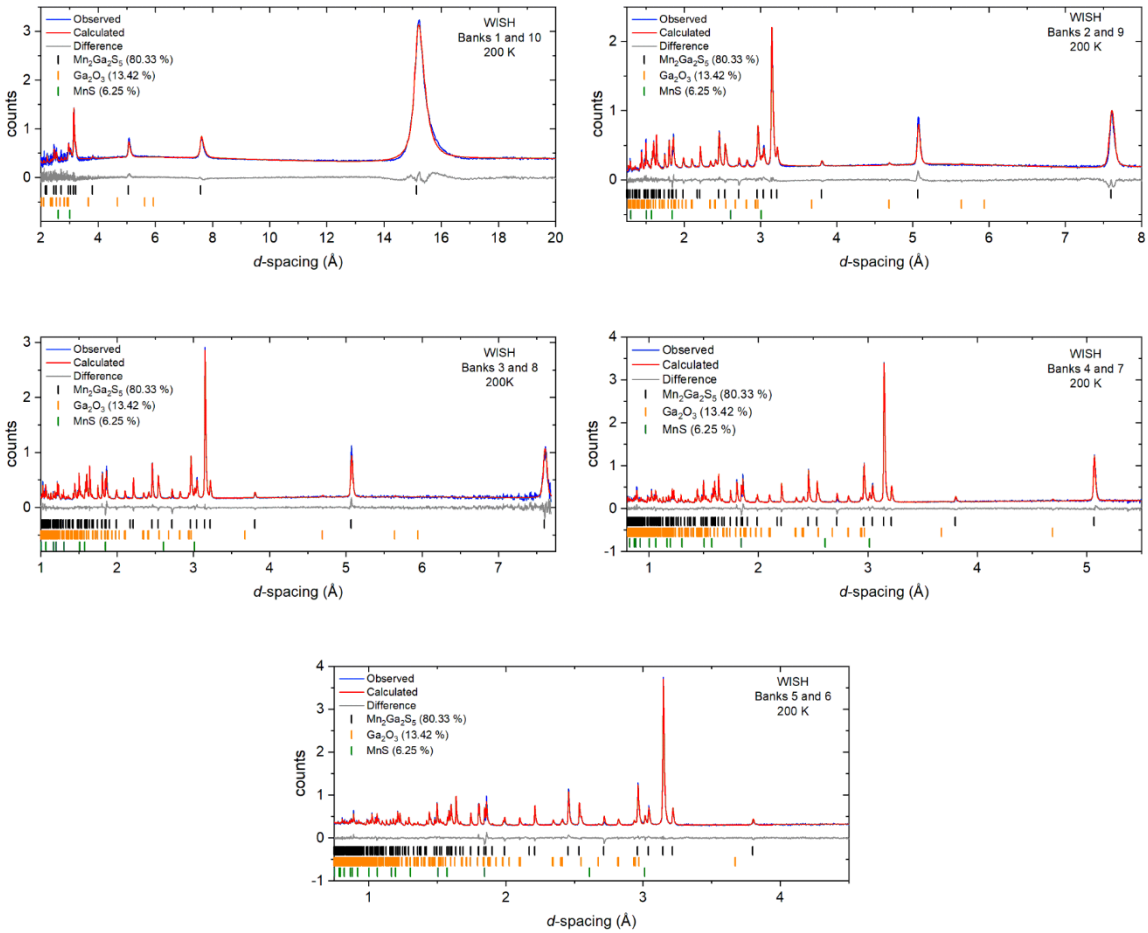


Figure 5.6: Rietveld refinement against ToF PND patterns of $Mn_2Ga_2S_5$ measured at WISH at 200 K R_{wp}: 6.76 %.

For the Ga site, adding Mn to this site resulted in the occupancy of Ga increasing by 0.05 to 0.852(2), with Mn refining to 0.107(4). These increases reflect the approximate 1:2 ratio of the magnitudes of the Mn and Ga scattering lengths and their opposite signs. The sum of these occupancies (0.852(2) and 0.107(4)) gives a total occupancy for the Ga site of 0.959(4), within error of the 0.966(8) occupancy obtained from the PXRD refinement. For the Mn site, adding Ga and allowing both Mn and Ga to freely refine resulted in an Mn occupancy of 0.99(1) and a Ga occupancy of 0.018(1). This indicates no vacancies on the Mn site, with the total occupancy marginally exceeding the maximum occupancy of 1 in an unconstrained refinement (although it was 1 within the error). The Mn site occupancy was therefore constrained to not exceed 1, resulting in an Mn occupancy of 0.984(3) and a Ga occupancy of 0.016(3). This would suggest 1-2 % Ga occupancy on the Mn site and correspond to a stoichiometry of $Mn_{2.18(1)}Ga_{1.74(1)}S_5$. There was no discussion on the possibility of mixed sites by Shen *et al.*[183] However, for $Mn_2In_2Se_5$, which is analogous to $Mn_2Ga_2S_5$ but crystallising in *R*-3*m*, the authors reported a 20 % occupation of the In tetrahedral site by Mn and an 18 % occupation of the Mn octahedral site by In.[184] In^{3+} has significantly larger electron count than Mn^{2+}, making the differentiation using XRD more reliable.

From the synchrotron PXRD data, the Ga_2O_3 impurity is ~ 5 % by mass. However, from PND, the % of Ga_2O_3 is ~ 14 % by mass. The impurities are more significant in the PND pattern, which is likely due to the fact that X-rays are far less penetrating than neutrons and therefore PXRD diffraction is more likely to examine the surface of the grain, whereas neutrons can penetrate further into the grain.

Table 5.1: Occupancy values of the Mn and Ga sites from the PXRD and PND Rietveld refinements.

	Element	Occupancy			
		PXRD	PND	PND-Mixed Sites	PND-Mixed sites (constraint)
Mn Octahedral Site	Mn	1	0.953(9)	0.99(1)	0.984(3)
	Ga	0	0	0.018(1)	0.016(3)
Ga Tetrahedral site	Ga	0.966(8)	0.801(4)	0.852(2)	0.853(3)
	Mn	0	0	0.107(4)	0.106(4)

Structural parameters obtained from the Rietveld refinement of both the PXRD and PND data are provided in Table 5.2.

Table 5.2: Structural parameters of $Mn_2Ga_2S_5$ (ME148) obtained from Rietveld refinement of synchrotron PXRD (MAC detector, 300 K) and PND (collected at WISH at 200 K). Values from PND are given in [ ].

$Mn_2Ga_2S_5$ (ME148)							
Space Group			***a* / Å**		***c* / Å**	**Volume / Å^3**	
***P*-3*m*1 (No. 164)**			3.71527(1) [3.71689(14)]		15.20988(7) [15.2167(6)]	181.817(1) [182.058(15)]	
Positional Parameters							
Atom	***x***	***y***	***z***	***Occupancy***	***Site***	***U_{11} = U_{22}* / Å^2**	***U_{33}* / Å^2**
Mn	⅓	⅔	0.6034(1) [0.5952(2)]	1 [Mn: 0.984(3) Ga: 0.016(3)]	2*d*	0.0155(6) [0.0385(13)]	0.0331(13)
Ga	⅓	⅔	0.1655(1) [0.1653(2)]	0.966(8) [Ga: 0.851(2) Mn: 0.107(4)]	2*d*	0.0136(6) [0.0117(6)]	0.0200(11) [0.0158(14)]
S(1)	0	0	0.5	1	1*b*	0.0279(19)	0.027(4) [0.022(2)]
S(2)	⅓	⅔	0.3122(1) [0.3095(2)]	1	2*d*	0.0106(10)	0.013(2) [0.022(2)]
S(3)	⅓	⅔	0.8970(2) [0.8916(2)]	1	2*d*	0.0182(11)	0.013(2) [0.022(2)]
***Bond Lengths* / Å**							
Mn-S(1) (× 3)						2.6601(10) [2.5891(16)]	
Mn-S(2) (× 3)						2.4996(15) [2.590(3)]	
Ga-S(2) (× 1)						2.231(3) [2.194(4)]	
Ga-S(3) (× 3)						2.3461(14) [2.3144(15)]	

5.2.2 $Fe_2Ga_2S_5$

Like the Mn variant, $Fe_2Ga_2S_5$ was synthesised using the binary sulfides FeS and Ga_2S_3. The pellet was heated to 1050 °C at 2 °C/min for 12 hours. Upon initial inspection of the synchrotron PXRD pattern, it appears that the 3*R* polytype is formed with minor impurities. However, closer examination of the diffraction pattern showed shoulder peaks to the right of the 006, 009 and 0012 Bragg reflections peaks and unaccounted intensities at the 101 and 104 reflections. Letting the occupancy of Fe and Ga refine made no difference to the intensities, with the values not deviating from 1. This would suggest another polytype of $Fe_2Ga_2S_5$ is present with a very minor reduction in lattice parameters (~ 0.03 % in the *a* and *c* parameters).

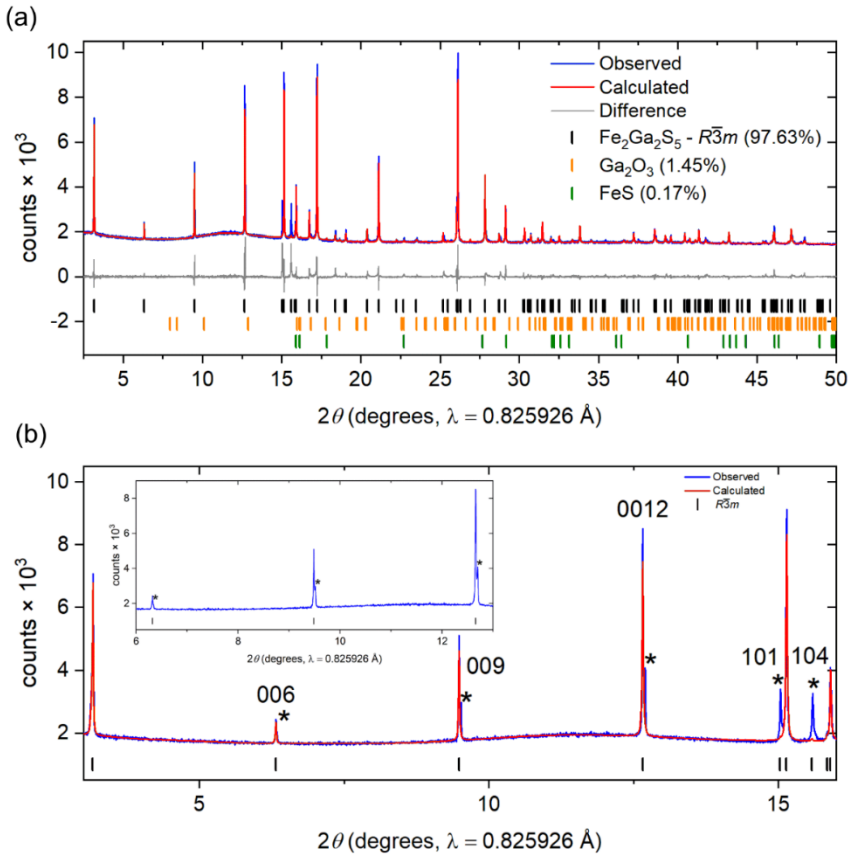


Figure 5.7: Rietveld refinement against I11 (MAC) PXRD pattern of $Fe_2Ga_2S_5$ with only the 3*R* polytype, R_{wp}: 12.02 %. (b) shows the shoulder peaks on the 00*l* reflections and unaccounted intensity at 101 and 104 Bragg reflections, suggesting another polytype present.

Adding the 1*T* model ($Mn_2Ga_2S_5$ structure) to the Rietveld refinement accounted for the shoulder peaks of the 00*l* Bragg reflections and for the 101 Bragg reflection (corresponds to the 100 Bragg reflection for the 1*T* structure). The R_{wp} decreases from 12.02 % to 10.35 %. However, the additional intensity at the 104 Bragg reflection remains unaccounted for. The extra intensity could not be accounted for by preferred orientation or anisotropic thermal displacement. No known compound in the ICSD was found to correspond to that reflection. The 2*H* polytype did not account for any additional intensity and can be excluded. It is plausible that extra intensity may arise from a stacking disorder in the 3*R* structure or an intergrowth of the 1*T* and 3*R* polytypes. This could be investigated further by using HAADF-STEM imaging like that found in the single layer $NiGa_2S_4$.[89]

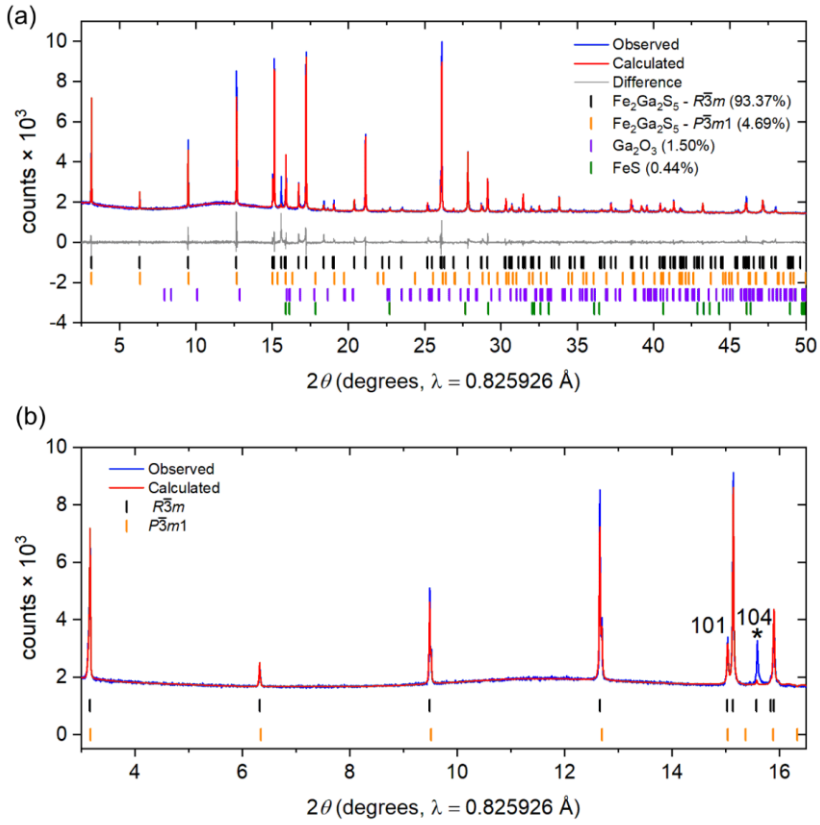


Figure 5.8: (a) Rietveld refinement against I11 (MAC) PXRD pattern of $Fe_2Ga_2S_5$ with the 3*R* and 1*T* polytypes, R_{wp}: 10.35 %. (b) shows that the addition of the 1*T* polytype accounts 00*l* shoulders peak and the 101 reflection (100 for the 1*T* structure).

In the PND, the 00*l* peaks are less resolved compared to the synchrotron PXRD and the shoulder peaks are less obvious. The pattern was modelled well with both the 3*R* and 1*T* polytypes, with the latter as a very minor side phase. Like with the PXRD pattern, the 104 Bragg reflection cannot be accounted for.

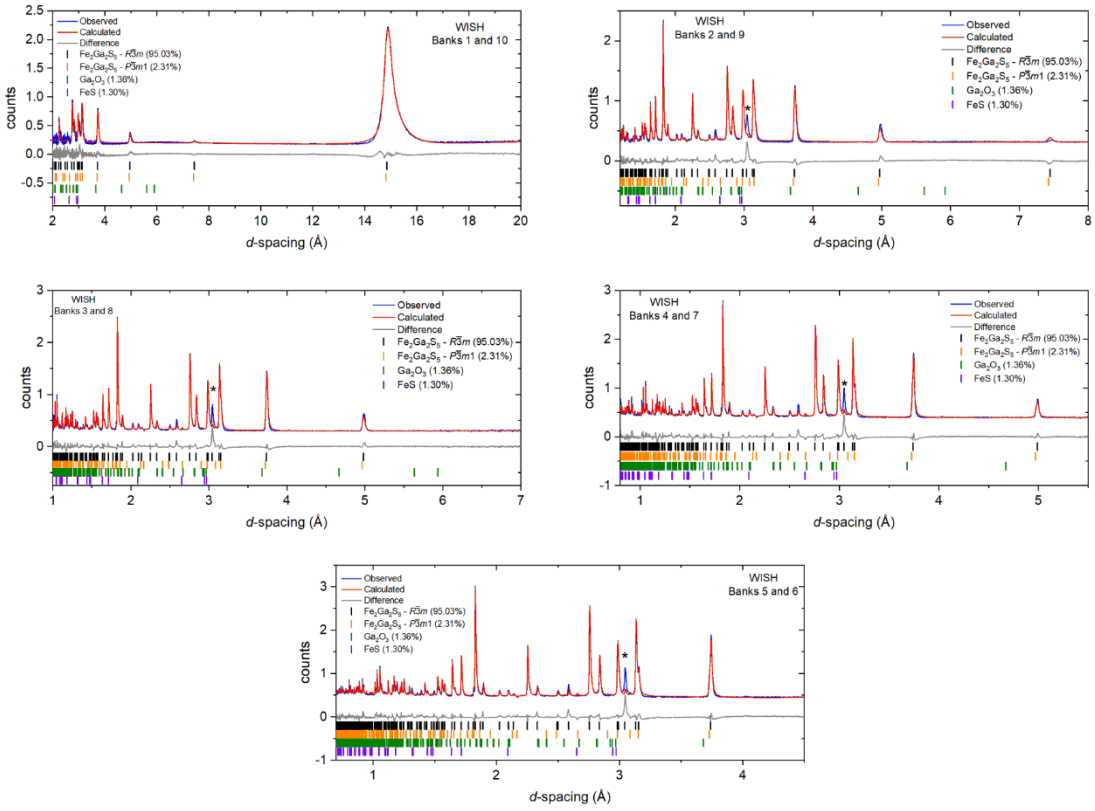


Figure 5.9: Rietveld refinement against ToF PND patterns of $Fe_2Ga_2S_5$ measured at WISH at 200 K, R_{wp}: 9.81 %. The * indicates the extra intensity at 104 Bragg reflection that was also unaccounted for in the PXRD refinement.

Another possibility is that perhaps a different polytype is formed, unlike what was previously reported. For example, $Fe_2In_2Se_5$ adopt a *P*-3*m*1 structure. However, it is different from $Fe_2Ga_2S_5$ in that instead of the Fe^{2+} bilayer being edge-sharing octahedra, one of the two layers is tetrahedrally coordinated like Ga.[185] This was attempted by taking the model of $Fe_2In_2Se_5$, replacing In and Se with Ga and S, reducing the lattice parameter such that the interlayer spacing matched that of the 1*T* and 3*R* structures. However, this attempt also was

unsuccessful and did not account for the extra intensity. Perhaps another stacking variant, crystallising in another space group, may exist but not reported. The diverse structural chemistry of these compounds and structure types can make analysis of powder diffraction patterns difficult. Further work is necessary with the use of imaging techniques to get a better insight.

Another differing feature is that the amount of Ga_2O_3 impurity detected in both the PXRD and PND patterns of $Fe_2Ga_2S_5$ is considerably lower than that seen in patterns of $Mn_2Ga_2S_5$ despite using the same Ga_2O_3 starting material. A possibility is that the reaction for $Mn_2Ga_2S_5$ is more susceptible to reaction with the silica tube compared to the Fe variant.

Table 5.3: Structural parameters of $Fe_2Ga_2S_5$ (ME151) obtained from Rietveld refinement of synchrotron PXRD (MAC detector, 300 K) and PND (collected at WISH at 200 K). Values from PND are given in [ ].

$Fe_2Ga_2S_5$ (ME151)							
Space Group			***a* / Å**		***c* / Å**	**Volume / Å^3**	
R-3*m* (No. 166)			3.65534(2) [3.6564(7)]		44.9604(8) [44.936(9)]	520.257(9) [520.2(2)]	
Positional Parameters							
Atom	***x***	***y***	***z***	***Occupancy***	***Site***	***U_{11} = U_{22}* / Å^2**	***U_{33}* / Å^2**
Fe	0	0	0.13285(5) [0.13290(5)]	1	6*c*	0.017(1) [0.0071(6)]	0.0155(2)
Ga	0	0	0.27706(5) [0.27739(6)]	1	6*c*	0.0128(7) [0.0083(9)]	0.0121(18)
S(1)	0	0	0.5	1	3*b*	0.023(2) [0.0102(9)]	0.018(5)
S(2)	0	0	0.2282(1) [0.2275(2)]	1	6*c*	0.0142(15) [0.0102(9)]	0.0129(4)
S(3)	0	0	0.3666(1) [0.3662(2)]	1	6*c*	0.025(2) [0.0102(9)]	0.018(4)
***Bond Lengths* / Å**							
Fe-S(1) (× 3)						2.6011(14) [2.6003(14)]	
Fe-S(2) (× 3)						2.450(3) [2.437(5)]	
Ga-S(2) (× 1)						2.198(6) [2.240(9)]	
Ga-S(3) (× 3)						2.351(3) [2.352(4)]	

5.3 Magnetism

5.3.1 SQUID Magnetometry

Room-temperature magnetisation vs field measurements resulted in a molar susceptibility χ_{mol} of $1.667(1)\times10^{-2}$ and $1.1211(1)\times10^{-2}$ emu mol^{-1} for $Mn_2Ga_2S_5$ and $Fe_2Ga_2S_5$, respectively. The magnitude of these values is typical of that seen for antiferromagnetic materials. The linear line seen in both indicates that there is no ferromagnetic impurity.

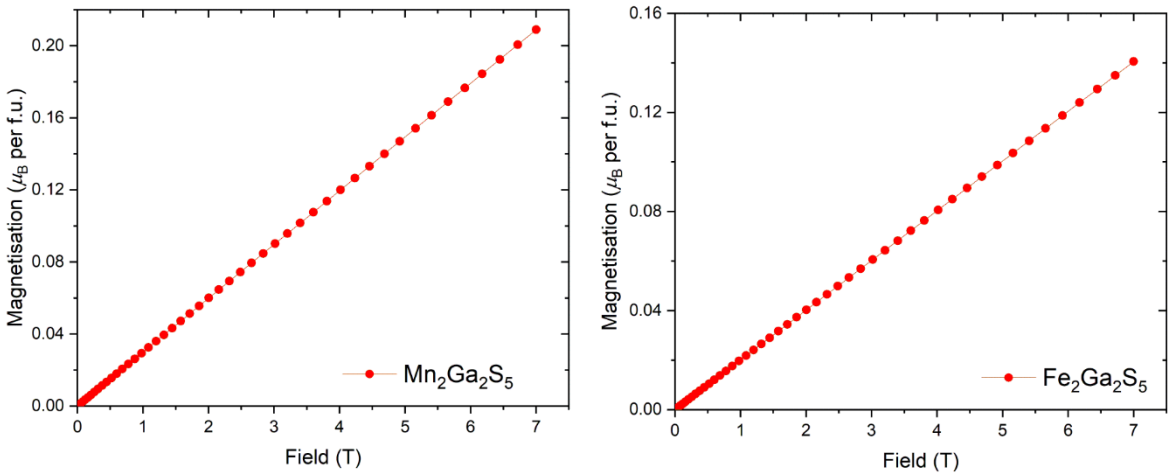


Figure 5.10: Magnetisation against field measurements at 300 K for $Mn_2Ga_2S_5$ (left) and $Fe_2Ga_2S_5$ (right).

Susceptibility vs temperature measurements measured at 100 Oe show a sharp antiferromagnetic-like transition for $Mn_2Ga_2S_5$ at a temperature of ~ 12 K, in agreement with Shen *et al.*[183] The curve seems to obey the Curie-Weiss law at high temperatures. A linear fit to $1/\chi_{mol}$ (see Equation 1.4 in section 1.4.5) yields a Weiss temperature (θ_w) of -282 K, in line with the -260 K value reported by Shen *et al.*[183] It should be noted that if the Weiss temperature is a large fraction of the maximum temperature used in the measurement, the Curie-Weiss law is often not obeyed well.

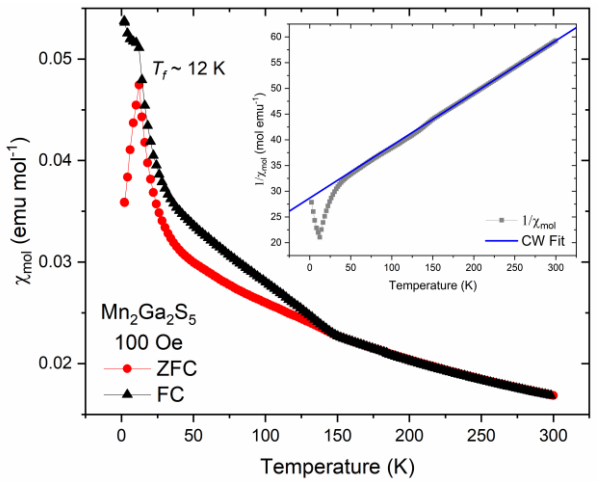


Figure 5.11: Molar susceptibility (χ_{mol}) against temperature measured at 100 Oe for $Mn_2Ga_2S_5$. Inset shows $1/\chi_{mol}$ and the Curie-Weiss fitting.

In typical antiferromagnetic non-frustrated systems, the ordering (Néel) temperature (T_N) is similar in value to θ_w. The large discrepancy between T_N and θ_w is indicative of spin frustration. The transition temperature is better represented for spin glass materials as the spin freezing temperature, T_f. The frustration can be expressed by an empirical value, f, which is given by:[186]

$$f = -\frac{\theta_w}{T_f} \qquad \text{Equation 5.1}$$

For $Mn_2Ga_2S_5$, this results in f ~ 23 which is much larger than f ~ 8 and 10 reported for the single layer $NiGa_2S_4$ and $FeGa_2S_4$, respectively,[91] and larger than other known geometrically frustrated magnets such as VCl_2 (f ~ 12) and $Gd_{0.8}La_{0.2}CuO_2$ (f ~ 16).[187,188] From the Curie-Weiss fitting, an effective moment (μ_{eff}) of 4.43(1) μ_B per Mn^{2+} is obtained. This value is lower than the expected spin-only value of 5.92 μ_B for high spin Mn^{2+} ($3d^5$, S = 5/2), possibly due to covalency. Lower than expected moments have been previously reported for other Mn^{2+} buckled-honeycomb compounds such as $BaMnSb_2$ (3.76 μ_B/Mn).[189] As mentioned previously, when the Weiss temperature is comparable to the maximum measurement temperature, then the Curie-Weiss law is often not obeyed well, and it is

possible here that the compound is simulating the Curie-Weiss law, so the effective moment extracted may not be truly reliable. There is a noticeable deviation in the zero-field-cooled (ZFC) and field-cooled (FC) curves above the ordering temperature. This feature is not uncommon for spin glasses as this arises due to the arrangement of local domains persisting above the global glass transition temperature. The deviation at higher temperatures is not seen when measuring at higher fields of 5 kOe and 10 kOe. Comparing the curves shown in Figure 5.12, no obvious transition is seen at higher fields. However, a closer inspection, as shown in the insets of Figure 5.12, shows the bifurcation of the ZFC and FC curves with T_f at approximately 8 K and 6 K at 5 kOe and 10 kOe, respectively. This is in line with the report by Shen *et al.*,[183] which reported T_f of 12 K at 500 Oe. However, at 5 kOe, they observe that the ZFC and FC curves split at 8.5 K. The shifting of T_f to lower temperatures has previously been reported in other spin glass materials, such as $Cr_{0.5}Fe_{0.5}Ga$ and $Ba_3TiRu_2O_9$.[190,191] For $Ba_3TiRu_2O_9$, T_f was observed to shift from 4.7 K at 60 Oe to 3.8 K and 2.5 K at 2.5 kOe and 10 kOe respectively.

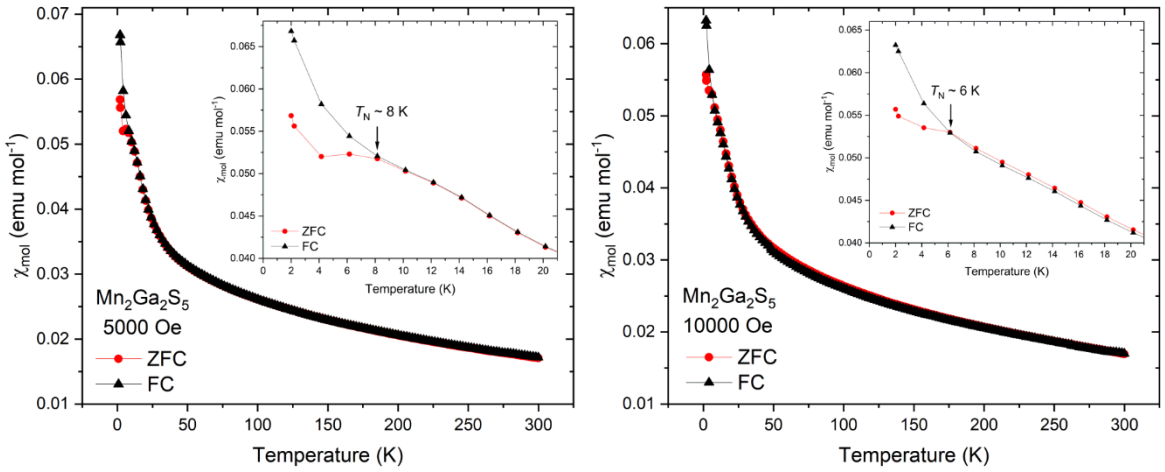


Figure 5.12: Molar susceptibility (χ_{mol}) against temperature measured at 5000 Oe (left) and 10000 Oe (right) for $Mn_2Ga_2S_5$, showing how the transition temperature decreases with increasing field.

For $Fe_2Ga_2S_5$, susceptibility vs temperature measurements show a broader transition at approximately 50 K, a considerable contrast to the reported 113 K and 160 K temperatures

obtained using experimental and computational methods, respectively.[91,181] Curie-Weiss fitting at high temperatures results in a θ_w of -398 K and a μ_{eff} of 3.92 μ_B per Fe ion, which is less than the 4.9 μ_B expected for Fe^{2+} ($3d^6$, $S = 2$). Nakatsuji *et al.*[91] reported θ_w values of -540 K and -480 K when measuring the sample along the 100 and 001 planes, respectively, and an effective moment of 5 μ_B. Again, these Weiss constants are large, so the Curie-Weiss law should be used with caution.

Using the θ_w of -398 K and approximating the transition to 50 K gives an f value of ~ 8, similar to its single-layer counterpart and also suggestive of frustration. The curves show what appears to be a ferromagnetic-like component at ~ 80 K, but when measuring at higher fields (1000 Oe), this transition is not apparent, with only a small bifurcation in the ZFC and FC curves seen at that temperature. The transition becomes sharper, and it can be seen in Figure 5.13 that T_f has shifted to lower temperatures and is now ~ 24 K, a much more significant change than that observed with $Mn_2Ga_2S_5$.

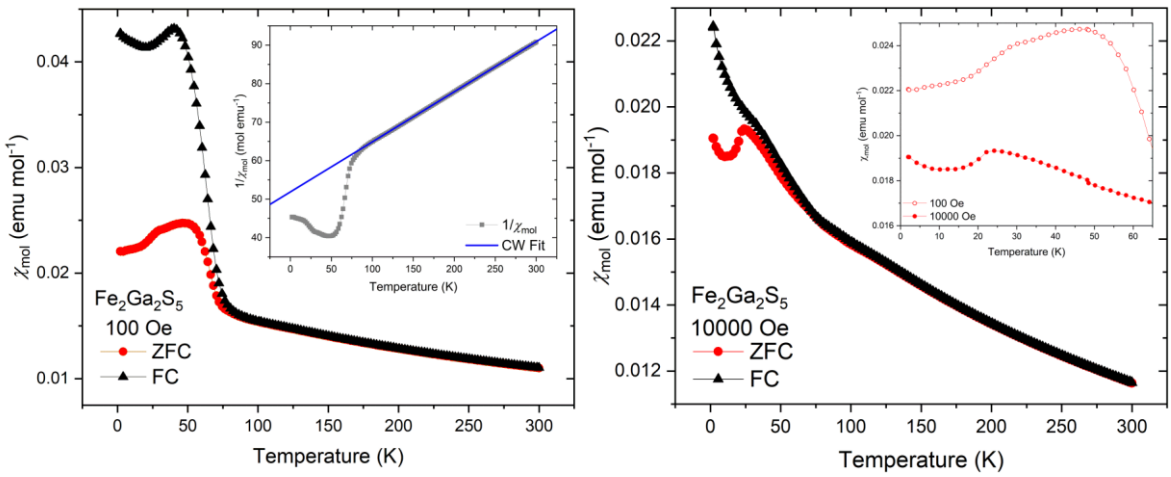


Figure 5.13: Molar susceptibility (χ_{mol}) against temperature measured at 100 Oe (left) and 10000 Oe (right) for $Fe_2Ga_2S_5$.

Table 5.4: Values obtained from the plots M against H, χ_{mol} against T and Curie-Weiss fitting.

	χ_{mol} (Room-temperature) / emu mol^{-1}	Transition temperature (at 100 Oe) / K	θ_w / K	μ_{eff} / μ_B per f.u.
$Mn_2Ga_2S_5$	$1.667(1)\times10^{-2}$	12 K	-282(1)	4.43(1)
$Fe_2Ga_2S_5$	$1.121(1)\times10^{-2}$	~ 50K	-398(1)	3.92(1)

Magnetisation against field isotherms for $Mn_2Ga_2S_5$ shows a straight line at room temperature. However, at 5 K, a hysteresis loop is observed between ±3 T. From initial inspection, it may appear that the hysteresis is symmetrically about the origin, but upon closer inspection, the hysteresis is off-centre. Figure 5.14 shows how the coercive fields (the reverse magnetic field needed to cancel the remnant magnetisation after saturation) are -0.27 T and 0.19 T, a difference of 0.08 T. The retentivity, a measure of the sample's ability to retain a certain amount of residual magnetic field when the magnetisation force is removed, is 0.019 μ_B / f.u. (5 % of the maximum magnetisation) when the positive field is removed. When the negative field is removed, the retentivity is 0.013 μ_B / f.u., a difference of 0.006 μ_B / f.u. The off-centre hysteresis loop is characteristic of spin glass materials. In a spin glass, the domains are locked and display a hysteresis with respect to the field aligning them. When a negative field is applied, domains may leave the locked state, but the memory of the initial state can remain. This means the magnetisation returns more easily when returning to a positive field.

The indication of spin glass behaviour is more evident in the magnetisation isotherm on $Fe_2Ga_2S_5$. Although the hysteresis at 5 K shows a very slim body compared to $Mn_2Ga_2S_5$, it is significantly off-centre and deviates from the origin by 0.02 μ_B / f.u. (~ 9 % of the maximum magnetisation).

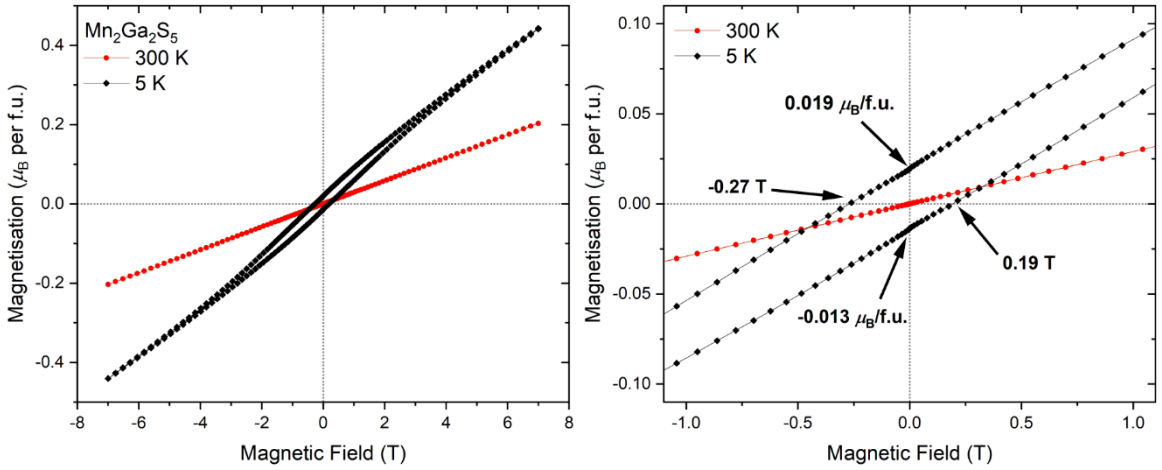


Figure 5.14: Magnetisation against field at 300K and 5 K for $Mn_2Ga_2S_5$. The graph on the right shows a close-up at ±1 T showing how the hysteresis is slightly displaced from the origin indicating glassy behaviour.

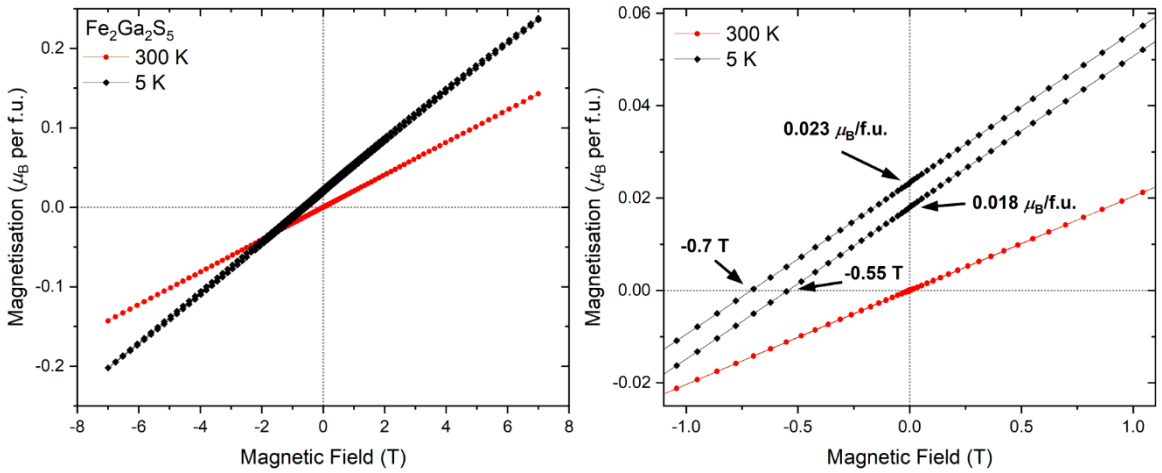


Figure 5.15: Magnetisation against field at 300K and 5 K for $Fe_2Ga_2S_5$. The graph on the right shows a close-up at ±1 T showing how the hysteresis is highly displaced from the origin indicating glassy behaviour.

To probe the dynamics of the spin-freezing transition in $Mn_2Ga_2S_5$, AC susceptibility was measured at temperatures around $T_f \sim 12$ K. Six frequencies were measured from 13 - 417 Hz using a small, fixed AC magnetic field of 3 Oe. From Figure 5.16, the real part of the AC susceptibility (χ') shows small frequency dependence with the peak shifting to higher temperatures and the peak height decreasing with increasing frequency (v). Across the measured frequency range, the peak shifts from approximately 12.3 K to 12.6 K and decreases in amplitude by ~ 1 memu mol^{-1}. This is indicative of the glassy behaviour and

was also observed by Shen *et al.*,[183] and is reported for other spin glasses such as $Cr_{0.5}Fe_{0.5}Ga$.[190]

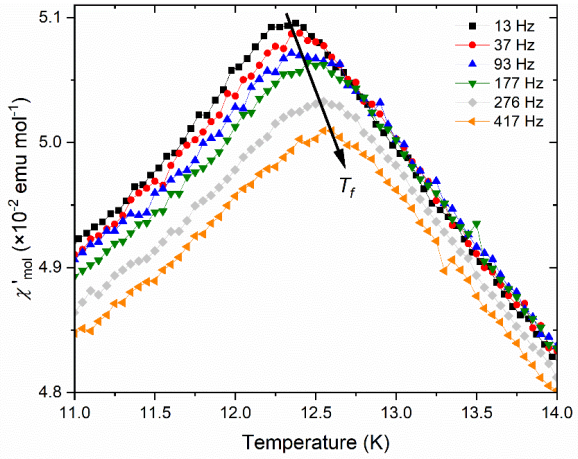


Figure 5.16: AC susceptibility measurement for $Mn_2Ga_2S_5$. The arrow shows how the T_f shifts to higher temperatures with increasing frequency.

The shift of the peak with respect to ν can be expressed by the Mydosh parameter, T_M,[192] which is expressed as:

$$T_M = \frac{\Delta T_f}{T_f \Delta \log_{10}(\nu)} \qquad \text{Equation 5.2}$$

Where $\Delta T_f = T_f(\nu_2) - T_f(\nu_1)$ and $\Delta\log_{10}(\nu) = \log_{10}(\nu_2) - \log_{10}(\nu_1)$. This parameter is used to compare other spin glass systems and reflects how sensitive the system is to the frequency, which depends on the strength of the interactions. For example, in a typical magnetic system, interactions between the magnetic ions are strong. Therefore, to observe any shift in the AC susceptibility, a very large frequency (in the MHz range) is needed.

Taking the two outermost frequencies, ν_1 = 13 Hz and ν_2 = 417 Hz, results in $T_M \approx 0.016(4)$. This value is similar to the 0.017 reported for the spin glass $Cr_{0.5}Fe_{0.5}Ga$,[190] and approximately an order of magnitude larger than other canonical spin glasses such as CuMn (T_M = 0.005) and AgMn (T_M = 0.0045).[192] The AC susceptibility of $Fe_2Ga_2S_5$ was measured,

but the lack of a defined sharp transition point, unlike that seen in the Mn variant, made it difficult to analyse.

5.3.2 Powder Neutron Diffraction

Powder neutron diffraction patterns were collected at 1 K. Both $Mn_2Ga_2S_5$ and $Fe_2Ga_2S_5$ show no sharp magnetic peaks. Instead, a very broad asymmetric peak around a *d*-spacing of 6.4 Å is observed. For $Mn_2Ga_2S_5$, amid the broad peak, a sharp peak is seen at $d \approx 6$ Å, which was identified as the magnetic peak arising from the MnS impurity. From the variable temperature measurements, only the magnetic MnS peak was seen at 100 K as MnS has a T_N of ~ 150 K.[79] The broad peak was seen at 20 K, above the 12 K transition temperature observed using SQUID magnetometry. Due to the lack of beam time, patterns were collected only at a few temperatures around the 12 K transition temperature. Further measurements are required to determine at what temperature between 20 to 100 K this magnetic feature emerges. Another feature seen upon cooling is that the background becomes non-linear in the *d*-spacing region of 3-8 Å. This is likely the consequence of the broad diffuse peak. The background was difficult to model as attempts to model it would model the peak as well.

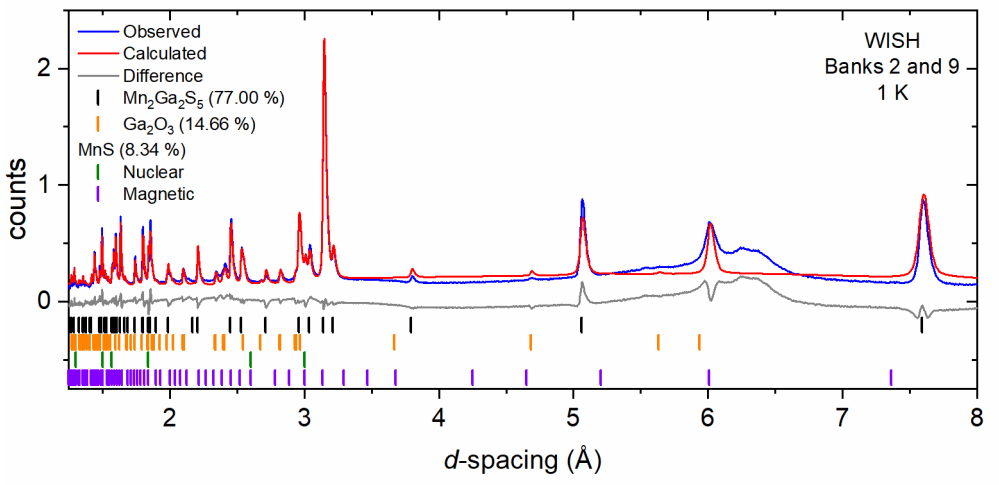


Figure 5.17: Rietveld refinement against ToF PND (WISH Bank 2-9) pattern of $Mn_2Ga_2S_5$ measured at 1 K showing the broad diffuse magnetic scattering. R_{wp}: 13.93 %.

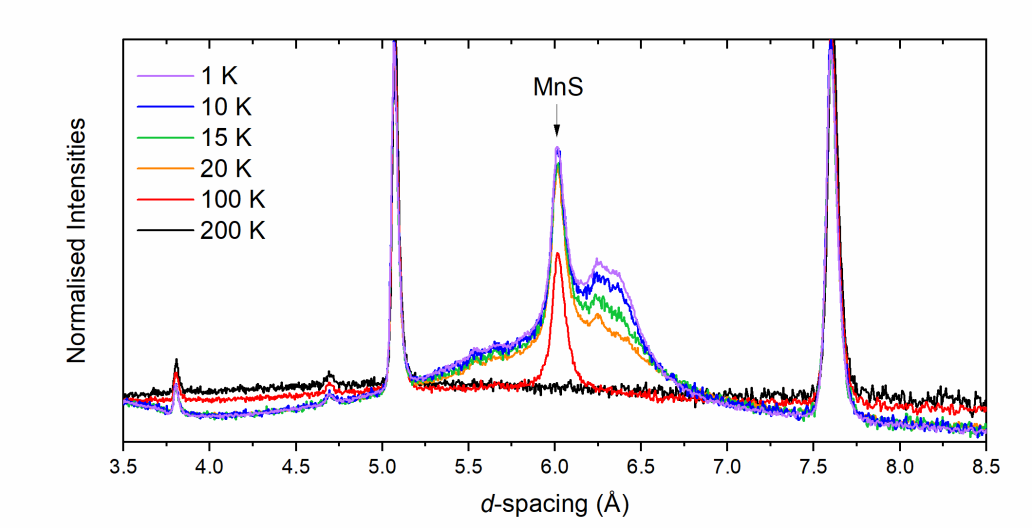


Figure 5.18: Variable temperature PND patterns of $Mn_2Ga_2S_5$ showing the formation of the MnS magnetic peak above 100 K and the presence of the broad asymmetric between 20-100 K.

For $Fe_2Ga_2S_5$, the broad asymmetric peak closely resembles that of $Mn_2Ga_2S_5$ in the same region of 6.1-6.3 Å. Variable temperature measurements show the peak present in the temperature range of 80-100 K, again above the transition temperature observed from SQUID magnetometry. The exact temperature of this transition was not determined due to the lack of beam time during the experiment. No other magnetic peaks from side phases are seen in the diffraction pattern.

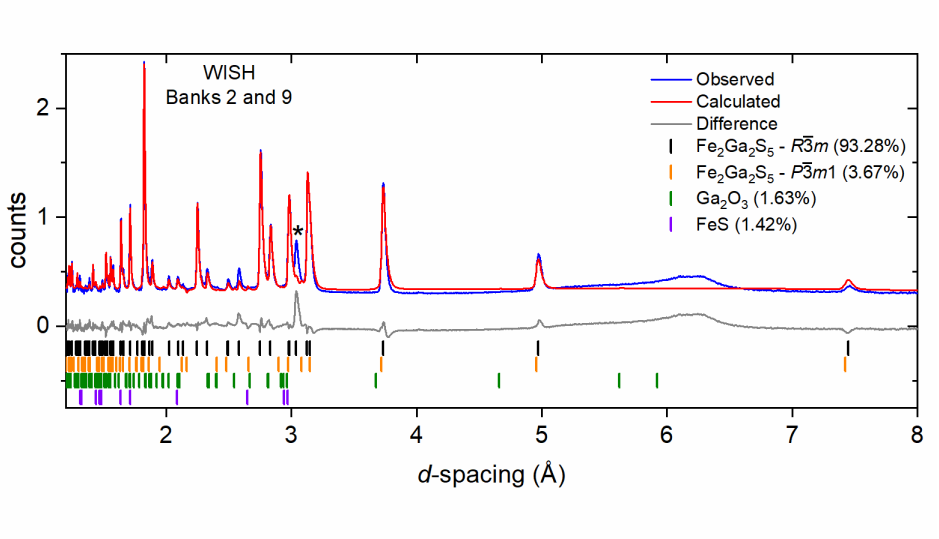


Figure 5.19: Rietveld refinement against ToF PND (WISH Bank 2-9) pattern of $Fe_2Ga_2S_5$ measured at 1 K showing the broad diffuse magnetic scattering. R_{wp}: 9.80%.

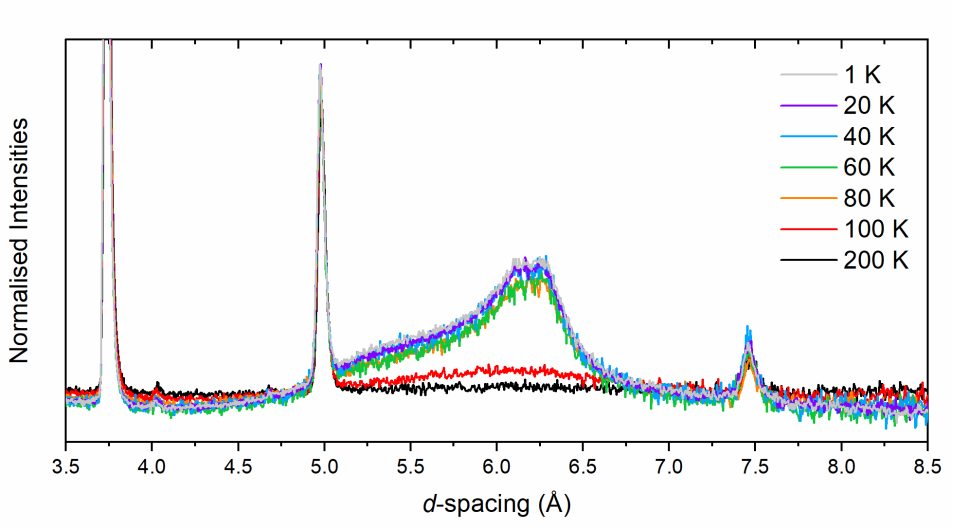


Figure 5.20: Variable temperature PND patterns of $Fe_2Ga_2S_5$ (Banks 2-9) showing the formation of the broad asymmetric between 80-100 K.

The absence of sharp magnetic peaks indicates no long-range magnetic ordering. The broad asymmetric bump would suggest only short-range ordering. The shape of the peak with the long tail is characteristic of a Warren-like peak.[193] The Warren peak-shape function was first used by Warren *et al*. in the PXRD analysis of two-dimensional carbon black,[194] which was found to be well ordered in the *ab* plane but disordered in the *c*-direction. More recently, magnetic peaks of compounds such as $La_2O_2Fe_2OSe_2$,[195] $Sr_2FFe_2O_2S_2$,[196] and $Sr_2MnO_2Cu_{2-x}Te_2$,[197] can be well described by the Warren peak-shape function. The Warren peak-shape function illustrates the short-range and two-dimensional nature of the magnetic ordering. To model the Warren-like peak, the diffraction patterns are plotted in reciprocal space, Q (= $2\pi/d$), rather than d-spacing. For the remainder of this chapter, the magnetic scattering will be discussed in Q-space. The function is given by:[193,196]

$$S(\boldsymbol{Q}) = \frac{1}{2\pi\sigma_{\perp}^2} exp\left[-\frac{1}{2}\left(\frac{|\boldsymbol{Q}-\tau_1|_{\perp}}{\sigma_{\perp}}\right)^2\right]\frac{\xi_c}{\pi}\frac{1}{1+(\xi_c|\boldsymbol{Q}-\tau_2|_{\parallel})^2} \qquad \text{Equation 5.3}$$

Where the long-range and short-range correlations along the c-axis are characterised by the Gaussian and Lorentzian components, respectively. $\sigma_{\perp}$ denotes the in-plane peak width, τ the

position of the peak centre and ξ_c the correlation length. For both $Mn_2Ga_2S_5$ and $Fe_2Ga_2S_5$, the patterns plotted in Q-space are shown below in Figure 5.21, along with the fit of the Warren function. The Warren function models the peak in both compounds well with the values from the fitting in Table 5.5. In $Mn_2Ga_2S_5$, the wave-like background due to the diffuse nature of the Warren peak can be fitted with the function. Although extra peaks are present within this range due to the nuclear part of $Mn_2Ga_2S_5$ and the MnS magnetic peak, this region can still be modelled by ignoring the extra intensity from these peaks. The good fit of the Warren peak shows that the magnetic behaviour is likely to be 2D. The distance between adjacent bilayers in both compounds is ~ 15 Å with a van der Waals gap separating them. It is expected that there would be little to no interaction between adjacent bilayers resulting in the magnetic ordering being 2D.

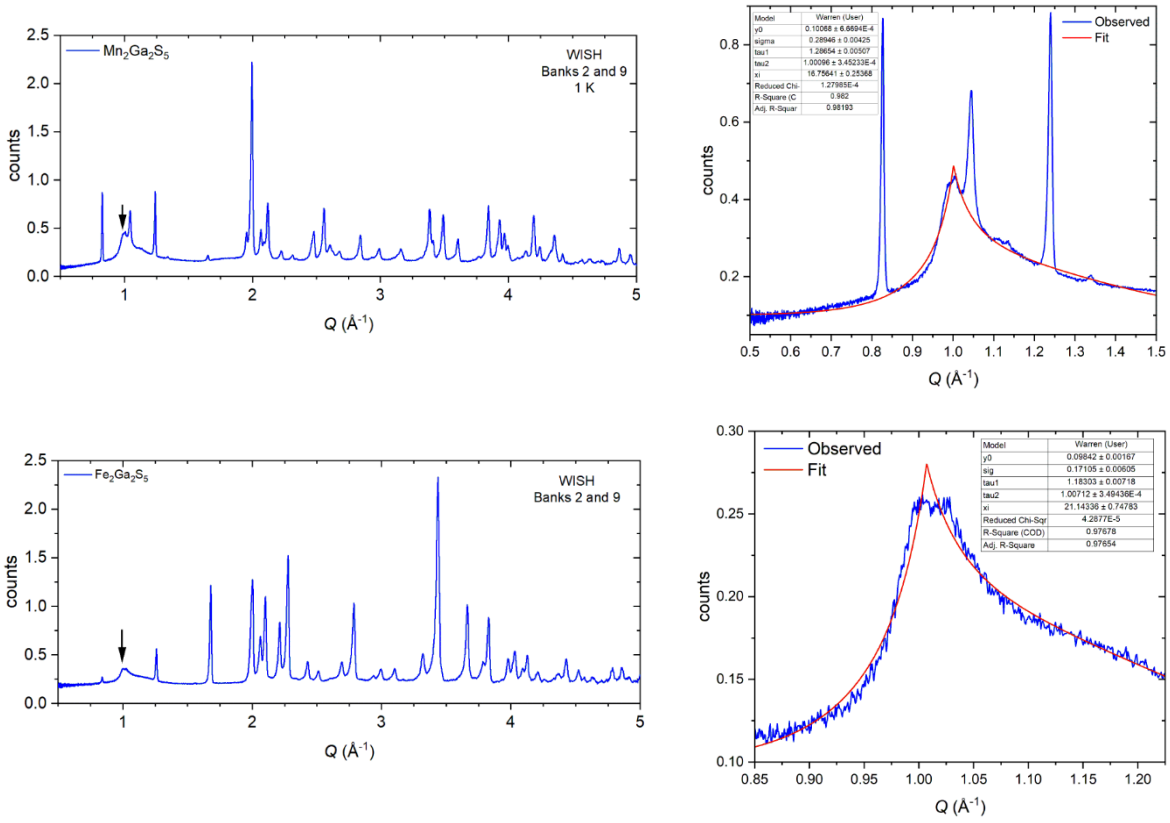


Figure 5.21: Plot of the PND patterns (Bank 2-9) of $Mn_2Ga_2S_5$ (top) and $Fe_2Ga_2S_5$ (bottom) at 1 K in Q-space. The arrows indicate the location of the magnetic scattering. The graphs on the right show the fit to the Warren function.

Table 5.5: Values obtained from the Warren peak fitting.

	$Mn_2Ga_2S_5$	**$Fe_2Ga_2S_5$**
$\sigma_\perp$ / Å^{-1}	0.289(4)	0.171(6)
τ_1 / Å^{-1}	1.286(5)	1.183(7)
τ_2 / Å^{-1}	1.001(1)	1.0071(3)
ξ_c / Å	16.7(2)	21.1(7)
y_0 (background value)	0.1006(7)	0.098(2)
R-Square (COD)	0.982	0.97678

Both compounds have a correlation length, ξ_c, of 16.7(2) Å and 21.1(7) Å for $Mn_2Ga_2S_5$ and $Fe_2Ga_2S_5$, respectively. The values for ξ_c indicate that the ordering is extremely short-range, less than the length of ten unit cells. For comparison, $Sr_2F_2Fe_2OS_2$ and $SrMnO_2Cu_{1.82}Te_2$ were found to have correlation lengths of 17 Å and 93 Å, respectively.[196,197] $Mn_2Ga_2S_5$ has a shorter correlation length compared to $Fe_2Ga_2S_5$, which would be consistent with the higher frustration index, f, found for $Mn_2Ga_2S_5$ ($f \sim 23$) compared to $Fe_2Ga_2S_5$ ($f \sim 8$). Neutron scattering on $NiGa_2S_4$, where f is also ~ 8,[91] reported a correlation length of 25 Å^{-1},[86] in line with $Fe_2Ga_2S_5$.

5.3.3 Monte Carlo Simulation

To get a greater insight into the magnetic behaviour, the magnetic scattering can be modelled using Monte Carlo simulations. These simulations were carried out using the Metropolis method described earlier in section 2.2.10.2. To carry out a Monte Carlo simulation, the unit cell with only the magnetic ions is defined with no symmetry elements. The four different magnetic configurations discussed by Liao *et al.*,[181] depicted in Figure 5.4, were first replicated, and their corresponding magnetic scattering was simulated. The likely magnetic configuration(s) could then be deduced. Then disorder was introduced, making the scattering more diffuse. A visualisation of the magnetic configuration was produced and viewed using

the FullProf software.[198] The simulation outputs the magnetic scattering in Q-space. Simulations were carried out using the $Mn_2Ga_2S_5$ structure. Both $Mn_2Ga_2S_5$ and $Fe_2Ga_2S_5$ have the exact arrangement of the A^{2+} bilayers. The magnetic scattering in both compounds is similar, with the highest intensity at ~ 1 $Å^{-1}$. Similar τ values were obtained from the Warren fitting. Therefore it would be reasonable to assume that the magnetic behaviour of both compounds is similar and that the slight differences in the position of the magnetic peak are due to the slightly different unit cell parameters. Therefore simulations carried out of $Mn_2Ga_2S_5$ can be a good approximation for $Fe_2Ga_2S_5$. Simulations were carried out using a box of dimensions 20×20×20 unit cells. Increasing the dimensionality has a significant effect on computing power and the time taken; for example, a 20×20×20 can be simulated in minutes, whereas increasing it to 50×50×50 takes a few hours. From the Warren function, the correlation length is very short (under 10 unit cell lengths), so a 20×20×20 box can be assumed to be reasonably sufficient to display the main features.

The J interactions were defined as shown previously in Figure 5.3, where J_1 corresponds to the nearest-neighbour (~ 90°) intralayer A-S-A superexchange, J_2 the interlayer variant, and J_3 the second nearest-neighbour (180°) superexchange. These J interactions can be assigned a numerical value (typically a maximum of 1 and a minimum of -1), with $J > 0$ corresponding to antiferromagnetic (AFM) behaviour and $J < 0$ for ferromagnetic (FM) behaviour.

Starting with $Mn_2Ga_2S_5$, the unit cell was initially defined with two distinct Mn sites, one from each layer, like that in the structural P-3m1 model shown below in Figure 5.22. Simulations are computationally demanding, and keeping the model as simple as possible is ideal. J_1 is defined as the Mn(1)-Mn(1) and Mn(2)-Mn(2) interactions, J_2 the Mn(1)-Mn(2) ~ 90° interaction and J_3 the Mn(1)-Mn(2) ~ 180° interaction. Each J interaction must be

defined with the unit cell translation that the specific exchange interaction corresponds to in order to simulate long-range ordering. For example, using the defined unit cell in Figure 5.22 as a guide, there are three J_2 interactions to consider: First is the J_2 exchange interaction of Mn(1) to the Mn(2) in the same unit cell. Secondly is the Mn(1) interaction with Mn(2) in the unit cell that is translated by (0, 1, 0) and thirdly, the Mn(1) interaction with Mn(2) in the unit cell translated by (-1, 0, 0).

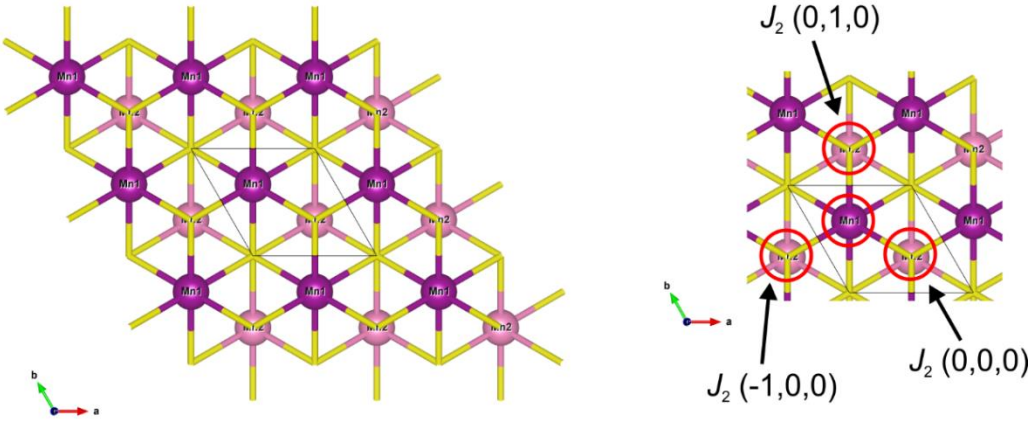


Figure 5.22: Visualization of the model used in the Monte Carlo simulation showing two distinct Mn sites and how the J interactions for each unit cell translation need to be considered. The non-magnetic ions are ignored.

Since J_1, J_2 and J_3 are all within a single bilayer and would therefore constitute two-dimensional ordering. An additional interaction, J_4, is defined as the interaction between the bilayers in the c direction to replicate long-range 3D ordering. This interaction is not mediated through bonds and is through space.

Firstly the fully FM configuration was simulated, corresponding to all ferromagnetic J interactions. For this configuration, it can be seen that the most intense magnetic scattering peaks are at Q values of 0.41 and 1.66 Å^{-1}, with smaller peaks at 0.82 and 1.24 Å^{-1}. Q = 0.41 Å^{-1} corresponds to $d \sim 15.3$ Å and was identified as the 001 magnetic Bragg reflection. The subsequent peaks are all at 00l (l = 2, 3, 4). Therefore, this configuration does not produce any intensity at the $Q \approx 1$ Å^{-1} and is unlikely to be the magnetic configuration

adopted. This is consistent with the antiferromagnetic-like transition seen in the SQUID magnetometry.

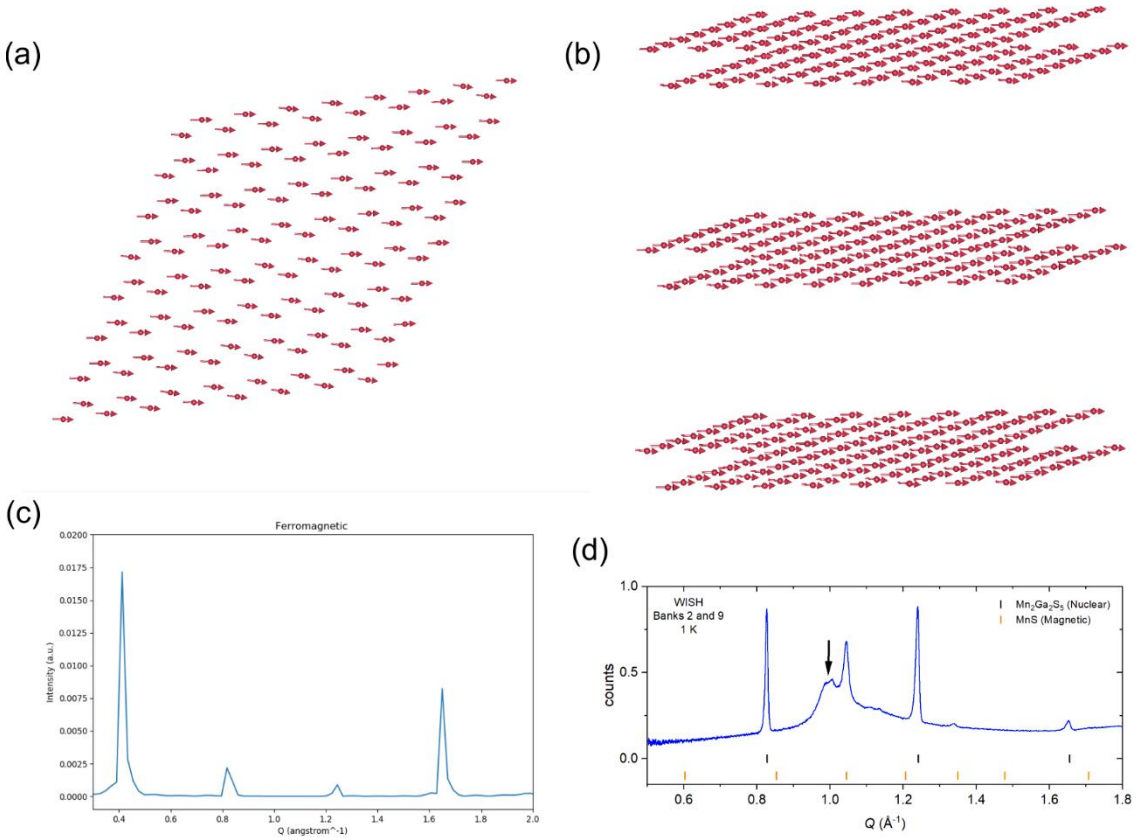


Figure 5.23: Simulation of the ferromagnetic configuration. (a) and (b) shows the simulated magnetic structure in FullProf software, with (a) the view down the *c*-axis. (c) shows the simulated pattern. (d) the observed scattering as a comparison.

In the AFM-Néel configuration, one Mn layer is arranged ferromagnetically but coupled to the other Mn layer antiferromagnetically. This corresponds to $J_1 < 0$ with J_2, $J_3 > 0$. From the simulated magnetic scattering, the magnetic peaks at similar Q values to that in the FM case. However, the intensities are swapped such that the peaks at 0.82 and 1.24 $Å^{-1}$ are the most intense.

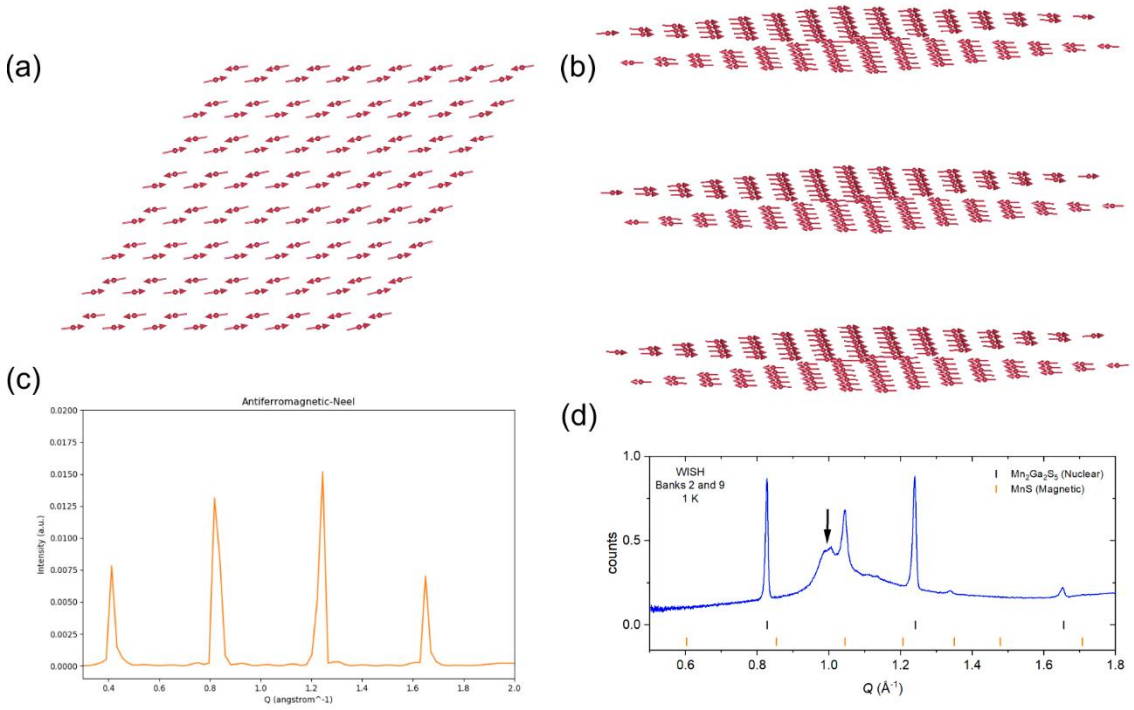


Figure 5.24: Simulation of the AFM-Néel configuration. (a) and (b) shows the simulated magnetic structure in FullProf software, with (a) the view down the *c*-axis. (c) shows the simulated pattern. (d) the observed scattering as a comparison.

The FM and the AFM-Néel configurations can be replicated with this model of two Mn ions in the unit cell. However, this model becomes flawed when considering the AFM zigzag and stripy magnetic configurations. Liao *et al*. predicted for $Fe_2Ga_2S_5$ that the zigzag configuration is the lowest energy configuration.[181] Replication of this is more complicated as the J interactions are now not distinctly FM or AFM and are a mixture of both types. For example, in the zigzag, although J_3 is AFM, J_1 consists of a 1:2 ratio of FM and AFM exchange interactions, and J_2 has a 2:1 ratio. The current model struggles to account for this, and it can be seen in Figure 5.25 how regions adopt this configuration, whereas other regions become disordered.

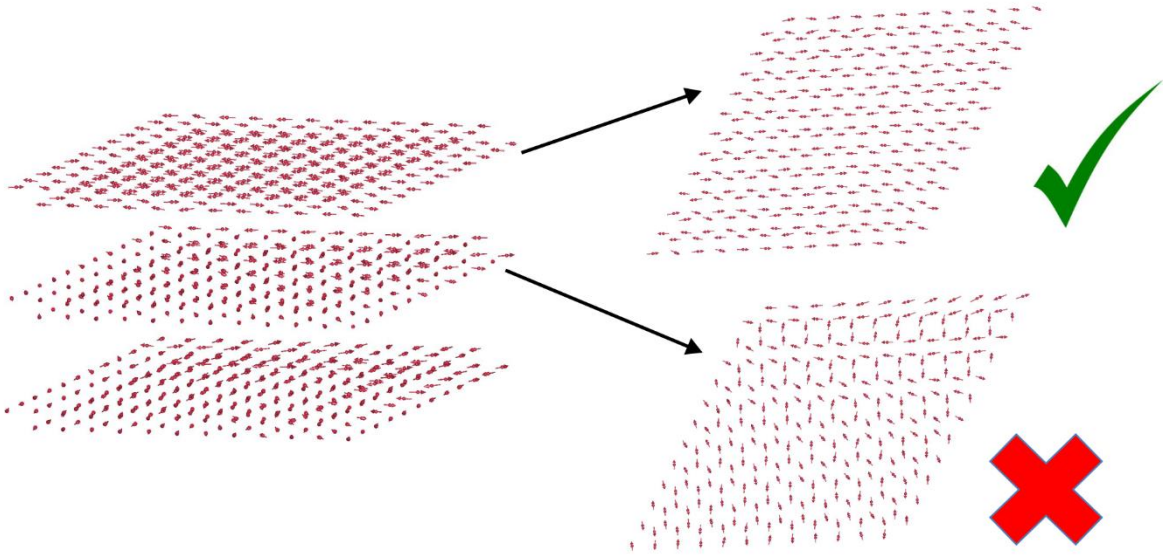


Figure 5.25: Attempted simulation of the zigzag configuration. Some regions are simulated correctly, whereas some areas are not, leading to a new model to be defined.

The same case applies to the stripy arrangement, where in this case, J_3 is FM, and both J_1 and J_2 have a 1:2 ratio of FM:AFM interactions. To overcome this, a different model needs to be established.

The model can be redefined by expanding the unit cell in the *ab* plane by $a \times \sqrt{3}a \times c$, resulting in an orthorhombic supercell, as shown below. In this model, the unit cell has four distinct Mn sites, two for each triangular lattice rather than one, and incorporates the hexagonal arrangement. This allows J_1 and J_2 to be each split into two different *J*s (defined as J_{11}, J_{12} and J_{21}, J_{22}). In this case, where J_1 was previously the ~ 90° exchange between intralayer Mn, now J_{11} can be assigned as the interaction between Mn(1) and Mn(2) (and also Mn(3)-Mn(4)), and J_{12}, the interaction between like-Mn (Mn(x)-Mn(x) where x = 1, 2, 3, 4). Similarly for J_2, the ~ 90° exchange between interlayer Mn, can be split into J_{21} which denote the Mn(1)-Mn(4) and Mn(2)-Mn(3) interactions, and J_{22} which denotes the Mn(1)-Mn(3) and Mn(2)-Mn(4) interactions. By incorporating this, the number of *J* interactions (with their specific unit cell translation that interaction corresponds to) increased by approximately 3-fold. This increases the time taken to carry out the simulations.

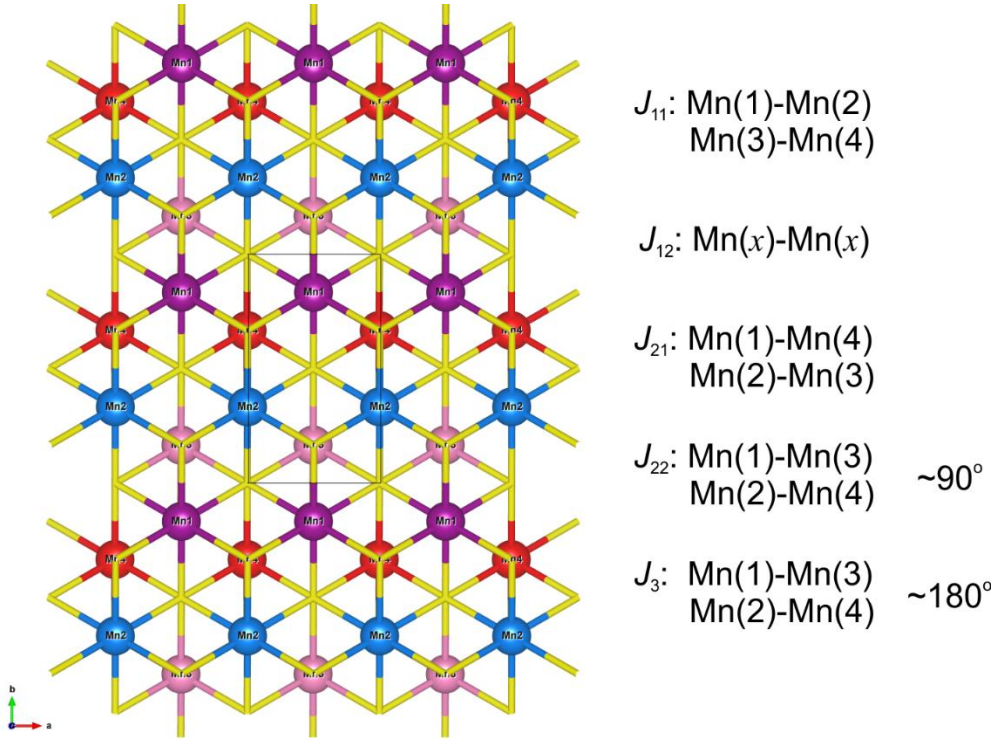


Figure 5.26 Visualisation of the improved model where four distinct Mn sites are defined. The definition of each J interaction is shown on the right.

The FM and Néel configurations can be replicated exactly as before. To simulate the zigzag configuration, J_{11} is AFM, with J_{12} being FM. J_{21} is FM, whereas J_{22} is AFM. This configuration can be accurately modelled, as shown in Figure 5.27. Table 5.6 shows the nature of each J interaction for the four magnetic configurations.

Table 5.6: The nature of each J interaction for the four configurations defined in the improved model.

	Ferromagnetic	**Néel**	**Zigzag**	**Stripy**
$\boldsymbol{J_{11}}$	FM	FM	AFM	AFM
$\boldsymbol{J_{12}}$	FM	FM	FM	FM
$\boldsymbol{J_{21}}$	FM	AFM	FM	AFM
$\boldsymbol{J_{22}}$	FM	AFM	AFM	FM
$\boldsymbol{J_3}$	FM	AFM	AFM	FM

The simulated magnetic scattering differs considerably from the fully FM and Néel scattering. It shows a greater resemblance to the experimental scattering with no intensity

predicted at $Q = 0.41$ Å^{-1} and intensity predicted around $Q \sim 1$ Å^{-1}, where the magnetic scattering is observed experimentally. Smaller peaks can be seen at 1.28 and 1.58 Å^{-1}.

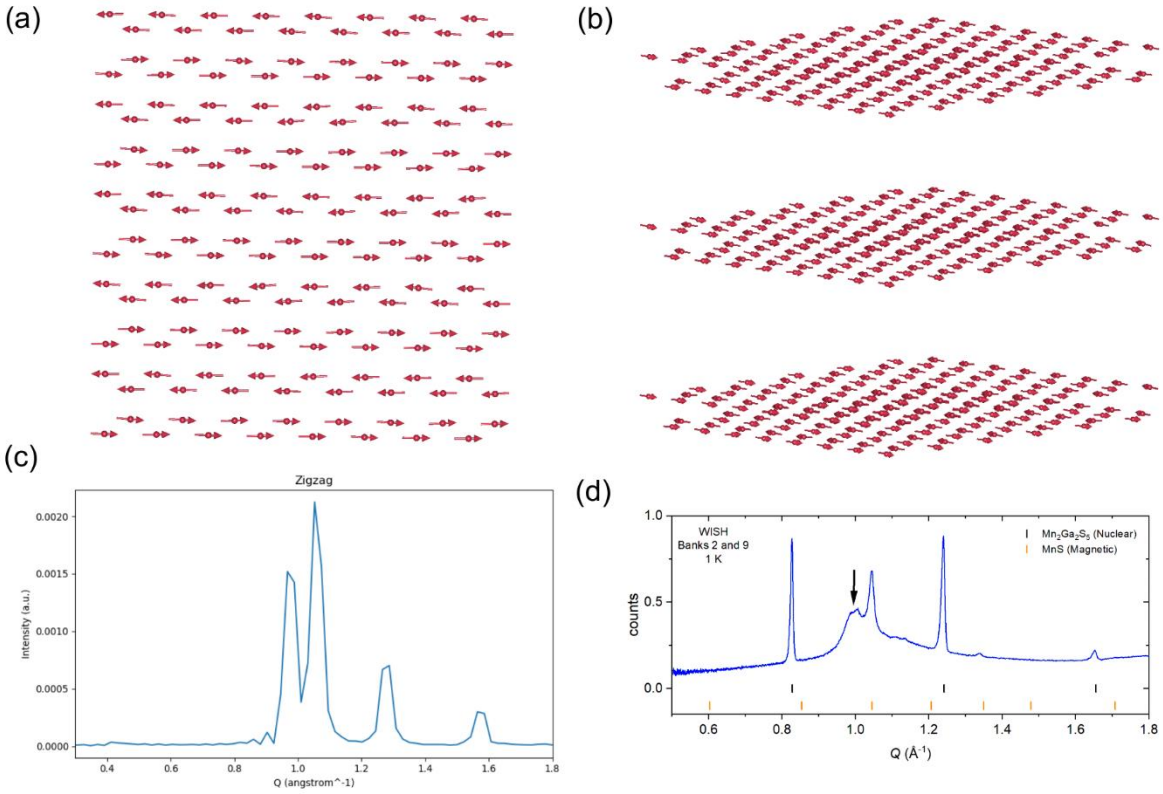


Figure 5.27: Simulation of the zigzag configuration using the improved model. (a) and (b) shows the simulated magnetic structure in FullProf software, with (a) the view down the *c*-axis. (c) shows the simulated pattern. (d) the observed scattering as a comparison. The simulated magnetic scattering (c) shows intense peaks at $Q \sim 1$ Å^{-1}, in line with the observed scattering.

To replicate the stripy arrangement, both J_{11} and J_{12} are similar to the zigzag (AFM and FM, respectively). However, J_{21} is now AFM, with J_{22} being FM. J_3 is also FM. The simulated magnetic scattering show peaks at similar Q values as the zigzag scattering with reduced intensity at ~ 1 Å^{-1} and greater intensity at 1.28 and 1.58 Å^{-1}.

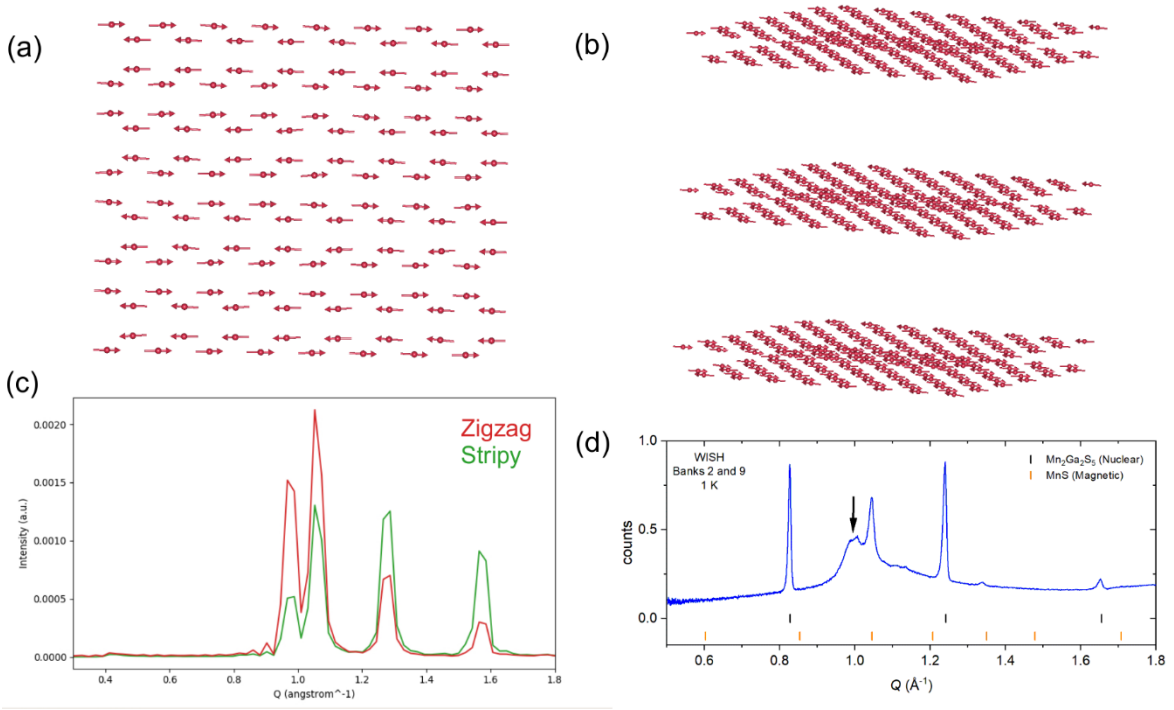


Figure 5.28: Simulation of the stripy configuration using the improved model. (a) and (b) shows the simulated magnetic structure in FullProf software, with (a) the view down the *c*-axis. (c) shows the simulated pattern with a comparison with the zigzag scattering. (d) shows the observed scattering as a comparison.

From the magnetic scattering of these four configurations, it can be deduced that the zigzag arrangement is the closest to the experimental scattering. Another method of confirming the simulated patterns are correct is by using the ISODISTORT software.[199] The expanded unit cell was loaded into ISODISTORT using a magnetic subgroup of $P1(1.1)$. The four magnetic configurations can be displayed by the $mGM3^+$, $mGM3^-$, $mM2^-$ and $mM1^+$ magnetic modes for the FM, Néel, zigzag and stripy configurations, respectively. The distortion file can be incorporated into TOPAS, and it can be seen that the zigzag $mM2^-$ mode gives the intensity at the same positions as that of the simulation. The magnetic *hkl* Bragg reflections at Q = 0.98, 1.06 and 1.28 $Å^{-1}$ are identified as the 010 and 011 and 012 reflections, respectively.

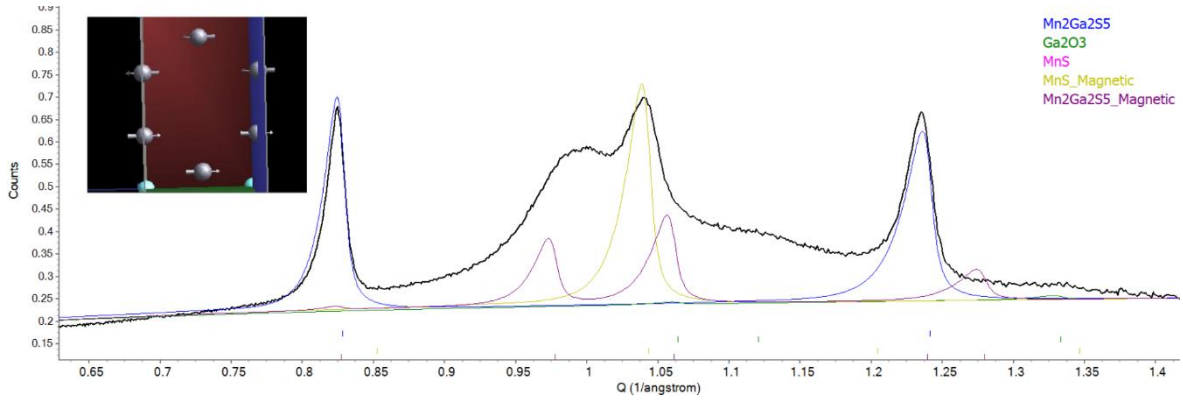


Figure 5.29: Implementation of the magnetic supercell in TOPAS showing how the zigzag spin configuration (mM2$^-$ mode depicted, with the magnetic scattering given by the purple line) is identical to the Monte Carlo version. The black line shows the observed scattering for $Mn_2Ga_2S_5$, with the yellow and blue lines showing the fit of MnS (magnetic) and $Mn_2Ga_2S_5$ (nuclear) phases, respectively, to the observed scattering.

Therefore, it is reasonable to assume that the observed diffuse magnetic scattering is likely arising from a disordered zigzag configuration. Disorder can be introduced into the modelling by altering the J values. For example, removing the J_4 interaction, which is responsible for the ordering to be 3D, significantly alters the magnetic scattering. With no interaction between the layers, the intensity at ~ 1.06 Å^{-1} decreases, and the peaks previously seen at 1.3 and 1.6 Å^{-1} disappear. The peaks with reduced intensity correspond to the *hkl* reflections where $l \neq 0$ (011 at Q = 1.06 Å^{-1} and 012 at Q = 1.28 Å^{-1}). In contrast, the unchanged peak at Q = 0.98 Å^{-1} is the 010 reflection. The simulated scattering has Warren-like characteristics, consistent with 2D ordering and shows a more remarkable resemblance to the observed scattering.

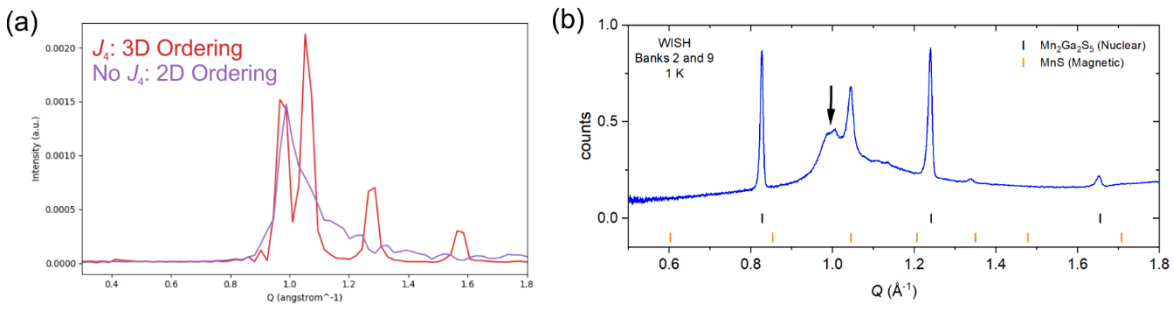


Figure 5.30 Simulation of the zigzag configuration removing the ordering in the *c*-direction. The simulated peak (a) closely resembles that observed experimentally(b).

A closer simulation can be achieved by introducing more disorder. An example of this can be by incorporating both zigzag and stripy models into the scattering by setting both J_{21} and J_{22} values to 0 and reducing the strength of the J_3 interaction. This allows the simulation to flip between both states. From the simulated structure, it can be seen that there are regions that are zigzag and stripy, and the simulated scattering shows a broader peak at ~ 1 Å^{-1} similar to that observed.

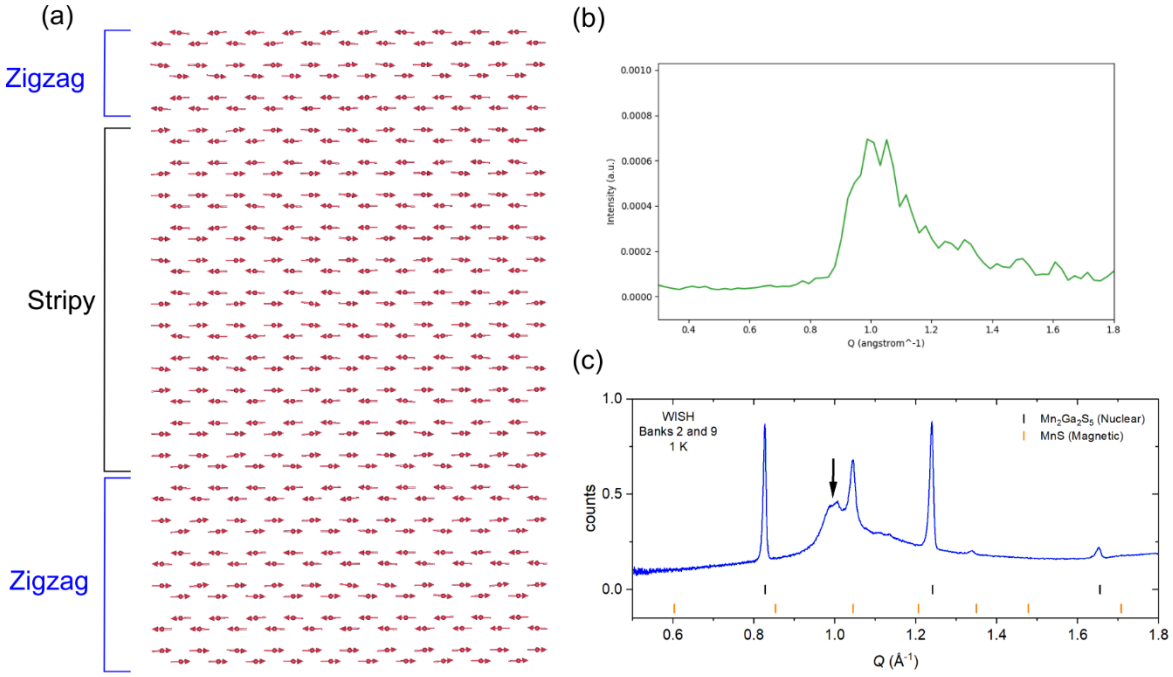


Figure 5.31: Simulation of the zigzag configuration whilst modifying the J values to incorporate the stripy. Regions of the different configurations can be seen here. The simulated magnetic scattering (b) shows a broad peak at Q ~ 1 Å^{-1}, in line with the observed scattering.

5.3.4 Heat Capacity

Heat capacity was measured by Dr Dharmalingam Prabhakaran in Oxford Physics as another useful technique to probe magnetic behaviour. Typically, in magnetic systems, magnetic signals can be seen as peaks or cusps in heat capacity, such as in $SrMn_2Sb_2$.[189] Here, a plot of C_p against T between 0-90 K for both compounds show no apparent transition. This is consistent with no long-range ordering and the observation of the Warren-like peak with a

short correlation length. A plot of the derivative C_p / T shows both curves plateau around 50 K and 70 K for $Mn_2Ga_2S_5$ and $Fe_2Ga_2S_5$, respectively. Shen *et al.* reported a broad peak for $Mn_2Ga_2S_5$ at 30 K in their plot of C_{mag}/T against T,[183] with Nakatsuji reporting a peak for $Fe_2Ga_2S_5$ at 113 K.[91] For $Fe_2Ga_2S_5$ no features were seen up to 300 K. It was attempted to extract the magnetic contribution by measuring C_p of a homologous non-magnetic compound. However, synthesising the homologous non-magnetic $Zn_2In_2S_5$ to calculate the lattice contribution was unsuccessful, as it led to phase separation to $ZnIn_2S_4$ and $Zn_3In_2S_6$.

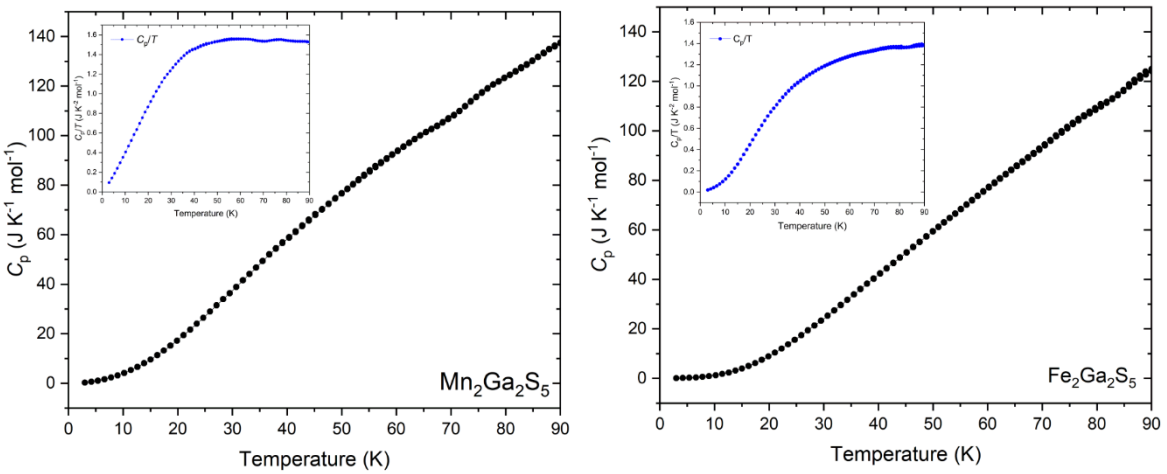


Figure 5.32: Plot of C_p against T and C_p/T against T (inset) for $A_2Ga_2S_5$ showing no clear transition.

5.4 Discussion

The magnetic behaviour in both $Mn_2Ga_2S_5$ and $Fe_2Ga_2S_5$ share many similarities. The presence of the Warren-like peak is a good indicator that the ordering is two-dimensional and, from the correlation lengths, extremely short-range. In the neutron diffraction, there is an indication of a 1-2 % Ga on the Mn site. It is unclear whether that amount of Ga would be disruptive of the magnetic ordering. However, the refinement points to an approximate 10 % Mn on the Ga site. Although it is uncertain the effects the Mn in the tetrahedral site could have on the magnetism, it is quite likely that it could be disruptive. The disorder could also be explained by looking at the nature of the J interactions. In the

redefined model used in the Monte Carlo simulation, J_1 and J_2 are each split into two different interactions (J_{11}, J_{12} and J_{21}, J_{22}) to simulate the zigzag and stripy configuration. In reality, there should be no difference between J_{11} and J_{12} and between J_{21} and J_{22}. J_1 and J_2 interactions are very similar in nature and would be expected to behave in the same way. Both J_1 and J_2 are approximately 90° interactions, and according to the Goodenough-Kanamori rule, they are expected to give rise to ferromagnetic coupling. The only significant difference between J_1 and J_2 is the distance of A-S-A. The bilayer has two cryptographically distinct S atoms, S(1) being the inner S in the metal bilayer and S(2) the outer S atoms of the bilayer. Therefore, J_1 can mediate through A-S(1)-A and A-S(2)-A pathways. J_2 is exclusively the A-S(1)-A superexchange.

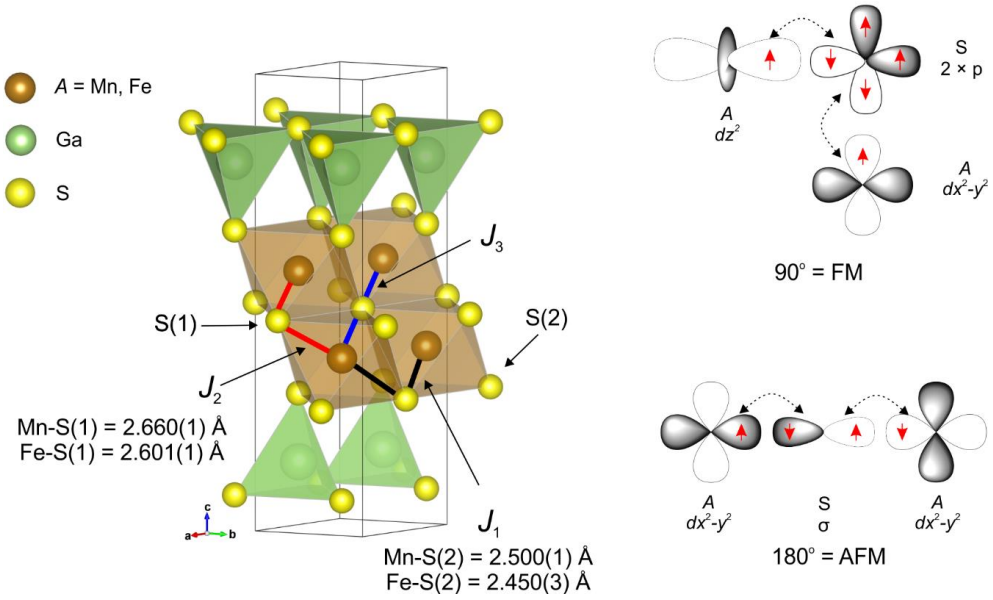


Figure 5.33: Left: diagram showing the J_1, J_2 and J_3 coupling interactions with the different A-S bond lengths suggesting $J_1 > J_2$. Right: the 90° and 180° superexchange interactions show the predicted ferromagnetic and antiferromagnetic behaviour, respectively.

From the synchrotron PXRD data, the A-S(1) and A-S(2) distances are not equal, with A-S(2) being ~ 0.15 Å shorter than A-S(1). This would make the J_1 coupling through A-S(2)-S stronger than J_2 due to the closer overlap of the orbitals.

If both J_1 and J_2 were FM, this would result in J_3, the 180° exchange, also being FM. This would be against the Goodenough-Kanamori rules that predict 180° exchanges are AFM. In the Néel configuration, having J_1 and J_3 being FM and AFM, respectively, results in J_2 being AFM. Therefore, there is competition between the superexchange J interactions, and this was seen when initially trying to model the zigzag and stripy arrangements in that J_1 and J_2 consisted of both FM and AFM interactions, resulting in frustration.

The Goodenough-Kanamori rule also would predict that the 180° superexchange would be stronger than the 90° superexchange. This is because the 180° pathway only involves the direct overlap with one orbital on S. Whereas the 90° pathway involves two *p* orbitals on S. Therefore, one would expect the J_3 coupling to be dominant. Looking closely at the buckled-honeycomb lattice, it can be seen, in Figure 5.34, that it consists of four sublattices of 180° pathways.

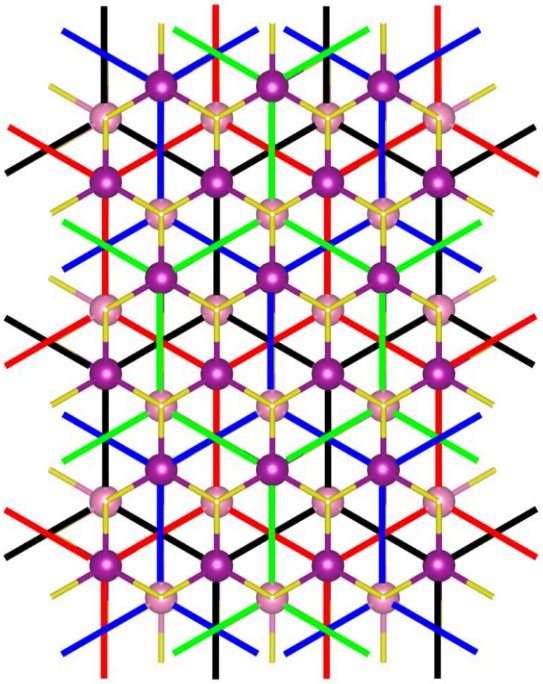


Figure 5.34: The four hexagonal sublattices of 180° *A*-S-*A* pathways indicated in black, red, blue and green.

If the strength of the J_1 and J_2 couplings are much weaker, then these four sublattices would essentially be independent of one another, resulting in multiple spin arrangements. This can be simulated by setting J_1 and J_2 to zero and only allowing AFM J_3. This results in a structure where regions have the zigzag or the Néel configuration or a combination of both. In Figure 5.35(a), it can be seen that there are regions where the spins alternate between zigzag and Néel. This would also give a simulated scattering with intensity at $Q \sim 1$ Å, similar to that observed experimentally.

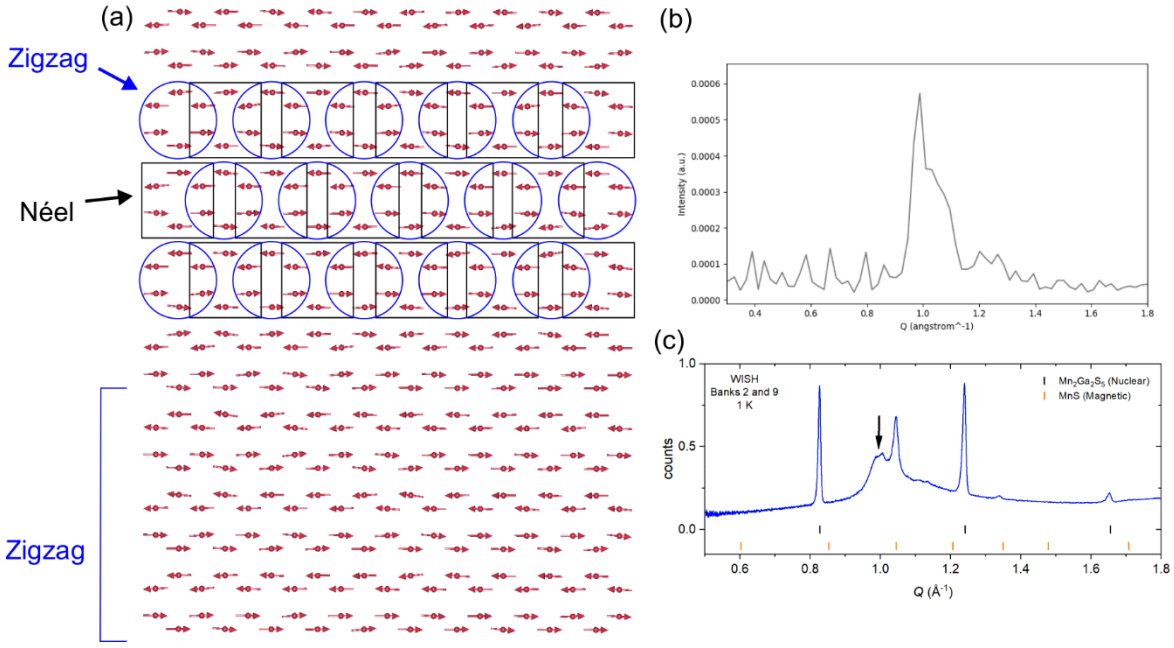


Figure 5.35: Simulation only considering the J_3 AFM superexchange and ignoring J_1 and J_2. Regions of the different configurations can be seen here. The simulated magnetic scattering (b) shows a peak again at $Q \sim 1$ Å^{-1}.

Another complication is factoring in the possible effects of direct exchange. For each J_1 and J_2 90° superexchange pathway, there is possible direct exchange interaction between the two A^{2+} metal centres. For J_{12} and J_{22}, direct exchange can occur through the d_{xy} orbitals. Whereas for J_{11} and J_{21}, direct exchange can occur through the d_{xz}/d_{yz} orbitals. Direct exchange between two similar half-filled orbitals is expected to be AFM, in competition with the 90° FM superexchange. Direct exchange can be a dominating interaction, even over 180°

superexchange, like that seen in $Sr_2CrO_2Cr_2OAs_2$ and $La_2O_2Mn_2OSe_2$.[200,201] In $La_2O_2Mn_2OSe_2$, the Mn^{2+}-Mn^{2+} nearest-neighbour distance is 2.93 Å. Whereas in $Mn_2Ga_2S_5$, the direct distance between A^{2+} in the same layer is the a lattice parameter, and the direct distance between A^{2+} in different layers is approximately 3.7 and 3.8 Å for $Fe_2Ga_2S_5$ and $Mn_2Ga_2S_5$, respectively. Both distances are considerably larger than that in $La_2O_2Mn_2OSe_2$, making the strength of these interactions difficult to predict. However, as the mechanism acts over short distances with an r^{-12} dependence, it is likely this contribution is weak, if not negligible, and superexchange is expected to be the more dominant exchange mechanism.

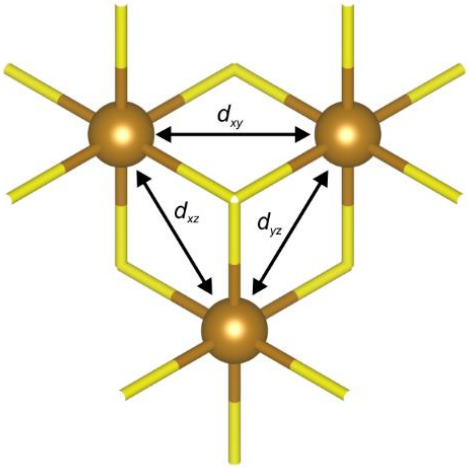


Figure 5.36: Diagram showing the possible direct exchange interactions.

This competition could be why the materials exhibit frustration and spin glass behaviour since the interactions cannot be completely satisfied. The zigzag is likely the most preferred of the four configurations as it is the only arrangement where both J_1 and J_2 have an FM component, and J_3 is AFM. However, one can postulate that there are multiple meta-stable states, resulting in a spin-glass. There is also the chemical disorder, especially in $Mn_2Ga_2S_5$, that cannot be modelled in the simulations and would likely also disrupt long-range magnetic ordering.

5.5 $Mn_{2-x}Fe_xGa_2S_5$

No reports of a solid solution of $Mn_{2-x}Fe_xGa_2S_5$ are reported in the literature. Here, the solid solution was synthesised to investigate the effects of doping on the structure and magnetism. A 2-x : x : 1 molar ratio (x = 0.25, 0.5, 0.75, 1, 1.25, 1.5, 1.75) of MnS : FeS : Ga_2S_3 were ground together and pelletised. Since $Mn_2Ga_2S_5$ and $Fe_2Ga_2S_5$ were synthesised at 900 °C at 1050 °C, the solid solutions were synthesised at intermediate temperatures. For $x < 1$, the synthesis temperature was 950 °C, whereas for $x \geq 1$, the synthesis temperature was 1000 °C. From the phase diagram reported by Pardo *et al.*,[202] $Mn_2Ga_2S_5$ was reported to decompose at 1030 °C therefore, for $MnFeGa_2S_5$, the temperatures tested were 950 °C, 1000 °C and 1050 °C. It was found that 1000 °C was the temperature which produced the most pure and crystalline product.

5.5.1 Characterisation

$Mn_2Ga_2S_5$ crystallises in the 1T structure with the P-3m1 space group, whereas $Fe_2Ga_2S_5$ crystallises most commonly in the 3R structure with the R-3mH space group. With increasing x in $Mn_{2-x}Fe_xGa_2S_5$, it can be seen from the refinement of the PXRD data that the ratio of 1T : 3R decreases, with the 1T structure becoming the minor composition at x = 0.5 and is not observed at x = 1. The unit cell also decreases in volume with increasing x, as expected since the Fe^{2+} is smaller in radius than Mn^{2+}. The trend in the changes in the a and c lattice parameters are almost linear with x (interlayer spacing is used as a comparison since the c parameter of the 3R symmetry is three times that of 1T).

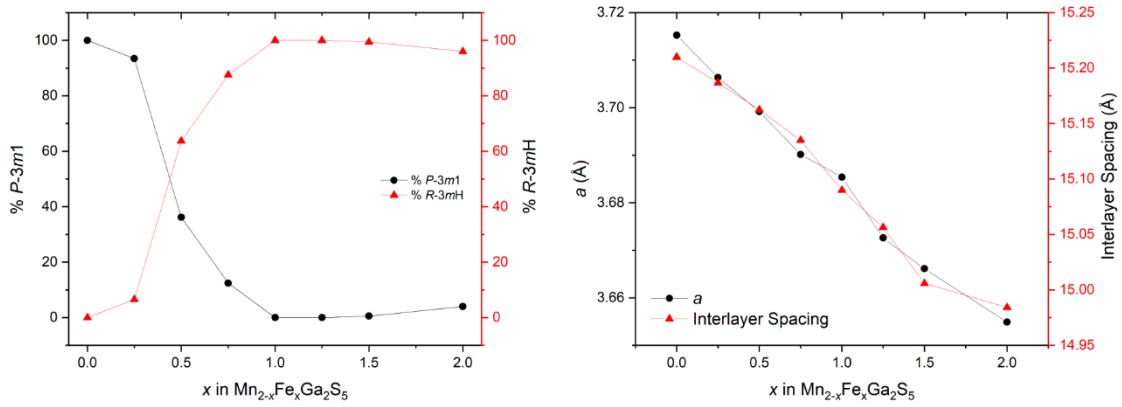


Figure 5.37: Left: Plot of the phase % of the 1T and 3R polytype (left) and lattice parameters (right) with increasing Fe content.

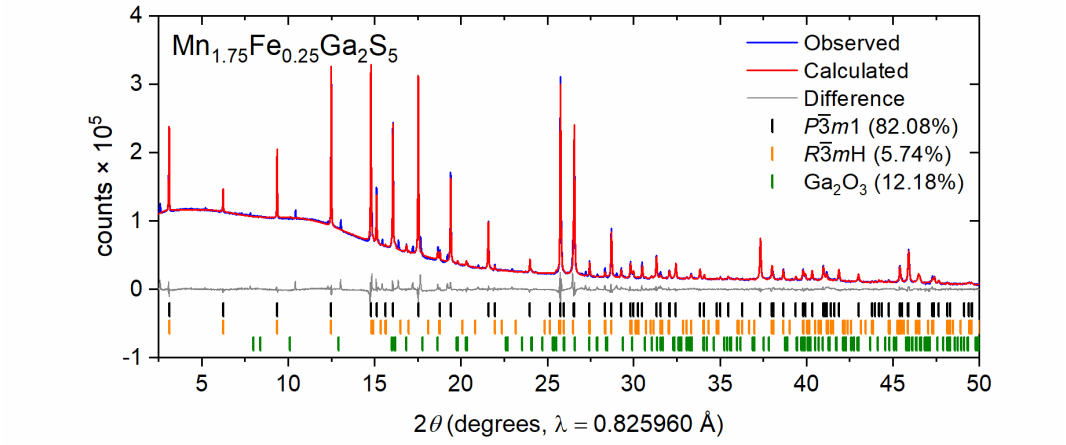


Figure 5.38: Rietveld refinement against I11 (PSD) PXRD pattern of $Mn_{1.75}Fe_{0.25}Ga_2S_5$ (ME154). R_{wp}: 2.37 %. The small unaccounted-for peaks are shown and indexed in Figure 5.42.

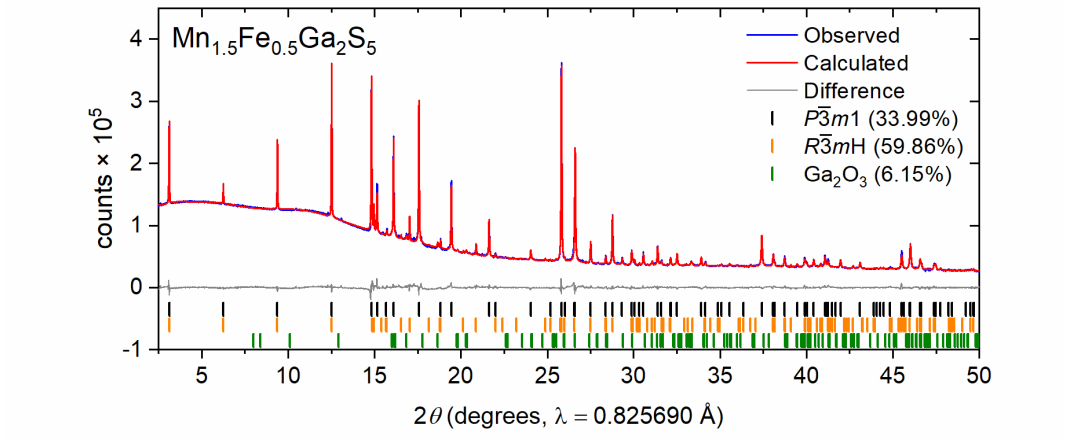


Figure 5.39: Rietveld refinement against I11 (PSD) PXRD pattern of $Mn_{1.5}Fe_{0.5}Ga_2S_5$ (ME155). R_{wp}: 1.70 %.

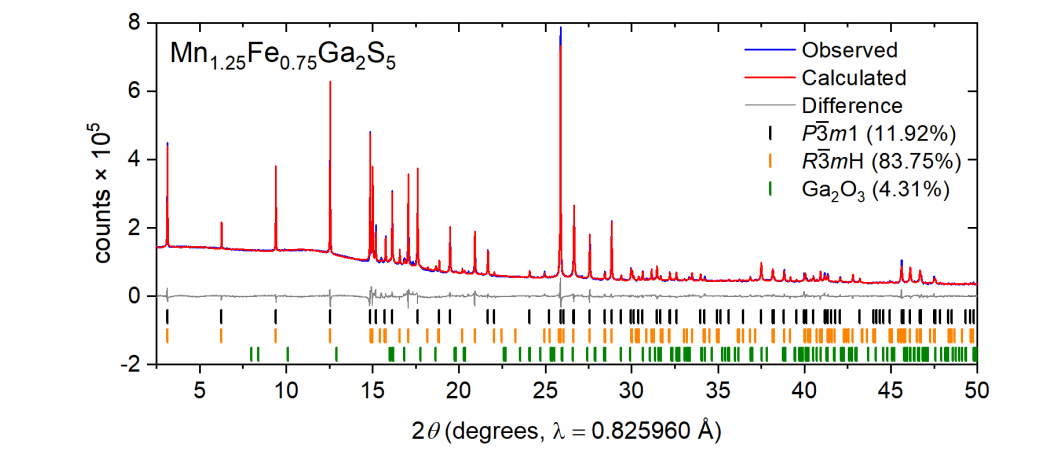


Figure 5.40: Rietveld refinement against I11 (PSD) PXRD pattern of $Mn_{1.25}Fe_{0.75}Ga_2S_5$ (ME156). R_{wp}: 2.77 %.

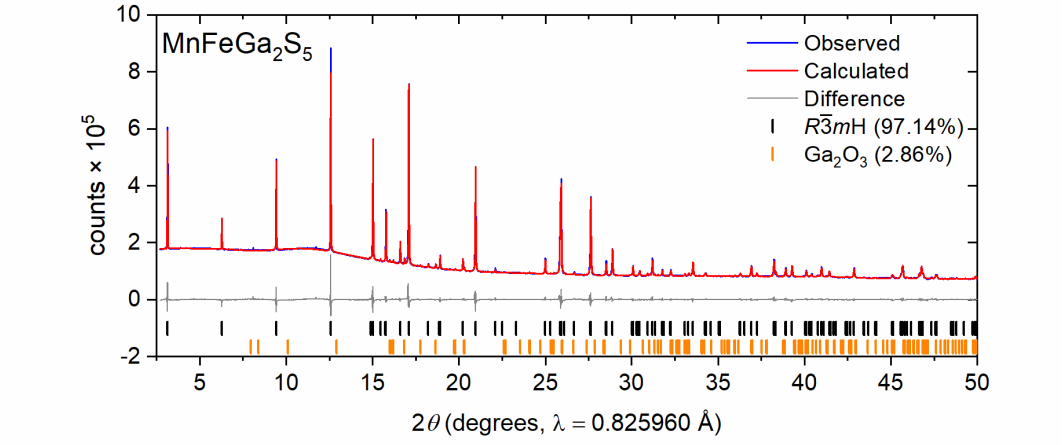


Figure 5.41: Rietveld refinement against I11 (PSD) PXRD pattern of $MnFeGa_2S_5$ (ME157). R_{wp}: 2.66 %.

Upon closer inspection of $Mn_{1.75}Fe_{0.25}Ga_2S_5$, low-angle reflections can be seen as highlighted in Figure 5.42, and these can be indexed to a single phase with 00(nl) reflections (n = 1, 2, 3, 4…). These reflections could not be matched to any side phases or other possible known phases in the ICSD database. The d-spacing of the 00l reflection of this unknown phase is ~ 3 Å larger than the d-spacing of the 00l of $A_2Ga_2S_5$, which in turn is ~ 3 Å larger than the d-spacing of the 00l of AGa_2S_4. It is plausible that the unknown phase may have an extra AS/GaS layer. A similar example is found for the Zn-In-S systems, in which $ZnIn_2S_4$, $Zn_2In_2S_5$ and $Zn_3In_2S_6$ have 3, 4 and 5 layers per slab, respectively.[203–205] However, these peaks are not seen in all the other solid solutions.

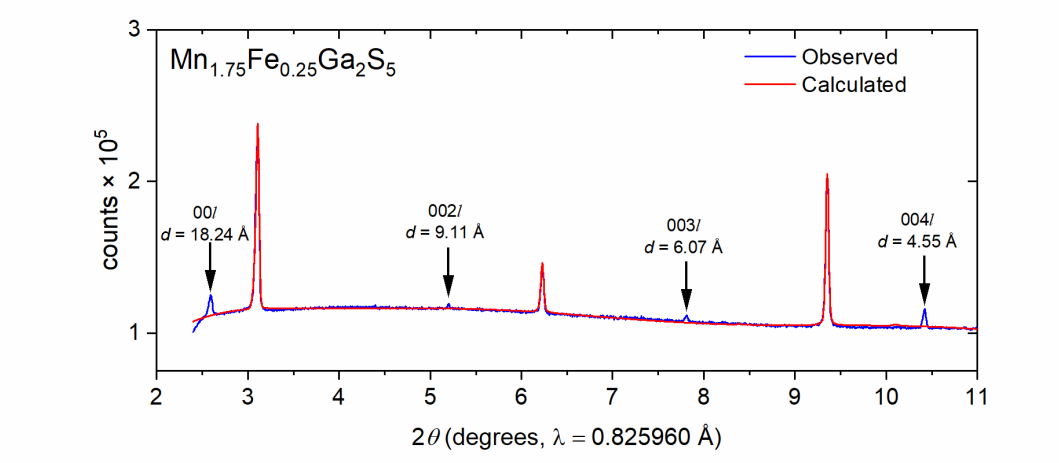


Figure 5.42: I11 (PSD) PXRD of $Mn_{1.75}Fe_{0.25}Ga_2S_5$ (ME154) showing the presence of another phase at low angles.

Due to the very close similarity between the electron count of Mn^{2+} and Fe^{2+}, the occupancy of both elements on the same crystallographic site cannot be refined reliably in the Rietveld refinement. SEM-EDX was used to analyse $MnFeGa_2S_5$, where signals from the Mn and Fe can be distinguished in the EDX spectrum, allowing a reasonable estimate of the proportion of the two elements. SEM images show a homogenous mix of Fe and Mn with no indication of Fe or Mn-rich areas at the resolution of the SEM. EDX gave a stoichiometry of $Mn_{0.95(1)}Fe_{1.15(1)}Ga_{1.8(1)}S_5$, corresponding to a 1:1.2 ratio of Mn:Fe instead of the starting 1:1. PND measurements would allow the occupancies to be confidently extracted, with the scattering lengths of Mn and Fe contrasting significantly (-3.73 fm for Mn against 9.45 fm for Fe). [131]

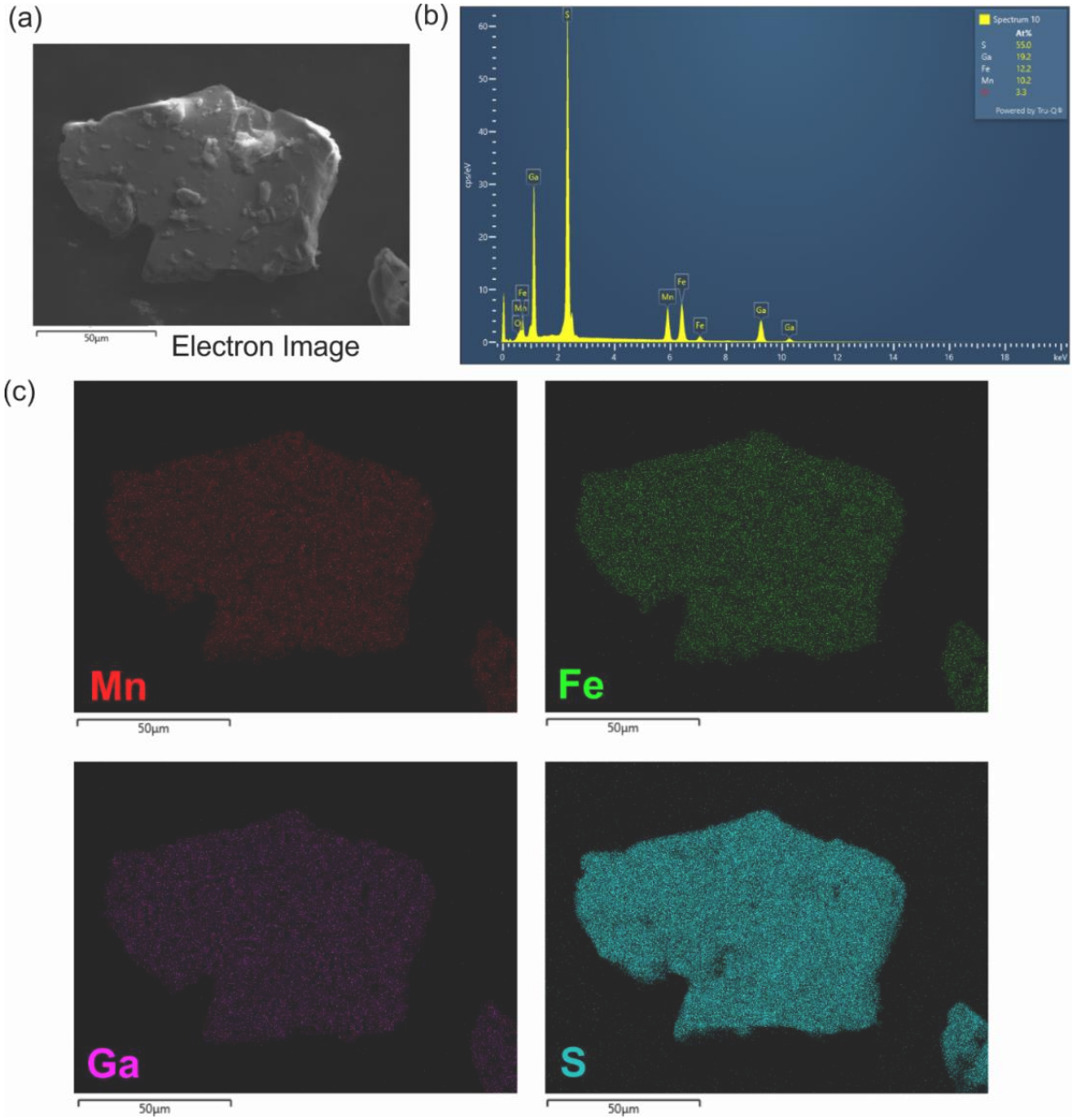


Figure 5.43: SEM-EDX on $MnFeGa_2S_5$ giving a stoichiometry of $Mn_{0.95(1)}Fe_{1.15(1)}Ga_{1.8(1)}S_5$.

When x exceeds 1, and the compound becomes more Fe-rich, the single layer $FeGa_2S_4$ is formed as a side phase. The crystallinity also decreases, especially for $Mn_{0.25}Fe_{1.75}Ga_2S_5$, where peaks become broader. The main features of the primary phase are still present with the 003, 006 and 009 reflections indicated in the inset of Figure 5.46. However, attempts at a Rietveld refinement were difficult due to the loss of crystallinity and significant peak overlap, especially around $2\theta \sim 15°$.

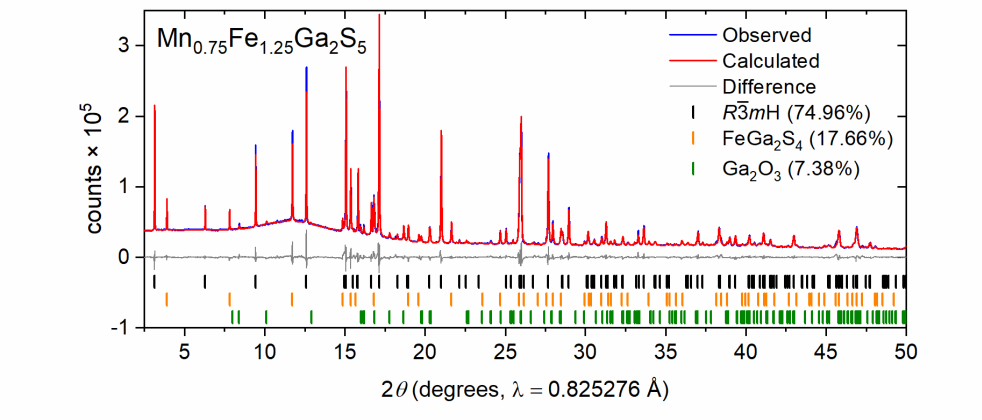


Figure 5.44: Rietveld refinement against I11 (PSD) PXRD pattern of $Mn_{0.75}Fe_{1.25}Ga_2S_5$ (ME165). R_{wp}: 4.26 %.

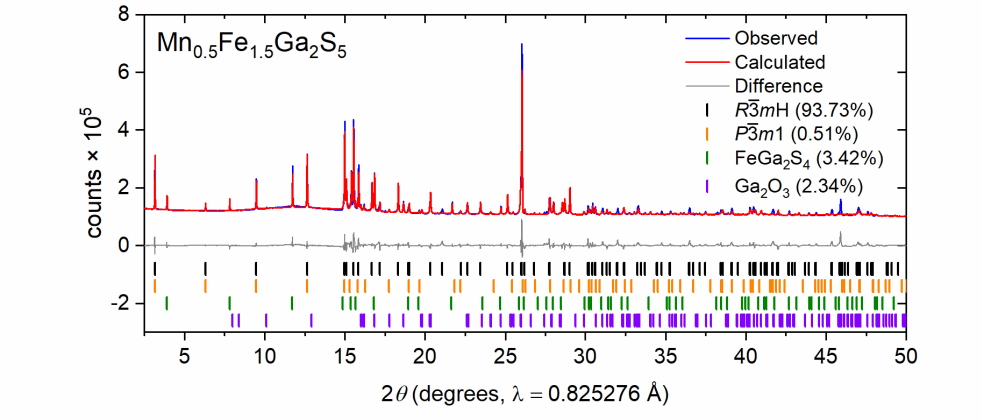


Figure 5.45: Rietveld refinement against I11 (PSD) PXRD pattern of $Mn_{0.5}Fe_{1.5}Ga_2S_5$ (ME166). R_{wp}: 10.86 %.

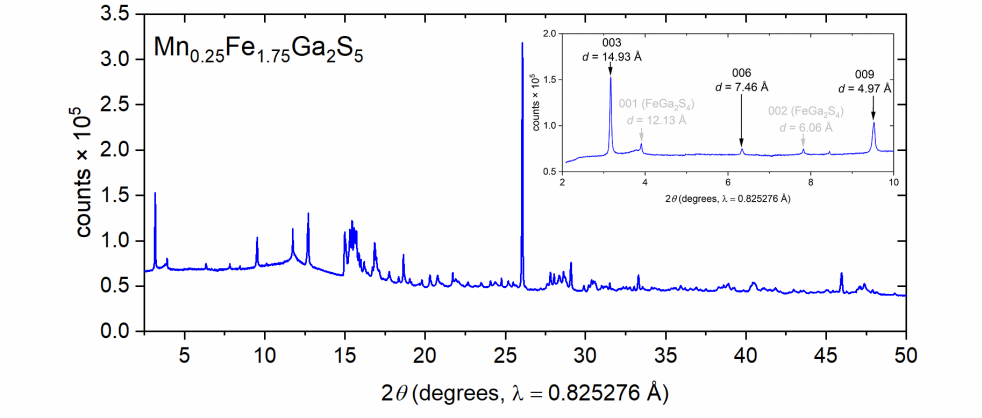


Figure 5.46: I11 (PSD) PXRD pattern of $Mn_{0.25}Fe_{1.75}Ga_2S_5$ (ME167). The significant peak overlap around $2\theta \sim 15°$ and 27° made it difficult to carry out a reliable Rietveld refinement. Inset shows the indexing of the 00l peaks for the primary phase (black) and the $FeGa_2S_4$ side phase (grey).

5.5.2 Magnetometry

Magnetic measurements were carried out on the $Mn_{2-x}Fe_xGa_2S_5$ solid solution to probe the effects of Fe doping on the magnetism. The solid solution for x = 0.25, 0.5, 0.75 and 1 was measured. For x > 1, the single layer $FeGa_2S_4$ was evident as a side phase from the PXRD. Therefore, these compounds were not measured as the impurity could influence the magnetic measurements. Magnetisation against field measurements, as shown in Figure 5.47, all show linear lines with the room-temperature χ_{mol} of the order of 10^{-2} emu mol^{-1} and decreased with increasing Fe content in an almost linear relationship.

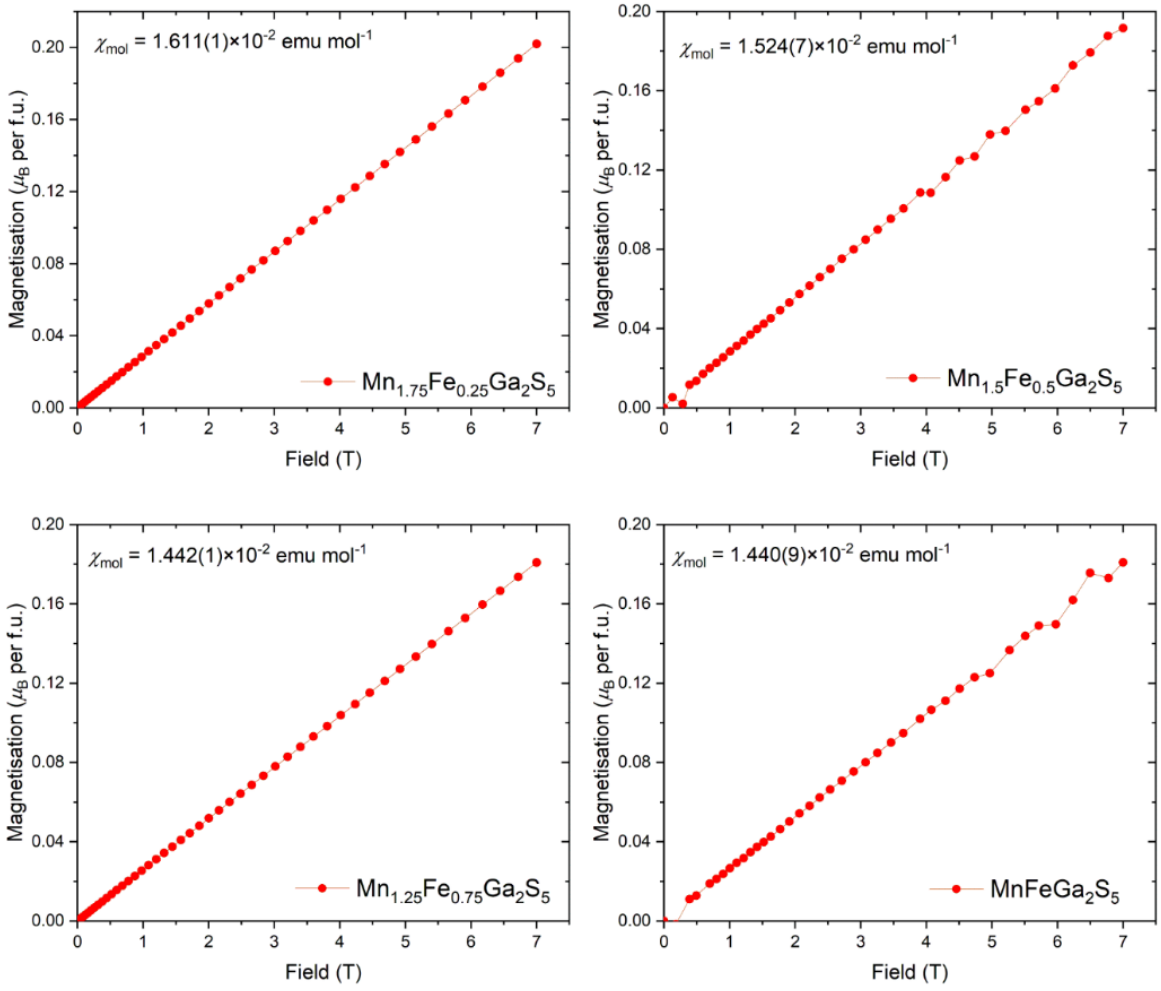


Figure 5.47: M against H at 300 K for $Mn_{2-x}Fe_xGa_2S_5$ (x = 0.25, 0.5, 0.75, 1).

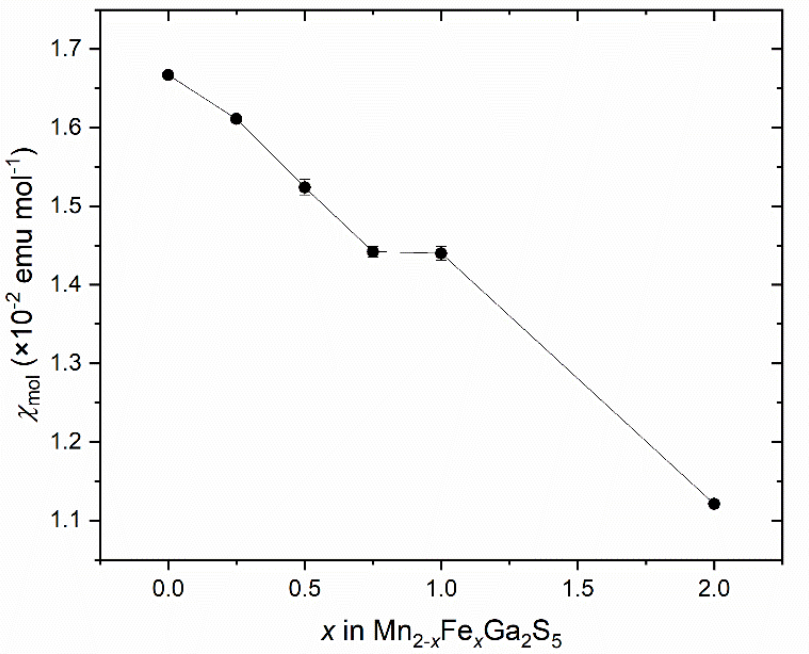


Figure 5.48: Plot of room temperature (300 K) molar susceptibility (χ_{mol})against Fe content x.

Measurement of χ_{mol} against temperature at 100 Oe show similar characteristics to $Mn_2Ga_2S_5$ and appears to obey the Curie-Weiss law in the high-temperature regime. All the curves show an antiferromagnetic-like, spin-freezing transition with T_f increasing with Fe content in an almost linear relationship, as shown in Figure 5.48. However, the Weiss temperature does not show a linear dependency. $Fe_2Ga_2S_5$ has a θ_w of -398(1) K, around 116 K greater than $Mn_2Ga_2S_5$. Initially, when increasing x, θ_w decreases with $\theta_w < 200$ K for $0.25 \leq x \leq 0.75$. Although for $MnFeGa_2S_5$, θ_w is ~ -290 K, similar in value to $Mn_2Ga_2S_5$. The frustration index ($f = -\theta_w/T_f$) decreased by approximately a half upon 0.25 Fe doping, with the solid solutions having f values ranging from 6 to 10, similar to $Fe_2Ga_2S_5$ (f ~ 8). There is no apparent trend in the effective moment (μ_{eff}). μ_{eff} decreases with Fe doping to a minimum of 3.79(1) μ_B per A^{2+} for x = 0.75 but increases to 4.19(1) μ_B per A^{2+} for $MnFeGa_2S_5$. Perhaps there may be small amounts of impurities undetectable by PXRD that could influence these values. Or it could be that the Curie-Weiss fits are unreliable with these high Weiss temperatures.

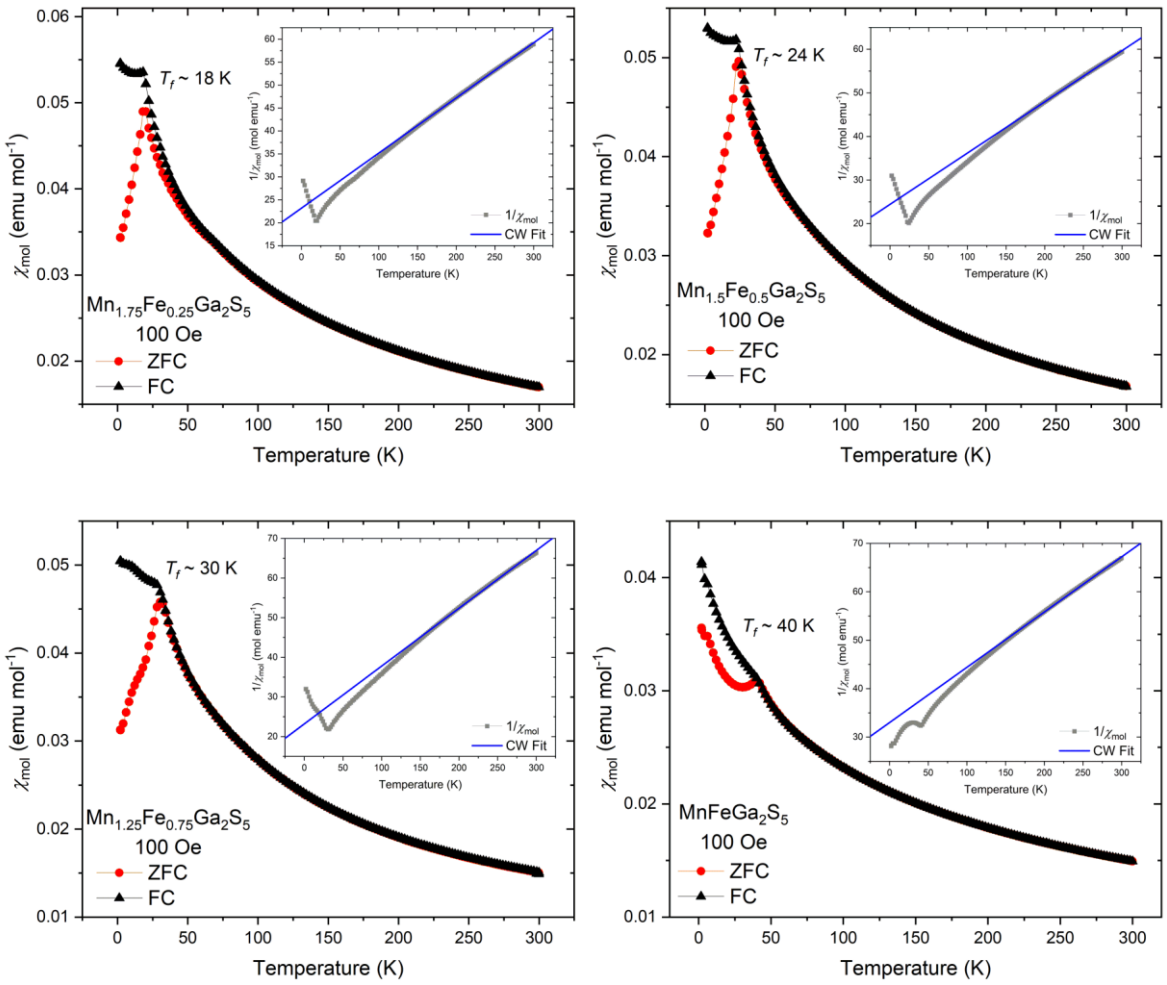


Figure 5.49: χ_{mol} against T for $Mn_{2-x}Fe_xGa_2S_5$ (x = 0.25, 0.5, 0.75, 1). Inset for each plot shows the 1/ χ_{mol} against T with the Curie-Weiss fitting.

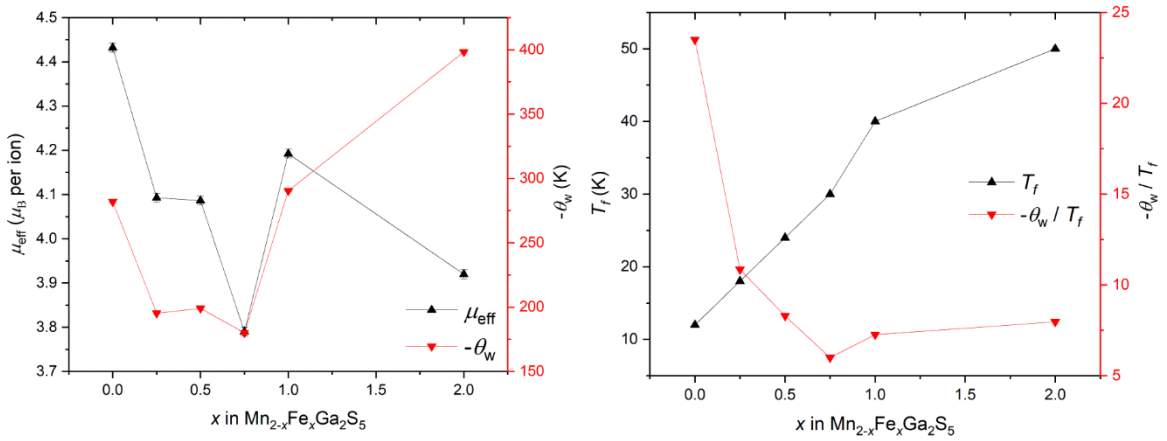


Figure 5.50: Plot of μ_{eff} and θ_w (left) and T_f and f =-θ_w/T (right) for $Mn_{2-x}Fe_xGa_2S_5$.

Table 5.7: Values obtained from the M against H plot and Curie-Weiss fitting for $Mn_{2-x}Fe_xGa_2S_5$.

Compound	χ_{mol} (Room-temperature) / emu mol^{-1}	Transition temperature (at 100 Oe) / K	θ_w / K	μ_{eff} / μ_B per A^{2+}
$Mn_2Ga_2S_5$	1.667(1)×10^{-2}	12	-282(1)	4.43(1)
$Mn_{1.75}Fe_{0.25}Ga_2S_5$	1.611(1)×10^{-2}	18	-195(1)	4.09(1)
$Mn_{1.5}Fe_{0.5}Ga_2S_5$	1.524(7)×10^{-2}	24	-199(1)	4.09(1)
$Mn_{1.25}Fe_{0.75}Ga_2S_5$	1.442(1)×10^{-2}	30	-180(1)	3.79(1)
$MnFeGa_2S_5$	1.440(9)×10^{-2}	40	-290(1)	4.19(1)
$Fe_2Ga_2S_5$	1.121(1)×10^{-2}	~ 50	-398(1)	3.92(1)

Magnetisation against field measurements showed similar characteristics to $Mn_2Ga_2S_5$ with a noticeable hysteresis loop that is not centred around the origin, again indicative of spin-glass behaviour. When increasing Fe content, the hysteresis becomes increasingly displaced away from the origin. The coercive force needed to return the magnetisation from negative values to zero shifts from +0.12 T in $Mn_{1.75}Fe_{0.25}Ga_2S_5$ to -0.33 T in $MnFeGa_2S_5$. After removing the negative field, the residual magnetism also shifts to less negative values and becomes positive when x = 0.75. $MnFeGa_2S_5$ resembles $Fe_2Ga_2S_5$ more so than $Mn_2Ga_2S_5$ with a narrow, off-centre hysteresis.

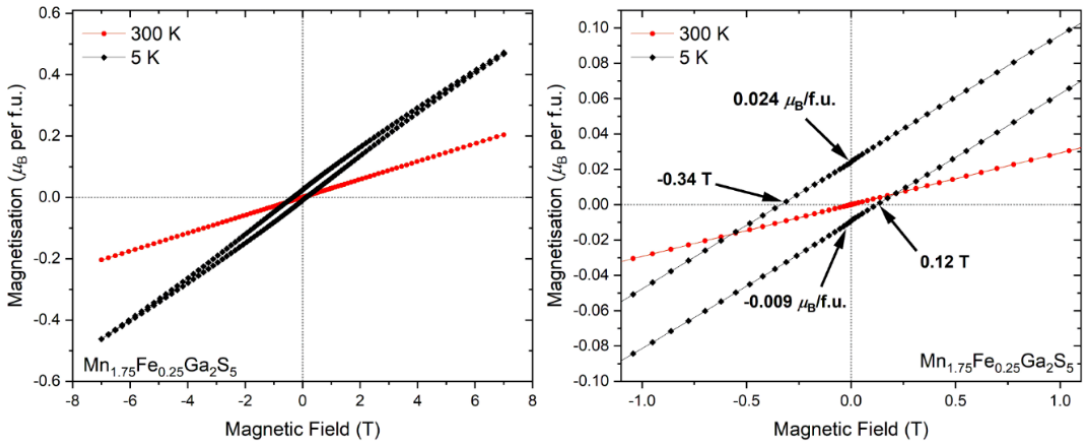


Figure 5.51: Magnetisation against field hysteresis loop at 300 K and 5 K for $Mn_{1.75}Fe_{0.25}Ga_2S_5$.

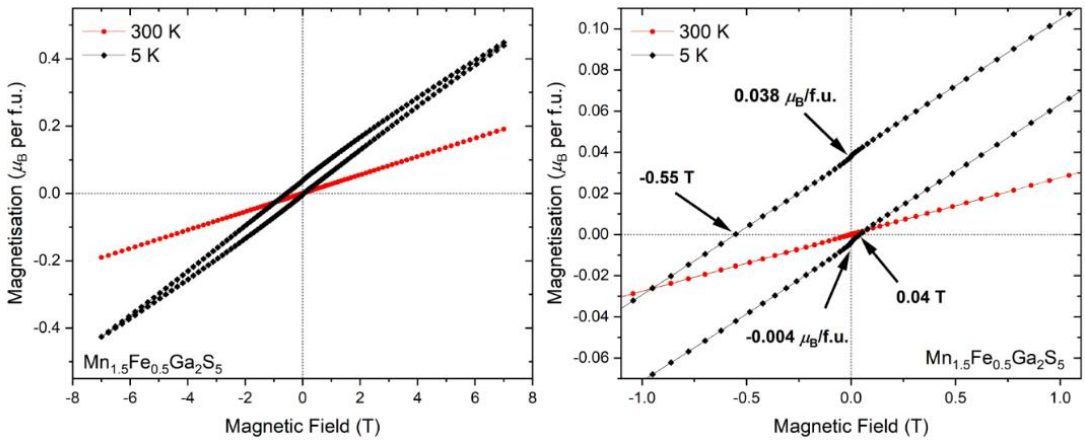


Figure 5.52: Magnetisation against field hysteresis loop at 300 K and 5 K for $Mn_{1.5}Fe_{0.5}Ga_2S_5$.

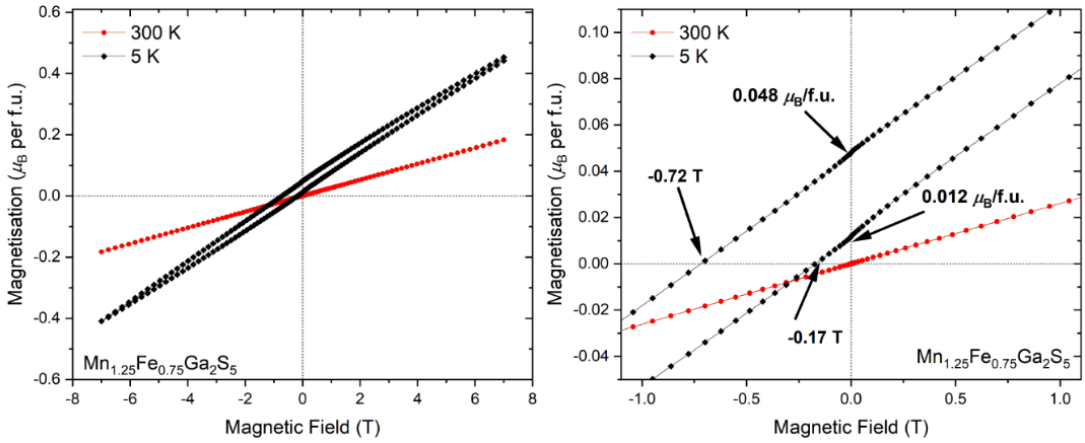


Figure 5.53: Magnetisation against field hysteresis loop at 300 K and 5 K for $Mn_{1.25}Fe_{0.75}Ga_2S_5$.

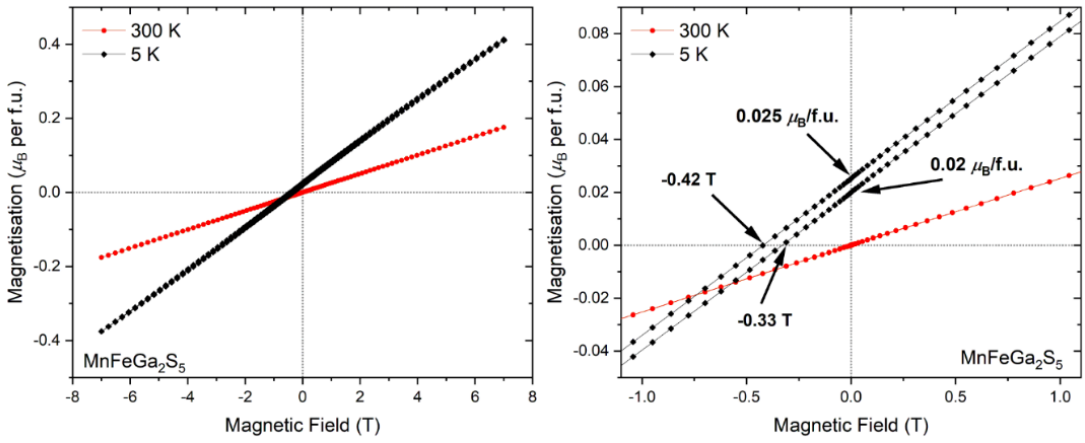


Figure 5.54: Magnetisation against field hysteresis loop at 300 K and 5 K for $MnFeGa_2S_5$.

5.6 Conclusion

This chapter has investigated the $A_2Ga_2S_5$ (A = Mn, Fe) compounds with a buckled honeycomb arrangement of A^{2+} layers. Structurally, $Mn_2Ga_2S_5$ exclusively adopts the 1*T* (*P*-3*m*1) polytype, whereas $Fe_2Ga_2S_5$ predominantly adopts the 3*R* (*R*-3*m*). In $Mn_2Ga_2S_5$, the combination of PXRD and PND indicated the Ga site being slightly mixed, with a Ga occupancy of ~ 0.85 and Mn occupancy of 0.1. This can be highlighted due to the stark contrast in Mn and Ga neutron scattering lengths. However, significant amounts of Ga_2O_3 are present during the synthesis, which may result from a reaction with the silica tube. A better synthesis route is needed to eliminate this impurity. In $Fe_2Ga_2S_5$, the shoulder peaks on the 00*l* reflections and unaccounted intensity at the 101 Bragg reflection can be accounted for by the 1*T* model. However, the extra intensity at 104 Bragg reflection remains the only unaccounted-for peak. The extra intensity may arise from a possible stacking disorder/intergrowth of the different polytypes. HAADF-STEM would be useful to see if any disorder/intergrowth is present.

SQUID magnetometry measurements show that both compounds exhibit an antiferromagnetic-like transition at 12 and ~ 50 K for $Mn_2Ga_2S_5$ and $Fe_2Ga_2S_5$, respectively. However, Curie-Weiss fitting showed that these compounds are highly frustrated with $f = -\frac{\theta_W}{T_f}$ of approximately 23 and 8 for $Mn_2Ga_2S_5$ and $Fe_2Ga_2S_5$, respectively. Hysteresis measurements show that both exhibit a hysteresis displaced from the origin, another spin glass property. This would be contrary to the report by Nakatsuji *et al*. that claimed $Fe_2Ga_2S_5$ is a long-range antiferromagnet with a T_N of 113 K.[91] Nakatsuji *et al*. reported the synthesis of $Fe_2Ga_2S_5$ as a single crystal using a chemical vapour transport (CVT) method. It may be possible that the different chemical synthesis gives a slightly different product with perhaps less chemical disorder, allowing long-range ordering to be seen. Investigating the effects of

varying the chemical synthesis would be an area of future study. However, the findings for $Mn_2Ga_2S_5$ are in-line with the recent study by Shen *et al.*,[183] who also synthesised single crystals of $Mn_2Ga_2S_5$ using CVT. Neutron diffraction measured at 1 K for both compounds showed no sharp magnetic peaks. Instead, a broad asymmetric peak around *d*-spacing of 6-6.5 Å was seen. This peak was identified as a Warren peak and was fitted well with the Warren function giving a correlation length of 16.7(2) and 21.1(7) Å for $Mn_2Ga_2S_5$ and $Fe_2Ga_2S_5$, respectively. The short correlation length of only a few unit cells suggests the magnetic ordering is two-dimensional and extremely short-range. Monte Carlo simulations were used to better understand the magnetic configuration in these highly disordered materials. The four magnetic configurations: FM, Neel, zigzag and stripy, were all simulated with the zigzag giving the most intense magnetic scattering where the observed scattering was seen. Disorder was introduced by making the ordering only two-dimensional and resembled a Warren-like peak. The scattering can be made broader by incorporating the zigzag and the stripy, although it is hard to unambiguously determine the arrangement. This disorder can be justified by competition between the *J* interactions and the possibility of an AFM direct exchange competing with the FM 90° superexchange, with the system not being completely satisfied, resulting in meta-stable states and hence spin-glass behaviour. The presence of chemical disorder, especially with the indication of ~ 10 % Mn on the Ga site, could also disrupt long-range ordering.

The solid-solution of $Mn_{2-x}Fe_xGa_2S_5$ was synthesised and first reported here. A linear decrease in the lattice parameters was observed with increasing Fe content. The phase percentage of the 1*T* polytype decreased with x and was zero at $MnFeGa_2S_5$, which was found to adopt the 3*R* polytype exclusively. For $x > 1$, the single layer $FeGa_2S_4$ was seen as a side-phase. The crystallinity decreased at high Fe content. Perhaps higher temperatures or quenching would be required and is a subject of future work to optimise the synthesis and

obtain a complete series. SEM measurements on $MnFeGa_2S_5$ show a homogenous spread of Mn and Fe. PND experiments would be beneficial in refining the occupancy of Mn and Fe due to the stark contrast in scattering lengths. Room temperature molar susceptibility (χ_{mol}) decreased almost linearly with x, whereas the spin freezing temperature (T_f) increased with x. However, for the Weiss temperature (θ_w) and the effective moment (μ_{eff}), no clear trend was observed, and further measurements would be required to investigate this further, including higher temperature magnetic susceptibility measurements at significantly higher temperatures than the Weiss temperatures indicated by the fits, to ensure that the use of the Curie-Weiss law is reasonable. Future AC susceptibility measurements on the solid solution would be helpful to see how the Mydosh parameter changes with Fe content.

Chapter 6

6 Summary and Conclusions

This thesis has explored the chemical tuning of three distinct layered chalcogenide systems: $ZrSe_3$, $Nb_2Pd_xCh_5$ (*Ch* = S, Se) and $A_2Ga_2S_5$ (*A* = Mn, Fe).

Chapter 3 discussed the intercalation chemistry of $ZrSe_3$. Intercalation of alkali metals K, Rb and Cs using metal/ammonia solution at low temperatures contrast with high-temperature variants previously reported.[119] Intercalation of K, forming $K_{0.45(2)}ZrSe_3$, was found to adopt the polymorph crystallising in $Cmc2_1$, unlike the high-temperature variant, which was reported to adopt a polymorph crystallising in *Immm*. The opposite was found for $Cs_{0.42(1)}ZrSe_3$, which crystallises in *Immm* at low temperatures, with the high-temperature variant adopting the $Cmc2_1$ polymorph. These polymorphs are related by the relative shifting of the $ZrSe_3$ layers. $Rb_{0.41(1)}ZrSe_3$ was found to adopt the *Immm* polymorph, in agreement with the high-temperature variant previously reported. The polymorphs found for the Rb and Cs intercalates are likely dictated by the large size of the cations, preferring to occupy the largest site possible, found in the *Immm* structure. Intercalation reduced the selenide-selenide dimers $[Se_2]^{2-}$ rather than the Zr^{4+}, with elongation of the dimer bond length and subsequent contraction of the distance between neighbouring dimers. Intercalation of Ca proceeded with co-intercalation of the NH_3 solvent. Chemical analysis indicated to a formula of $Ca_{0.2}(NH_3)_{0.45(7)}(NH_2)_{0.15(7)}ZrSe_3$. The diffraction pattern could not be modelled with either the *Immm* or the $Cmc2_1$ structures. The co-intercalation of NH_3 resulted in larger interlayer separation, with the $ZrSe_3$ being free to shift, leading to severe stacking disorder. This was modelled by splitting the structure into $ZrSe_3$ and Ca/NH_3 rigid subunits and allowing them to shift independently in the axes. The stacking fault refinement fitted the PXRD and PND

patterns well, with the *Immm*-type arrangement of $ZrSe_3$ layers having the largest probability. Ca/NH_3 layer shifts in the neutron refinement show a clear favourability of the NH_3 being in closer proximity to the Se, presumably to facilitate hydrogen bonding. Magnetic measurements show the compounds remain diamagnetic upon intercalation, confirming Zr^{4+} oxidation state remains unchanged. It would be expected that partial reduction of $[Se_2]^{2-}$ would give rise to paramagnetism. It is likely that only a fraction of the dimers are being fully reduced to Se^{2-}, with the bond lengths found in the PXRD refinements likely as a result of averaging. Raman spectroscopy showed the presence of the non-reduced selenide dimer (A_g^8) mode and a new peak at lower wavenumbers. This would suggest that in this system, there is a mixture of reduced and non-reduced slabs, consistent with the chemical analysis and the presence of stacking faults.

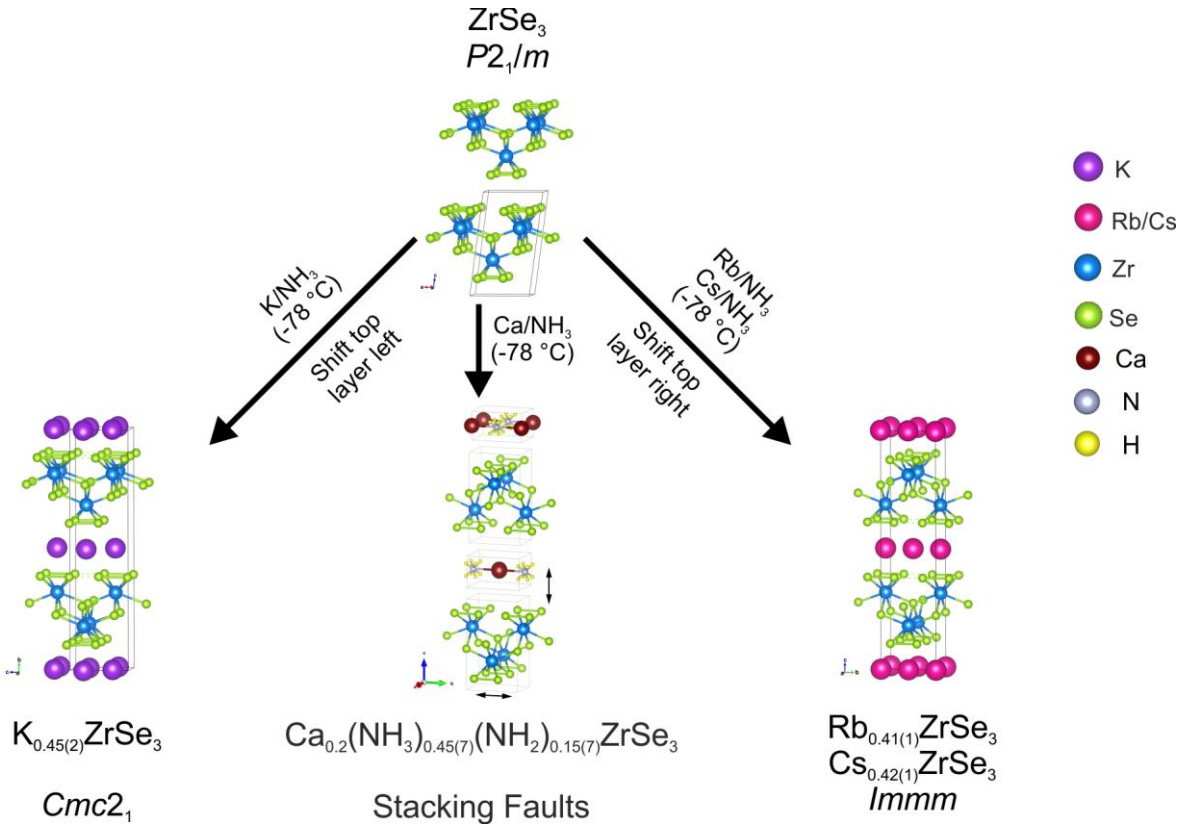


Figure 6.1: Overview of the work carried out in Chapter 3.

Future work on these compounds can involve UV-Vis spectroscopy and DFT calculations on the density of states, investigating the changes in the band gap upon intercalation. $ZrSe_3$ is a black semiconductor. However, upon intercalation of alkali metal, the intercalates are brown in colour, suggesting changes in the band-gap. The intercalation of other alkaline earth metals, such as Sr and Ba, can be another area of future study to investigate whether they also facilitate co-intercalation like Ca.

Chapter 4 explored the Li intercalation chemistry of the isostructural superconductors $Nb_2Pd_xS_5$ (T_c = 6.5 K) and $Nb_2Pd_xSe_5$ (T_c = 6.5 K). The intercalation chemistry of these compounds has been shown to be complicated. Intercalation using Li/NH_3 into $Nb_2Pd_{0.74}S_5$ produced a single intercalated phase, with the unit cell volume expanding by ~ 2 %. The product retained its *C*2/*m* symmetry due to the $Pd(2)S_4$ linking the layers. PND was used to locate Li in a triangular prismatic site, with the Li occupancy being refined to 0.33(4). Subtle changes in the structures were observed in the structure as a consequence of intercalation, with the rotation of $Pd(1)S_4$ units to undistort the triangular prismatic site. A single peak was observed in the solid-state ^{7}Li MAS NMR, indicative of one Li site, or was exchanging rapidly on the NMR timescale. DFT calculations on the energies of the possible Li sites within the structure showed that the triangular prismatic site was the lowest in energy, in-line with the findings from PND refinement. Deintercalation using I_2 returned the starting material, albeit with slightly larger lattice parameters and broader peaks, suggesting some regions within the material that contain small quantities of Li. No superconducting transition was observed down to 2 K upon intercalation. Susceptibility vs temperature measurements showed a reduction in the Pauli susceptibility by ~ 40 %. Since the Pauli susceptibility is proportional to the density of states at the Fermi level, this was consistent with the suppression of superconductivity and with traversing the negative gradient of the density of states around the Fermi level. Deintercalation partially restored superconductivity, with an

onset transition temperature observed at ~ 3.5 K. However, the superconducting volume fraction dropped significantly from 80 % in the original parent compounds to 7 % in the deintercalated compound.

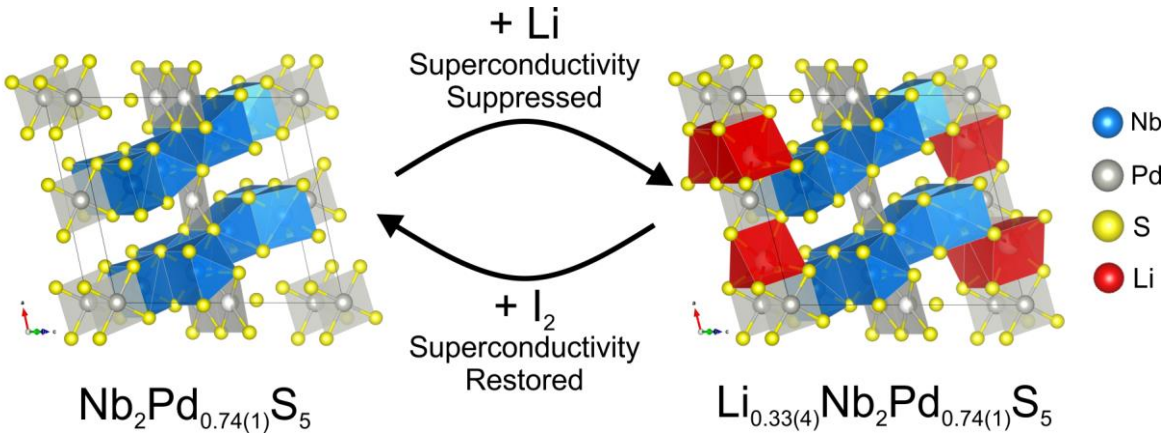


Figure 6.2: Li intercalation and deintercalation of $Nb_2Pd_{0.74}S_5$

Electrochemical intercalation was also shown here to be a viable method of intercalation. Samples were discharged to specific capacities corresponding to a theoretical Li content (x in $Li_xNb_2Pd_{0.74}S_5$) of 0.19, 0.4 and 0.79, respectively. A step in the discharge curve observed at $x \sim 0.4$ indicated new phase formation. At $x \sim 0.19$, the sample closely resembled the chemically intercalated $Li_{0.33(4)}Nb_2Pd_{0.74}S_5$. However, at $x = 0.4$, the compound has undergone phase separation. The intercalate showed expansion in the *a*-axis and contraction in the *c*-axis and β angle. The subtle structural changes observed earlier for $Li_{0.33(4)}Nb_2Pd_{0.74}S_5$ appeared to revert to the starting parent. This would allude to Li perhaps occupying another site. The triangular prismatic sites, stacked along the *b*-axis, are in close proximity to one another. It is unlikely this site can have a high degree of Li occupancy without unfavourable electrostatic repulsion. PND and NMR measurements on the more intercalated samples would be beneficial to determine where the Li resides.

Optimising the synthesis of $Nb_2Pd_xSe_5$ was challenging, as the starting Pd stoichiometry has a significant effect on the superconductivity, reducing the starting Pd stoichiometry,

although increases the phase purity, it reduces the T_c. It was found for polycrystalline samples, a starting Pd content $x = 0.95$ in $Nb_2Pd_xSe_5$ was a good compromise.

Li intercalation into $Nb_2Pd_xSe_5$ proved complicated. Intercalation using *n*-BuLi shows an emergence of a side phase that appears to match an intercalated Li_yNbSe_2, which would allude to decomposition. Using Li/naphthalene was found to be the most optimal reagent to maximise Li intake whilst keeping decomposition at a minimum. However, attempts at refining the Li position in the PND data were unsuccessful, with the data being insensitive to the Li position. This is likely reflective of the much larger scattering lengths of Se compared to S. DFT calculations were used to calculate the lowest energy Li sites, with predicted ^{7}Li NMR chemical shifts which were compared with the experimental NMR spectra. The calculated Li sites energy ordering was analogous to that found for the sulfide variant. The NMR calculations suggested Li occupied the octahedral site, which can have an occupancy of 0.87 (determined from ICP-MS) without any unfavourable electrostatic repulsion. Electrochemical intercalation showed a plateau in the potential vs specific capacity graph at a Li content x (in $Li_xNb_2Pd_{0.82}Se_5$) of ~ 1, which would be consistent with Li occupying a site until maximum occupancy before phase-separation/decomposition. The electrochemical intercalate $Li_{0.49}Nb_2Pd_{0.81}Se_5$ was found to be a single crystalline phase, with a single peak observed in the NMR spectra. However, further intercalation at $x = 1.1$ showed a close resemblance to chemical intercalation using a 1:1 molar ratio of *n*-BuLi, with the NMR spectra showing extra peaks alluding to some decomposition to Li_yNbSe_2 and Li_2Se.

In both compounds, *in-situ* PXRD on the electrochemical intercalation would be an effective technique to observe these structural changes and get a greater understanding of the intercalation chemistry of these compounds and why the details are significantly different.

Electrochemistry allows greater control of intercalation, although producing quantities sufficient for PND measurements would be difficult. Deintercalation using electrochemistry may be a better method to fully restore the superconductivity. The work presented here can be extended to the other members of this superconducting family: $Ta_2Pd_xS_5$ and $Ta_2Pd_xSe_5$.

Chapter 5 investigated the magnetic behaviour of $A_2Ga_2S_5$ (A = Mn, Fe). Both compounds adopt a buckled-honeycomb arrangement of A^{2+}. The main difference is that $Mn_2Ga_2S_5$ crystallises in the 1T polytype (P-3m1 space group), with the $Fe_2Ga_2S_5$ predominantly adopting the 3R polytype (R-3m space group). PND measurements on $Mn_2Ga_2S_5$ indicated mixed sites with an ~ 10 % Mn occupancy on the Ga site and a 1-2 % Ga occupancy on the Mn site – a new observation. For $Fe_2Ga_2S_5$, the 1T polytype was found as a minority phase, with the indication that perhaps there is some stacking disorder/intergrowth of the two polytypes, which can be further investigated using HAADF-STEM. SQUID magnetometry on both compounds suggested these systems are glassy and highly frustrated with a T_f of 12 K and ~ 50 K and θ_w of -282(1) K and -398(1) K for $Mn_2Ga_2S_5$ and $Fe_2Ga_2S_5$, respectively. Both compounds also displayed displaced hysteresis loops, characteristic of a spin-glass. PND at 1 K showed no sharp magnetic peaks but, instead, a broad Warren-like peak. This alluded to 2D magnetic behaviour and fitting to the Warren function, suggesting very short correlation lengths of 16.7(2) Å and 21.1(7) Å for $Mn_2Ga_2S_5$ and $Fe_2Ga_2S_5$, respectively. The diffuse peak was modelled using Monte Carlo simulations. Initially, the four magnetic configurations: Ferromagnetic, Antiferromagnetic-Néel, zigzag and stripy, were replicated. This was achieved using $a \times \sqrt{3} \times c$ expansion of the nuclear unit cell. The zigzag configuration gives the most intensity at $Q \sim 1$ Å, in-line with experimental observation. This is also in agreement with a previous theoretical study, which predicted the zigzag to be the lowest in energy.[181] It is likely that the diffuse peak stems from a disordered zigzag arrangement of spins, although it is difficult to unambiguously determine the

configuration adopted. This magnetic disorder could be explained by competition of different *A*-S-*A* superexchange interactions, which cannot all be satisfied. The chemical disorder, with the mixed site occupancy, is also likely to lead to some disorder in the magnetic behaviour.

Both compounds were tuned by doping, forming a solid solution of $Mn_{2-x}Fe_xGa_2S_5$ (x = 0.25, 0.5, 0.75, 1, 1.25, 1.5, 1.75). Lattice parameters decreased almost linearly with x, whilst T_f increased with x. The transition from the 1*T* polytype to the 3*R* polytype was observed with $MnFeGa_2S_5$ found to adopt the 3*R* structure exclusively. The hysteresis loops showed an increasing displacement away from the origin with increasing Fe content. The solid solution can open up an avenue for future work with studies using PND, which could be useful to determine Mn/Fe content and investigate how the magnetic peak changes upon doping.

This thesis has shown the diverse nature and behaviour of layered chalcogenides, with intercalation being a great tool to tune a compound's structure and properties. Correlating the chemical structure with the properties observed is paramount to understanding the chemistry of these materials. The work presented here has laid the groundwork on the chemistry of these compounds, opening up potential avenues upon which future studies can be built on.

References

1 K. Mizushima, P. C. Jones, P. J. Wiseman and J. B. Goodenough, *Mater Res Bull*, 1980, **15**, 783–789.

2 R. Dronskowski, *Adv Funct Mater*, 2001, **11**, 27–29.

3 J. H. Judy, *J Magn Magn Mater*, 2005, **287**, 16–26.

4 S. P. Denbaars, D. Feezell, K. Kelchner, S. Pimputkar, C. C. Pan, C. C. Yen, S. Tanaka, Y. Zhao, N. Pfaff, R. Farrell, M. Iza, S. Keller, U. Mishra, J. S. Speck and S. Nakamura, *Acta Mater*, 2013, **61**, 945–951.

5 A. Piegari and F. Flory, *Optical Thin Films and Coatings: From Materials to Applications*, Elsevier, Second Edition., 2018.

6 G. Buxbaum and G. Pfaff, *Industrial Inorganic Pigments: Third Edition*, Wiley-VCH, 2005.

7 M. Parizh, Y. Lvovsky and M. Sumption, *Supercond Sci Technol*, 2017, **30**, 014007.

8 M. A. Hayward, M. A. Green, M. J. Rosseinsky and J. Sloan, *J Am Chem Soc*, 1999, **121**, 8843–8854.

9 C. Tassel, L. Seinberg, N. Hayashi, S. Ganesanpotti, Y. Ajiro, Y. Kobayashi and H. Kageyama, *Inorg Chem*, 2013, **52**, 6096–6102.

10 H. B. Li, S. Kobayashi, C. Zhong, M. Namba, Y. Cao, D. Kato, Y. Kotani, Q. Lin, M. Wu, W. H. Wang, M. Kobayashi, K. Fujita, C. Tassel, T. Terashima, A. Kuwabara, Y. Kobayashi, H. Takatsu and H. Kageyama, *J Am Chem Soc*, 2021, **143**, 17517–17525.

11 P. A. Madden and M. Wilson, *Chem Soc Rev*, 1996, **25**, 339–350.

12 G. H. Chan, B. Deng, M. Bertoni, J. R. Ireland, M. C. Hersam, T. O. Mason, R. P. Van Duyne and J. A. Ibers, *Inorg Chem*, 2006, **45**, 8264–8272.

13 V. Johnson and W. Jeitschko, *J Solid State Chem*, 1974, **11**, 161–166.

14 S. J. Cassidy, M. J. Pitcher, J. J. K. Lim, J. Hadermann, J. P. Allen, G. W. Watson, S. Britto, E. J. Chong, D. G. Free, C. P. Grey and S. J. Clarke, *Inorg Chem*, 2019, **58**, 3850.

15 W. Nieuwenkamp and J. M. Bijvoet, *Z Kristallogr Cryst Mater*, 1932, **81**, 469–474.

16 R. R. Chianelli, J. C. Scanlon and A. H. Thompson, *Mater Res Bull*, 1975, **10**, 1379–1382.

17 M. S. Whittingham, *Science*, 1976, **192**, 1126–7.

18 P. D. Fleischauer and R. Bauer, *Tribology Transactions*, 1988, **31**, 239–250.

19 Y. Li, H. Wang, L. Xie, Y. Liang, G. Hong and H. Dai, *J Am Chem Soc*, 2011, **133**, 7296–7299.

20 G. Li, D. Zhang, Q. Qiao, Y. Yu, D. Peterson, A. Zafar, R. Kumar, S. Curtarolo, F. Hunte, S. Shannon, Y. Zhu, W. Yang and L. Cao, *J Am Chem Soc*, 2016, **138**, 16632–16638.

21 M. N. Ali, J. Xiong, S. Flynn, J. Tao, Q. D. Gibson, L. M. Schoop, T. Liang, N. Haldolaarachchige, M. Hirschberger, N. P. Ong and R. J. Cava, *Nature*, 2014, **514**, 205–208.

22 R. C. Morris, R. V. Coleman and R. Bhandari, *Phys Rev B*, 1972, **5**, 895–901.

23 G. Brostigen, A. Kjekshus, E. E. Astrup, V. Nordal, A. A. Lindberg and J. C. Craig, *Acta Chem Scand*, 1969, **23**, 2186–2188.

24 Y. Jin, X. Li and J. Yang, *Physical Chemistry Chemical Physics*, 2015, **17**, 18665–18669.

25 W. Kong, C. Bacaksiz, B. Chen, K. Wu, M. Blei, X. Fan, Y. Shen, H. Sahin, D. Wright, D. S. Narang and S. Tongay, *Nanoscale*, 2017, **9**, 4175–4182.

26 J. Dai and X. C. Zeng, *Angewandte Chemie - International Edition*, 2015, **54**, 7572–7576.

27 J. O. Island, A. J. Molina-Mendoza, M. Barawi, R. Biele, E. Flores, J. M. Clamagirand, J. R. Ares, C. Sánchez, H. S. J. Van Der Zant, R. D'Agosta, I. J. Ferrer and A. Castellanos-Gomez, *2d Mater*, 2017, **4**, 022003.

28 J. O. Island, R. Biele, M. Barawi, J. M. Clamagirand, J. R. Ares, C. Sánchez, H. S. J. Van Der Zant, I. J. Ferrer, R. D'Agosta and A. Castellanos-Gomez, *Sci Rep*, 2016, **6**, 1–7.

29 J. O. Island, M. Buscema, M. Barawi, J. M. Clamagirand, J. R. Ares, C. Sánchez, I. J. Ferrer, G. A. Steele, H. S. J. van der Zant and A. Castellanos-Gomez, *Adv Opt Mater*, 2014, **2**, 641–645.

30 J. Wu, D. Wang, H. Liu, W. M. Lau and L. M. Liu, *RSC Adv*, 2015, **5**, 21455–21463.

31 S. Takahashi, T. Sambongi, J. W. Brill and W. Roark, *Solid State Commun*, 1984, **49**, 1031–1034.
32 H. Nakajima, K. Nomura and T. Sambongi, *Physica B+C*, 1986, **143**, 240–242.
33 D. J. Eaglesham, J. W. Steeds and J. A. Wilson, *Journal of Physics C: Solid State Physics*, 1984, **17**, L697–L698.
34 Th. Weber, J. C. Muijsers and J. W. Niemantsverdriet, *J Phys Chem*, 1995, **99**, 9194–9200.
35 W. Krönert and K. Plieth, *Naturwissenschaften*, 1958, **45**, 416.
36 W. Krönert and K. Plieth, *ZAAC - Journal of Inorganic and General Chemistry*, 1965, **336**, 207–218.
37 L. Brattas and A. Kjekshus, *Acta Chem Scand*, 1972, **26**, 3441–3449.
38 S. Furuseth, L. Brattås, A. Kjekshus, A. F. Andresen and P. Fischer, *Acta Chem Scand*, 1975, **29a**, 623–631.
39 S. Furuseth, H. Fjellvåg, L.-G. Johansson, V. P. Gultyai, I. Persson and L. I. Elding, *Acta Chem Scand*, 1991, **45**, 694–697.
40 E. Bjerkelund, J. H. Fermor, A. Kjekshus, M. Wagnières, D. H. Williams, E. Bunnenberg, C. Djerassi and R. Records, *Acta Chem Scand*, 1966, **20**, 1836–1842.
41 J. L. Hodeau, M. Marezio, C. Roucau, R. Ayroles, A. Meerschaut, J. Rouxel and P. Monceau, *Journal of Physics C: Solid State Physics*, 1978, **11**, 4117–4134.
42 J. Gopalakrishnan and K. S. Nanjundaswamy, *Bulletin of Materials Science*, 1983, **5**, 287–306.
43 J. Rijnsdorp and F. Jellinek, *J Solid State Chem*, 1978, **25**, 325–328.
44 E. Bjerkelund and A. Kjekshus, *Z Anorg Allg Chem*, 1964, **328**, 235–242.
45 C. Tan, P. Yu, Y. Hu, J. Chen, Y. Huang, Y. Cai, Z. Luo, B. Li, Q. Lu, L. Wang, Z. Liu and H. Zhang, *J Am Chem Soc*, 2015, **137**, 10430–10436.
46 C. Zhu, Z. Zeng, H. Li, F. Li, C. Fan and H. Zhang, *J Am Chem Soc*, 2013, **135**, 5998–6001.
47 S. A. Sunshine and J. A. Ibers, *Inorg Chem*, 1985, **24**, 3611–3614.
48 D. A. Keszler, P. J. Squattrito, N. E. Brese, J. A. Ibers, S. Maoyu and L. Jiaxi, *Inorg Chem*, 1985, **24**, 3063–3067.
49 D. A. Keszler, J. A. Ibers, S. Maoyu and L. Jiaxi, *J Solid State Chem*, 1985, **57**, 68–81.
50 D. A. Keszler and J. A. Ibers, *J Solid State Chem*, 1984, **52**, 73–79.
51 Y. Lu, T. Takayama, A. F. Bangura, Y. Katsura, D. Hashizume and H. Takagi, *J Physical Soc Japan*, 2014, **83**, 023702.
52 F. J. Di Salvo, C. H. Chen, R. M. Fleming, J. V. Waszczak, R. G. Dunn, S. A. Sunshine and J. A. Ibers, *Journal of The Less-Common Metals*, 1986, **116**, 51–61.
53 R. S. Knox, in *Collective Excitations in Solids*, ed. B. Di Bartolo, Springer US, Boston, MA, 1983, pp. 183–245.
54 T. I. Larkin, A. N. Yaresko, D. Pröpper, K. A. Kikoin, Y. F. Lu, T. Takayama, Y. L. Mathis, A. W. Rost, H. Takagi, B. Keimer and A. V. Boris, *Phys Rev B*, 2017, **95**, 195144.
55 L. Dogguy-Smiri, N. H. Dung and M. P. Pardo, *Mater Res Bull*, 1980, **15**, 861–866.
56 L. Dogguy-Smiri and N. H. Dung, *Acta Crystallogr B*, 1982, **38**, 372–375.
57 Y. Ōnuki, R. Inada, S. Tanuma, S. Yamanaka and H. Kamimura, *Solid State Ion*, 1983, **11**, 195–201.
58 K. Nikonov, N. Ehlen, B. Senkovskiy, N. Saigal, A. Fedorov, A. Nefedov, C. Wöll, G. Di Santo, L. Petaccia and A. Grüneis, *Dalton Transactions*, 2018, **47**, 2986–2991.
59 R. Schöllhorn and A. Weiss, *Zeitschrift für Naturforschung B*, 1972, **27**, 1277–1278.
60 M. S. Whittingham, *J Chem Soc Chem Commun*, 1974, 328.
61 F.-C. Hsu, J.-Y. Luo, K.-W. Yeh, T.-K. Chen, T.-W. Huang, P. M. Wu, Y.-C. Lee, Y.-L. Huang, Y.-Y. Chu, D.-C. Yan and M.-K. Wu, *Proceedings of the National Academy of Sciences*, 2008, **105**, 14262–14264.
62 T. P. Ying, X. L. Chen, G. Wang, S. F. Jin, T. T. Zhou, X. F. Lai, H. Zhang and W. Y. Wang, *Sci Rep*, 2012, **2**, 426.
63 M. Burrard-Lucas, D. G. Free, S. J. Sedlmaier, J. D. Wright, S. J. Cassidy, Y. Hara, A. J. Corkett, T. Lancaster, P. J. Baker, S. J. Blundell and S. J. Clarke, *Nat Mater*, 2013, **12**, 15–19.

64 S. J. Sedlmaier, S. J. Cassidy, R. G. Morris, M. Drakopoulos, C. Reinhard, S. J. Moorhouse, D. O'Hare, P. Manuel, D. Khalyavin and S. J. Clarke, *J Am Chem Soc*, 2014, **136**, 630–633.

65 M. E. Kamminga, S. J. Cassidy, P. P. Jana, M. Elgaml, N. D. Kelly and S. J. Clarke, *Dalton Transactions*, 2021, **50**, 11376–11379.

66 H. Sun, D. N. Woodruff, S. J. Cassidy, G. M. Allcroft, S. J. Sedlmaier, A. L. Thompson, P. A. Bingham, S. D. Forder, S. Cartenet, N. Mary, S. Ramos, F. R. Foronda, B. H. Williams, X. Li, S. J. Blundell and S. J. Clarke, *Inorg Chem*, 2015, **54**, 1958–1964.

67 D. N. Woodruff, F. Schild, C. V Topping, S. J. Cassidy, J. N. Blandy, S. J. Blundell, A. L. Thompson and S. J. Clarke, *Inorg Chem*, 2016, **55**, 9886–9891.

68 K. J. Koski, C. D. Wessells, B. W. Reed, J. J. Cha, D. Kong and Y. Cui, *J Am Chem Soc*, 2012, **134**, 13773–13779.

69 J. P. Motter, K. J. Koski and Y. Cui, *Chemistry of Materials*, 2014, **26**, 2313–2317.

70 K. J. Koski, J. J. Cha, B. W. Reed, C. D. Wessells, D. Kong and Y. Cui, *J Am Chem Soc*, 2012, **134**, 7584–7587.

71 K. P. Chen, F. R. Chung, M. Wang and K. J. Koski, *J Am Chem Soc*, 2015, **137**, 5431–5437.

72 P. J. Squattrito, S. A. Sunshine and J. A. Ibers, *Solid State Ion*, 1986, **22**, 53–63.

73 S. Nakamura, T. Noji, T. Hatakeda, K. Sato, T. Kawamata, M. Kato and Y. Koike, *J Phys Conf Ser*, 2018, **969**, 012076.

74 S. A. Holgate, *Understanding solid state physics*, CRC PRESS, 2009.

75 M. Konagai, M. Sugimoto and K. Takahashi, *J Cryst Growth*, 1978, **45**, 277–280.

76 W. Massa and M. Steiner, *J Solid State Chem*, 1980, **32**, 137–143.

77 P. Day, M. T. Hutchings, E. Janke and P. J. Walker, *J. Chem. Soc., Chem. Commun.*, 1979, 711–713.

78 H. Deiseroth, K. Aleksandrov, C. Reiner, L. Kienle and R. K. Kremer, *Eur J Inorg Chem*, 2006, 1561–1567.

79 J. J. Banewicz and R. Lindsay, *Physical Review*, 1956, **104**, 318–320.

80 B. C. Sheath, S. J. Cassidy and S. J. Clarke, *J Solid State Chem*, 2021, **293**, 121761.

81 S. J. C. Herkelrath, J. N. Blandy and S. J. Clarke, *J Solid State Chem*, 2018, **264**, 119–123.

82 F. Ye, J. A. Fernandez-Baca, R. S. Fishman, Y. Ren, H. J. Kang, Y. Qiu and T. Kimura, *Phys Rev Lett*, 2007, **99**, 157201.

83 T. Kurumaji, T. Nakajima, M. Hirschberger, A. Kikkawa, Y. Yamasaki, H. Sagayama, H. Nakao, Y. Taguchi, T. hisa Arima and Y. Tokura, *Science (1979)*, 2019, **365**, 914–918.

84 Y. Shimizu, K. Miyagawa, K. Kanoda, M. Maesato and G. Saito, *Phys Rev Lett*, 2003, **91**, 107001.

85 S. Nakatsuji, Y. Nambu, H. Tonomura, O. Sakai, S. Jonas, C. Broholm, H. Tsunetsugu, Y. Qiu and Y. Maeno, *Science (1979)*, 2005, **309**, 1697–1700.

86 S. Nakatsuji, Y. Nambu, K. Onuma, S. Jonas, C. Broholm and Y. Maeno, *Journal of Physics: Condensed Matter*, 2007, **19**, 145232.

87 H. Takeya, K. Ishida, K. Kitagawa, Y. Ihara, K. Onuma, Y. Maeno, Y. Nambu, S. Nakatsuji, D. E. MacLaughlin, A. Koda and R. Kadono, *Phys Rev B*, 2008, **77**, 054429.

88 D. E. MacLaughlin, Y. Nambu, S. Nakatsuji, R. H. Heffner, L. Shu, O. O. Bernal and K. Ishida, *Phys Rev B*, 2008, **78**, 220403.

89 Y. Nambu, R. T. Macaluso, T. Higo, K. Ishida and S. Nakatsuji, *Phys Rev B*, 2009, **79**, 214108.

90 C. Stock, S. Jonas, C. Broholm, S. Nakatsuji, Y. Nambu, K. Onuma, Y. Maeno and J.-H. Chung, *Phys Rev Lett*, 2010, **105**, 037402.

91 S. Nakatsuji, H. Tonomura, K. Onuma, Y. Nambu, O. Sakai, Y. Maeno, R. T. MacAluso and J. Y. Chan, *Phys Rev Lett*, 2007, **99**, 157203.

92 T. Tomita, Y. Nambu, S. Nakatsuji, S. Koeda, M. Hedo and Y. Uwatoko, *J Physical Soc Japan*, 2009, **78**, 094603.

93 G. Rousse, J. Rodríguez-Carvajal, C. Wurm and C. Masquelier, *Chemistry of Materials*, 2001, **13**, 4527–4536.

94 H. Kamerlingh Onnes, *Commun. Phys. Lab. Univ. Leiden*, 1911, **12**, 120.

95 W. Meissner and R. Ochsenfeld, *Naturwissenschaften*, 1933, **21**, 787–788.

96 F. London and H. London, *Proc R Soc Lond A Math Phys Sci*, 1935, **149**, 71–88.

97 E. Maxwell, *Physical Review*, 1950, **78**, 477.
98 J. Bardeen, L. N. Cooper and J. R. Schrieffer, *Physical Review*, 1957, **108**, 1175–1204.
99 J. Nagamatsu, N. Nakagawa, T. Muranaka, Y. Zenitani and J. Akimitsu, *Nature*, 2001, **410**, 63–64.
100 A. P. Drozdov, M. I. Eremets, I. A. Troyan, V. Ksenofontov and S. I. Shylin, *Nature*, 2015, **525**, 73–76.
101 E. Helfand and N. R. Werthamer, *Physical Review*, 1966, **147**, 288–294.
102 K. Maki and T. Tsuneto, *Progress of Theoretical Physics*, 1964, **31**, 945–956.
103 B. T. Matthias, T. H. Geballe, S. Geller and E. Corenzwit, *Physical Review*, 1954, **95**, 1435.
104 M. K. Wu, J. R. Ashburn, C. J. Torng, P. H. Hor, R. L. Meng, L. Gao, Z. J. Huang, Y. Q. Wang and C. W. Chu, *Phys Rev Lett*, 1987, **58**, 908–910.
105 A. Schilling, M. Cantoni, J. D. Guo and H. R. Ott, *Nature*, 1993, **363**, 56–58.
106 P. A. Lee, N. Nagaosa and X.-G. Wen, *Rev Mod Phys*, 2006, **78**, 17–85.
107 X. Gui, K. Górnicka, Q. Chen, H. Zhou, T. Klimczuk and W. Xie, *Inorg Chem*, 2020, **59**, 5798–5802.
108 Y. Kamihara, H. Hiramatsu, M. Hirano, R. Kawamura, H. Yanagi, T. Kamiya and H. Hosono, *J Am Chem Soc*, 2006, **128**, 10012–10013.
109 Y. Kamihara, T. Watanabe, M. Hirano and H. Hosono, *J Am Chem Soc*, 2008, **130**, 3296–3297.
110 S. Medvedev, T. M. McQueen, I. A. Troyan, T. Palasyuk, M. I. Eremets, R. J. Cava, S. Naghavi, F. Casper, V. Ksenofontov, G. Wortmann and C. Felser, *Nat Mater*, 2009, **8**, 630–633.
111 X. F. Lu, N. Z. Wang, G. H. Zhang, X. G. Luo, Z. M. Ma, B. Lei, F. Q. Huang and X. H. Chen, *Phys Rev B Condens Matter Mater Phys*, 2014, **89**, 20507.
112 A. Krzton-Maziopa, E. V Pomjakushina, V. Y. Pomjakushin, F. Von Rohr, A. Schilling and K. Conder, *Journal of Physics Condensed Matter*, 2012, **24**, 382202.
113 N. Higashihara, Y. Okamoto, Y. Yoshikawa, Y. Yamakawa, H. Takatsu, H. Kageyama and K. Takenaka, *J Physical Soc Japan*, 2021, **90**, 63705.
114 Q. R. Zhang, D. Rhodes, B. Zeng, T. Besara, T. Siegrist, M. D. Johannes and L. Balicas, *Phys Rev B Condens Matter Mater Phys*, 2013, **88**, 24508.
115 Q. Zhang, G. Li, D. Rhodes, A. Kiswandhi, T. Besara, B. Zeng, J. Sun, T. Siegrist, M. D. Johannes and L. Balicas, *Sci Rep*, 2013, **3**, 1446.
116 S. Khim, B. Lee, K.-Y. Choi, B.-G. Jeon, D. H. Jang, D. Patil, S. Patil, R. Kim, E. S. Choi, S. Lee, J. Yu and K. H. Kim, *New J Phys*, 2013, **15**, 123031.
117 J. Zhang, J. K. Dong, Y. Xu, J. Pan, L. P. He, L. J. Zhang and S. Y. Li, *Supercond Sci Technol*, 2015, **28**, 115015.
118 R. R. Chianelli and M. B. Dines, *Inorg Chem*, 1975, **14**, 2417–2421.
119 K. O. Klepp, N. A. Harringer and Andreas. Kolb, *Zeitschrift für Naturforschung B*, 2002, **57**, 1265–1269.
120 Q. Chen, X. Yang, X. Yang, J. Chen, C. Shen, P. Zhang, Y. Li, Q. Tao and Z.-A. Xu, *Front Phys (Beijing)*, 2017, **12**, 127402.
121 R. Goyal and V. P. S. Awana, *J Supercond Nov Magn*, 2017, **30**, 3355–3360.
122 P. Hyde, *Part II Thesis: Intercalation Chemistry of Layered Chalcogenides, University of Oxford*, 2019.
123 W. H. Bragg and W. L. Bragg, *Proceedings of the Royal Society of London. Series A, Containing Papers of a Mathematical and Physical Character*, 1913, **88**, 428–438.
124 A. Altomare, G. Cascarano, C. Giacovazzo, A. Guagliardi, M. C. Burla, G. Polidori and M. Camalli, *J Appl Crystallogr*, 1994, **27**, 435–435.
125 A. L. Patterson, *Physical Review*, 1934, **46**, 372–376.
126 G. Oszlányi and A. Süto, *Acta Crystallogr A*, 2004, **60**, 134–141.
127 P. Barnes, J. K. Cockcroft, S. Jacques and M. Vickers, How do Synchrotrons Work?, http://pd.chem.ucl.ac.uk/pdnn/inst2/work.htm.
128 P. Barnes, S. Jacques and M. Vickers, Insertion Devices, http://pd.chem.ucl.ac.uk/pdnn/inst2/insert.htm.

129 S. P. Thompson, J. E. Parker, J. Potter, T. P. Hill, A. Birt, T. M. Cobb, F. Yuan and C. C. Tang, *Review of Scientific Instruments*, 2009, **80**, 075107.
130 A. Lennie, J. Parker, C. Tang and S. Thompson, *Beamline I11 User Manual*, 2015, 1–54.
131 V. F. Sears, *Neutron News*, 1992, **3**, 26–37.
132 G. Caglioti, A. Paoletti and F. P. Ricci, *Nuclear Instruments*, 1958, **3**, 223–228.
133 J. K. Cockcroft and S. Jacques, Production of Spallation Neutrons, http://pd.chem.ucl.ac.uk/pdnn/inst3/pulsed.htm.
134 R. I. Smith, S. Hull, M. G. Tucker, H. Y. Playford, D. J. McPhail, S. P. Waller and S. T. Norberg, *Review of Scientific Instruments*, 2019, **90**, 115101.
135 L. C. Chapon, P. Manuel, P. G. Radaelli, C. Benson, L. Perrott, S. Ansell, N. J. Rhodes, D. Raspino, D. Duxbury, E. Spill and J. Norris, *Neutron News*, 2011, **22**, 22–25.
136 K. D. Liss, B. Hunter, M. Hagen, T. Noakes and S. Kennedy, *Physica B Condens Matter*, 2006, **385–386**, 1010–1012.
137 M. Avdeev and J. R. Hester, *J Appl Crystallogr*, 2018, **51**, 1597–1604.
138 H. M. Rietveld, *Acta Crystallogr*, 1967, **22**, 151–152.
139 H. M. Rietveld, *J Appl Crystallogr*, 1969, **2**, 65–71.
140 ICSD, https://icsd.products.fiz-karlsruhe.de/.
141 A. A. Coelho, *J Appl Crystallogr*, 2018, **51**, 210–218.
142 B. H. Toby, *Powder Diffr*, 2006, **21**, 67–70.
143 G. S. Pawley, *J Appl Crystallogr*, 1981, **14**, 357–361.
144 J. Clarke, *Sci Am*, 1994, **271**, 46–53.
145 A. J. Dent, G. Cibin, S. Ramos, A. D. Smith, S. M. Scott, L. Varandas, M. R. Pearson, N. A. Krumpa, C. P. Jones and P. E. Robbins, *J Phys Conf Ser*, 2009, **190**, 012039.
146 B. Ravel and M. Newville, *J Synchrotron Radiat*, 2005, **12**, 537–541.
147 E. R. Andrew, A. Bradbury and R. G. Eades, *Nature*, 1958, **182**, 1659.
148 D. R. Artree and W. Artree, *Proc R Soc Lond A Math Phys Sci*, 1935, **150**, 9–33.
149 P. Hohenberg and W. Kohn, *Physical Review*, 1964, **136**, B864–B871.
150 N. Metropolis, A. W. Rosenbluth, M. N. Rosenbluth, A. H. Teller and E. Teller, *J Chem Phys*, 1953, **21**, 1087–1092.
151 P. Debye, *Ann Phys*, 1912, **344**, 789–839.
152 Y. M. C.Sourisseau, S.P. Gwet, P.Gard, *J Solid State Chem*, 1988, **211**, 257–211.
153 E. Canadell, C. Thieffry, Y. Mathey and M. hwan Whangbo, *Inorg Chem*, 1989, **28**, 3043–3047.
154 H. Sommer and R. Hoppe, *ZAAC - Journal of Inorganic and General Chemistry*, 1977, **429**, 118–130.
155 F. F. Y. Wang and D. E. Cox, *Acta Crystallographica Section A*, 1970, **26**, 377–379.
156 T. Sichla and H. Jacobs, *Z Anorg Allg Chem*, 1996, **622**, 2079–2082.
157 C. M. Ainsworth, J. W. Lewis, C. H. Wang, A. A. Coelho, H. E. Johnston, H. E. A. Brand and J. S. O. Evans, *Chemistry of Materials*, 2016, **28**, 3184–3195.
158 S. Bette and R. E. Dinnebier, in *Crystallography in Materials Science*, eds. S. Schorr and C. Weidenthaler, De Gruyter, 2021, pp. 55–92.
159 G. A. Bain and J. F. Berry, *J Chem Educ*, 2008, **85**, 532.
160 K. Osada, S. Bae, M. Tanaka, H. Raebiger, K. Shudo and T. Suzuki, *Journal of Physical Chemistry C*, 2016, **120**, 4653–4659.
161 K. Patel, J. Prajapati, R. Vaidya and S. G. Patel, *Bulletin of Materials Science*, 2005, **28**, 405–410.
162 J. Neu, D. Graf, K. Wei, A. Gaiser, Y. Xin, Y. Lai, T. E. Albrecht-Schmitt, R. Baumbach, D. J. Singh and T. Siegrist, *Chemistry of Materials*, 2020, **32**, 8361–8366.
163 P. J. Squattrito, S. A. Sunshine and J. A. Ibers, *J Solid State Chem*, 1986, **64**, 261–269.
164 C. Y. Shen, B. Q. Si, H. Bai, X. J. Yang, Q. Tao, G. H. Cao and Z. A. Xu, *EPL (Europhysics Letters)*, 2016, **113**, 37006.
165 C. Q. Niu, J. H. Yang, Y. K. Li, B. Chen, N. Zhou, J. Chen, L. L. Jiang, B. Chen, X. X. Yang, C. Cao, J. Dai and X. Xu, *Phys Rev B Condens Matter Mater Phys*, 2013, **88**, 104507.
166 H. Yu, M. Zuo, L. Zhang, S. Tan, C. Zhang and Y. Zhang, *J Am Chem Soc*, 2013, **135**, 12987–12989.

167 H. Lohani, P. Mishra, R. Goyal, V. P. S. Awana and B. R. Sekhar, *Physica B Condens Matter*, 2017, **509**, 31–35.
168 M. U. M. Patel, I. Arčon, G. Aquilanti, L. Stievano, G. Mali and R. Dominko, *ChemPhysChem*, 2014, **15**, 894–904.
169 P. A. Salyer, M. G. Barker, A. J. Blake, D. H. Gregory and C. Wilson, *Acta Crystallogr C*, 2003, **59**, i4–i6.
170 T. Marchandier, S. Mariyappan, A. M. Abakumov, S. Jobic, B. Humbert, J. Y. Mevellec, G. Rousse, M. Avdeev, R. Dedryvère, D. Foix, A. Iadecola, M. L. Doublet and J. M. Tarascon, *Chemistry of Materials*, 2022, **34**, 325–336.
171 F. Kubel, B. Bertheville and H. Bill, *Zeitschrift fur Kristallographie - New Crystal Structures*, 1999, **214**, 302.
172 G. R. Stewart, *Rev Mod Phys*, 2011, **83**, 1589–1652.
173 C. S. McEwen, *Inorg Chem*, 1985, **24**, 1656–1660.
174 S. Dey, J. Lee, S. Britto, J. M. Stratford, E. N. Keyzer, M. T. Dunstan, G. Cibin, S. J. Cassidy, M. Elgaml and C. P. Grey, *J Am Chem Soc*, 2020, **142**, 19588–19601.
175 J. Cabana, L. Monconduit, D. Larcher and M. R. Palacín, *Advanced Materials*, 2010, **22**, E170–E192.
176 P. T. Cunningham, S. A. Johnson and E. J. Cairns, *J Electrochem Soc*, 1971, **118**, 1941.
177 S. N. Patel and A. A. Balchin, *Z Kristallogr Cryst Mater*, 1983, **164**, 273–278.
178 M. P. Pardo, L. Dogguy-Smiri, J. Flahaut and N. H. Dung, *Mater Res Bull*, 1981, **16**, 1375–1384.
179 K. Hayashi and A. Kawamura, *Mater Res Bull*, 1986, **21**, 1405–1410.
180 M. P. Pardo, P. H. Fourcroy and J. Flahaut, *Mater Res Bull*, 1975, **10**, 665–675.
181 C. Liao, Y. Jin, W. Zhang, Z. Zhu and M. Chen, *Chinese Physics Letters*, 2020, **37**, 107505.
182 N. Sivadas, M. W. Daniels, R. H. Swendsen, S. Okamoto and D. Xiao, *Phys Rev B Condens Matter Mater Phys*, 2015, **91**, 235425.
183 J. Shen, X. Xu, M. He, Y. Liu, Y. Han and Z. Qu, *Chinese Physics B*, 2022, **31**, 067105.
184 K. -J Range, U. Klement, G. Döll, E. Bucher and J. R. Baumann, *Acta Crystallographica Section C*, 1992, **48**, 355–356.
185 C. Cedeño, G. Díaz De Delgado, J. M. Delgado, L. M. De Chalbaud and V. Sagredo, *Journal of Physics and Chemistry of Solids*, 2005, **66**, 2049–2051.
186 A. P. Ramirez, *Annual Review of Materials Science*, 1994, **24**, 453–480.
187 K. Hirakawa, H. Kadowaki and K. Ubukoshi, *http://dx.doi.org/10.1143/JPSJ.52.1814*, 2013, **52**, 1814–1824.
188 A. P. Ramirez, R. Jager-Waldau and T. Siegrist, *Phys Rev B*, 1991, **43**, 10461.
189 N. S. Sangeetha, V. Smetana, A. V. Mudring and D. C. Johnston, *Phys Rev B*, 2018, **97**, 014402.
190 P. Bag, P. R. Baral and R. Nath, *Phys Rev B*, 2018, **98**, 144436.
191 L. T. Nguyen and R. J. Cava, *J Magn Magn Mater*, 2019, **476**, 334–336.
192 J. A. Mydosh, *Spin Glasses : An Experimental Introduction*, CRC Press, 1st edn., 1993.
193 B. E. Warren, *Physical Review*, 1941, **59**, 693–698.
194 B. E. Warren and P. Bodenstein, *Acta Crystallogr*, 1966, **20**, 602–605.
195 E. E. McCabe, C. Stock, E. E. Rodriguez, A. S. Wills, J. W. Taylor and J. S. O. Evans, *Phys Rev B*, 2014, **89**, 100402.
196 L. L. Zhao, S. Wu, J. K. Wang, J. P. Hodges, C. Broholm and E. Morosan, *Phys Rev B*, 2013, **87**, 20406.
197 J. N. Blandy, D. R. Parker, S. J. Cassidy, D. N. Woodruff, X. Xu and S. J. Clarke, *Inorg Chem*, 2019, **58**, 8140–8150.
198 J. Rodríguez-Carvajal, *Physica B Condens Matter*, 1993, **192**, 55–69.
199 B. J. Campbell, H. T. Stokes, D. E. Tanner and D. M. Hatch, *J Appl Crystallogr*, 2006, **39**, 607–614.
200 B. C. Sheath, X. Xu, P. Manuel, J. Hadermann, M. Batuk, J. O'Sullivan, R. S. Bonilla and S. J. Clarke, *Inorg Chem*, 2022, **61**, 12373–12385.
201 D. G. Free, N. D. Withers, P. J. Hickey and J. S. O. Evans, *Chemistry of Materials*, 2011, **23**, 1625–1635.

202 J. Pardo, Marie-Paule; Julien-Pouzol, Maud; Jaulmes, Sylvie; Flahaut, *Comptes Rendus des Seances de l'Academie des Sciences, Serie C: Sciences Chimiques*, 1973, **277**, 1021–1023.
203 N. Berand and K.-J. Range, *J Alloys Compd*, 1994, **205**, 295–301.
204 S. I. Radautsan, F. G. Donika, G. A. Kyosse, I. G. Mustya and V. F. Zhitar, *physica status solidi (b)*, 1969, **34**, K129–K131.
205 F. G. Donika, G. A. Kiosse, S. I. Radautsan, S. A. Semiletov and V. F. Zhitar, *Kristallografiya*, 1967, **12**, 854–859.
206 G. Kresse and J. Hafner, *Phys Rev B*, 1993, **47**, 558–561.
207 G. Kresse and J. Furthmüller, *Comput Mater Sci*, 1996, **6**, 15–50.
208 G. Kresse and J. Furthmüller, *Phys Rev B Condens Matter Mater Phys*, 1996, **54**, 11169–11186.
209 P. E. Blöchl, *Phys Rev B*, 1994, **50**, 17953–17979.
210 D. Joubert, *Phys Rev B Condens Matter Mater Phys*, 1999, **59**, 1758–1775.
211 J. P. Perdew, A. Ruzsinszky, G. I. Csonka, O. A. Vydrov, G. E. Scuseria, L. A. Constantin, X. Zhou and K. Burke, *Phys Rev Lett*, 2008, **100**, 136406.
212 S. Kavanagh, Defect Oriented Python Environment Distribution Title, https://github.com/SMTG-UCL/doped.
213 D. Broberg, B. Medasani, N. E. R. Zimmermann, G. Yu, A. Canning, M. Haranczyk, M. Asta and G. Hautier, *Comput Phys Commun*, 2018, **226**, 165–179.
214 S. P. Ong, W. D. Richards, A. Jain, G. Hautier, M. Kocher, S. Cholia, D. Gunter, V. L. Chevrier, K. A. Persson and G. Ceder, *Comput Mater Sci*, 2013, **68**, 314–319.
215 A. Hjorth Larsen, J. Jørgen Mortensen, J. Blomqvist, I. E. Castelli, R. Christensen, M. Dułak, J. Friis, M. N. Groves, B. Hammer, C. Hargus, E. D. Hermes, P. C. Jennings, P. Bjerre Jensen, J. Kermode, J. R. Kitchin, E. Leonhard Kolsbjerg, J. Kubal, K. Kaasbjerg, S. Lysgaard, J. Bergmann Maronsson, T. Maxson, T. Olsen, L. Pastewka, A. Peterson, C. Rostgaard, J. Schiøtz, O. Schütt, M. Strange, K. S. Thygesen, T. Vegge, L. Vilhelmsen, M. Walter, Z. Zeng and K. W. Jacobsen, *Journal of Physics: Condensed Matter*, 2017, **29**, 273002.
216 S. J. Clark, M. D. Segall, C. J. Pickard, P. J. Hasnip, M. I. J. Probert, K. Refson and M. C. Payne, *Zeitschrift fur Kristallographie*, 2005, **220**, 567–570.
217 C. J. Pickard and F. Mauri, *Phys Rev B Condens Matter Mater Phys*, 2001, **63**, 2451011–2451013.
218 J. R. Yates, C. J. Pickard and F. Mauri, *Phys Rev B Condens Matter Mater Phys*, 2007, **76**, 024401.
219 D. Vanderbilt, *Phys Rev B*, 1990, **41**, 7892–7895.
220 S. G. Louie, S. Froyen and M. L. Cohen, *Phys Rev B*, 1982, **26**, 1738–1742.
221 J. P. Perdew, K. Burke and M. Ernzerhof, *Phys Rev Lett*, 1997, **78**, 1396.
222 C. Bonhomme, C. Gervais, F. Babonneau, C. Coelho, F. Pourpoint, T. Azaïs, S. E. Ashbrook, J. M. Griffin, J. R. Yates, F. Mauri and C. J. Pickard, *Chem Rev*, 2012, **112**, 5733–5779.
223 S. Sturniolo, T. F. G. Green, R. M. Hanson, M. Zilka, K. Refson, P. Hodgkinson, S. P. Brown and J. R. Yates, *Solid State Nucl Magn Reson*, 2016, **78**, 64–70.
224 T. F. G. Green, Magres-format, https://github.com/tfgg/magres-format.
225 I. D. Brown and D. Altermatt, *Acta Crystallogr B*, 1985, **41**, 244–247.

Appendix

Appendix I

Density Functional Theory Method

Plane wave density functional theory code VASP (version 5.4.4) was used to determine lithium site energies.[206–208] A plane wave cut off energy of 600 eV and Γ-centred Monkhorst-Pack (MP) grids with a maximum spacing of 0.043 2π Å^{-1} were used with projector augmented wave pseudopotentials from dataset PBE.54 (Li_sv, Nb_pv, Ta_pv, Ni_pv, Pd and Se).[209,210] PBEsol generalised gradient approximation (GGA) functional was used to model the exchange and correlation effects.[211] Tolerances of 10^{-6} eV and 10^{-2} eV Å^{-1} were applied to total energy and forces during electronic minimisation and geometry optimisation, respectively.

Input files for lithium site calculations were prepared using the doped python package with a 32-atom supercell.[212,213] Force tolerance was raised to 2×10^{-2} eV Å^{-1} for lithium interstitials during relaxations, with fixed lattice parameters. The pymatgen and ase python packages were used to manipulate structures and to assist symmetry analysis of the lithium sites.[214,215]

NMR parameters were calculated using the gauge-including projector augmented-wave (GIPAW) approach in CASTEP (version 19.11).[216–218] Lithiated structures were subject to geometry optimisation with the default LBFGS method prior to NMR calculations. Ultrasoft pseudopotentials, [219,220] generated on the fly, were defined in the built-in C19 library and GGA-PBE exchange-correlation functional was used as it is the most widely used functional in GIPAW calculations.[221,222] A plane wave cutoff energy of 700 eV was used with MP k-point grids with a maximum spacing of 0.04 2π Å^{-1}. The calculations generated absolute

magnetic shielding tensors and MagresPython library was used for computing the chemical shift values with LiF referenced at -1 ppm.[223,224]

Bond Valence Sum

The bond valence sum method is a method to obtain an approximation of the valence of a particular ion. This is achieved by approximating that the valance of an atom is the sum of the individual valences (v_i) surrounding the atom. These individual bond valances are obtained form the observed bond lengths and is expressed as

$$v_i = e^{\frac{r_0 - r_i}{b}} \qquad \text{Equation A.1}$$

Where r_i is the observed cation-anion bond length. r_0 is a reference bond length which is a tabulated parameter based on observation made for a large number of standard compounds. b is a constant and had the value 0.37 Å.[225]

Appendix II

Table A.1: Structural parameters of the $ZrSe_3$ layer (subunit A).

Subunit A				
	***a* / Å**	***b* / Å**	***c* / Å**	
	3.7630	5.3496	9.14654	
Atom	***x***	***y***	***z***	***Occupancy***
Zr(1)	0.0000	0.5000	0.3340	1
Zr(2)	0.5000	0.0000	0.6660	1
Se(1)	0.5000	0.2648	0.1617	1
Se(2)	0.5000	0.7352	0.1617	1
Se(3)	0.0000	0.2352	0.8383	1
Se(4)	0.0000	0.7648	0.8383	1
Se(5)	0.5000	0.5000	0.5482	1
Se(6)	0.0000	0.0000	0.4518	1

Table A.2: Structural parameters of the Ca/NH_3 layer (subunit B).

Subunit B				
	***a* / Å**	***b* / Å**	***c* / Å**	
	3.76301	5.3496	2.9584	
Atom	***x***	***y***	***z***	***Occupancy***
Ca(1)	0.5000	0.5000	0.5000	0.2
N(1)	0.5000	0.0000	0.5000	0.6
H(1)	0.3000	0.0900	0.3000	0.205
H(2)	0.3000	0.0900	0.7000	0.205
H(3)	0.7000	0.0900	0.3000	0.205
H(4)	0.7000	0.0900	0.7000	0.205
H(5)	0.3000	0.9100	0.3000	0.205
H(6)	0.3000	0.9100	0.7000	0.205
H(7)	0.7000	0.9100	0.3000	0.205
H(8)	0.7000	0.9100	0.7000	0.205

Appendix III

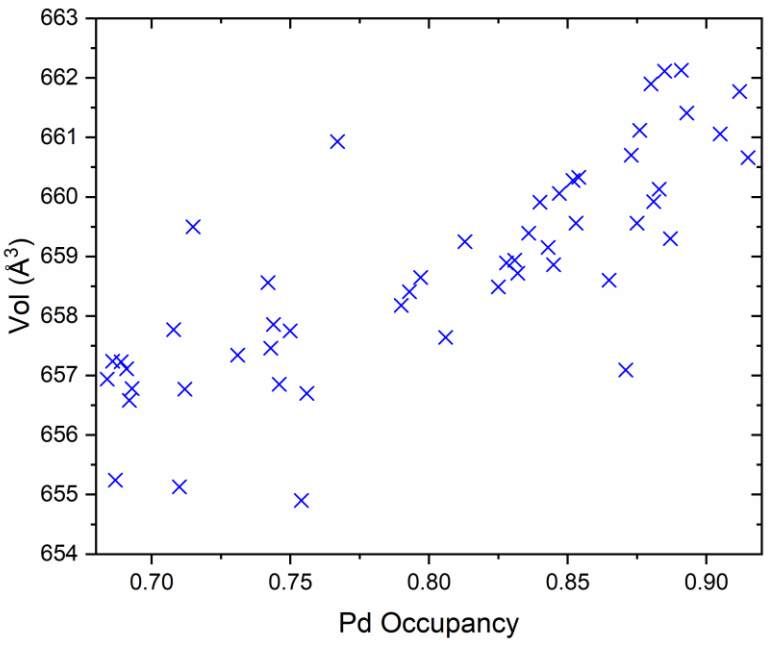


Figure A.1: Unit cell volume of the $Nb_2Pd_xSe_5$ phases measured by Neu *et al.*[162]

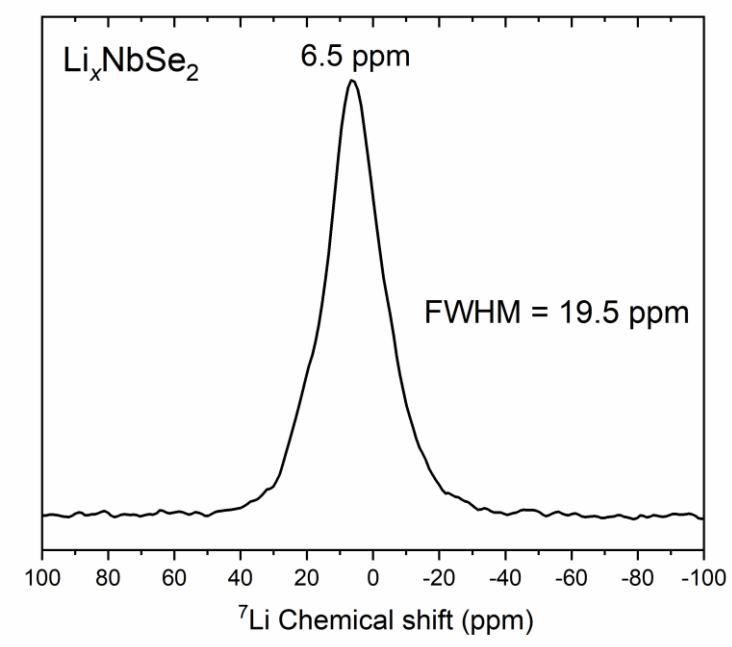


Figure A.2: Solid-state ^{7}Li MAS NMR spectra of Li intercalated $NbSe_2$, showing a peak at 6.5 ppm.

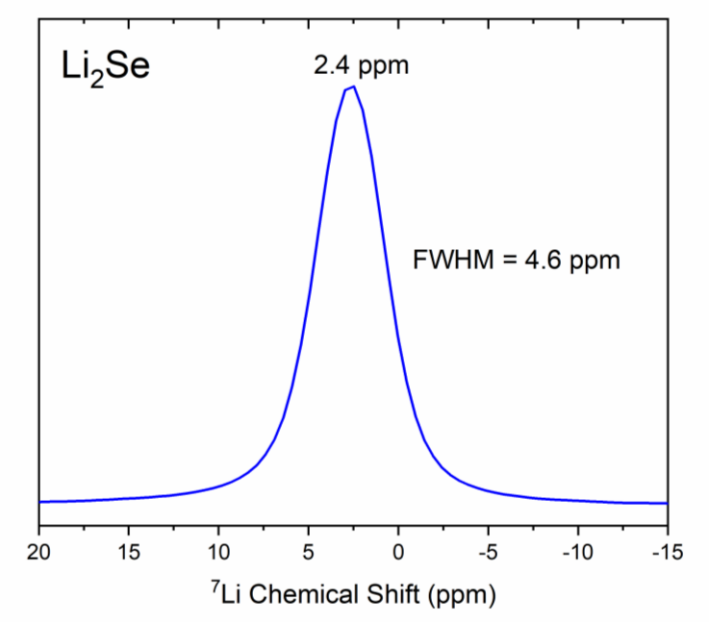


Figure: A.3: Solid-state ^{7}Li MAS NMR spectra of Li intercalated $NbSe_2$, showing a peak at 2.4 ppm